Segmentation and Skeletonization Techniques for Cardiovascular Image Analysis

Segmentatie- en skeletonisatietechnieken voor cardiovasculaire beeldanalyse

Danilo Babin

Promotoren: prof. dr. ir. W. Philips, prof. dr. ir. A. Pižurica
Proefschrift ingediend tot het behalen van de graad van
Doctor in de Ingenieurswetenschappen: Computerwetenschappen

Vakgroep Telecommunicatie en Informatieverwerking
Voorzitter: prof. dr. ir. H. Bruneel
Faculteit Ingenieurswetenschappen en Architectuur
Academiejaar 2013 - 2014

UNIVERSITEIT GENT

ISBN 978-90-8578-632-0
NUR 954
Wettelijk depot: D/2013/10.500/65

I do not think there is any thrill that can go through the human heart like that felt by the inventor as he sees some creation of the brain unfolding to success.
—Nikola Tesla

Members of the jury

prof. dr. ir. Rik Van de Walle (Ghent University, chairman)
prof. dr. ir. Guy De Tré (Ghent University, secretary)
prof. dr. ir. Wilfried Philips (Ghent University, supervisor)
prof. dr. ir. Aleksandra Pižurica (Ghent University, supervisor)
prof. dr. ir. Rudi Deklerck (Vrije Universiteit Brussel)
prof. dr. md. Luc Defreyne (Ghent University Hospital)
prof. dr. ir. Cornelis H. Slump (University Twente)
prof. dr. ir. Patrick Segers (Ghent University)
dr. ir. Ewout Vansteenkiste (Ghent University)
dr. ir. Hiêp Luong (Ghent University)

Affiliations

Research Group for Image Processing and Interpretation (IPI)
iMinds
Department of Telecommunications and Information Processing (TELIN)
Faculty of Engineering and Architecture
Ghent University

Sint-Pietersnieuwstraat 41
B-9000 Ghent
Belgium

Acknowledgements

This work would never have been carried out without the help and support of colleagues, friends and family. I would like to express my gratitude to the following people:

First and foremost, I would like to thank my advisers, Prof. dr. ir. Aleksandra Pižurica and Prof. dr. ir. Wilfried Philips for the opportunity to conduct research in attractive research field of image processing. I would also like to thank them for numerous constructive discussions about my research topic and for allowing me a great freedom in following my interests.

I would also like to thank all my TELIN colleagues and ex-colleagues for creating a nice atmosphere that makes work pleasant. Patrick Schaillée, Annette Nevejans, Sylvia Moeneclaey and Alice Verheylesonne provided me with their precious administrative help. I would also like to thank Philippe Serbruyns and Davy Moreels who were always ready to help me in solving (sometimes exotic) software and hardware problems.

I would especially like to express my gratitude to all my ex-YU friends and colleagues for always being there when I needed them. I am deeply grateful to Ewout Vansteenkiste and Dan Devos for investing a lot of effort in putting my work to practical use (and for having some great times in the process).

Finally, I would like to thank my family and relatives for their love and support. I am grateful to my uncle Dimitrije for being a constant work inspiration and to my brother Vitomir for all the laughs when I needed to relax from work. I am grateful to my parents Milica and Nestor for their trust, support and love. Last, but not least, I would like to thank my girlfriend Milica for her love, support and everlasting patience.

Danilo Babin
October, 2013.

Samenvatting

Tegenwoordig zijn cardiovasculaire aandoeningen ongeveer verantwoordelijk voor een derde (33 %) van alle sterfgevallen. Dat is het hoogste percentage van alle ziekten. Twee specifieke cardiovasculaire problemen worden aangepakt in dit proefschrift. Het eerste probleem is de nauwkeurige ontleding van een arterioveneuze malformatie (AVM) in bloedvaten waaruit de AVM bestaat. Deze ontleding kan gebruikt worden bij de embolisatie procedure. Het tweede probleem is het kwantificeren van de stijfheid van de aorta, die wordt gebruikt bij de diagnose en de prognose van ziektes. Om deze cardiovasculaire problemen op te lossen worden verschillende beeld modaliteiten gebruikt.

Medische beeldvorming ontwikkelde zich snel sinds de ontdekking van röntgenstraling in 1895. Medische beelden zijn geëvolueerd van eenvoudige 2-D projecties naar multi-dimensionele data (bijvoorbeeld 4-D of zelfs 5-D beelden). Deze complexe beelden zijn echter vaak moeilijk te interpreteren. Medische beelden tonen een groot aantal weefsels en organen, waarvan sommige moeilijk van elkaar te onderscheiden zijn (dit is over het algemeen de situatie bij bloedvaten). Het probleem is dat een efficiënte manier nodig is om klinisch relevante informatie uit deze beelden nauwkeurig te extraheren. Gelukkig evolueerden computers net zoals de medische hulpmiddelen. Het beschikbare computergeheugen en rekenkracht zijn voldoende om de overvloed aan gegevens te verwerken die door medische scanners gegenereerd worden. Graphics Processing Units (GPU) laten een snelle parallelle data-analyse toe. Hierdoor is aan alle voorwaarden voldaan voor de uitvoering van beeldverwerkingsmethoden die de relevante informatie uit complexe medische beelden kunnen extraheren. Deze methoden worden medische beeldanalysemethoden genoemd.

Beeldanalyse is een kwantificatie proces van afbeeldingen en bestaat dusdanig het uit wiskundige metingen. Om de metingen te verrichten, moeten we de bloedstructuren scheiden van hun omgeving. De methoden die de bloedvaten scheiden van de omliggende weefsels zijn bloedvaten segmentatie methoden (zij detecteren pixels die tot de

bloedvaten behoren). Een andere belangrijke klasse van beeldanalysemethoden zijn skeletonisatie methoden (extraheren de middellijnen van de gesegmenteerde vaten). Dit proefschrift gaat over de analyse van cardiovasculaire beelden: wij ontwikkelen segmentatie en skeletonisatie methoden voor het kwantificeren van vasculaire structuren en functies. Ons doel is om de artsen te ondersteunen in de diagnose en de behandeling van cardiovasculaire ziekten.

Bij aortastijfheid willen wij voorzien van pulse wave velocity (PWV) en distensibiliteit berekening (om de stijfheid van de aorta te schatten). Methoden zijn nodig om de aorta middellijn te extraheren, zijn lengte te meten, om de aortawand te segmenteren en om de pulse waves te analyseren. In het geval van de AVM ontleding hebben wij methoden nodig voor de analyse van de complete cerebrale bloedvaten structuur, deze analyse kan helpen bij de AVM embolisatie procedure. De methoden moeten volgende punten realiseren: de segmentatie van de cerebrale bloedvaten, de extractie van de bloedvaten middellijnen, de berekening van de beste paden moeten door bloedvaten structuur (dit voor verschillende criteria) en tot slot de extractie van de AVM regio met zijn ontleding van slagaders, aders en de nidus.

Veel segmentatiemethoden gebruiken hoge hoeveelheid voorkennis over de bloedvaten. De invoering van hogere-niveau kennis levert goede segmentatie resultaten in geval van gezonde vaten, want ze kunnen goed worden gemodelleerd met cilindrische of buisvormige vormen. Echter, vaatafwijkingen zijn zeer moeilijk te modelleren. Ze verschijnen op verschillende posities en hebben “onvoorspelbare” vormen. Anderzijds zijn de structuren van vaatafwijkingen van het grootste belang voor chirurgen, aangezien hun duidelijke afbakening en structuuranalyse aanzienlijk bijdraagt tot de klinische praktijk. Dit is het geval indien we arterioveneuze malformaties segmenteren.

We hebben veralgemeende profielen ontwikkeld voor de AVM segmentatie, als een veralgemening van morfologische profielen (MP). Nieuwigheden van onze methode zijn: (1) de introductie van een structuurelement (SE) gedefiniëerd door twee parameters, die een meer algemene pixel verzameling is in vergelijking met klassieke structuur elementen; (2) we maken gebruik van verschillende operatoren en hun combinaties, in tegenstelling tot het minimum en maximum als de basis van morfologische operaties; (3) we ontwikkelen een methode voor de beoordeling van de profiel operatoren. De resultaten op fantomen en echte beelden tonen aan dat veralgemeende profielen beter presteren dan de huidige state of the art methoden voor AVM segmentatie.

Bij het uitvoeren van de AVM embolisatie moeten we de hele structuur van de cerebrale bloedvaten kennen om de katheter met succes naar de AVM te begeleiden. Dit betekent dat de gehele bloedvatenstructuur moet gesegmenteerd worden. De veralgemeende profielen methode is een multiscale methode en is tijdrovend wanneer toegepast op grote datasets. Segmentatie algoritmen in de klinische praktijk moeten echter zo snel mogelijk zijn. Om de hele cerebrale bloedvatstructuur te segmenteren (inbegrip van de AVM), hebben we een lijnvormige profielen methode geïntroduceerd. Het basisidee van deze benadering is om simpele structuur elementen (lijnen) te gebruiken, maar met toepassing van complexere operatoren. De belangrijkste nieuwe aspecten van deze methode zijn: (1) een nieuw wiskundig kader voor lijnvormige profielen; (2) het aantonen van de voordelen in termen van kwaliteit van de resultaten en de verbetering van de uitvoersnelheid ; (3) de introductie van een nieuw type van profiel operatoren. De resultaten op fantoom beelden tonen dat de lijnvormige profielen beter presteren dan de huidige state of the art methoden in termen van de hoeveelheid van gesegmenteerde bloedvatstructuren en Dice coëfficiënten.

Voor de AVM embolisatie procedure is de segmentatie alleen niet genoeg. De gesegmenteerde AVM bloedvaten moeten in slagaders, aders en de nidus worden ingedeeld om de katheter succesvol te navigeren en om embolisatie uit te voeren. Om deze reden hebben we een skeletonisatie methode ontwikkeld die de AVM ontleedt. De belangrijkste nieuwe aspecten zijn: (1) een nieuwe werkwijze voor de berekening van labels in geordende skeletonisatie die resulteert in zeer nauwkeurige middellijnen; (2) een methode voor het maken van een graaf skelet structuur van de verkregen skeletonisatie beelden; (3) een automatische methode voor AVM detectie en extractie, met de afbakening van de ader. De voorgestelde aanpak is gevalideerd op bloedvatfantomen van de ader en de AVM-structuur, en ook op de hersenen CTA beelden voor en na embolisatie. De resultaten tonen potentieel voor gebruik in chirurgische planning.

Ten slotte hebben we onze ontwikkelde segmentatie en skeletonizatie methoden aangepast om aortastijfheid te schatten. Aortastijfheid wordt geschat door pulse wave velocity (PWV) en aorta distensibiliteit berekening. De PWV en de aorta distensibiliteit worden berekend op basis van magnetische resonantie beelden (MRI). Dit vereist diverse segmentatie taken: de extractie van de aorta middellijn en segmentatie van de aorta wand, gecombineerd met signaalverwerking voor de analyse van de puls golf propagatie. We hebben ons onderzoek op gezonde vrijwil-

ligers en Marfan syndroom patiënten uitgevoerd. De resultaten van de PWV metingen werden vergeleken met gevalideerde software. De resultaten toonden hoge nauwkeurigheid en effectiviteit van de werkwijze voor de aorta PWV en distensibiliteit berekening.

Ons werk resulteerde in één gepubliceerd en vier ingediende artikelen in internationale tijdschriften in de Science Citation Index, waarvan drie als eerste auteur. Tien andere artikelen verschenen in de proceedings van internationale en nationale conferenties, waarvan negen als de eerste auteur.

Summary

In the present-day world cardiovascular diseases account for approximately one third (33%) of all deaths, which is the highest rate among all diseases. Two specific cardiovascular problems are addressed in this thesis. The first is the accurate decomposition of an arteriovenous malformation (AVM) into its comprising vessels for embolization procedure. The second problem is quantifying the aortic stiffness, which is used in diagnosis and prognosis of disease outcome. To aid solving these cardiovascular problems, various imaging modalities are used.

Medical imaging developed rapidly since the discovery of X-rays in 1895. Medical images have evolved from simple 2-D projections to multi-dimensional data (e.g. 4-D or even 5-D images). However, these complex images are often hard to interpret. Medical images show a multitude of tissues and organs, some of which are very hard to tell apart (this is a common case of blood vessels). The problem is that an efficient way is needed to accurately extract the clinically relevant information from these images. Fortunately, as medical devices advanced in development, so did computers. The available computer memory and processing power are sufficient to handle the abundancy of data produced by medical scanners. Graphics processing units (GPU) allow for fast parallel data analysis. Hence, all conditions are met for implementation of image processing methods that extract the relevant information from the complex medical data. These methods are called medical image analysis methods.

Image analysis is a process of quantifying images and as such, it is comprised of mathematical measurements. To perform the measurements we have to separate the blood vessel structures from their surrounding. The methods that separate the blood vessels from surrounding tissues are vessel segmentation methods (they extract pixels that belong to vessels in the image). Another important class of image analysis methods are skeletonization methods that extract centerlines of the segmented vessels. This thesis is about analysis of cardiovascular images: we develop segmentation and skeletonization methods for

quantifying vascular structures and functions. Our goal is to aid the physician in decision making for diagnostics and treatment of cardiovascular diseases.

In case of the aortic stiffness we want to provide for pulse wave velocity (PWV) and distensibility calculation (to estimate the aortic stiffness). Methods are needed to extract the aortic centerline and measure its length, to segment the aortic wall and analyze propagation of pulse waves. In case of the AVM decomposition we need methods for complete cerebral blood vessel tree analysis to aid in the AVM embolization procedure. The methods must allow for segmentation of the cerebral blood vessels tree, extraction of vessel centerlines, calculating best paths through the vessel tree for different criteria and extracting the AVM region with its decomposition to arteries, veins and the nidus.

Many segmentation methods incorporate a high amount of prior knowledge on blood vessels. The introduction of higher-level knowledge yields good segmentation results in case of healthy vessels, because they can be modeled well using cylindrical or tubular shapes. However, vessel anomalies are very hard to model. They appear at various positions and constitute "unpredictable" shapes. On the other hand, vessel abnormalities are the structures of the highest interest for surgeons, since their clear delineation and structure analysis significantly aids in clinical practice. This is the case when segmenting arteriovenous malformation.

For the AVM segmentation, we have developed generalized profiles, as a generalization of morphological profiles (MP). Novelties of our method are: (1) introduction of a structuring element (SE) controlled by two parameters, as a more general pixel set in comparison to classical structuring elements; (2) using various operators and their combinations applied to SE as opposed to minimum and maximum as the basis of morphological operations; (3) a method for evaluation of profile operators. The results on phantoms and real data show that generalized profiles outperform the current state of the art methods for AVM segmentation.

When performing the AVM embolization, the structure of the whole cerebral blood vessel tree needs to be known in order to efficiently guide the catheter to the AVM. This means that the whole blood vessel tree needs to be segmented. The generalized profiles method is a multiscale method, and is time consuming when applied to large data sets. However, the clinical practice requires from the segmentation algorithms to be as fast as possible. Hence, for the purposes of segmenting the whole cerebral blood vessel tree (including the AVM), we have intro-

duced a line-shaped profiling method. The main idea of this approach is to use simple structuring elements (lines), but to apply more complex operators on them. The main novelties of this method are: (1) a new mathematical framework for line-shaped profiling, (2) the demonstration of the advantages in terms of quality of results and the execution speed-up, (3) the introduction of a new type of profile operators. The results on phantom data show that line-shaped profiles outperform current state of the art methods in terms of the amount of segmented blood vessel structures and Dice coefficients.

For the AVM embolization procedure, the segmentation alone is not enough. The segmented AVM blood vessels need to be classified into feeding arteries, draining veins and the nidus in order to successfully navigate the catheter and perform embolization. For this reason we have designed a skeletonization method to perform AVM decomposition. The main contributions are: (1) a method for calculation of labels in ordered skeletonization yielding highly accurate centerlines; (2) a method for inferring skeleton structure from the obtained skeletonization images and (3) an automatic method for AVM detection and extraction, with the delineation of the draining vein. The proposed approach is validated on blood vessel phantoms representing the vein and the AVM structure, as well as on brain CTA images before and after embolization. The results indicate potentials for use in surgical planning.

Finally, we adapted our developed segmentation and skeletonization methods with the goal to create an application for estimating aortic stiffness through pulse wave velocity (PWV) and aortic distensibility. Obtaining the PWV and the aortic distensibility from magnetic resonance imaging (MRI) data requires diverse segmentation tasks, namely the extraction of the aortic center line and the segmentation of aortic walls, combined with signal processing methods for the analysis of the pulse wave propagation. In our study was performed on healthy volunteers and Marfan syndrome patients and the results of PWV measurements were compared to a validated software. The results showed high correctness and effectiveness of our method for the aortic PWV and distensibility calculation.

Our work resulted in one published and four submitted papers in journals in the Science Citation Index, of which 3 as first author. In total, 10 other papers appeared in the proceedings of international and national conferences, of which 9 as the first author.

Contents

Symbols and acronyms used in this thesis

Symbols

$\mathbf{p}$	Pixel (voxel)
$g(\mathbf{p})$	Gray value of pixel
S_n	Structuring element of size n
$D_{r,n}$	Structuring element with parameters r and n
$R_{r,n}$	Ring-shaped structuring element with parameters r and n
L_n	Line-shaped structuring element of orientation n
$\mathrm{opr}^{(i)}$	An operator determined by superscript i
$f^{(i)}$	Profile operator determined by superscript
$h^{(i,j)}$	Second order base profile operator determined by superscripts
$\overline{f}$	Average operator value for pixels in image
$s(A, B)$	The Dice coefficient for sets A and B
$d_H(A, B)$	The Hausdorff distance for sets A and B
$d(\mathbf{p}, \mathbf{q})$	The Euclidean distance between positions $\mathbf{p}$ and $\mathbf{q}$
B	Base profile function set
$\rho(\mathbf{p})$	R-profile measure
$\nu(\mathbf{p})$	N-profile measure
G	Graph
E	Edge set
V	Vertex set
$G[V']$	Graph induced from vertex set V'
$A(v)$	Set of vertices adjacent to vertex v
S	Graph-type skeleton
L	Skeleton link set
N	Skeleton node set

Acronyms

1-D	One Dimensional
2-D	Two Dimensional
3-D	Three Dimensional
3DRA	3-D Rotational Angiography
AVM	Arteriovenous Malformation
CMR	Cardiac Magnetic Resonance imaging
CNN	Cellular Neural Networks
CT	Computed Tomography
CTA	Computed Tomography Angiography
CURVES	Curve evolution for Vessel Segmentation
DOHT	Distance Ordered Homotopic Thinning
DSA	Digital Subtraction Angiography
DTI	Diffusion Tensor Imaging
ECG	Electrocardiogram
GAC	Geodesic Active Contours
GP	Generalized Profiles
GVF	Gradient Vector Flow
HCVM	Highest Cost Vertex Merging
LP	Line-shaped Profiles
MAT	Medial Axis Transform
MP	Morphological Profiles
MR	Magnetic Resonance
MRA	Magnetic Resonance Angiography
MRI	Magnetic Resonance Imaging
ND	Normalized Dice coefficient
PC	Personal Computer
PWV	Pulse Wave Velocity
RBF	Radial Basis Function
RCAC	Region Competition based Active Contour
ROI	Region Of Interest
RSE	Ring-shaped Structuring Element
SE	Structuring Element
VMTK	Vascular Modeling Toolkit
VTK	Visualization Toolkit
XR	X-Rays

1

Introduction

Nowadays cardiovascular diseases account for approximately one third of all deaths, which is the highest rate among all diseases. Various imaging modalities are used for diagnosing and treatment of cardiovascular diseases. The problem is that an efficient way is needed to accurately extract the clinically relevant information from these images. In other words, we need accurate and fast image analysis algorithms. This thesis is about analysis of cardiovascular images: we develop segmentation and skeletonization methods for quantifying vascular structures and functions. Our goal is to aid a physician in decision making for diagnostics and treatment of cardiovascular diseases.

1.1 Vascular image analysis

Image analysis is a process of quantifying images and as such, it is comprised of measurements. To perform the measurements we have to separate the blood vessel structures from their surrounding. Methods that perform this are vessel segmentation methods. In this thesis we propose novel methods for vessel segmentation (extracting pixels that belong to vessels in the image) and skeletonization (finding centerlines of the segmented vessels).

In the beginning of medical imaging, the images were assessed visually. A physician would look at the image, perform manual segmentation (e.g. by drawing on the image or just by rough estimation of regions of interest), which was used for decision making. However, as the time passed, more advanced medical scanners have been designed, yielding high quantity of complex data. Some of these data are very hard to interpret because of their multi-dimensionality (e.g. 4-D images have become common in today's practice). Manual analysis (in 2-D

slice-by slice manner) has become exceedingly time consuming (manual analysis of some images can take weeks to perform). Furthermore, the images show a multitude of tissues and organs, some of which are very hard to tell apart (this is a common case with blood vessels). Hence, image analysis algorithms have been designed to derive relevant information from abundant and complex medical data for decision making. The parallel processing on Graphics Processing Units (GPU) allows for fast and often real-time data analysis. Image analysis methods allow for easy quantification of medical images, while lowering the intra-observer variability.

One problem with segmentation methods is that their performance is hard to evaluate due to nonexistent ground truth (golden standard information). In other words, the segmented vessels are in reality often physically inaccessible (e.g. a surgery would be needed to access the cerebral blood vessels). This issue is mostly resolved by designing (either software or hardware) phantoms. In case of a software phantom, the imaging artifacts and noise are added to create realistic scanner images. These images are processed and the segmentation result is compared to the phantom. Although designing good segmentation algorithms is a difficult task, there is a clear advantage of using them in diagnostic and clinical practice instead of visual image interpretations. The segmentation algorithms will allow quantitative measurements on vascular images giving an added value to decision making.

1.2 Cardiovascular diseases and anomalies

1.2.1 Cerebral Arteriovenous malformation (AVM)

Cerebral arteriovenous malformation (AVM) represents a highly entangled vessel structure with a high possibility of rupture, posing a great health risk factor. It appears at locations where the arterial vessels merge directly with venous vessels (capillary vessels are omitted). Since the vessel walls of the veins are more elastic than the aortic ones, these walls deform into a *nidus*. The nidus permits shunting of high pressure arterialized blood from *feeding arteries* (they "feed" the AVM with blood) to thin-walled *draining veins* (they drain the blood from the AVM).

AVMs most often cause cerebral hemorrhage, which is associated with 10-20% morbidity and 10-30% mortality. Seizure is the second most frequent result of an AVM. It is mostly associated with superficial

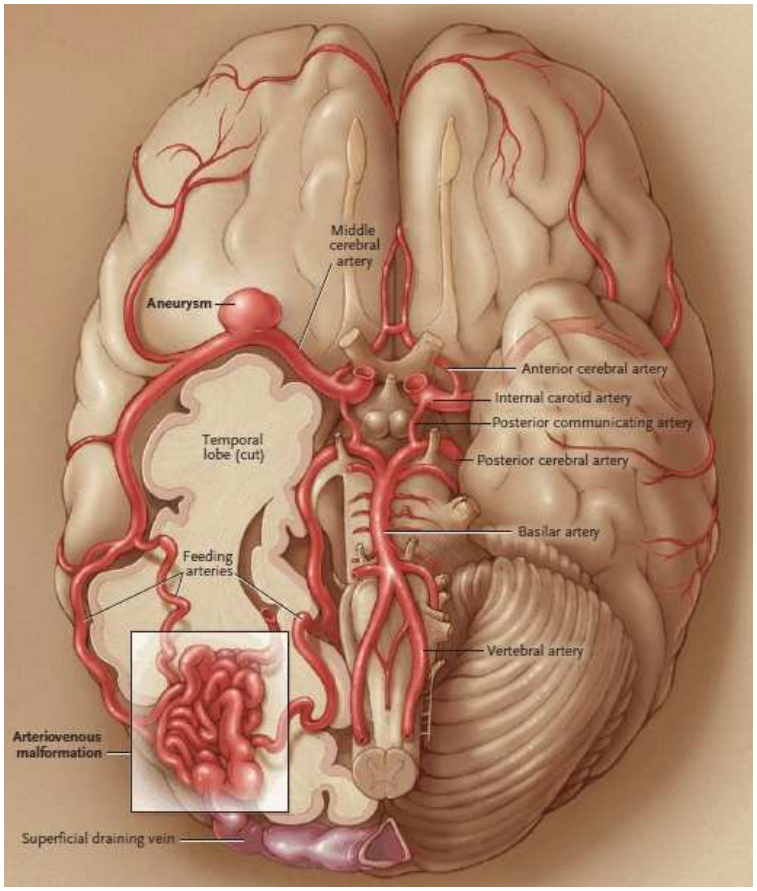

Figure 1.1: Illustration of a brain arteriovenous malformation (AVM) [Friedlander 07].

AVMs and in particular those residing within the temporal lobe. AVM can also cause headache or progressive neurological decline. Unfortunately, most AVMs are completely asymptomatic and are diagnosed as an incidental find (i.e. they are usually found by accident during an examination of another type).

Most AVMs are well visible on CT and MRI images, although small lesions might sometimes prove difficult to identify. However, for thorough examination and clinical planning, all AVMs require catheter angiography to fully assess their architecture and to examine for associated aneurysms. Fig. 1.2 shows images from a digital subtraction angiography (DSA) time sequence taken for the examination of an AVM.

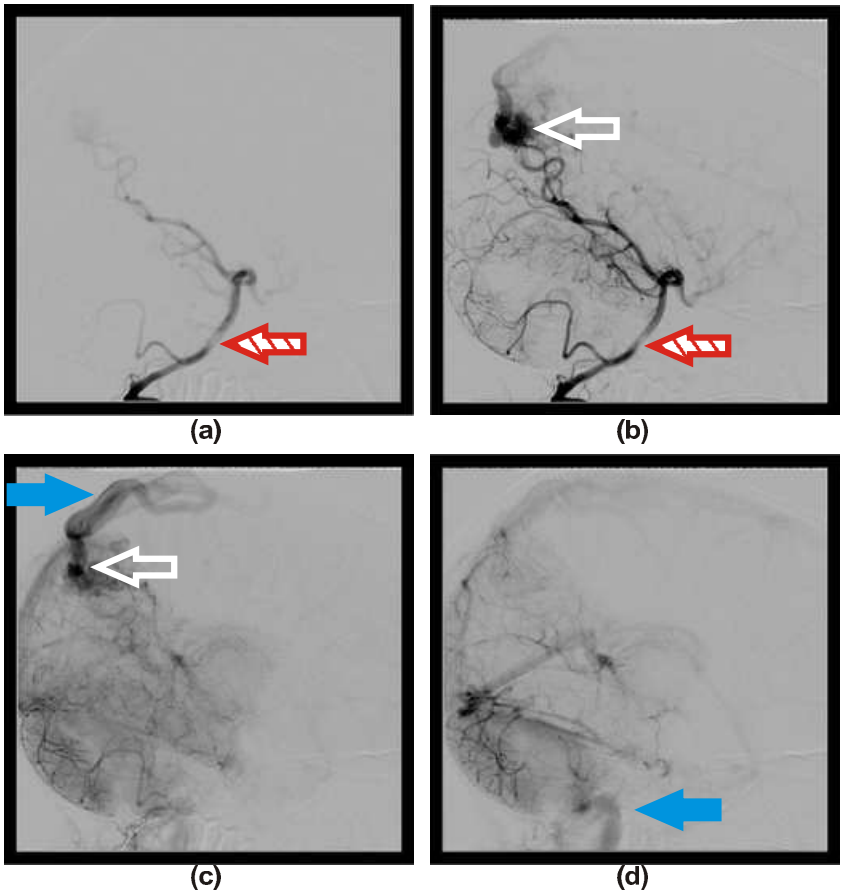

Figure 1.2: Digital subtraction angiography (DSA) of a cerebral AVM. (a) Arterial phase where only arteries are visible (striped arrow). (b) Arteries are visible with the AVM (outlined arrow) and a part of a vein. (c) Contrast agent diffuses into capillaries, but vein is very visible (filled arrow). This indicates that blood flows directly from arteries into the vein. (d) Venous phase shows mostly venous blood vessels.

Three phases can be distinguished during the injection of the contrast material into an artery. The first phase is the *arterial phase*, where only the arteries are covered by the injected contrast agent (hence, they are the only vessels visible as seen in Fig. 1.2a). The second phase is the one during which the contrast agent diffuses into the capillaries (see Fig. 1.2c). Finally, in the *venous phase* the contrast agent has entered venous blood vessels (therefore, veins are visible as in Fig. 1.2d). The

listed angiography phases are often used to determine the existence of small AVMs. In case of AVM the arterial blood flows directly into veins. Hence, the arterial and venous phase are not going to be clearly separated. Fig. 1.2b shows a part of the vein visible in the arterial phase, which clearly indicates the presence of an AVM.

The following options exist for AVM treatment: micro-surgical resection, Gamma Knife radiosurgery, endovascular embolization, observation or multimodality treatment. Microsurgical resection is a surgery to acutely remove the brain AVM. The disadvantage of this approach is its high invasiveness (longer hospitalization is needed), and it sometimes carries a significant risk. Radiosurgery involves stereo-tactically targeting an AVM with high-dose radiation in order to thicken the AVM. It is important to minimize the radiation dose in the surrounding brain tissue. The advantage of this procedure is a very short period of recovery with low risk of the procedure. However, the main disadvantage is that it takes about 1 to 3 years for the AVM to thicken, during which the risk of hemorrhage remains. This procedure is also limited to smaller lesions (i.e. diameter smaller than 3 cm). Endovascular embolization involves guiding a microcatheter through the blood vessel tree into the AVM nidus, after which the embolic agent is administered to fill in the nidus and reduce blood flow. Its advantages include a less invasive procedure (compared to surgery), a short period of hospitalization, and a relative short period of overall recovery. Its disadvantages are that endovascular therapy can at times carry significant risk and that it uncommonly leads to complete AVM obliteration. Because of these reasons, embolization is often combined with radiosurgery and surgical resection. In this thesis we have developed a number of image processing methods to reduce the risk of embolization procedure and to improve AVM obliteration rate.

In order to determine the optimal approach to AVM treatment, several grading systems have been developed. The most common AVM grading system is the Spetzler-Martin (S-M) Grading System (see Table 1.1), which is based on the size, position and type of venous drainage of AVMs. The points assigned for each of the listed characteristics are summed up to give the grade of the AVM. AVMs of grade 1 and 2 are generally considered operable. They are small, superficial, and located in non-eloquent site (they are not proximate to one of the following: sensimotor, language, visual cortex, hypothalamus, thalamus, internal capsule, brain stem, cerebellar peduncles or cerebellar nuclei). AVMs of grade 3 and 4 require discussion on a case-by-case basis for best course of treatment. They are large, deep, and situated in neurologically critical

Table 1.1: Spetzler-Martin (S-M) Grading System for AVMs.

Characteristic	Points
AVM Size	
Small (<3 cm)	1
Medium (3-6 cm)	2
Large (>6 cm)	3
Location	
Non-eloquent site	0
Eloquent site	1
Venous drainage	
Superficial	0
Deep	1

areas. Malformations of grade 5 are considered inoperable.

1.2.2 Stiffness of abdominal aorta

The aorta is the largest artery in the human body that represents the main "highway" of the blood traveling from the heart into other organs and tissues (see Fig. 1.3). Normal functioning of aorta includes expanding of vessel walls to absorb energy passed by the heart that pumps blood into the aorta. For this reason, the aorta needs to be elastic. As the age increases, the aorta becomes stiffer, which yields an increase in systolic blood pressure and decrease in diastolic pressure after the age of 60. Increasing the systolic blood pressure and lowering the diastolic blood pressure reduces coronary perfusion. This means that the risk of the pressure-induced damage on coronary and cerebral arteries is increased, together with increased susceptibility to myocardial ischemia (higher possibility of getting a heart attack). Many (common) diseases have been associated with the increase of aortic stiffness (e.g. hypertension and diabetes).

Arterial stiffness is defined as the arteries' capacity to expand and contract during the cardiac cycle. *Aortic compliance* is used to estimate the aortic stiffness and is defined as the change in volume for a given pressure change. It is related to the change in diameter during the heart cycle. *Aortic distensibility* is the change in the initial aortic volume or diameter. A loss of arterial elasticity results in reduced arterial compliance and distensibility. A number of methods exist for assessment of arterial stiffness.

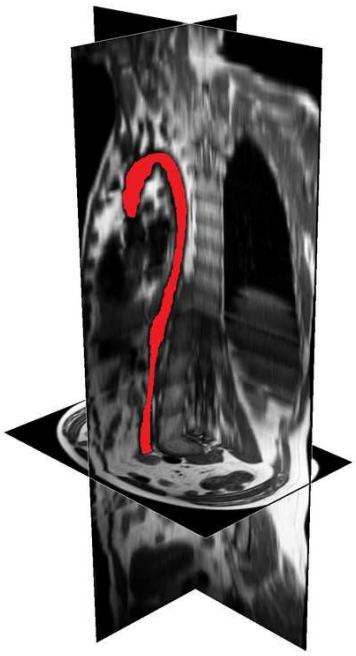

Figure 1.3: 3-D MRI image of abdomen with marked aorta [Babin 13a].

Pulse pressure is the difference between systolic and diastolic blood pressure and it is the consequence of cardiac contraction. Its main characteristic is that it is strongly influenced by the properties of the arterial tree. As we mentioned earlier, systolic blood pressure increases with age, while diastolic pressure tends to decrease because of the aortic stiffening. This results in significant increase in pulse pressure. Pulse pressure, as an estimate of the aortic stiffness, can be measured with a standard sphygmomanometer that is widely available. However, this measure can be highly inaccurate due to pulse wave amplification from the aorta to the peripheral arteries, which mostly influences systolic blood pressure.

Pulse wave velocity (PWV) is the speed of the pressure wave, generated by cardiac contraction, which travels from the aorta to the peripheral arteries. It is mostly influenced by the aortic stiffness and lumen diameter. PWV is calculated by measuring the time for the pulse to pass between two points with known distance. The measurement usually involves recording the pulse wave at (at least) two locations. The recorded pulse waves are compared to the start moment of the R

wave of a simultaneously recorded ECG. The PWV can be measured using Doppler ultrasound or magnetic resonance (MR) imaging, which we discuss in this thesis. Pulse wave velocity is a method for estimating the aortic stiffness, which has been widely applied and has been found to be both robust and reproducible. It is a good predictor of cardiovascular disease and mortality in hypertensive patients, patients with end-stage renal disease, as well as in diabetic and elderly population samples.

Pulse wave analysis (PWA) involves comparing the recorded pulse waves with the expected pulse wave outcomes [Wilkinson 97]. Recorded pressures and a validated generalized transfer function are used to generate the corresponding pulse waveform [Fetics 99]. The augmentation index (AIx), as a measure of arterial stiffness, is calculated as the difference between the first and second systolic peaks expressed as a percentage of the central pulse pressure. Satisfactory waveform recordings from the radial artery are typically obtained within a few minutes by a trained examiner. The problem when using AIx is that it is also influenced by peripheral vascular resistance and by the distending effect of an elevated blood pressure. Another problem is that the generalized transfer function is not appropriate for all patients (e.g. diabetes) or drugs, which makes this measure unreliable [Kelly 01]. *Diastolic pulse contour analysis* is used for compliance assessment. In this case, the diastolic portion of the pressure pulse contour is analyzed.

Imaging modalities used to estimate aortic stiffness are ultrasound and magnetic resonance imaging (MRI). *Ultrasound* is used to calculate aortic stiffness by measuring its distensibility and compliance. This is done by measuring the minimum and maximum aortic diameters from the obtained images. The advantage of ultrasound is its non-invasiveness, ease of use and fast examination. *Magnetic resonance imaging* (MRI) can be used for the most thorough estimation of aortic stiffness. MRI allows for stiffness assessment through distensibility, compliance, pulse wave velocity and pulse wave analysis. MRI measurements have proven as the most accurate and reproducible. The problem is that this examination requires expensive equipment, while being time-consuming.

1.2.2.1 Factors that affect aortic stiffness

We address in this section factors that affect aortic stiffness. This will show that aortic stiffness is a good estimate of overall patient health.

Age is an important factor influencing the aortic stiffness. It

has been proven that the stiffness increases with age, which in turn increases the risk of heart disease.

Hypertension is a wide-spread cardiovascular disease, which makes it a very important influencing factor of arterial stiffness [Laurent 01]. Large number of studies found an increase in aortic stiffness due to hypertension. Recent research shows that the connection between hypertension and aortic stiffness is twofold: lower arterial elasticity is related to the development of hypertension. Hence, aortic stiffness is an independent predictor of progression to hypertension.

Physical activity was proven to have a positive effect on overall cardiovascular health. Physical activity modifies cardiovascular risk factors such as blood pressure, lipid profile, and body weight in a favorable manner [Rönnback 07].

Muscle fiber-type distribution is related to type of physical activity performed and differs between elite athletes of various types of sports [Hernelahti 05]. A high proportion of type I (slow-twitch) fibers is generally found in endurance sports athletes, while speed and power sports athletes have a preponderance of type II (fast-twitch) fibers. Endurance athletes have a substantially lower risk of developing atherosclerotic disease and hypertension compared with power sport athletes and the general population. Age-induced aortic stiffening is less pronounced in those who engage in regular endurance exercise.

Apart from the mentioned factors, the relation of aortic stiffness has been established with the metabolic syndrome, inflammation levels in healthy individuals, renal insufficiency, smoking and alcohol consumption.

1.2.2.2 Treatment of arterial stiffness

Vasodilating agents easily reduce the dynamic component of arterial stiffness by relaxing smooth muscle cells in muscular arteries and arterioles. This treatment improves multiple measures of aortic stiffness (blood pressure, pulse wave velocity and reflection).

Drugs affecting vessel wall structure actually modify the structure of arterial walls. Besides reducing arterial stiffness (measured through pulse wave velocity), the drugs are proven to cause significant reduction in pulse pressure. Other drugs that are used to treat diseases related to aortic stiffness (e.g. diabetes) can also help in treating the stiffness

Sodium intake has a high influence on the aortic stiffness. High

salt intake accelerates arterial aging, and both short-term and long-term sodium restriction decreases arterial stiffness independently from the effect on mean blood pressure.

Weight loss reduces both blood pressure, which in turn has a positive effect on aortic stiffness. However, it has also been shown that weight loss reduces arterial stiffness independently of blood pressure (the examination was done on type 2 diabetes patients).

1.2.3 Clinical goals

This thesis presents the work on solving two problems in connection to vascular structures: quantifying the aortic stiffness and accurate AVM decomposition for the embolization procedure. In order to estimate the aortic stiffness we want to measure aortic pulse wave velocity and distensibility. Methods are needed to extract the aortic centerline and measure its length, to segment the aortic wall and analyze propagation of pulse waves. In the case of the AVM decomposition we need methods for complete cerebral blood vessel tree analysis to aid in the AVM embolization procedure. The methods must allow for segmentation of the cerebral blood vessels tree, extraction of vessel centerlines, calculating best paths through the vessel tree for different criteria and extracting the AVM region with its decomposition to arteries, veins and the nidus.

1.3 Novelties and contributions

The novelties and contributions of this thesis can be divided in two categories: (i) novel methods for image analysis, and (ii) novel applications for clinical use. The novelties in terms of vessel analysis approaches are:

1. Generalized profiling method used for the detailed segmentation of arteriovenous malformations. The algorithm outperforms the current state of the art segmentation methods [Babin 12a].

2. Line-shaped profiling method used for the segmentation of cerebral blood vessel system containing arteriovenous malformations. The method outperforms all other segmentation methods in terms of quality of segmentation, while achieving much higher computational efficiency than the generalized profiling method [Babin 13b].

3. A vessel skeletonization method for angiographic CT images with algorithms for extracting the highest radii and contrast agent intensity paths. The method automatically locates an AVM in the

blood vessel tree and performs its decomposition into constituting vessels (arteries, veins and the nidus) [Babin 13c].

4. A method for aortic pulse wave propagation analysis comprising of the method for segmentation of cardiac magnetic resonance images and the pulse wave analysis method [Babin 13a].

5. AVM and blood vessel tree phantoms used for validation of the segmentation and skeletonization results.

6. An aortic centerline extraction method for black blood MRI images. It incorporates the generalized profiling principle into creation of a grid type skeleton used for best path calculation. The method is robust to various artifacts and high presence of noise [Babin 12b]. A variation of this approach is used for segmentation of the abdominal aorta [Babin 09b].

In terms of clinical use, the listed methods have been implemented for two cases:

1. The application for complete cerebral blood vessel tree analysis with an emphasis on aiding in the AVM embolization procedure. This package allows a physician to segment the blood vessels tree, extract vessel centerlines, calculate best paths through the vessel tree for different criteria, extract the AVM region and decompose it into its main vessels.

2. The application for aortic pulse wave velocity (PWV) and aortic distensibility calculation to estimate stiffness of the aorta. The developed methods allow for centerline extraction and length measurements of the aorta, aortic wall segmentation, blood flow analysis. The results of PWV measurement correspond well to the results obtained with the validated software.

In terms of publications, so far this work resulted in two A1-publications [Babin 12a, Babin 13b], with three other A1-papers that are currently in review: [Babin 13c, Babin 13a, Devos 13]. Next to that, six publications were published in the proceedings of international peer-reviewed conferences: [Babin 08, Babin 09b, Babin 10, Babin 11c, Babin 12b, De Vylder 12] and three publications and abstracts in national conferences [Babin 09a, Babin 11a, Babin 11b].

1.4 Organization of the thesis

This section presents an overview of the content of the various chapters of the thesis.

Chapter 2: Cardiovascular imaging. In this chapter the most common cardiovascular imaging approaches and functions are introduced. The underlying imaging principles of the listed modalities are explained in order to clarify the properties of the obtained images. We focus on imaging aimed at solving two cardiovascular problems: embolization of arteriovenous malformations (AVM) and quantification of aortic stiffness. In the AVM case, X-ray based imaging is predominantly used: X-ray computed tomography (CT), digital subtracted angiography (DSA) and 3-D rotational angiography (3DRA), while magnetic resonance imaging (MRI) is mostly used for diagnosis and post-operative evaluation. However, for estimating the aortic stiffness MR imaging is used to asses both anatomy (bright-blood imaging and black-blood imaging) and the aortic function (velocity encoded imaging). Finally, we analyze techniques available to a physician to visualize the obtained images.

Chapter 3: Vessel Delineation Methods. This chapter reviews some of the common approaches in vessel delineation aimed at gaining information on the structure of blood vessels. The methods can be classified into three basic groups according to the type of the resulting delineation, namely segmentation, skeletonization and vessel enhancement. However, most of the algorithms today incorporate multiple methods into one to obtain more information on the vascular structure. Hence, our classification of vessel analysis techniques is based on the amount of higher-level (structural) information on vessels that they use. This results in four classes of algorithms that are sorted in ascending manner according to the amount of used vessel-specific information, namely: thresholding and region growing, local pixel neighborhood analysis, model based methods and other structure based methods. The conclusion of this chapter is that multiscale segmentation methods show high robustness without a need for fine parameter tuning. Hence, these methods are the motivation for our work presented in this thesis.

Chapter 4: Generalized Profiles. In this chapter we introduce generalized profiles (GP) method with the goal of using it to perform fine structure segmentation and vessel delineation of arteriovenous malformation (AVM). For surgery or embolization of AVM, a clear distinction between feeding arteries, nidus and vein of the AVM is of the

utmost importance. Novelties of our method are: (1) introduction of a structuring element (SE) controlled by two parameters, instead of only one parameter; (2) using various operators and their combinations applied to the structuring element, as opposed to minimum and maximum as the basis of morphological operations; (3) a method for evaluation of different operators. The results on AVM phantoms and real data demonstrate its effectiveness and potentials for fine delineation of the AVM.

Chapter 5: Line-shaped Profiles. In this chapter we examine the use of line segments as oriented SEs. The line segments will differ only in orientation, while having the maximum size (defined by the image). The goal is to segment the cerebral blood vessel tree together with an AVM, while achieving high computational efficiency (which is reduced when multiscale SEs are used). The main novelties of this method are: (1) a new mathematical framework for orientation-dependent profiling, (2) the demonstration of the advantage of using line segments as strictly oriented SEs (in terms of quality of results and the execution speed-up), (3) the introduction of a new type of profile operators (*second order profile operators*) and the method for their evaluation, and (4) the application to segmentation of the whole cerebral blood vessel tree. The method was validated on blood vessel tree and AVM phantoms, while the results on real 3-D image data show well segmented smooth blood vessel structures

Chapter 6: Skeletonization. In this chapter we propose a novel ordered thinning-based skeletonization used for arteriovenous malformation (AVM) vessel decomposition. The goal is to classify the segmented AVM blood vessels into feeding arteries, draining veins and the nidus in order to successfully navigate the catheter and perform AVM embolization. The main contributions are: (1) a new method for calculation of distances in ordered skeletonization yielding highly accurate centerlines; (2) two methods for inferring skeleton structure from the obtained skeleton images; (3) an automatic method for AVM detection and extraction, with the delineation of the draining vein. The proposed approach is validated on blood vessel phantoms representing the vein and the AVM structure, as well as on brain CTA images before and after embolization. The vein delineation method results show high correspondence to ground truth vein structures.

Chapter 7: Pulse Wave Velocity Calculation. In this chapter we present robust segmentation techniques for the pulse wave velocity (PWV) and aortic distensibility calculation as a complete image

and signal processing toolbox. The segmentation techniques are combinations of methods and ideas from preceding chapters on generalized profiles, line-shaped profiles and skeletonization. The introduced novelties are: (1) graph-based method for the centerline extraction of the thoraco-abdominal aorta for the length calculation from 3-D MRI data robust to artifacts and noise; (2) a new projection-based segmentation method for transverse aortic region delineation in cardiac magnetic resonance (CMR) images (3) a novel method for analysis of velocity curves in order to obtain pulse wave propagation times; (4) an application incorporating these methods for effective aortic stiffness measurement. In order to validate the proposed method we compare the obtained results with manually determined aortic centerlines and a region segmentation by an expert, while the results of the PWV measurement were compared to a validated software (LUMC, Leiden, the Netherlands). The obtained results show high correctness and effectiveness of our method for the aortic PWV and distensibility calculation.

Chapter 8: Conclusions. The final chapter states the global conclusions of the thesis and points out in which direction further related research might proceed.

2

Cardiovascular imaging

In this chapter we introduce some of the most common cardiovascular imaging modalities and their use. We focus on imaging for the two cardiovascular problems introduced in this thesis, namely: embolization of arteriovenous malformations (AVM) and quantifying aortic stiffness. In the AVM case, X-ray imaging is predominantly used: X-ray computed tomography (CT), digital subtraction angiography (DSA) and 3-D rotational angiography (3DRA), while magnetic resonance imaging (MRI) is mostly used for diagnosis and post-operative evaluation. For estimating the aortic stiffness MR imaging is used to asses both anatomy (bright-blood imaging and black-blood imaging) and the aortic function (velocity encoded imaging). We describe in this chapter the underlying imaging principles of the listed modalities and the resulting properties of the obtained images. Finally, we analyze visualization techniques available to a physician to represent the images.

2.1 X-ray Computed Tomography

In this and the next two sections we will explain the principles of X-ray imaging. For a more elaborate explanation refer to [Bushberg 11, Webb 12].

X-rays (discovered by Wilhelm Röntgen in 1895) are high energy photons able to pass through the human body. The X-rays are attenuated by traveling through the body. Beer's law relates the attenuation in a fixed medium to the travel distance x as follows [Webb 12]:

$$I(x) = I_0 \, e^{-\mu x}, \tag{2.1}$$

where the μ is the linear absorption coefficient, x is the object thickness and I_0 the incident beam energy. It is important to emphasize that the

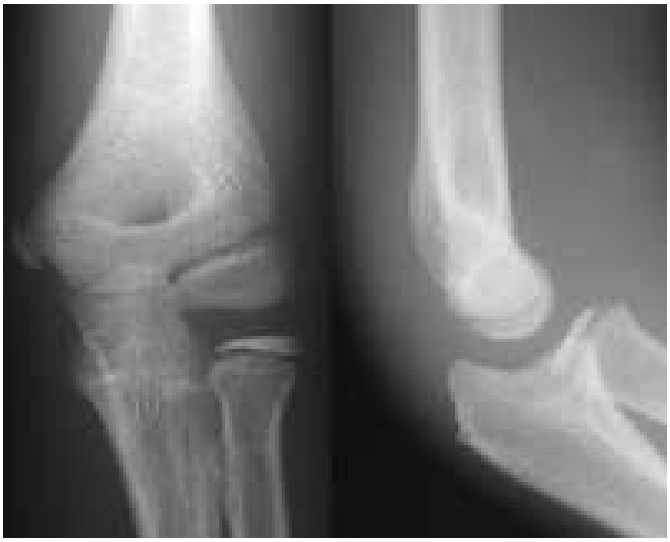

Figure 2.1: Typical X-ray image. Bones are well visible because they absorb more photons than the surrounding tissue. The 2-D image does not give enough depth information as a 3-D image (source: Wikipedia).

linear absorption coefficient is linked to the local density of the material that the beam passes through. In other words, the objects that have higher density will absorb more photons and appear bright in the X-ray image (e.g. bones and metal implants). On the other hand, objects with lower density will absorb fewer photons and appear dark in the X-ray image. A typical X-ray image is shown in Fig. 2.1. The obvious problem of conventional X-ray radiography is the loss of depth (3-D) information, because the structure of the body has been projected onto a 2-D film. For this reason, computed tomography (CT) was introduced (see Fig. 2.2).

With the CT approach, the 3-D body is scanned in planar slices. Hence, the resulting 3-D image is in fact a sequence of 2-D slices. In general, the X-ray source is rotated with respect to the patient to obtain projections from various angles (see illustration in Fig. 2.3). A linear array of detectors measure the energy of X-rays for each specific source location through the body of the patient. The system rotates at the constant speed around the patient, acquiring a projection at each step. After the required number of projections is obtained, the Radon Transform is applied to reconstruct the 2-D image from the obtained projections. A CT slice of lungs is shown in Fig. 2.4.

Figure 2.2: An X-ray CT scanner [Gupta 08].

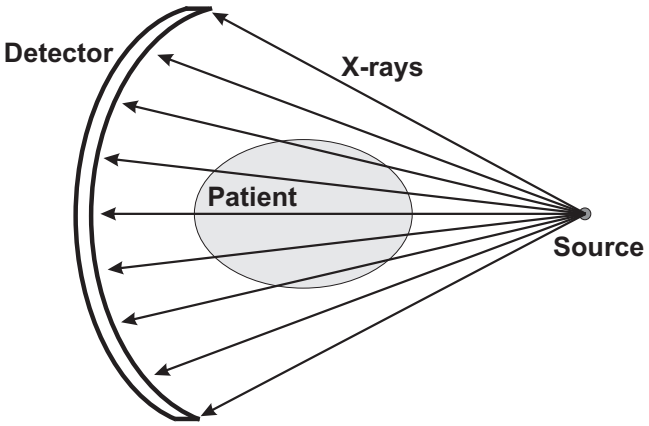

Figure 2.3: X-ray fan beam source and detector. The source (and the detector) can move in various configurations depending on the generation of the CT scanner [Webb 12].

Conventional X-ray radiographs are not suited for displaying blood in the blood vessels and other soft-tissue details (as heart anatomy). In order to make blood vessels visible, a liquid contrast agent has to be injected into blood. The contrast agent increases the linear

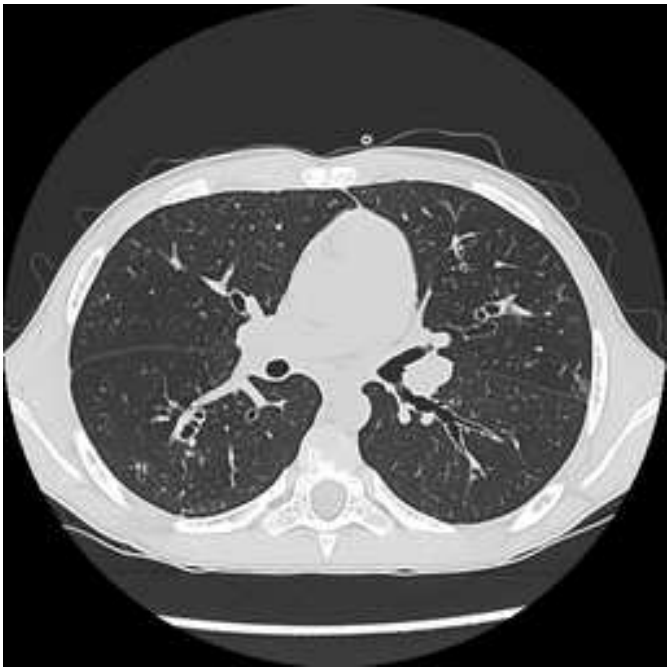

Figure 2.4: A CT image of lungs [Babin 10].

attenuation coefficient of the blood, which makes blood vessels clearly visible in the images. The use of a contrast agent for the visualization of blood vessels is called *angiography* (or *arteriography*). The contrast agent injection is performed either as an intravenous or intra-arterial injection using a catheter. The advantage of the catheter is that it can be guided to the location of interest in the blood vessel tree. Using the catheter the contrast agent is only locally injected, which allows for higher image quality, while affecting only the region of interest.

2.2 Digital Subtraction Angiography

As discussed earlier, angiography presents a good way to visualize blood vessels in CT images. However, angiographic images are not always easy to interpret, because of other organs and tissues that are present in the images. A special case is the imaging of brain blood vessels, where the region of interest is surrounded by the skull, which reduces the contrast of blood vessels compared to their surrounding (see left and middle image in Fig. 2.5). The solution to this problem is to record two

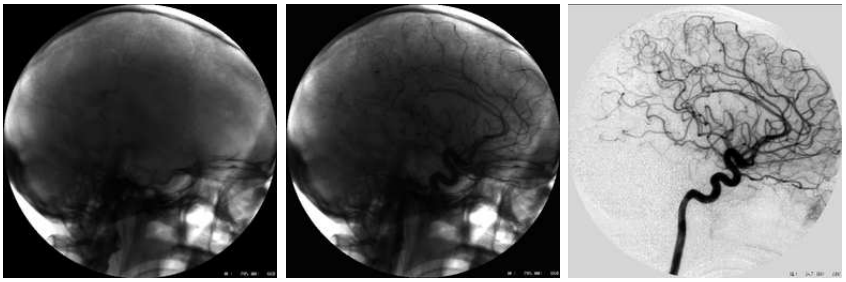

Figure 2.5: Subtraction of angiographic images. Left: image mask (non-contrast enhanced). Middle: contrast enhanced image. Right: result of subtraction of previous images (DSA) [Kerrien 00].

sets of images: the first one without the contrast agent and the second one after the contrast agent was injected. The bony structures in the image are removed by subtracting the recorded images, as seen in Fig. 2.5.

The described modality is called *Digital Subtracted Angiography* (DSA) and is the modality on which the interventional neuroradiology is based. DSA is an example of a temporal subtraction, which means that a number of images are taken from the same view point at periodic time intervals. This allows us to follow the propagation of contrast agent through the blood vessel system over time. The quality of subtracted images is usually high in detail, depending on the movement of the patient in between the two scans. A number of registration techniques have been developed to solve any misregistration problems caused by patient movement [Kerrien 00].

2.3 3D Rotational Angiography

3-D Rotational Angiography (3DRA) can acquire and display three-dimensional volumes of the cerebral vessels during interventional procedures. As such, it is of a great aid in understanding the vascular morphology during the interventions for guideline positioning of catheters, coils, balloons, stents and glue [Moret 98].

In rotational acquisition the images are acquired as a sequence of 2-D projections while the C-arm rotates around the head of the patient (see Fig. 2.6). When the 3-D imaging of blood vessels is required, an injection of contrast fluid is performed during the acquisition. In that case data sets are obtained from rotational series consisting of two

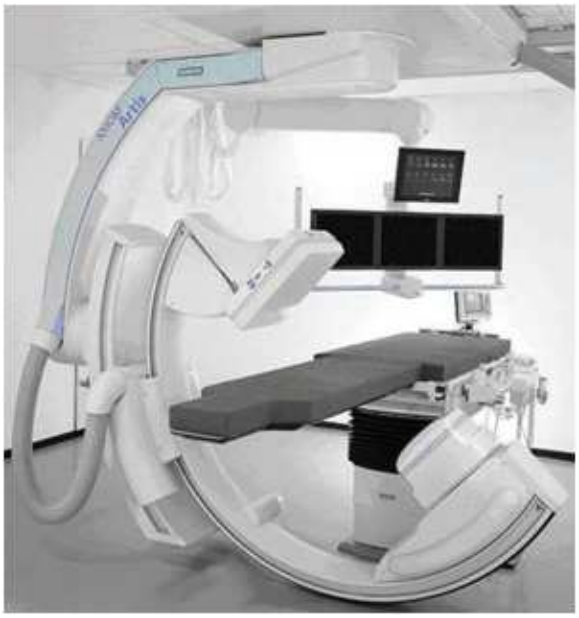

Figure 2.6: An X-ray C-arm scanner [Gupta 08].

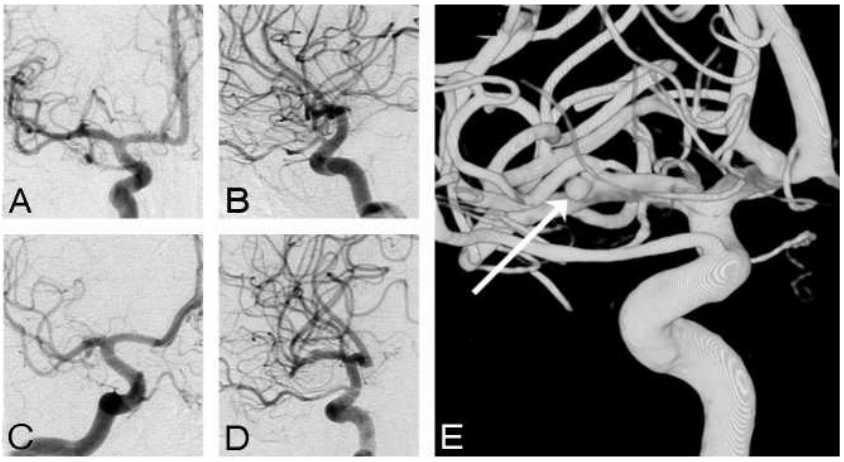

Figure 2.7: 3-D visualization from 3-D rotational angiography (3DRA) [van Rooij 08]. (A), (B), (C), (D) Four DSA projections and (E) 3RDA visualization of a blood vessel tree with an aneurysm (arrow).

rotations, where the first acquires the subtraction mask (see Fig. 2.7).

State of the art scanners have high stability of the C-arm, which

allows for the reproducible acquisition of the rotational sequence. The system is calibrated to compensate for various factors (e.g. pincushion distortion and varying distortion) and remains stable for at least four months. This, in turn, allows us to perform a subtracted acquisition, where the first rotational acquisition is performed without injection contrast, and the second acquisition is performed with the injection of contrast agent.

In order to acquire a 3-D image with a fixed C-Arm, the C-Arm is positioned at the body part in question so that this body part is in the isocenter between the x-ray tube and the detector. The C-Arm then rotates around that isocenter, the rotation being between 200° and 360° (depending on the equipment manufacturer). Such a rotation takes between 5 and 20 seconds, during which a few hundred 2-D images are acquired. A piece of software then performs a cone beam reconstruction. The resulting voxel data can then be viewed as a multiplanar reconstruction, i.e. by scrolling through the slices from three projection angles, or as a 3-D volume, which can be rotated and zoomed.

2.4 Magnetic Resonance Imaging

In this section we will explain the basic magnetic resonance (MR) principles needed to understand the properties of obtained images. For a more elaborate explanations refer to [Kwong 06].

Magnetic Resonance Imaging (MRI) is based on the hydrogen atoms contained in the water molecule. The abundance of water in physiological tissues is the reason for usefulness of MRI. The MRI signal is generated from the hydrogen nucleus (for this reason MRI is also known as nuclear magnetic resonance). Each atom is characterized by its spin, which we represent by a vector. In general, the spins are randomly oriented until an external magnetic field B_0 is applied. Then the spins align parallel or anti-parallel to B_0. Crucially, there will be a *higher number of positively oriented spins than the negative ones*. This difference creates a detectable MR signal.

The frequency with which the spins precess about the external magnetic field ν_0 increases as the strength of B_0 increases. This is described by the Larmor equation:

$$\nu_0 = \gamma B_0, \tag{2.2}$$

where γ represents gyromagnetic ratio of the nucleus involved. For the

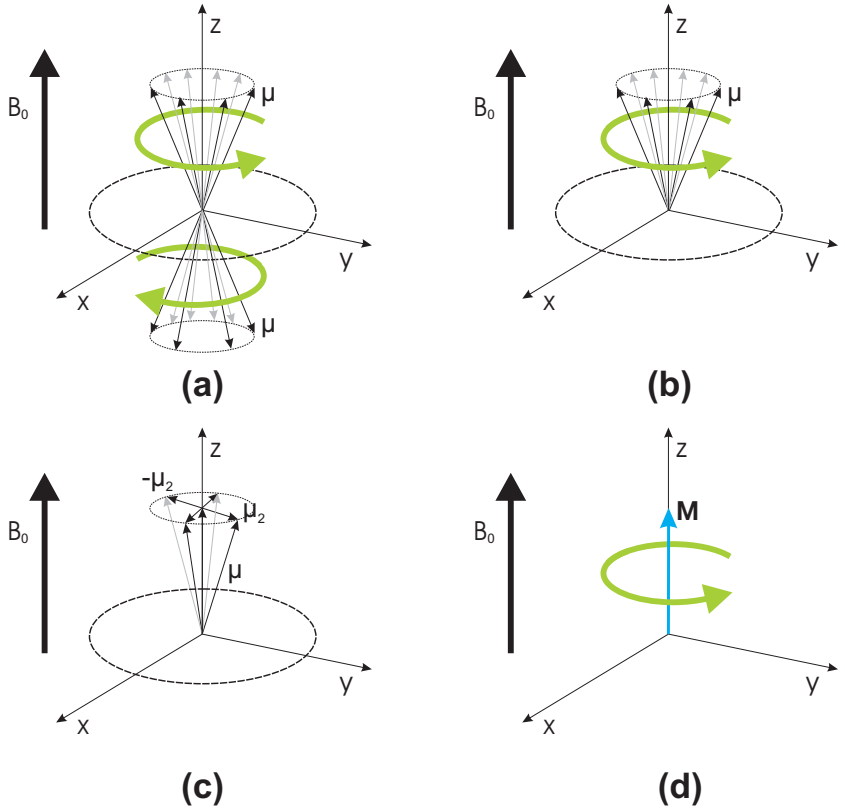

Figure 2.8: Illustration of magnetization process and spins [Kwong 06]. (a) Spins precess on the surface cones (more positive than negative spins exist). (b) Illustration for positive spins. (c) Vector components of spins in xy plane cancel out, only the component in z direction remains. (d) Main magnetization vector M.

hydrogen nucleus, it is 42.58 MHz/T, which results in a precessional frequency of $\nu_0 = 64$ MHz for a typical clinical MRI scanner (1.5 T).

In reality the spins precess on the surface cones (in positive and negative directions) as seen in Fig. 2.8. Each spin vector can be decomposed into a component along the z axis and a component on the base of the cone. The vector components situated in the cone base cancel out (add up to zero). Hence, the components of positive spins along the z axis create the *main magnetization vector* M.

The MR signal is created by application of a secondary magnetic field B_1 for a short time interval (1.5 ms) known as *radio frequency* (RF) signal. It is applied at 90° angle to B_0 field (x axis) and rotates the

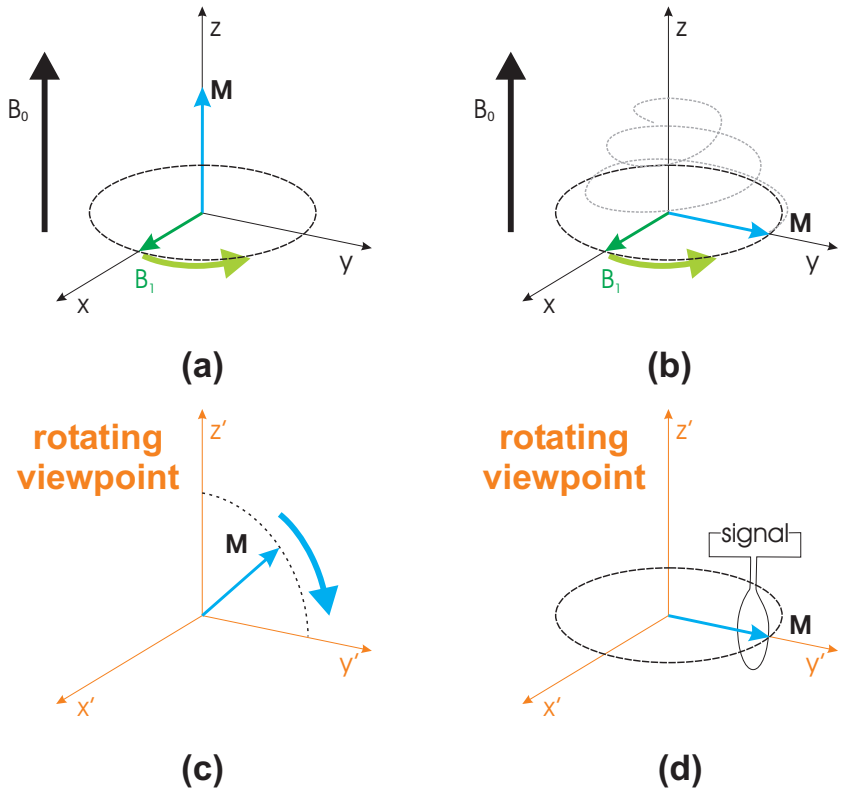

Figure 2.9: Influence of RF signal on the main magnetization vector M [Kwong 06]. (a) Secondary magnetic field B_1 is introduced. (b) B_1 rotates the magnetization vector M to the xy plane in a spiral trajectory. (c) From a rotating point of view the M vector simply dropped to the local y' axis. (d) The magnetization vector M produces a signal.

magnetization vector M to the transversal xy plane. The RF signal has a frequency ν_1, which means that vector B_1 is rotating in the xy-plane as seen in Fig. 2.9. In order to record the MR signal, the rotation of B_1 around z axis needs to be at the same frequency that the spins precess, which means that $\nu_1 = \nu_0$. In the Rotating Frame of Reference the net magnetization produces a signal onto a wire antenna. (see Fig. 2.9d). The produced signal is called the *free-induction decay* (FID) signal.

Fig. 2.10 illustrates the one-pulse experiment used to create an FID signal. It consists of introducing the 90° RF pulse for a short period of time followed by turning on the receiver (ACQ) to acquire the MR signal.

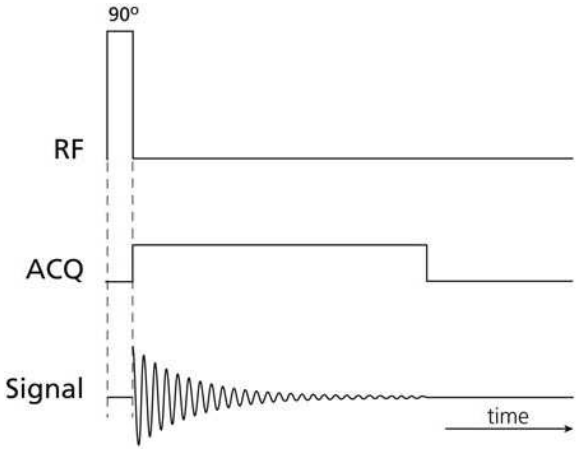

Figure 2.10: One-pulse experiment (creating an FID signal) [Kwong 06]. The 90° RF pulse is introduced, after which the acquisition (ACQ) starts.

2.4.1 Relaxation times T1, T2 and T2*

T_2 *relaxation* happens due to spin-spin interaction. The interaction of spin magnetizations modify the magnetic field observed by each spin, causing them to precess at different rotational speeds. In other words, the spins acquire a phase. This process is known as *dephasing*, where the spins eventually return to randomness they had before the RF signal was introduced (see Fig. 2.11). The signal loss over time follows an exponential decay:

$$M_{xy}(t) = M_{xy}(0)\ e^{-\frac{t}{T_2}}, \tag{2.3}$$

where $M_{xy}(0)$ refers to the magnetization observed at time $t = 0$ on the transverse xy plane.

$T_2{}^*$ *relaxation* happens due to spin-spin interaction (the same as T_2 relaxation), but also due to inhomogeneities in static magnetic field B0. Inhomogeneity of magnetic field is a result of the presence of a human body in the magnetic field. As with T_2, the signal loss over time follows an exponential decay:

$$M_{xy}(t) = M_{xy}(0)\ e^{-\frac{t}{T_2^*}}. \tag{2.4}$$

$T_2{}^*$ relaxation happens faster than T_2 relaxation. The one-pulse experiment (Fig. 2.10) experiences T2* relaxation. In order to acquire an MR signal that decays with T2 (and exploit the longer acquisition windows) we use the *spin echo* pulse sequence (see Subsection 2.4.2).

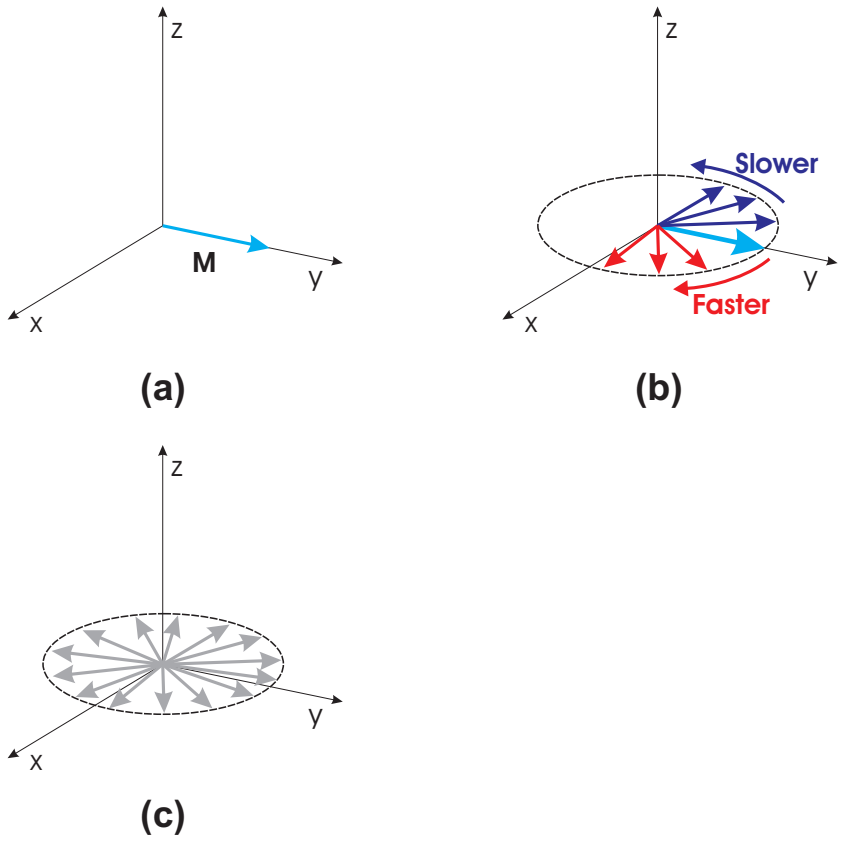

Figure 2.11: Illustration of dephasing [Kwong 06]. (a) The magnetization vector. (b) Because of the spin-spin interactions, the spin magnetizations are modified and they start to precess at different rotational speeds. (c) Completely dephased magnetization.

T_1 *relaxation* refers to spin-lattice relaxation, which happens due to energy exchange between the spins and their surrounding. This means that the magnetization vector M moves back to the z axis. This occurs at a relatively slow rate:

$$M_z(t) = M_z\ (1 - e^{-\frac{t}{T_1}}). \tag{2.5}$$

where the M_z refers to the z axis component of magnetization vector M under the influence of field B0.

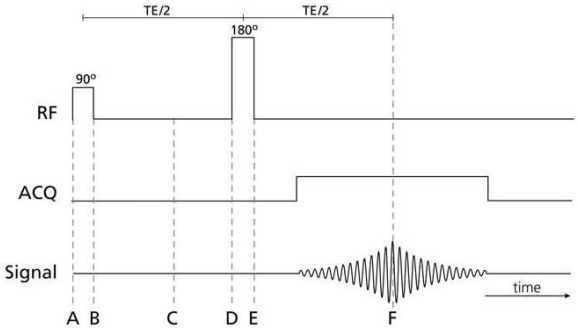

Figure 2.12: Spin-echo pulse sequence diagram [Kwong 06]. The signal is acquired after the sequence of the 90° RF pulse, waiting TE/2 period of time and the introduction of a 180° RF pulse.

2.4.2 Spin echo

The one-pulse experiment reflects the T2* decay. If we are interested in the T2 decay rather than T2* decay, we have to create a spin echo sequence. The pulse sequence diagram to achieve this is presented in Fig. 2.12.

A spin echo sequence differs from the FID sequence in that the signal is not acquired right after the 90° RF pulse. Instead the signal is acquired after a TE/2 waiting period and the introduction of a 180° RF pulse, followed by the acquisition at the right moment. Fig. 2.13 illustrates the effect of the described pulse sequence to the magnetization vector. As the 90° B1 pulse along the x axis is introduced into the magnetic field (Fig. 2.13a), the M vector is moving onto the y-axis of the transverse plane (Fig. 2.13b).

The signal loss (decrease in absolute value of M) is caused by spin-spin interactions and additional loss caused by dephasing as a result of static magnetic field (B0) inhomogeneities. We focus here on dephasing caused by static field inhomogeneities (Fig. 2.13c), which comprises the difference between T2 and T2*. Faster spins will have positive phase (they move clockwise), while slower spins will have negative phase (they move counterclockwise).

When we introduce a 180° B1 pulse along x axis, we cause the dephasing spins to rotate along the x-axis (Fig. 2.13d). The dephasing spins rotate to the other half of the xy-plane (Fig. 2.13e). After we remove the 180° pulse, spins continue to dephase at their previous speeds, causing them to realign (rephase) at $-y$. The time interval for rephasing

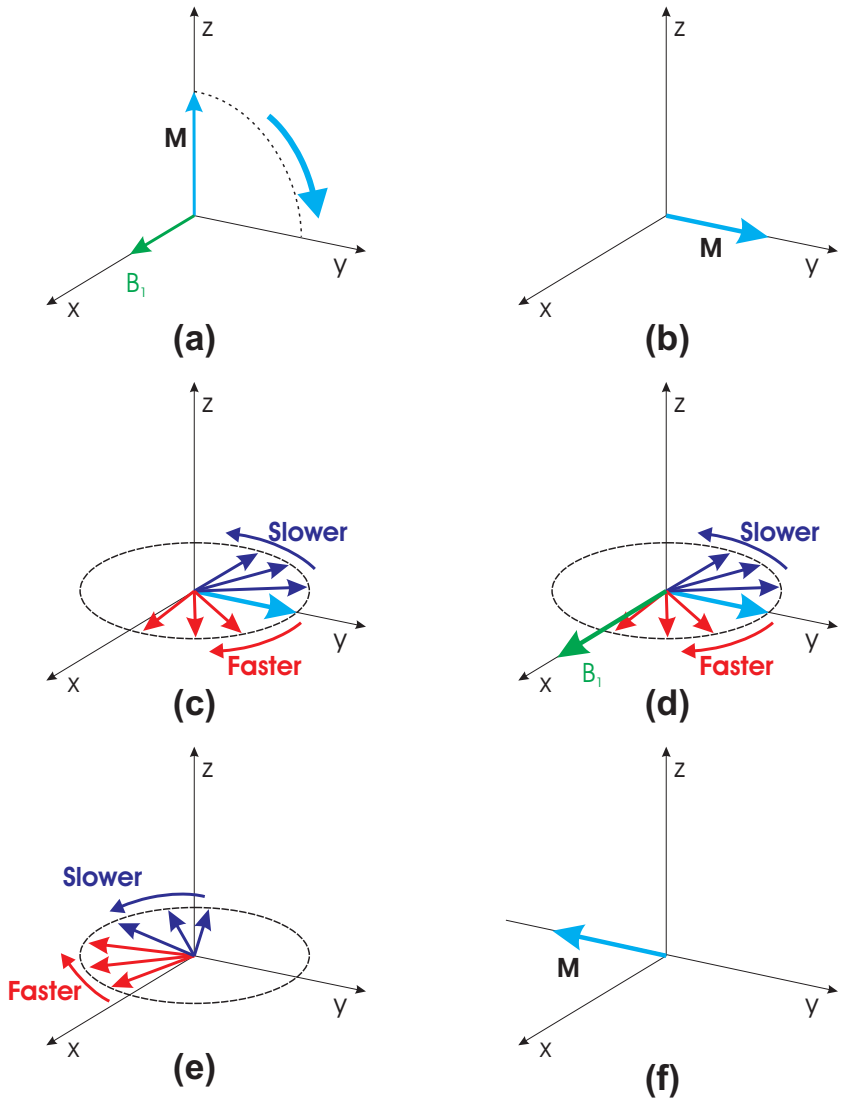

Figure 2.13: The spin-echo principle [Kwong 06]. (a) and (b) A 90° RF signal puts magnetization vector to the xy plane. (c) The spins start dephasing. (d) A 180° RF signal is introduced, (e) The RF signal rotates all the spins by 180°. (f) Spins get into phase again.

will be exactly the same as dephasing interval and is known as *echo time* (TE). Dephasing will take place after TE, and the signal will decay past TE (Fig. 2.12).

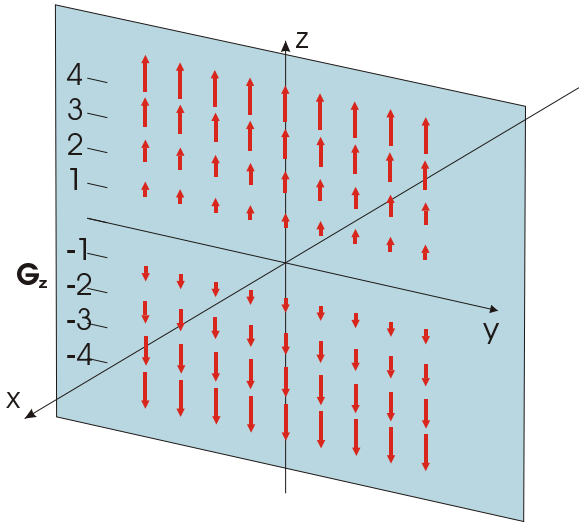

Figure 2.14: Gradient magnetic vector field [Kwong 06].

2.4.3 Gradient echo and position selection

Gradient echoes are created by means of a gradient magnetic field. This means that the field strength depends on the position in space (unlike the case of static magnetic field B0) and is proportional to the distance from the center of the magnet (the isocenter). Gradients can be applied in each of the directions: Gx, Gy and Gz for x, y and z axis, respectively.

Fig. 2.12 illustrates Gz gradient magnetic field where the magnetic field strength depends on the z position. This modifies the Larmor equation to:

$$\nu_0 = \gamma(B_0 + xG_x + yG_y + zG_z). \tag{2.6}$$

It is important to notice that based on the given spin's precessional frequency (Larmor equation) we are able to determine the position of the spin on the axis of interest (e.g. z axis based on the gradient field Gz). Conversely, given a location on the axis we are able to determine the precessional speed at that location. Typical gradient strengths on state-of-the-art MR scanners are 0.040 T/m.

Slice selection is performed by applying a gradient field along the z axis at the same time when the RF pulse is introduced (see Fig. 2.15). The gradient field Gz will perform "slicing" in such fashion that each transversal plane (orthogonal to z axis) will have spins that precess with the same frequency. Only the spins in a transversal

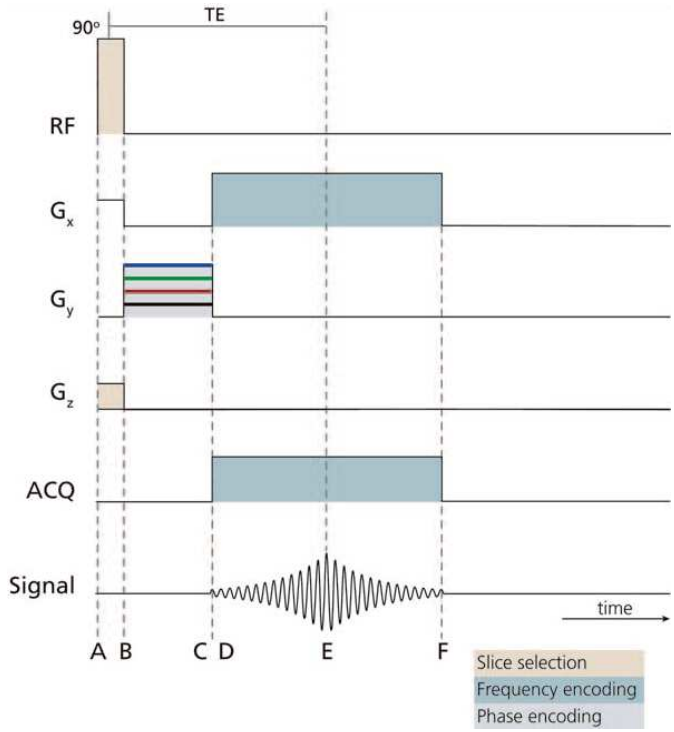

Figure 2.15: Gradient echo pulse sequence [Kwong 06]. It allows us to acquire magnetization of every position in 3-D space.

plane where the precessional Larmor frequency ν_0 is equal to the frequency ν_1 of our RF pulse will respond to the RF pulse (only those spins will produce a signal). In other words, by selecting the proper RF pulse frequency, we can select any desired transversal plane (slice orthogonal to z axis). With a higher field gradient Gz, it is possible to select thinner slices. In order to allow signal recording in each position of the 3-D space, we need to encode the signal along the remaining two dimensions x and y.

Frequency encoding is performed to encode spins along the x axis. The Gx gradient is introduced during the "read-out" interval (acquisition window interval in Fig. 2.15) and is called the readout gradient. It forces spins at different locations on the x axis to precess at different speeds (see Fig. 2.16). In this fashion the magnetization of each row of the x axis is unique (i.e. spins in the same row have the same precessional frequency), which is used to extract information along the x axis. The

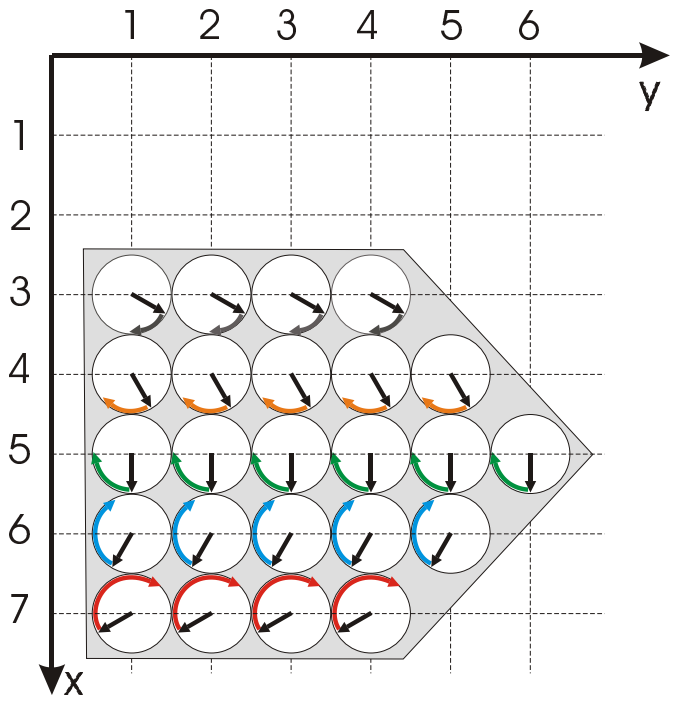

Figure 2.16: Frequency encoding principle [Kwong 06]. Different arrows indicate different precessing frequencies along the x axis.

information about each frequency is extracted using the Fourier Transform (FT). At this point we only need to extract information along the y axis to complete the 3-D information gathering.

Phase encoding is performed to encode spins along the y axis by introducing a Gy pulse immediately after the RF pulse but also before the acquisition begins. If we introduce a short Gy gradient pulse right after the RF pulse (see Gy in Fig. 2.15) along the y axis, the spins will precess at different speeds according to their position on the y axis (as long as Gy is present). As soon as Gy stops, spins will precess with the same frequency (as before the Gy was introduced), but with different phase (see Fig. 2.17). This means that the information about their position onto the y axis has been encoded onto their phase and the magnetization vectors will be at progressively larger angles relative to the y axis (i.e., they will have acquired more phase) the further away from zero they are located.

In order to acquire the y axis position-encoded information

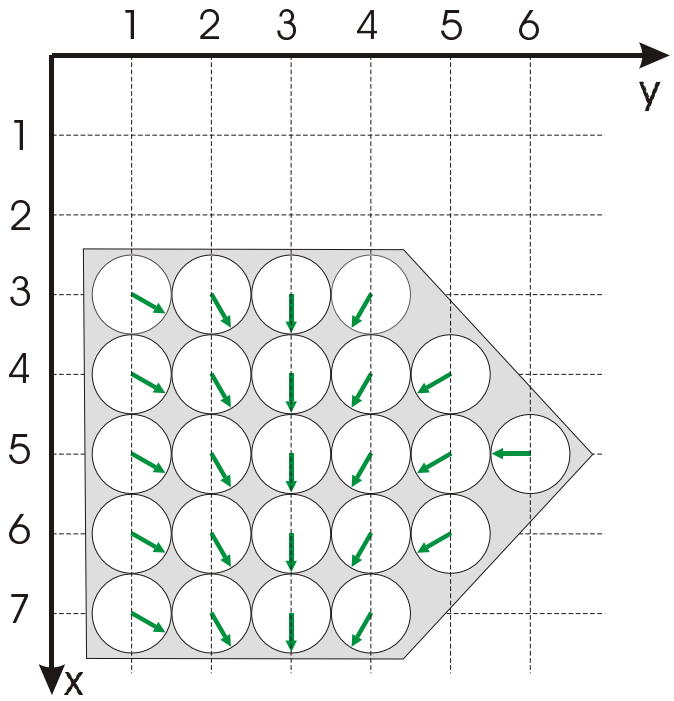

Figure 2.17: Phase encoding principle [Kwong 06]. Different arrow directions indicate different phases along the y axis.

from the phase, we have to "convert" the phase information into frequency information, after which we can use the Fourier transform. This is done by multiple measurements using different values of Gy (represented by different colors for Gy in Fig. 2.15) with a constant difference in Gy values along consecutive measurements. The phase sum along y axis for each experiment will be different, yielding a "speed" of change in phase across repeating experiments (with increasing phase-encoding gradient strengths in consecutive experiments). Hence, similarly to the frequency encoding, we use FT to derive the phase information (i.e. information along the y axis). The data from multiple phase-encoded experiments are placed in a 2-D matrix we call *k-space*, whose FT results in a 2-D image.

2.5 Cardiac Magnetic Resonance imaging

Cardiac magnetic resonance imaging (CMR) is a medical imaging technology for the non-invasive assessment of the function and structure of the cardiovascular system. It is comprised of basic MRI principles that have been optimized for imaging of the cardiovascular system. Its advantages over Conventional MRI imaging modalities when cardiovascular analysis is considered are: the capability for tissue characterization, qualitative and quantitative evaluation of the motion of both the blood and the myocardium, and assessment of regional perfusion [Klepac 06]. A cardiac MRI examination is typically performed by initial screening of the patient and setting up of cardiac gating. Optionally an intravenous access for contrast administration is prepared. The initial MRI scan gives a quick insight into overall chest anatomy, after which more detailed scans can be performed.

2.5.1 Electrocardiographic gating

The main obstacle in the MR cardiovascular imaging is cardiac motion (heart movement). The problem of cardiac motion is resolved by cardiac gating (using electrocardiogram - ECG). The ECG gating allows us to acquire imaging data at the same stage of the cardiac cycle over several heart beats, thus yielding "static" images. Two gating approaches exist.

Prospective gating uses QRS (part of ECG signal that corresponds to the depolarization of the right and left ventricles) detection to trigger acquisition at the start of each cardiac cycle, typically over several cardiac cycles. Disadvantages of this approach are prolonged acquisition times, the fact that the end of cardiac cycle can not be sampled (a dead period is needed to allow for variation in length of cardiac cycle) and possible delay in recognizing the R wave (data acquisition is late).

Retrospective gating performs continuous acquisition over several cardiac cycles. The acquired data is interpolated to reconstruct images at selected moments in time (based on the heart rate, the rate of data acquisition and the number of requested time moments per cardiac cycle). Advantages of this method are higher robustness to arrhythmia and it can be used to image the whole cardiac cycle (there is no need to stop image data acquisition to wait for the next QRS detection). One disadvantage of this approach is that images are more blurry because of the interpolation performed in post-processing.

2.5.2 Bright blood imaging

An advantage of CMR is that blood can appear either bright or dark in the images, depending on the acquisition. When imaging with rapid T1-weighted gradient echo imaging (e.g. Fast Low-Angle Shot [FLASH]), the blood can appear relatively bright compared to the surrounding tissue. This is caused by blood flow, where the less magnetically saturated blood (left in the slice being imaged from the last excitation) is replaced by fully magnetized blood flowing into the slice. The higher magnetized blood produces a stronger signal and appears bright in the images.

Spoiled gradient echo imaging uses "spoiling" to suppress the residual transverse magnetization. The residual magnetization is a consequence of a common case where the TR is shorter than the T2 of most tissues, and the transverse magnetization will not have fully decayed before the next RF pulse. Thus, the residual transverse magnetization will add T2 contrast (in addition to T1 contrast) to the image. The spoiling can be accomplished with an RF pulse or gradients.

Steady-state gradient echo (or Steady-State Free Precession (SSFP)) is performed without spoiling and residual transverse magnetization. This means that the residual magnetization is retained, it increases the SNR (compared to the spoiled sequences) and the contrast will depend on the T2/T1 ratio. In steady-state sequences, only fluid and fat will have a high signal (fluid and fat have comparable T1 and T2 times, while in most other tissues, the T2 time is much shorter than T1 time). In many cases this is an undesired effect. However, in bright blood cardiac MRI, the high intensity blood compared to other tissues is exactly what is needed. Therefore, steady-state gradient echo sequences are optimal for cine cardiac imaging, which will be discussed later.

Balanced steady-state free precession (bSSFP) sequences are used in cardiac imaging. Commercial names for these sequences are TrueFISP (Siemens), FIESTA (GE), and balanced FFE (Phillips). SSFP sequences do not depend on flow; they have a higher SNR; and they are faster. Spoiled gradient echo sequences are T1 weighted and depend on through plane flow enhancement (similar to time-of-flight MR angiography) to generate contrast (blood may become saturated if the flow is slow or the TR is short).

High-quality SSFP imaging depends on a low TR, a high flip angle FA (the angle to which the net magnetization is rotated relative to the main magnetic field direction using the RF pulse), and a uniform magnetic field. SSFP sequences are very sensitive to field inhomogeneities. In regions of high local magnetic-field variations, SSFP images

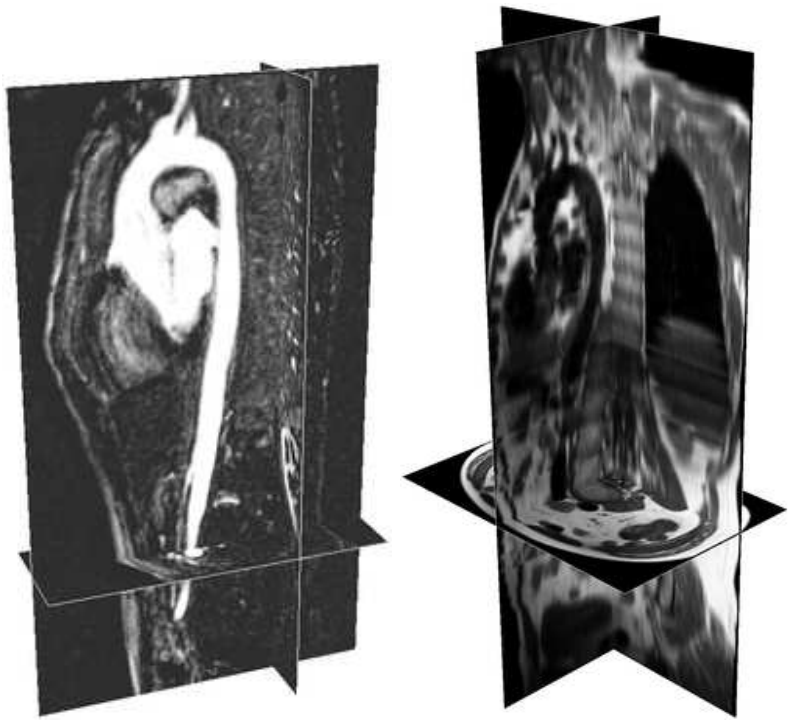

Figure 2.18: MRI images of abdomen [Babin 13a]. Left: bright blood imaging shows aorta as a bright blood vessel. Right: black blood imaging shows aorta as a black blood vessel.

often suffer from characteristic bands of signal loss (off-resonance banding artifact), which can disrupt the steady-state. In SSFP sequences, the SNR does not change substantially with different flip angles, but the T2/T1 weighting will increase with an increasing flip angle. SSFP sequences, therefore, should use the largest flip angle achievable (range from 40° to 70°), because this will maximize the contrast-to-noise ratio.

2.5.3 Black blood imaging

The goal of the black blood MR imaging is to cancel out the influence of blood flow in order for the blood to appear black in the acquired images. These images are usually used to analyze the anatomy of the heart and blood vessels (because they contain no interference of blood).

Black blood imaging is based on spin echo pulse sequences (this means that spins must experience a 90° pulse followed by a 180° pulse to

generate a signal). If the blood that was in the slice when the 90° pulse was applied has left the slice when the 180° pulse is applied (at TE/2), there will be no prepared magnetization to refocus and form an echo from the blood. The blood in the slice at the time of the 180° pulse will not have received the 90° pulse, and so there will be no magnetization in the transverse plane to refocus to an echo. This means that blood will not generate any signal (or a very weak signal will be generated), so it will appear dark in the image. Black blood imaging is best achieved by decreasing the volume of the slice (thinner slices), positioning the slice orthogonal to blood flow or imaging during the high speed blood flow (during systole). Another method is to increase the time interval between the 90° and 180° pulses (increase TE, or echo time).

The purpose of black blood imaging most usually is to examine anatomy. This means that TR should be as short as possible to shorten imaging time (that is why black blood MRI scans are most often T1-weighted). For cardiac mass evaluation, specific T2-weighted sequences may be performed.

Fast spin echo (FSE) imaging is used in clinical practice because the acquisition can be performed during a breath-holding time (unlike standard spin echo). Fast spin echo has the same pulses as the spin echo, followed by multiple 180°pulses (i.e. "echo train", "echo factor" or "turbo factor"). The FSE sequence has a much faster scan time than a spin echo. However, a disadvantage of FSE over spin echo is image blurring as a result of acquiring data at different echo times during the echo train. To minimize this artifact, FSE cardiac MRI is often performed during the diastole. As mentioned earlier, the fastest blood flow happens at systole (not diastole). In order to get low blood signal the FSE cardiac MRI is often performed with the addition of double inversion recovery (see below) pulses to achieve optimal nulling of blood signal.

Double inversion recovery is used to cancel out the signal from flowing blood. It is composed of a non-selective 180° RF pulse and a selective 180° RF pulse. The non-selective 180° RF pulse inverts all spins (in the imaged object). The selective 180° RF pulse is applied only to the spins in the imaged slice. This means that the spins in the imaged slice revert to their original alignment (before these 2 pulses were introduced). Note that this applies only to the spins in the imaged slice, while all other spins (in the imaged object) are inverted. This means that due to blood flow, the blood from the slice (whose spins were reverted to original alignment) will go away and will be replaced by blood from

neighboring slice whose spins were inverted. If the imaging begins at the time the blood from the neighboring slice replaces the blood originally present in the slice, the blood will not produce any signal.

For analysis of vessel morphology half-Fourier, single-shot, fast spin echo (SS-FSE) sequences are the fastest. Different trade names for these half-Fourier single shot sequences are HASTE (Half-Fourier Acquired Single-shot Turbo spin Echo; Siemens) and SS-FSE (GE, Phillips).

2.5.4 T1 and T2 weighting

The T1 and T2 relaxation times influence the acquisition based on the imaging method and TR and TE times. In general, if the TR is shorter the magnetization will have a shorter time period for its recovery between two excitations. This means that regions with shorter T1 values (e.g. fat or contrast enhanced blood) will tend to appear relatively brighter (T1 weighting). In a similar fashion, the longer TE times will allow for longer signal decay before signal detection. This means that regions with longer T2 values (e.g. fluid or swelling tissue) will tend to appear relatively brighter (T2 weighting).

2.5.5 Cine imaging

The ECG gating allows us to synchronize the image acquisition with the cardiac cycle. In turn, this allows us to record high-quality movies (cine imaging) of the different phases of the cardiac cycle. This is possible even though the image data may be acquired over the course of multiple cardiac cycles: it depends on the assumption that cardiac cycles are reasonably consistent with each other. This may not be the case in the presence of cardiac arrhythmia. For examination of abdominal aorta, velocity encoded Cine images are of interest, which are composed of modulus sequence (defines vessel anatomy), and phase-contrast sequence (defines blood flow), as depicted in Fig. 2.19.

Cine imaging can be readily implemented with gradient echo imaging (e.g., FLASH imaging). Both types of gating (retrospectively or prospectively) can be used. In gradient echo cine imaging the TE is kept as short as possible to obtain the highest imaging speed.

SSFP imaging approaches are also used for cine imaging. In this case only retrospective gating is used. The bright signal from blood in SSFP cine imaging depends on the relaxation times of blood rather

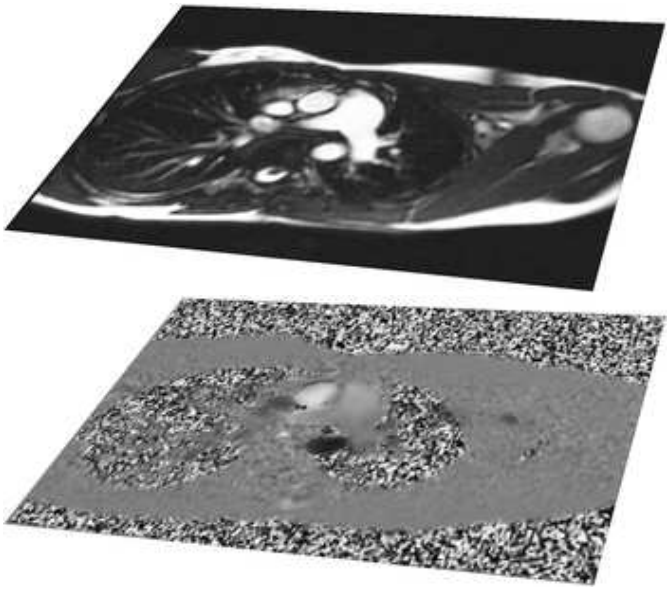

Figure 2.19: Velocity encoded Cine images of abdominal aorta at ascending and descending levels [Babin 13a]. Up: modulus image. Down: phase-contrast image. Pixel values in the phase-contrast image depend on the direction and intensity of blood flow.

than on its motion, leading to a more consistent bright blood appearance independent of image orientation or blood flow patterns.

2.5.6 Phase-contrast images

Phase-contrast images are a type of cine images that use motion-induced phase shifts to represent velocities in vascular and cardiac structures. Two main parameters have to be set: the imaging plane and velocity encoding value (venc).

Only one spatial component of velocity can be measured at a time. This is typically the component perpendicular to the imaging plane as this is most useful for flow volume calculations (perpendicular to the axis of the vessel lumen of interest).

The velocity encoding value (venc) is the velocity for which the corresponding phase shift will be $\pm 180°$. Greater velocities, leading to greater phase shifts than this, will be indistinguishable (aliased) from velocities with smaller magnitudes and possibly opposite sign (usually venc on the order of 150 cm/s is used).

2.5.7 Contrast-enhanced images

Another way that blood can appear bright in the image is by injection of an MRI contrast agent, which will lead to increased signal in the presence of T1 weighting. If a 3D volume is rapidly and repeatedly imaged after the injection of a bolus of contrast agent, then the blood vessels with high concentrations of the agent at the time of image acquisition will appear bright. If the image acquisition is fast enough, then the delay after the injection can be adjusted to have prominent enhancement of only a desired portion of the vascular tree (e.g. arteries vs veins or pulmonary vs systemic). Choosing the timing of this delay can be aided by acquiring a rapid series of sequential images of a representative vessel after the injection of a small test bolus of the agent, often called a timing run. The bright vessel images in the imaged region can then be processed with a suitable computer program to produce a synthetic angiographic display of the vessels from any desired point of view (an MRA).

2.6 Visualization

Visualization techniques have become the inseparable part of medical imaging. A number of visualization methods have been implemented in hardware on vendor workstations. We will summarize here the most important visualization approaches illustrated in Fig. 2.20.

Multiplanar reconstruction is the simplest method of visualization by displaying 2-D images as planes that cut through the 3-D image. This is usually performed for three orthogonal planes: transversal, coronal and sagittal. However, most visualization software packages allow for oblique (non-orthogonal) display planes, so that the optimal plane can be chosen to display an anatomical structure.

Surface rendering (also known as "Surface Shaded Display") displays a set of voxels from the 3-D image as a surface. The set of voxels to be visualized is usually defined by a threshold value. Hence, the surfaces represent *isosurfaces* (surfaces with the same scalar quantity). The surfaces can be colored according to the isosurface value or set to a single color manually. The marching cubes algorithm is one of the most known surface generation methods.

Volume rendering is used to directly visualize the 3-D image without intermediate geometric representation of the volume (as in surface rendering). The idea is to visualize a volume using voxels or other volume elements with predefined visual properties (opacity, color and

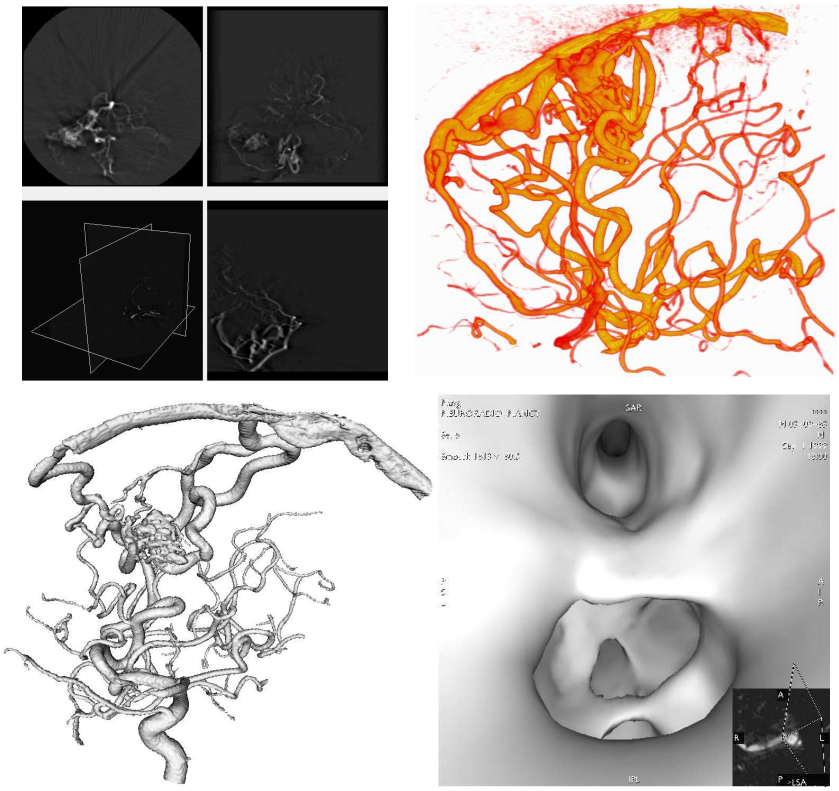

Figure 2.20: Visualization methods [Babin 13c,Kerrien 00]. Upper left: Multiplanar reconstruction. Upper right: volume visualization. Lower left: surface rendering. Lower right: virtual endoscopy.

shading). Several different approaches for volume rendering exist. *Ray casting* determines the visual properties projected on a viewing plane by casting a ray through the volume . At a predetermined number of evenly spaced locations along the ray the color and opacity values are obtained by interpolation. The interpolated colors and opacities are merged with each other and with the background by compositing in back-to-front order to yield the color of the pixel. The color and opacity of voxels is controlled by transfer functions. Manipulation of the transfer function yields various visualization results. *Splatting* uses convolving filters to compute visual properties of a neighborhood of pixels. This method is faster than ray casting, but also less accurate. *Maximum intensity projection* (MIP) works in a similar way as ray casting, except that only the voxels that have maximum intensity along rays are projected. This

method is computationally fast, but the 2-D results do not provide a good sense of depth of the volume.

Virtual endoscopy is a visualization that simulates the navigation of a (virtual) camera through the 3-D surface representation of a patient's anatomy. It is especially useful for tubular structures, enabling the internal exploration in order to assist in surgical planning.

2.7 Conclusion

In this chapter we gave a broad overview of imaging modalities and functions that are most common in cardiovascular examinations, and we discussed their advantages and limitations. Especially, we aimed to introduce modalities used in this thesis. In other words, we concentrated on imaging required for surgery on cerebral vascular malformations and for defining and quantifying the function of the abdominal aorta. Additionally, we introduced various visualization techniques that are widely used today and implemented in hardware. Although various imaging modalities combined with diverse visualization approaches give a good insight into vascular anatomy and function, the performed examination is not quantitative. Visualization alone does not allow a physician to perform measurements on vascular structures. In order to quantify vascular anatomy and function, more sophisticated algorithms are required that can extract and analyze vascular anatomy. These are image segmentation algorithms.

3

Vessel Delineation Methods

This chapter reviews some of the common approaches in vessel delineation aimed to gain information on the structure of blood vessels. The methods can be classified into three basic groups according to the type of the resulting delineation, namely segmentation, skeletonization and vessel enhancement. However, most of the algorithms today incorporate multiple methods into one to obtain a higher amount of information of the vascular structure. Current medical imaging reviews use different classifications of state-of-the-art methods. The work of [Kirbas 04] classifies vessel delineation methods based on their mathematical framework, while the [Yaniv 06] classifies methods from a user and application point of view. The review of [Lesage 09] classifies algorithms according to three criteria: appearance and geometric models, image features and extraction schemes. Our classification relates mostly to the algorithmic classification of [Kirbas 04]. This chapter gives an overview of delineation techniques grouped and sorted according to the amount of higher-level (structural) information on vessels that they use. Hence, four classes of algorithms have been formed and sorted in ascending way according to the amount of incorporated vessel-specific information, namely: thresholding and region growing, local pixel neighborhood analysis, model based methods and other structure based methods.

3.1 Thresholding and region growing

Angiography is one of the most common vascular imaging modalities, which leads to relatively clear distinction of blood vessels in angiographic images (due to the use of contrast medium the vessels stand out in comparison to other tissues in the image). Hence, thresholding, as the most basic segmentation technique, is often used to extract blood vessels.

The main advantage of thresholding is its low computational complexity, which results in fast execution. This is particularly suitable in clinical practice, where the results have to be obtained in real time for performing surgeries. This method is susceptible to noise and imaging artifacts. The main disadvantage is its inability to segment vessel regions with the range of pixel intensities that overlaps with intensity ranges of other tissues. Therefore, thresholding is often used in combination with *region growing*, where a seed point has to be defined (either by a predefined automatic seed point determining algorithm or manually by specifying the seed point). The region is grown from the initial seed point based on the pixel value similarity and spatial proximity [Kirbas 04]. Multiple seed points result in a number of segmented regions, which are often initially disconnected, and because of this subsequent *region merging* is needed. The criteria for merging the initially obtained regions range from simple intensity comparisons to extensive use of prior knowledge on the vessel shape and structure. It should be emphasized that many algorithms today use basic principles of region growing and region merging in combination with more advanced criteria for growing or merging. Therefore, segmentation algorithms have been classified by the prior information implemented in these basic mechanisms.

The simplest thresholding is *single threshold value* operation where all the pixel intensities higher than the threshold value are considered as the final segmentation result. This method is sufficient only for obtaining a general preview of the region of segmented object since finer details are often not visible and the segmentation result often contains a lot of incorrectly segmented regions. However, the result of this operation (often in combination with binary connectivity filtering) is used as the input *mask* in a preprocessing step for defining the region of interest for more advanced segmentation algorithms. This shortens the execution times of demanding segmentation methods [De Bock 10].

Multiple threshold value algorithms are often used to extract multiple objects from a single image with different ranges of pixel intensities, where the extracted regions can be used as mask regions or bounding regions for a finer segmentation of another object. The drawback of these methods is the manual threshold setting, with often different threshold values in different parts of 3-D data sets. This problem is solved using automatic threshold setting algorithms, which adjust the threshold values by examining the intensities in different slices or pixel neighborhoods.

Histogram-based techniques analyze the histogram of the image

(usually each slice is processed separately) to obtain the criteria for automatic threshold selection. The simplest methods work under assumption that different objects in the image have different pixel intensity ranges, which do not significantly overlap. The method of [Otsu 79] calculates the lowest point between two classes. [Brink 96] propose the cross-entropy as a non-metric measure to determine the optimum threshold. Other histogram-based approaches include moment-preserving thresholding [Tsai 85] and minimum error thresholding under assumption of object and pixel intensities being normally distributed [Kittler 86].

Since the conditions presented by the aforementioned method are rarely met, other methods use prior knowledge on the pixel intensity distribution in the image. In this fashion, pixels are classified according to probabilities of belonging to various objects in the image, which is then employed for thresholding. The work of [Chung 99] implements such a method with proving that the Rician distribution gives better quality-of-fit than a Gaussian distribution. Illustration of threshold based on histogram analysis is shown in Fig. 3.1. Two peaks in the histogram in Fig. 3.1 indicate the lowest background values (image corners) and highest background values (circular background). Since the images are contrast-enhanced and the contrast agent disperses into capillaries, it is logical that the highest curvature in the histogram represents gray values corresponding to the least visible capillary vessel pixels (before the contrast disperses into the bright background). Hence, the threshold value is determined as the point at the maximum planar curvature in the histogram. The problem of the cited methods is that the number of classes has to be known a priori in order to segment multiple objects. The adaptive thresholding approach of [Wilkinson 03] makes use of either flat or Gaussian weighted windows for local thresholding with robust automatic threshold selection. The most common use of thresholding and region growing in vascular imaging is the segmentation of cerebral angiographic (CTA and MRA) images [Wilkinson 03, Chung 99] and retinal angiographic images [Jiang 03, Hoover 00].

3.2 Local neighborhood analysis methods

Local neighborhood analysis methods incorporate knowledge about features of vessel pixel neighborhoods. This is the most basic prior information on the local pixel neighborhood level: although neighborhoods of pixels are examined, the segmentation decision is made on a pixel-by-pixel basis.

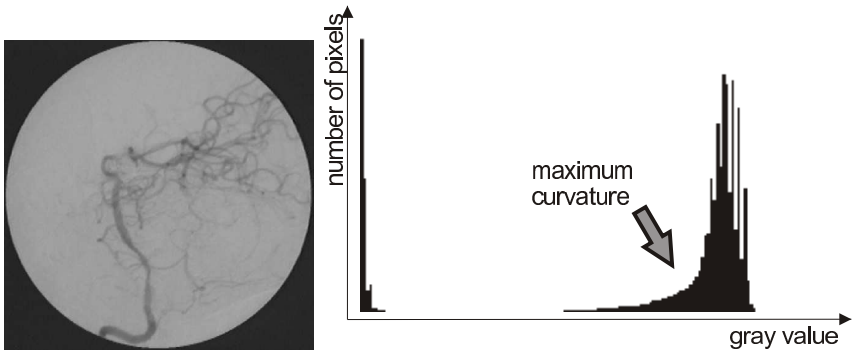

Figure 3.1: An illustration of histogram analysis-based thresholding [Chung 99]. (a) A digital subtracted angiography (DSA) image of cerebral blood vessels. (a) Histogram of the corresponding DSA image. The threshold is determined by finding the point at the maximum planar curvature.

3.2.1 Mathematical morphology

Mathematical morphology [Serra 82,Soille 86], is a popular tool in image processing and can be used for very diverse tasks such as noise reduction, feature extraction, segmentation, etc. Let $\mathbf{p} \in \mathbb{Z}^2$ denote a pixel with gray value $g(\mathbf{p})$, from a range of discrete gray scale values. The structuring element (SE) $S_n(\mathbf{p})$ is defined as a set of points in $\mathbb{Z}^2$, of certain shape and size n, centered at $\mathbf{p}$. With this notation, the result of morphological *erosion* is:

$$(g \ominus S_n)(\mathbf{p}) = \min_{\mathbf{p}' \in S_n(\mathbf{p})} g(\mathbf{p}'). \tag{3.1}$$

The result of morphological *dilation* is:

$$(g \oplus S_n)(\mathbf{p}) = \max_{\mathbf{p}' \in S_n(\mathbf{p})} g(\mathbf{p}'). \tag{3.2}$$

From these two basic operations, morphological *opening* is defined as:

$$g \circ S_n = (g \ominus S_n) \oplus S_n, \tag{3.3}$$

while the *closing* is:

$$g \bullet S_n = (g \oplus S_n) \ominus S_n. \tag{3.4}$$

Morphological openings and closings remove objects (connected components) in the image smaller than the structuring element (see

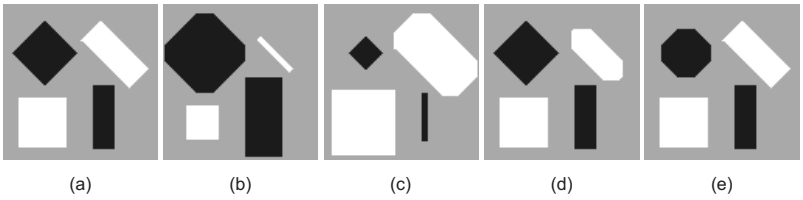

Figure 3.2: An illustration of morphological operations with a rectangular SE. (a) Original image, and the results of (b) erosion, (c) dilation, (d) opening and (e) closing.

Fig. 3.2). Openings modify bright objects, because the erosion reduces their scale, while the dilation "rescales" them. Accordingly, closings modify dark objects because the dilation reduces their scale, while the erosion restores it. This is illustrated in Fig. 3.2, together with the effects of morphological erosion and dilation. The result of the morphological opening and closing depend also on the shape of the SE. For the square-shaped SE like in the example of Fig. 3.2a the rectangular objects (with horizontal and vertical edges) will not be modified by opening or closing, while those with diagonal edges will be affected (see Fig. 3.2d and Fig. 3.2e). The diagonally-placed white object will be modified in the case of morphological opening, as shown in Fig. 3.2d, but will not be affected by morphological closing, as shown in Fig. 3.2e. On the other hand, the diagonally-placed black object will be modified in the case of morphological closing, as shown in Fig. 3.2e, but will not be modified by morphological opening, as shown in Fig. 3.2d. Mathematical morphology is used in the segmentation of retinal vessel images, where different combinations of morphological operators are used [Zana 01, Huang 06, Bouchet 07].

The most common SE shapes are square and circle-like neighborhoods in 2-D and cube and sphere-like neighborhoods in 3-D (these can be defined as equidistant neighborhoods by using different metrics). In multiscale morphological approaches multiple SE sizes are used in order to better distinguish between different objects (classes). *Morphological profiles* (MP) [Pesaresi 01, Plaza 04] are a multiscale morphological method introduced in the context of remote sensing and have proven useful for segmentation and classification of remote sensing imagery [Bellens 08, Benediktsson 05]. Morphological profiles are defined using a sequence of openings or closings with increasing structuring el-

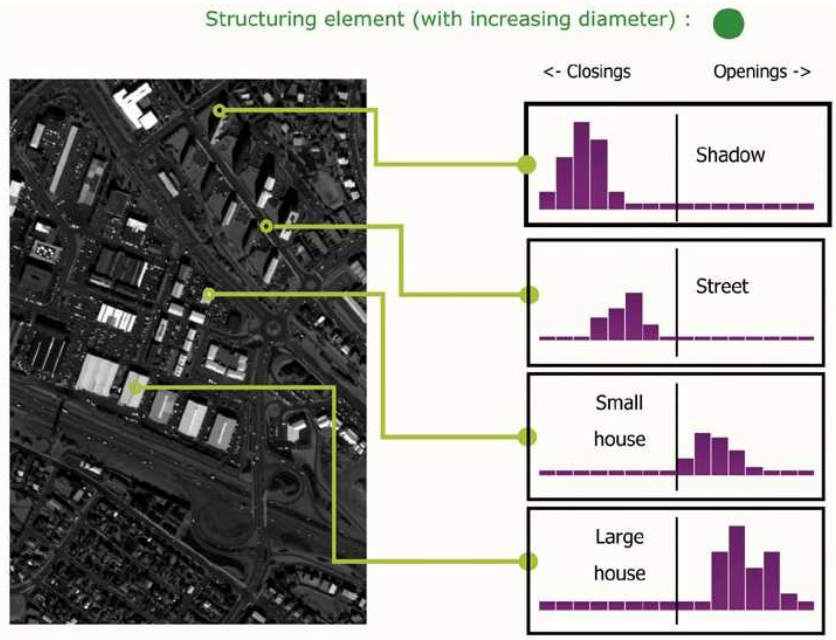

Figure 3.3: Differential morphological profiles where circular structuring element was used with an increasing diameter for four information classes (Shadow, Street, Small house, and Large house). Obviously, classes can be differentiated based on the calculated profiles [Benediktsson 05].

ement size. In other words, the result of the opening (or closing) for a given pixel is calculated for a number of different SE sizes. This yields a sequence of the opening (or closing) operation results, which is called a morphological profile (MP). The main principle of segmentation and classification using MPs is to determine the size of the objects in the image. This is done by examining the values (results of opening or closing) found in the MP and identifying the scale at which their change is maximal [Bellens 08], which allows us to classify each pixel independently of the size of the object (see Fig. 3.3).

The novel methods developed in this PhD thesis are a generalization of MPs, with the difference that more general SEs are defined, shaped by variation of two parameters (instead of only one "size" parameter in classical MPs). Also, a number of additional operators are proposed as opposed to only minimum and maximum operators in MPs [Babin 11c, Babin 12a].

3.2.2 Multiscale and geometric methods

Multiscale segmentation methods make use of pixel neighborhoods of different sizes (MP is an example of using morphological methods at different scales). Usually, multiscale segmentation is more robust to variations in object size, since it combines segmentation at higher and lower scales. [Sarwal 94] register and extract centerlines in three coronary arteriography images by applying linear programming and relaxation based consistent skeleton labeling at three different scales. [Chwialkowski 96] describe a robust system for automated extraction of flow information from velocity-sensitive, phase contrast aortic MR images using multiresolution analysis based on wavelet transform, while employing a multivariate scoring criterion.

Watershed transform considers an image as a topographic landscape in which "valleys" correspond to the interior of segments and the "mountains" correspond to the boundaries of segments. This correspondence is defined in terms of the gradient magnitude of the input image as the topographic landscape for the watershed transform. The watershed transform derives the interconnecting "valleys" from the topographic landscape, which, in turn, delineate the image into micro segments. The main characteristic of the watershed transform is that it performs an over-segmentation of an image, which means that the segments need to be merged afterward into larger ("more meaningful") regions using a *region merging* algorithm [Haris 98]. In other words, region merging techniques (e.g. graph cuts) often use fast watershed algorithms to produce an initial over-segmentation and reduce computation time [De Bock 05]. [Passat 07] incorporates a watershed transform with prior structure information for superior sagittal sinus brain vessel segmentation. It should be emphasized that the watershed transform is closely related to mathematical morphology, and various reviews on the topic [Kirbas 04, Lesage 09] classify it under morphology. Fig. 3.4 illustrates the *watershed flooding* technique.

The *ridge detection* approach is similar to the watershed approach in that it converts the gray scale image into a 3-D elevation map (see Fig. 3.5). However, the processing of the map differs from the watershed approach. While the watershed transform processes the map by over-segmenting it using "valley" tracking, the ridge-based methods extract local maxima by tracking maximum ascents from each pixel. The segmented pixels are parts of vessel centerlines, and hence, are often used in skeletonization algorithms. [Thirion 92] develop Marching Lines algorithm to extract characteristic lines from 3D images.

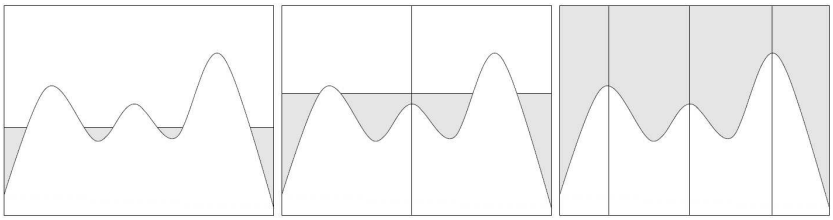

Figure 3.4: An illustration of time stages of watershed flooding principle for image segmentation [De Bock 05].

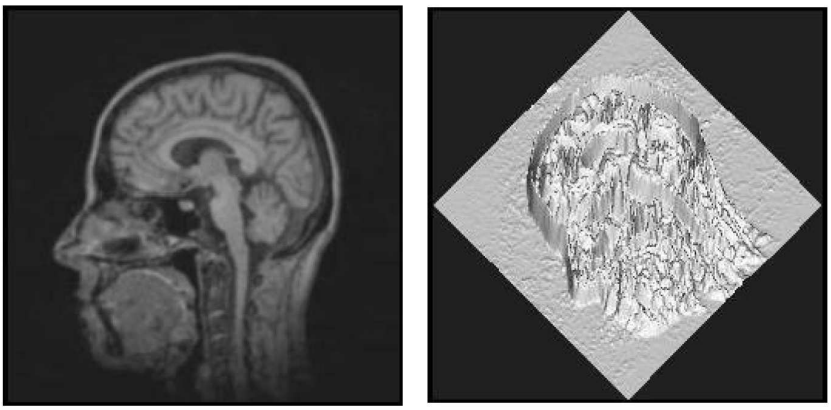

Figure 3.5: The original image and ridges as a 3-D map [Aylward 96].

[Eberly 94, Pizer 98] describe the use of ridges in image processing and the mathematical background. [Staal 04] uses the ridge detection algorithm described in [Kalitzin 02] to segment 2-D retina images. Ridge detection algorithms are also widely used in Diffusion Tensor Tractography (DTI) [Kindlmann 06, Kindlmann 07].

A similar approach to the watershed transform is used in *differential geometry-based* techniques, where the input images are segmented by transforming 2-D and 3-D gray scale images to 3-D and 4-D hypersurfaces, respectively. The segmentation is performed using the curvature and the crest lines (lines corresponding to vessel centerlines) of the surface. Applications of hypersurfaces to vessel extraction are presented in [Prinet 95, Monga 94].

3.2.3 Segmentation by filtering

Segmentation by filtering (also known as filter matching) is obtained by correlating the designed filter with the image. The operation is performed at each image pixel and the obtained response value describes how well the pixel neighborhood correlates to the given filter. The filter is designed to correspond to characteristic neighborhoods of vessels structures. In this fashion, the filtering will yield high response values at the vessel pixels and low values at background pixels. After the response values are calculated, they are thresholded using the local thresholding or morphological operations to obtain the final segmentation result. Obviously, the segmentation depends on accurate and representative design of filters, which means that they must represent all possible vessel configurations and orientations. Because of this, multiple kernels are used that represent different parts of vessels that we want to detect. This is a problem, because the execution time increases together with the number of used kernels.

The *hit-and-miss transform* is an example of a binary segmentation by filtering, which is often used for extracting centerlines (skeletons) of a binary structure. [Hoover 00] performs a type of hit-and-miss procedure by repeatedly thresholding a gray-scale image (with decreasing threshold values) and calculating the filter response. [Sato 98] segment curvilinear structures such as vessels and bronchi in three-dimensional (3-D) medical images by designing a filter based on a combination of the eigenvalues of the 3-D Hessian matrix. This is also a multiscale integration approach performed by taking the maximum among single-scale filter responses and its characteristics formulate the criteria for parameter selection. [Al-Rawi 07] propose filter parameters for matching and detecting retina images. [Lowell 04] uses matching filters approach to localize optic disk for optic nerve segmentation.

3.2.4 Centerline extraction

Skeletonization and centerline-tracking techniques extract centerlines of objects. Centerline extraction is an essential process in the examination of tubular objects (like blood vessels or lung airways) due to their graph-like structure, which supports distance and radii calculations, best path determination and bifurcation detection. In other words, centerline extraction offers higher-level object information by simplifying object structure, usually obtained using segmentation methods. We divide centerline extraction algorithms into tracking and skeletonization

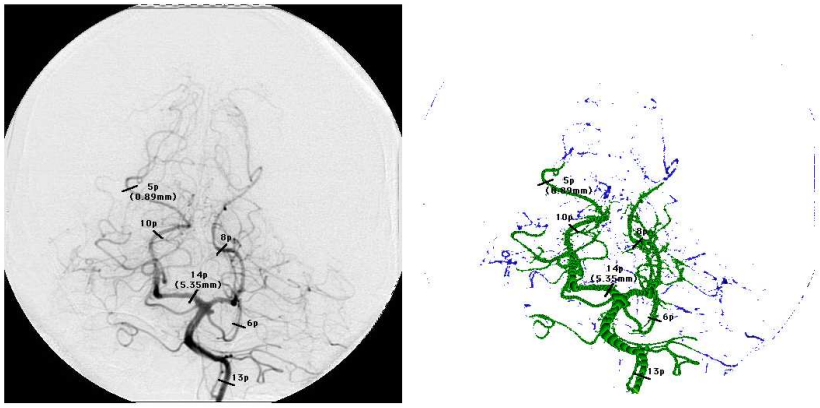

Figure 3.6: Original image and the result of vessel tracking methods proposed by [Quek 01].

methods. Tracking methods perform, in fact, the ordered propagation (region growing) from which the centerlines are extracted "on the way". Besides the centerlines, tracking methods produce segmentation, which is a product of ordered region growing. On the other hand, skeletonization algorithms produce only centerlines as a simplified representation of the object.

3.2.4.1 Vessel tracking methods

Based on the review of centerline extraction techniques from [Bühler 02], we classify centerline-tracing techniques into three categories based on the type of tracing wave front propagation.

Wave front propagation tracing is often described as an ordered region growing method. The idea is to grow a region from a seed point, and to track the propagation of the surface of the region. In the process, the centerlines are extracted by tracking the surface growth (propagation). This approach can also locate vessel bifurcations by detecting the places where the surface of the region "splits" (continues propagating in different directions). [Quek 01] presents a 2-D algorithm for vessel extraction by wave propagation, while its 3-D extension is presented in [Kirbas 03]. [Al-Kofahi 02] develop algorithms for tracking neurites, following an assumed 3-D tube-like local geometry. [Tyrrell 07] develop an advanced tracing technique capable of tracking non-connected structures, while being robust to low-contrast and noisy data. [Abdul-Karim 03] describe an automated method for tracing

and analysis of changes in angiogenic vasculature obtained by a multi-photon laser-scanning confocal microscope. [Carrillo 05] use the evolution connected components to extract 3-D vascular skeletons. [Yu 04] use both segmented and original (gray-scale) 3-D image for centerline tracking, for which a generalized cylinder model is used. [Luboz 05] design an algorithm for vessel surface extraction, which is used as a skeletonization input. [Mohan 09] create an initial vessel tube from given seed points and evolve it by a variational energy optimization approach to capture the vessel while automatically detecting branches in the vessel tree. [Yim 00] present a method for centerline extraction of small vessels in MRA.

Directional path tracking from a seed point and a given direction is an interactive method for extracting single vessel [Wink 00]. The difference with the wave propagation approach is that the region growing is performed in the predefined direction (and not in all directions). This method relies extensively on user interaction if multiple vessels need to be extracted, since a seed point and direction have to be specified for each vessel separately.

Best path tracking from a seed point to given multiple end-points uses the Dijkstra's shortest path algorithm [Dijkstra 59]. [Kanitsar 01] use the best path tracking for extracting centerlines of lower extremities in CTA images. The 3-D CTA image is considered as a graph, with voxels representing nodes and links representing neighboring voxels. Metric cost for best path calculation of graph links is derived from absolute difference of node values (voxel intensities). This method works well in clearly visible vessels (ones with higher diameter values) without higher presence of noise or artifacts.

3.2.4.2 Skeletonization

The difference between skeletonization and vessel tracking methods is that the skeletonization algorithms process all the pixels of a region of interest (or the whole image), while the tracking methods work only on local image data starting from a vessel seed point.

Different skeleton definitions exist, which are based on the type of skeletonization algorithm. [Blum 67] defines the *skeleton* in terms of *maximal inscribed circles (spheres)*, where the skeleton is the set of points equidistant from at least 2 points on the boundary of the object. In this case, skeleton is called a *medial axis* and skeletonization is a *medial axis transform* (MAT) [Choi 97]. Sometimes additional criteria are imposed on the skeletons for objects in real images: the skeleton should

be smooth, thin and continuous. Moreover, the skeleton must preserve the topology of the original shape, it must approximate the central axis and it should allow full object recovery [Bühler 02].

The *grass fire (prairie fire)* method extracts the centerlines of an object "as if the object boundaries were set on fire" and the skeleton points are formed at the places were fire fronts meet. This principle is related to wave propagation using the Eikonal equation, as a type of Hamilton-Jackobi equation [Siddiqi 02]. The *distance surface skeleton* is defined using the distance of object points from the object boundary and represents the set of points where the distance surface is not continuously differentiable. *Voronoi diagram skeleton* in 2-D is defined as Voronoi diagram of boundary object points [Naf 96, Näf 97]. In case of the 3-D object, the method is transformed into a Delaunay tetrahedralization, where the skeleton is the set of centers of tetrahedra.

A number of reviews exist on skeletonization algorithms [Klette 02,Bühler 02,Krissian 04,Žitkevičius 07]. [Suri 02] compares segmentation and skeletonization methods for vessel extraction. The reviews listed above mostly consider skeletonization algorithms applied to binary images (images that have been previously segmented). The problem with this approach is that the skeletonization result relies heavily on the result of segmentation algorithm, which often contains errors due to noise or image artifacts. Hence, some important structural details are often lost and some non-existent branches get detected due to noise and artifacts. For this reason, we divide centerline extraction algorithms to the *binary segmentation methods*, which take a segmented object as input, and the *gray-scale segmentation methods*, which operate directly on (original) gray-scale images.

Binary skeletonization algorithms can be classified into three basic groups: thinning methods, distance-based methods and hybrid methods.

Thinning skeletonization methods repeatedly apply the thinning procedure on object boundaries until one-pixel wide centerlines remain. A thorough review of thinning methods for centerline extraction can be found in [Saeed 10]. The methods are classified into iterative and non-iterative methods, where iterative methods can be further classified into sequential and parallel (parallel methods differ mostly in performance represented as a number of subcycles needed for execution). [Hilditch 69] performs pixel connectivity check and pixel deleting in a raster scan order. [Palágyi 02] presents a three subiteration thinning algorithm, with the fully parallel thinning algorithm in [Palágyi 08].

Figure 3.7: Hierarchical skeleton example [Yuan 09].

[Klette 06] defines different notions of junctions in 3-D skeletons and uses them for branch voxel classification. [Gerig 93] present a thinning skeletonization method applied to centerline extraction of segmented MRA vessel data. [Gagvani 99] define a thinness parameter to control the thinning process and the density of the skeletal structure, and apply the method to various medical images. [Haris 01] extract skeletons of coronary artery trees.

Distance-based skeletonization methods use weighting of object pixels to define their proximity to centerlines or directionality towards the desired skeleton curve. The simplest approach was defined by [Blum 67] as a *medial axis transform* (MAT), which defines the skeleton as the set of pixels equidistant to at least two pixels on the object boundary. The Euclidean distance of each pixel to the object boundary determines the skeleton points at pixels where the distance values are not continuously differentiable. [Chang 07] describes a method of skeleton extraction from distance maps. [Montanari 68] introduced a quasi-Euclidean distance, as an approximation of the Euclidean distance, for skeleton extraction. Following the given approach, various force fields based on the object structure can be defined, where the backtracking of force vectors determines the object skeleton.

In [Cornea 05], *hierarchical curve-skeletons* are extracted using the repulsive force field [Ahuja 97] and concepts from vector field topology are employed to extract skeletons. This principle allows different hierarchies of skeletons to be computed (they are skeletons of different level-of-detail in multiscale approach), where each hierarchical level is included in the next level. The idea of the potential-based algorithm developed in [Ahuja 97] is extended to 3-D in [Chuang 00]. [Wu 03] uses the "visible repulsive force" model, which is the sum of all repulsive forces derived from the visible charged planes, so the faces invisible from the seed point do not contribute in the force model. Connected local minimum positions complete the skeleton. [Ma 03] compute skeletons using radial basis functions (RBF), where the gradient vector field is constructed with the partial derivatives of RBF. Surface points converge to

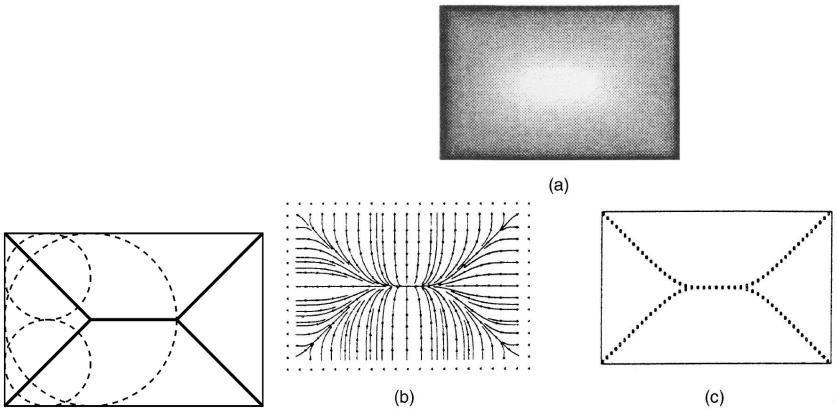

Figure 3.8: Different skeletonization principles [Chuang 00]. Left: Medial Axis Transform. Right: skeletonization based on the potential field. (a) Potential field depicted with gray values, (b) streamlines of force field and (c) derived skeleton.

the local maxima, which are linked with a snake (active contour model), which is, in turn, pushed by the external force toward the direction that decreases the potential energy until the potential energy is minimized. [Hassouna 07] derived a new energy function as a combination of the Euclidean distance field and a variant of the magnitude of the gradient vector flow (GVF), where the first energy controls the identification of the shape topological nodes from which curve skeletons start, while the second one controls the extraction of curve skeletons. Skeleton structures can also be extracted from point clouds, e.g. using rotational symmetry axis (ROSA) [Tagliasacchi 09].

Hybrid skeletonization methods combine the good characteristics of thinning and distance-based approaches, where the distance map is used to define the order in which thinning procedure will be applied, while the thinning ensures that the resulting skeleton will be composed of thin centerlines. *Distance Ordered Homotopic Thinning* (DOHT) uses a basic thinning procedure that is done in an ordered way, usually being controlled by a distance map (e.g. a map obtained by a distance transform applied to the segmented image). This means that the voxels are removed in the increasing order of distance, leading to a thinned, centered skeleton. [Schirmacher 98] use a distance gradient map to control thinning order. [Fouard 04] uses the DOHT approach for skeletonization of extremely large images of micro-vascular network by dividing

the large image into sub-images and overlapping them.

Gray-scale skeletonization algorithms compose an important group of skeletonization algorithms that try to extract centerlines directly from gray-scale images. The gray-scale skeletonization uses segmentation principles with the difference that the resulting "segmented structure" represents centerlines or sparse centerlines connected afterward using a connecting algorithms (usually based on active contours). [Hanger 01] present a skeletonization approach that utilizes planar images at different angular rotations combined with unfiltered backprojection to locate the central axes of the pulmonary arterial tree in high resolution micro-CT images. [Abeysinghe 09] create an interactive method for gray-scale image skeletonization by graph calculation. [Antunez 08] propose a gray-scale thinning algorithm for protein structure determination.

[Yu 04] develop an anisotropic vector diffusion based skeletonization method, where the diffused vector field (skeleton strength map) provides a measure of possibility of a pixel belonging to a skeleton. [Mersa 99] design a gray-scale thinning skeletonization algorithm based on conditional erosion (designed to preserve connectivity) of the gray level objects in the image until a one pixel thick pattern is obtained along the center of the high intensity region. The method of [Dokladal 99] is similar, with the difference that the gray values are thresholded with different threshold value and binary erosion is applied to object boundaries. [Jang 01,Jang 02] calculate a pseudo-distance map from the original image using a nonlinear governing equation. [Wang 06] propose a technique using the watershed algorithm to extract the skeletons of vein patterns from gray-scale images. [Yuan 09] develop gray scale skeletonization algorithm that is constrained by a structural complexity penalty using the minimum description length (MDL) principle for 3-D images of neurons acquired by confocal or multi-photon fluorescence microscopy.

3.3 Model-based segmentation methods

Model based approaches differ from pattern analysis approaches in the application of structural prior knowledge, i.e. they use knowledge about configurations of pixels rather than about individual pixels. In this fashion, a configuration of pixels is segmented in case they agree with the predefined model well. Clearly, there exists a significant overlap between model-based and local pixel neighborhood analysis algorithms, where the

multiscale methods are often extended to model-based approaches yielding hybrid methods (this is especially the case with methods using the Hessian or Weingarten matrix to estimate the orientation of low vessel curvature). We divide the model-based approaches into two categories, namely: deformable models and template shape matching.

3.3.1 Deformable models

Two major categories of deformable models are: *parametric models* based on the energy minimization of deforming curves and *geometric models* based on the level set theory.

Active contours (snakes) were first introduced by [Kass 88] as an energy minimizing deformable model. The snake is a set of connected control points (snaxels) that form a deforming model, where each snaxel has an associated energy depending upon the forces that act on it. The energy of a snaxel is composed of internal energy and external energy. Internal forces impose smoothness constraints on the contour while external forces pull the snake towards the desired image features like lines and edges. The disadvantage of snakes is that they usually require user initialization and to manually set parameters. [Al-Diri 09] use the *ribbon of twins* contour model, which uses two contours inside the vessel moving outwards to the internal side of the edges (linked together to maintain vessel width consistency, hence the "ribbon") and two located outside the edges and moving inward the internal contours. In that fashion, the edge is squeezed between the two ("twin") external and internal contours.

[Makowski 02] proposed two-phased segmentation, where *ballooning* is used to approximate vertices and is used as the input for snakes in the second phase of the algorithm. [Florin 06] use particle filters to learn the variations in direction and shape of the blood vessels during the segmentation for active contour guiding. [Li 07] develop a *region-based active contour* model for image segmentation with a variational level set formulation and apply it to different medical images. [Kaus 04] integrate deterministic, parametric model of the variation of surface features, inter-subject and intra-subject shape variation, and spatial relationships to handle multiple objects into deformable models and apply them for segmentation of cardiac 3-D MRI time series. [Toledo 00] define *eigensnakes* for segmentation of elongated structures, where the snake learns the optimal object description and searches for such image feature in the target image by applying principal component analysis on image

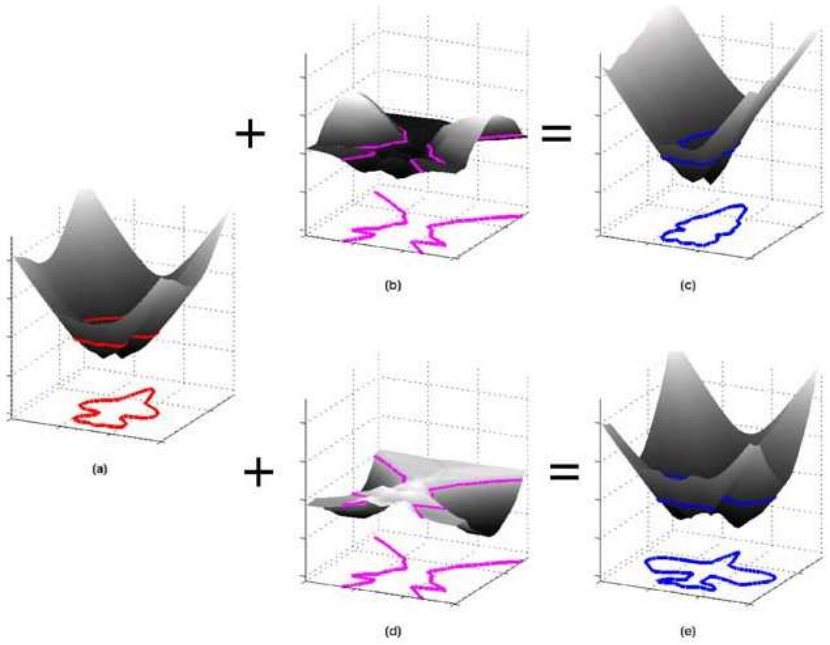

Figure 3.9: Principal component analysis on the level set function. Airplane shapes are used to show the mean level set function and its deformation along the first eigenmode [Cremers 07].

responses of a bank of Gaussian derivative filters.

[Caselles 95] and [Malladi 95] developed *Geodesic Active Contours* (GAC) by introducing of geodesic parametrization of active contours as a type of *level set methods* [Osher 88]. The level set methods represent propagating curves as zero level set of a higher dimensional function in the Eulerian coordinate system. Intuitively, this principle can be described by an arbitrary surface (of a volume) cut by a plane (which represents a level). The curve resulting from the intersecting positions of the plane and the surface is called a level set. The advantage of such an approach over classical energy-minimizing active contours is that the level set approach is capable of handling complex shapes and sharp curve turns (angles). Another drawback of snakes in comparison to GAC is that snakes require a regridding (or reparameterization) process to avoid self-intersection and overlap. [Cremers 07] gives an overview of level set techniques. [Lorigo 00] develop consider 1-D curves in 3-D ("codimension-two") for automatic segmentation of MRA images of blood vessels. The work is based on their method of

curve evolution for vessel segmentation (CURVES) [Lorigo 01], which represents active contours with adjusted parameters and prior knowledge for vessel segmentation using both pixel intensities and local boundary smoothness properties. The approach of [Manniesing 06] optimizes relevant parameters of the level set evolution using a training set. This principle can be very efficient, but only in the case if the images are well represented by the training set, which has to be carefully chosen. [van Bemmel 03] developed a semi-automatic method for artery-vein separation by simultaneous evolving of two level set curves (venous and arterial curve), where the pixels are classified based on the arrival time of respective curve. [Hernandez 07] propose a geometric deformable model that uses an energy functional. It incorporates the estimated statistical region-based information, obtained from a high-order multiscale non-parametric model. The method was applied to segmentation of cerebral aneurysms in 3DRA and CTA images. [Yan 06] introduce the capillary geodesic active contour that is optimized for surface evolution into very thin branches of blood vessels. [Nain 04] presented a soft shape prior that can be combined with any other image force to deform an active contour and penalize leaks. [Deschamps 04] use level sets to perform vessel segmentation and blood flow simulation. [Shang 08, Shang 11] introduced a *region competition based active contour* (RCAC) model exploiting the Gaussian mixture model to robustly segment thick vessels and the vascular vector field is built using the Hessian based vesselness measure to evolve the contours.

3.3.2 Parametric models

The most common parametrically defined models are ellipsoids and cylinders. The circular representation [Chan 00] is not as common and has lower capabilities than the 3-D models.

Ellipsoid models have proven successful when segmenting healthy, "ordinary" vessel structures, but encounter problems when segmenting structures of non-healthy vessels (e.g. aneurysms or arteriovenous malformations). [Pellot 94] use ellipses to initially model healthy vessels and stenosis in angiographic images. [Frangi 98] use second order ellipsoid models (all eigenvalues of a Hessian matrix) to obtain a vesselness measure, which is a probability of a pixel to belong to the blood vessel structure (this is not a segmentation, but a *vessel enhancement method*).

[Schmitt 04] use *generalized cylinders* with circular cross sec-

tions, where the user interactively provides a rough initialization by marking the branching points. [Worz 07] develop a method based on a 3-D cylindrical parametric intensity model, directly fitted to the image intensities through an incremental process based on a Kalman filter. [Florez-Valencia 06] present a vascular segmentation method based on the right generalized cylinder state model, which includes a curvilinear axis associated to a stack of contours. The axis is described by a state vector (local curvature, torsion and rotation), while the contours are described by a Fourier series decomposition. [Santamarıa-Pang 06] implement learning and predicting tubular models in 3D images by using Support Vector Machines to estimate the posterior probability of an element belonging to a tube-like object. A vesselness principle similar to [Frangi 98] is used by [Qian 09], except that the single cylinder assumption is relaxed and the method relies more on multiscale pixel intensities. [Tyrrell 07] introduce *superellipsoids* that are explicitly defined and take shape from ellipsoids to cylindroids.

3.4 Template matching and atlas-based methods

Methods described in this section rely on matching vascular structures in the image with explicitly defined shapes (templates) to perform segmentation. Hence, the templates are *a priori* models used by *top-down* approach algorithms. The vessel models are often represented in a graph-like manner and the algorithms perform by deforming the predefined model based on the image properties. Different predefined shapes can be used to detect "unusual" (unhealthy) structures in vessel trees, which are not easily detected using parametric or deformable models, since these models are mostly optimized to detect healthy vessel structures. An overview of shape searching techniques is given in [Iyer 05]. [Lemaitre 11] proposed an approach to curvilinear and wiry object detection and matching based on a curvilinear region detector (CRD) and a shape context-like descriptor (COH).

Atlases can be defined as n-dimensional images that model the higher-level knowledge of structure properties. They are often used in segmentation of head and brain tissues. However, due to the tortuosity and variability of brain vessels, the creation of vascular atlas is a hard task. Vessels are very "unpredictable" in their structure (e.g. circle of Willis), position and abnormalities. [Musse 03] designed one of the

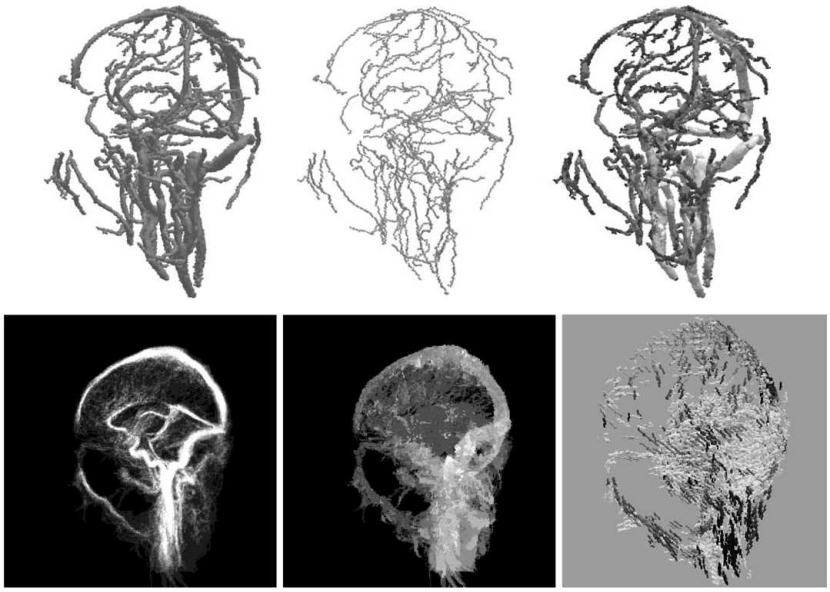

Figure 3.10: Visualization of segmentation and atlas throughout the building process [Passat 06]. Top row from left to right: segmented vessels, skeleton, vessel diameters. Bottom row fro left to right: vascular density (brighter regions indicate higher probability of finding a vessel), average vessel diameters (the brighter the region, the larger the vessels) and 3D visualization of a part of the orientation image.

first vessel segmentation methods using the deformable image matching to 3-D atlas. [Cool 03] built a brain atlas of *vascular density* using the tissue-based registration, to identify a standard vascular tree with expected variance. [Chillet 03] developed a method for forming vascular atlas using vascular distance maps and apply it to liver and brain vasculature. The general approach of these methods is to calculate an inverted distance map for each blurred image, after which the elements in the data base are given the distance from an arbitrarily chosen element. [Passat 05a] design the atlas from MRA magnitude image (similar to a classical T1 MRI), using semi-automated segmentation tools. Its main purpose is to provide a set of regions presenting homogeneous properties about vessel size, orientation and position relative to other brain structures. This atlas is then used for guidance of region-growing segmentation from phase contrast MRA images. [Passat 06] designed a method to generate model knowledge as vector fields, thus overcoming the drawback of classical image atlas that divide the structure into finite

set of vascular areas [Passat 05a]. The most recent works are the works of [Nowinski 09, Nowinski 11], where the cerebral vascular atlases were created using images with 3T and 7T scanners.

3.5 Other segmentation methods

The blood vessel delineation is a wide and repeatedly examined field of study, yielding high number of various methods for vessel segmentation. Some of the other most important methods in vessel segmentation are described next.

Artificial intelligence-based methods use higher level knowledge to guide the segmentation process. The implemented knowledge can contain information on image properties (imaging modality dependent) or on the structure of objects that need to be delineated. *Knowledge-based* methods apply low level image processing algorithms (e.g. thresholding or morphology) and use a priori (high-level) knowledge of the anatomical structure to guide the segmentation process. The drawback is that it has a higher complexity when compared to average image processing techniques. [Rost 98] described a knowledge-based system for automatic adapting of low-level image processing algorithms, where the image processing operators are configured using explicitly formulated expert knowledge rules. [Bombardier 97] design a knowledge based approach for the automatic and reproducible identification of artery boundaries based on the cooperation of two fuzzy segmentation operators.

The most interesting property of *neural networks* is its possibility of learning. The learning process requires a training set, which has to be representative, meaning that it has to include all the possible vessel characteristics. The network is composed of elementary processors (nodes). A node has multiple inputs, performs elementary computations, and generates a single output. A cost function is defined, which measures how close a particular solution is to the optimal solution. The costs are parameters adjusted (learned) through training and used in the analysis (segmentation) process. A drawback of neural networks is that they require a large diversity of training samples. The segmentation may fail in case an image is processed that has characteristics not found in the training set. [Jiang 10] give an overview of neural network methodologies with the focus on medical image analysis. [Kobashi 01] uses the watershed to perform initial segmentation. The neural network classifies each primitive (a group of voxels) by evaluating the intensity and the 3D shape. [Perfetti 07] propose a cellular neural networks (CNNs) ap-

proach to retinal vessel segmentation. The CNN design is characterized by a virtual template expansion obtained through a multistep operation, based on linear space-invariant templates. [Lasch 06] demonstrate how optimized network models can be utilized to re-assemble false color images from infrared spectral maps of tissue sections.

3.6 Conclusion

In this chapter we gave a broad overview of methods used for segmentation of vascular structures obtained using various imaging modalities, and we discussed their advantages and limitations. The techniques are rated according to the amount of the incorporated "higher-level" knowledge on vessel pixel neighborhoods, models and structures. Currently, many methods use lower-level techniques (less prior knowledge) to produce an input for higher-level methods (model- or template-based techniques that incorporate high amount of prior knowledge). The introduction of higher-level knowledge yields good segmentation results in case of healthy vessels, because they can be modeled well using cylindrical or tubular shapes. However, vessel anomalies are very hard to model. They appear at various positions and constitute "unpredictable" shapes, and for this reason, the model-based or template-based approaches often have problems when segmenting these structures. On the other hand, vessel abnormalities are the structures of the highest interest for surgeons, since their clear delineation and structure analysis significantly aids in clinical practice. For this reason, our opinion is that multiscale methods (as local pixel neighborhood analysis-based techniques) play a critical role in analysis of "unpredictable" structures.

4

Generalized Profiles

Multiscale segmentation methods show high robustness without a need for fine parameter tuning. These properties are of great value for segmentation of cerebral blood vessels with an emphasis on cerebral aneurysms and arteriovenous malformations (AVM). For surgery or embolization of an AVM, a clear distinction between feeding arteries, nidus and vein of the AVM is of the utmost importance. However, techniques addressing the problem of the AVM inner structure segmentation are rare. In this chapter we introduce generalized profiles, as a generalization of morphological profiles (MP). Novelties of our method are: (1) introduction of a structuring element (SE) controlled by two parameters, as a more general pixel set in comparison to classical structuring elements; (2) using various operators and their combinations applied to SE as opposed to minimum and maximum as the basis of morphological operations; (3) a method for evaluation of profile operators. Our algorithm stands out in situations with low resolution images and high variability of pixel intensity. The results on phantoms and real data demonstrate its effectiveness and potentials for fine delineation of the AVM. The work presented in this chapter has been published on international conferences [Babin 09b, Babin 12b], as well as a journal article [Babin 12a].

4.1 Introduction

The cerebral arteriovenous malformation (AVM) is a collection of dense, intertwined blood vessels (see Section 1.2.1). It is formed at the location where the arterial blood flows directly into the vein without passing through a capillary system. Because of a higher elasticity of a venous blood vessel wall and a high arterial blood pressure (when compared

to venous blood pressure), the vessel is repeatedly deformed. The malformation often consists of numerous small blood vessels with a high probability of a rupture, leading to an intra cranial hemorrhage (i.e. internal head bleeding). The main components of the AVM are feeding arteries, the draining vein and the nidus. Feeding arteries are blood vessels that bring the blood into the malformation. The draining vein is the blood vessel that takes the blood out of the malformation. The nidus is a collection highly intertwined vessels, which usually rupture. In order to cure a patient, an embolization procedure is performed. The embolization is a way to occlude the nidus by inserting a glue-like substance using a guided catheter. It is essential to occlude the whole nidus structure to prevent bleeding. It is also very important to keep the draining vein clear to allow a continuous blood flow from feeding arteries into the vein. Therefore, accurate delineation between the nidus, the draining vein and feeding arteries is required. The resolution typically used in CTA brain vessel imaging is often not sufficient for visualization of the AVM, which consists of large number of intertwined vessels in a very small volume (see Fig. 4.1).

Multiple imaging approach of [Säring 07] combine 3-D and 4-D MR image sequences to visualize and analyze malformations. Digital subtraction angiography (DSA) methods [Coste 01, Söderman 00] have proven crucial in AVM related surgery [Zhang 03], and validation methods for this imaging modality have also been developed [Berger 08]. However, DSA methods [Coste 01,Söderman 00], while efficient in determining volume of the AVM, are not able to delineate the inner structure of the malformation. Based on the current reviews of vessel extraction techniques [Kirbas 04, Lesage 09, Yaniv 06], we classify the existing methods for AVM extraction into visualization and segmentation methods.

The goal of a blood vessel segmentation is to provide a surgeon with a blood vessel tree model. The resulting model can be analyzed to provide valuable vessel information (e.g. vessel radii, bending angles and the best paths). The segmentation of blood vessels is a difficult task in general, because of a varying structure, size and direction of blood vessels in a 3-D image and these problems escalate in the case of the AVM segmentation, because of its highly unpredictable structure. Therefore, prior knowledge concerning the position of blood vessels and even their number in the malformation is limited. Simple approaches as adaptive thresholding and connected components methods [De Bock 10] have difficulties in dealing with high variety of pixel intensities. Active

contours [Shang 08, Shang 11] give good results when segmenting blood vessels in images of sufficient resolution, which is not the case in AVM segmentation. Shape and flow driven methods optimized for segmenting tubular structures [Cebral 05, Castro 07, Hoi 04, Nain 04] are able to segment vessels going in or out of the malformation, but are not applicable for segmenting complex structure (such as the nidus of the malformation) at lower resolutions.

The goal of the visualization is to enhance the existing blood vessel images in order to aid a surgeon in decision making and surgery. Visualization is performed either by application of advanced image processing and computer graphics methods or by using multiple imaging modalities and acquisitions (multiple data sets acquired by a single modality). A large number image processing studies treat visualization of cerebral aneurysms and malformations, as well as blood vessels of brain in general [Antiga 06, Bullitt 01, Coenen 05, Forkert 09, Piccinelli 09]. However, these visualizations are usually not capable of fine delineation between the feeding arteries, draining vein and nidus, which is exactly the focus of this work. The approach of [Qian 09] examines the polar neighbor intensity profile of a voxel in order to determine a "vesselness measure" for characterizing vascular structures. The vesselness measure is usually obtained on the basis of eigenvalues of the Hessian as in [Frangi 98], where an assumption is used that a single cylinder exists around each voxel. However, the vesselness measure is hard to determine in case of complex AVM structures. Diffusion tensor (DT) fiber tractography has also been applied in AVM examination and is more suitable for therapeutic stages [Okada 07]. A disadvantage of visualization is that the blood vessel models are not explicitly generated. Hence, computational analysis of the blood vessel structure and the best path calculations are not possible.

In this chapter we propose a new segmentation method based on multiscale operators, taking into account both local spatial context of a pixel and pixel intensities. Our method is related to mathematical morphology in combination with a multiscale approach. Classical morphological operators [Serra 82, Soille 86] make use of a structuring element (SE) of a given shape (like square or circle) and size. The SE shape and size can also be adaptive, like in [Cheng 00]. Our approach can be seen as a generalization of the morphological profiles (MP) [Pesaresi 01, Plaza 04], introduced in the context of segmentation and classification of remote sensing imagery [Bellens 08, Benediktsson 03]. Morphological profiles are a multiscale approach defined using a se-

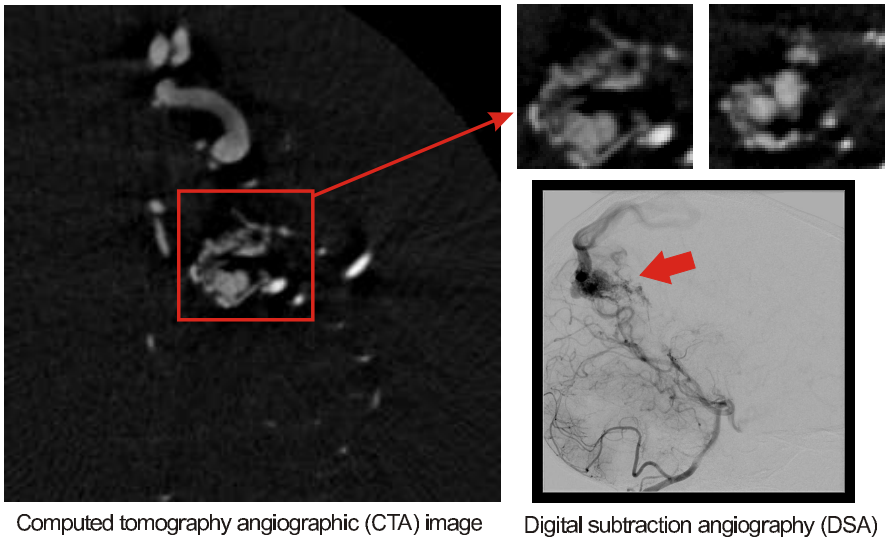

Figure 4.1: Left: a slice from a 3-D CTA image of cerebral blood vessels. CTA AVM images (upper right) are extracted from the data set of cerebral blood vessels images. The AVM vessels show no clear structure compared to normal vessels. Lower right: DSA image of the brain blood vessel tree with marked AVM region (arrow). Note that the AVM is a highly dense structure of entangled vessels.

quence of morphological openings or closings with an increasing structuring element size. It is necessary to identify the scale at which the change of values is maximal in order to determine the size of the object the pixel belongs to [Bellens 08].

The main novelties of our work in comparison to existing morphological profiles (MP) are the following. Firstly, we introduce an SE with two size parameters (instead of only one size parameter in classical MPs) to produce a wider variety of SE shapes. Secondly, we define more general operators as opposed to only minimum and maximum operators in MPs. We calculate the operator values for various SE parameters. The obtained values represent the profile of a pixel. Finally, we introduce the *profile measure*, which is used to quantify (measure) calculated profiles and to obtain the final segmentation. The experimental results show a clear benefit from both of these extensions to classical morphological profiles. Moreover, in earlier reports only remote sensing applications were considered and to our knowledge this is the first application of this type of methods for blood vessel segmentation.

The chapter is organized as follows. In Section 4.2 we explain the idea of generalized profiles. The choice of profile operators and their combinations is explained and the relation to morphological profiles is shown. Section 4.3 presents the results of the proposed algorithm applied to the phantom and CTA images of cerebral AVM. We discuss the advantages of using structuring elements defined with two parameters instead of one, and we discuss the 2-D approach in case of CTA images of cerebral vessels. Section 4.5 concludes this chapter.

4.2 The proposed method

4.2.1 Segmentation using the spherical mean

In this subsection we present for clarity reasons a simplified case of our generalized profiles method. The method was used for segmenting low quality 3-D MRI images of an abdominal aorta and was published in an international conference [Babin 09b]. Fig. 4.2 shows several slices of a 3-D MRI data set. The MRI images were taken without injecting a contrast fluid, so blood vessels appear dark (contrary to CTA images, where blood vessels are bright). A number of artifacts are present in these images like: noise in the aorta due to heart movements and breathing, "merging" of adjacent vessels due to low contrast and misalignment of vessels in neighboring slices due to low inter-slice resolution (large spacing between slices). The hardest part of the data for segmentation is the lower abdomen and legs, where all of the mentioned artifacts are present. Therefore, we need a robust segmentation algorithm that is capable of separating adjacent blood vessels with various contrast. This is the exact requirement as for the CTA AVM images depicted in Fig. 4.1. In case of CTA images of an AVM, the available resolution is typically low, so that the structure changes significantly from one slice to the other. Due to a very large inter-slice spacing (6.6mm) in abdominal MRI images and registration problems, the method would benefit from a 2-D approach (later in this chapter we will extend the idea to the 3-D case). Hence, we propose to segment each slice separately. Multiple segmentation candidates will be produced for each slice and a separate algorithm will select the best candidate as a final segmentation for that slice. An advantage of the slice-by-slice approach is that it is computationally much more efficient (reduces computation times).

We will now explain our simplified profiling segmentation method in case of abdominal MRI images (blood vessels appear dark

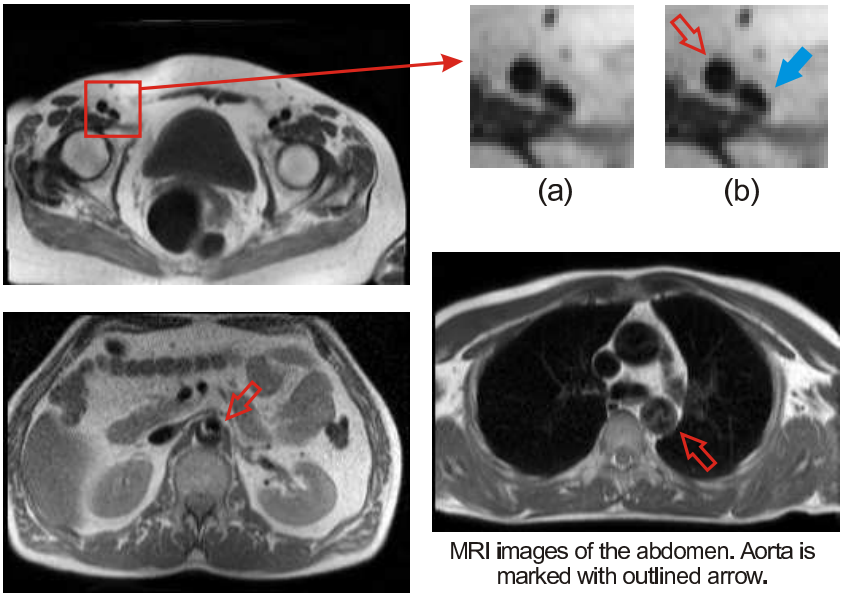

Figure 4.2: Slices of a 3-D MRI image of the abdominal aorta. The images are not contrast-enhanced, so blood vessels appear as dark regions. A lot of noise and artifacts are often present in the aortic regions (outlined arrows). (a), (b) Part of the original MRI slice with marked arterial vessels (outlined arrows) and venous vessels (full arrow).

in these images). Consider a dark pixel in the image (see Fig. 4.4). We want to compare the pixel gray value to the average gray value of its neighborhood. The average gray value of the neighborhood tells us how bright or dark the neighborhood is. Therefore, if we compare the gray pixel value with the average gray value in the neighborhood, we could say if the pixel is "darker" or "brighter" than the neighborhood. Let us assume that the pixel was darker than its closest neighborhood. We can repeat this analysis by examining the average gray value in the next larger pixel neighborhood. Let us repeat this process until we come to the opposite conclusion: that the pixel is not darker than its neighborhood any more (i.e. pixel gray value is higher than the average gray value of the neighborhood). The size of the last neighborhood for which the condition was fulfilled represents a distance to which the pixel is darker than all its neighborhoods. This distance will be the new pixel gray value. In other words, our analysis results in a distance map image. The calculated (distance) gray value we call the *profile measure*. The profile measure tells us which pixels are the "darkest" in the image

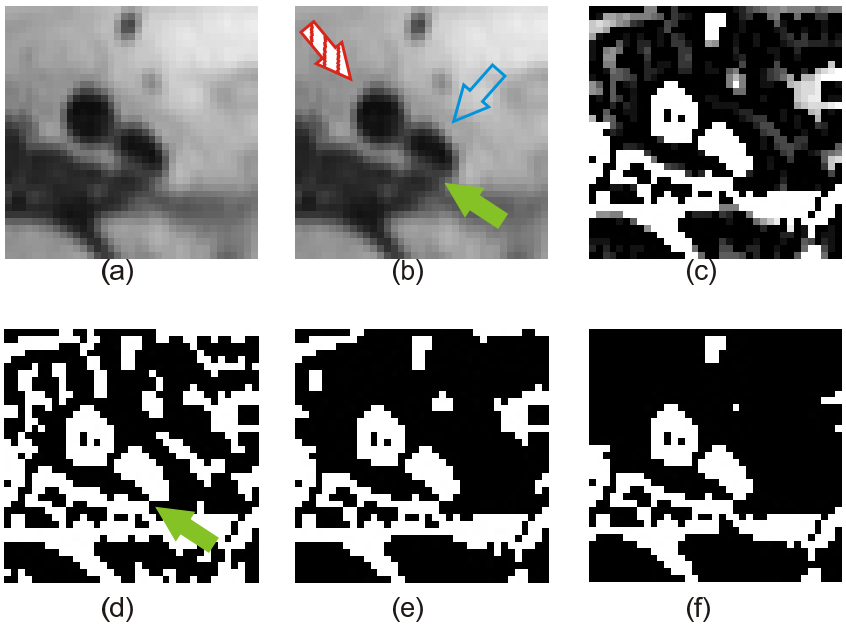

Figure 4.3: (a) A part of the original MRI slice. (b) Important regions in the original image: striped arrow shows the artery, outlined arrow the vein and full arrow the region that needs to be well separated. (c) The transformed image using the spherical mean. (d) The segmented image using spherical means for low threshold value. There is noise in the artery and the vein could be better delineated (full arrow). (e) The segmented image using spherical means for median threshold value. Less area is segmented. (f) The segmented image using spherical means for the highest threshold value. Note that the separation of vessels and presence of noise did not change for any of the given threshold values.

when compared to their multiscale neighborhoods. This is a valuable information in images affected by noise and artifacts.

The result of finding the average of all pixel gray values in an equidistant neighborhood is called the *spherical mean*. The spherical mean operator on a function at a point is the average of all values of the function on a sphere of given radius centered at that point. Since we consider the multiscale 2-D approach, we actually compare the pixel gray value to the spherical means of the image, centered at the given pixel, for different radii r.

We will now present the described algorithm in a more formal way. Let $\mathbf{p} \in \mathbb{Z}^2$ denote the pixel position in a 2-D discrete image g with pixel gray value range [0,255]. For the given pixel position $\mathbf{p} = (x_\mathbf{p}, y_\mathbf{p})$

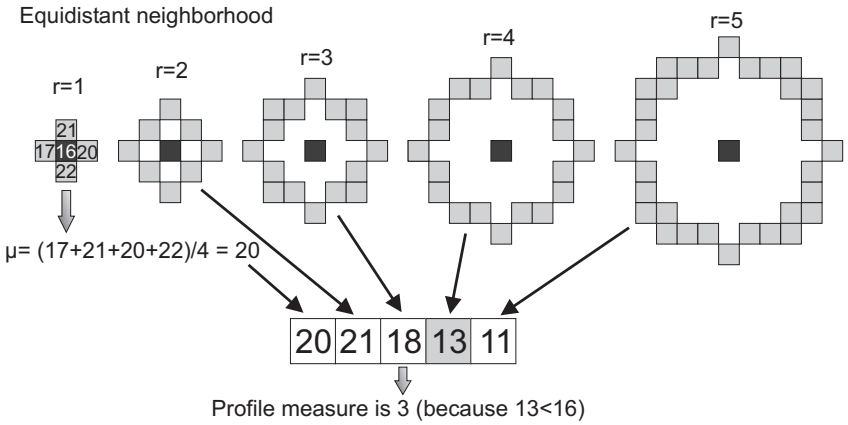

Figure 4.4: The spherical mean of a function is the average of the values on a sphere. In case of a 2-D function, samples are taken on a circle (function values are represented as a height map).

we define a set of equidistant pixels at a radius $r \in \mathbb{N}$ as:

$$R_r(\mathbf{p}) = \left\{ \mathbf{q} \in \mathbb{Z}^2 \mid (r-1)^2 < (x_\mathbf{q} - x_\mathbf{p})^2 + (y_\mathbf{q} - y_\mathbf{p})^2 \leq r^2 \right\} \quad (4.1)$$

The average of all gray values in this set can be expressed as:

$$\mu_r(\mathbf{p}) = \frac{1}{|R_r(\mathbf{p})|} \sum_{\mathbf{q} \in R_r(\mathbf{p})} g(\mathbf{q}), \quad (4.2)$$

where $|R_r(\mathbf{p})|$ denotes the number of pixels in the equidistant neighborhood.

Definition 1 *Let r be the longest consecutive $r' \in \mathbb{N}$ for which $g(\mathbf{p}) \leq \mu_{r'}(\mathbf{p})$. We then define the* profile measure *as $\rho(\mathbf{p}) = r$.*

The segmented image is obtained by thresholding the profile measure image. It should be noted that a similar principle will be used to segment bright blood vessel pixels in CTA images by replacing $\leq$ with $\geq$ in Definition 1.

A part of the original MRI slice is shown in Fig. 4.3a and its corresponding transformed image in Fig. 4.3c. As mentioned earlier, we perform segmentation by thresholding the profile measure image. In fact, our goal is to obtain various candidate segmentations, from which a separate algorithm will select the best one. Candidates are obtained by thresholding the transformed image with different threshold values.

If the profile measure image contains m distinct pixel values, we can obtain $m-1$ distinct segmentation candidate images by thresholding the transformed image. Some of the obtained candidates for Fig. 4.3a are shown in bottom row of Fig. 4.3. From these images, a "higher level" algorithm estimates the likelihood of each binary connected region being a vessel structure. This estimation is done on the basis of circularity of and expected size of blood vessel (this is a known parameter). Our focus in this chapter is on the "lower level" segmentation (i.e. creating candidate images). Therefore, at this point we will not go further into explaining the details of the candidate image evaluation.

Let us examine the segmentation candidate images in Fig. 4.3. In general, blood vessel regions are separated from surrounding tissues. However, Fig. 4.3a shows a blood vessel region that could be better separated from non-vessel region (it is connected to the tissue if 8-connected neighborhood is considered). An important observation comes from examining segmentation candidate images in the bottom row of Fig. 4.3. These images were obtained by thresholding the transformed image with the lowest, median and the highest possible threshold value. It should be observed that in each of these images the blood vessel regions appear the same; the threshold value only affects the other regions.

Since the threshold does not affect the separation between the blood vessels and other tissues, we will examine another approach that redefines how the "brightness" of the neighborhood is calculated. In other words, instead of using the spherical mean value as the brightness of the neighborhood, we will try using other operators (for illustration we will show the results when the median operator is used to define the brightness). In fact, since the threshold does not play such a significant role in defining the separation of blood vessels, it could be fixed to the highest possible value (corresponding to the highest gray value found in the profile measure image). Instead, different segmentation candidate images could be generated using various operators on pixel values in the neighborhood. This idea is motivated by *order statistic filters* (*Ll filters*) [Pitas 92].

Let $s_1 \leq s_2 \leq \ldots \leq s_{\mathrm{R}}$ be the gray values in $R_r(\mathbf{p})$ ordered from dark to bright. Then s_i is called the *i-th order statistic*. With R we denote the number of elements in neighborhood $R_r(\mathbf{p})$. For our purposes we define the Ll filter as:

$$l = \sum_{i=1}^{\mathrm{R}} a_i s_i, \tag{4.3}$$

where the weights a_i are real numbers. The formulation (4.3) allows us to define various filters (e.g. moving average, median, rth ranked-order, α-trimmed mean and midpoint) by appropriate selection of coefficients a_i.

The following choice of a_i will result in a *median* filter:

$$\text{med}: \begin{cases} a_i = \begin{cases} 1, & i = \mathrm{R}/2+1 \\ 0, & i \neq \mathrm{R}/2+1 \end{cases}, & \mathrm{R} \text{ is odd} \\ a_i = \begin{cases} 0.5, & i = \mathrm{R}/2 \ \vee \ i = \mathrm{R}/2+1 \\ 0, & i \neq \mathrm{R}/2 \ \wedge \ i \neq \mathrm{R}/2+1 \end{cases}, & \mathrm{R} \text{ is even} \end{cases} \tag{4.4}$$

Fig. 4.5b shows the transformed and the segmented image in case the median operator is used (equations (4.3) and (4.4)) instead of the spherical mean (4.2). The segmented image (obtained by thresholding with the highest possible threshold value) shows a better separation of blood vessels from the surrounding tissue. Moreover, all dark circular structures are well delineated, independently of their size. This is an advantage when small blood vessels need to be segmented.

The median operator gave a better result than the mean operator in this example, although this might not be the case for each of the blood vessel structures or image modalities. However, it proves the benefit of examining multiple operators and using them to create various segmentation candidates, from which a "higher level" algorithm will select the best result.

Before introducing a more general framework, we will now address the question of size and shape of the pixel neighborhood. The segmented blood vessels in Fig. 4.5b are well separated from the neighboring dark tissue regions. However, some pixels in the darkest (arterial) blood vessels are not included in the segmented region. This happens due to noise that makes these pixels slightly brighter than their surrounding. Therefore, these pixels have low values in the transformed (profile measure) image and are discarded by thresholding. In case of the lowest radius $r = 1$, the equidistant neighborhood consists of a small number of elements. Hence, a small difference in neighboring pixel intensities might stand out as a large difference in values of corresponding pixels in the transformed image. A drawback is that small neighborhoods also increase sensitivity to noise. However, it also clearly delineates fine structures, which is an important property for the segmentation of CTA AVM images. In case when we need to segment large blood vessels (e.g. aorta), fine detail delineation is not essential. Hence, we propose to use larger neighborhoods.

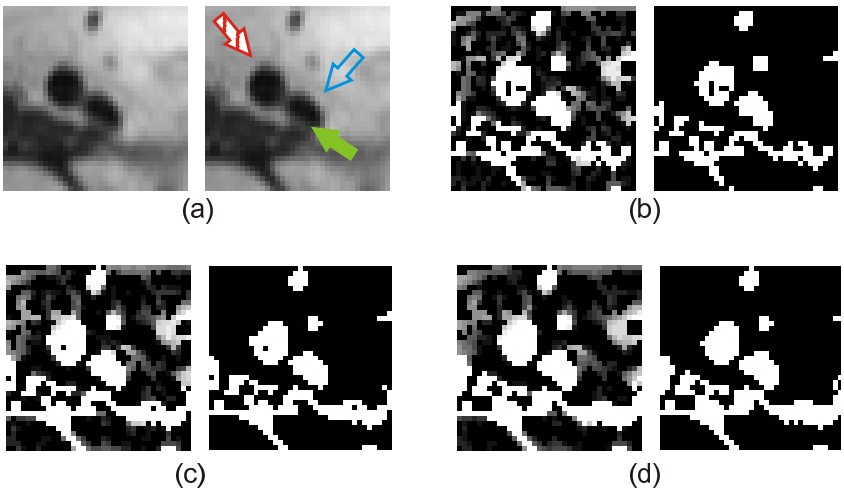

Figure 4.5: Illustration how neighborhood size influences segmentation in case of a median operator. (a) The original image (artery indicated with striped arrow, vein with outlined arrow and region of interest for separation with full arrow). (b) Transformed and the segmented image for thickness of the neighborhood $n = 2$. The delineation is fine, but there is segmentation noise in the aorta. (c) Transformed and the segmented image for thickness of the neighborhood $n = 3$. The delineation is fine and very little noise is present. (d) Transformed and the segmented image for thickness of the neighborhood $n = 4$. There is no noise in the aorta, but the delineation is not as good as before.

Let us consider a neighborhood defined in terms of 2 parameters $r, n \in \mathbb{R}$:

$$R_{r,n}(\mathbf{p}) = \\ = \{(x,y) \in \mathbb{Z}^2 \mid (r-1)^2 < (x - x_\mathbf{p})^2 + (y - y_\mathbf{p})^2 \leq (r+n-1)^2\} \ . \tag{4.5}$$

The transformed image in Fig. 4.5c was obtained using the median operator and a pixel neighborhood with a constant parameter $n = 2$ (the area of the neighborhood is increased). The corresponding segmented image has well separated blood vessels well with less segmentation noise. The reason for this is that each neighborhood includes more pixels in the transformed value calculation than in the previous case (see equation (4.5)). If we further increase the parameter $n = 3$, the influence of noise is completely eliminated (see Fig. 4.5d). However, note that as the pixel neighborhood area increases, the proposed algorithm tends to merge dark regions together. We conclude that in case of CTA AVM images, it is of interest to use the neighborhood with $n = 1$, since fine

details need to be segmented and the influence of noise is not drastic. In the case of aortic MRI images, it is better to use neighborhoods with higher n parameter values to eliminate noise from the segmentation, but still achieve good delineation.

For clarity, we summarize our most important observations (confirmed in practice on multiple experiments):

- It is of interest to use multiple operators (defined using Ll filter) for segmentation purposes.
- The size and shape of the pixel neighborhood also play role in the final segmentation result. With increasing the neighborhood size, robustness to noise increases but less details are obtained in the segmentation result (and the other way around).

4.2.2 Generalized profiling

In the previous subsection we have gradually (through examples) introduced novelties in our profiling method. In this subsection we will introduce a more general framework for our method. We introduced a ring-shaped pixel neighborhood with 2 parameters $R_{r,n}$, where the first controls the neighborhood size and the second the thickness of the neighborhood (from now we consider $R_{r,n}$ without argument as $R_{r,n}(0)$). The neighborhood in (4.5) is a filter window, which we call *ring-shaped structuring element* (RSE). The idea of an equidistant neighborhood with controllable size and thickness can be extended to the 3-D space. The *layer structuring element* $D_{r,n}$ can be thought of as a difference between two structuring elements (SE) S_r (a structuring element with a single size parameter in either 2-D or 3-D) of different size:

$$D_{r,n} = S_{r+n} \backslash S_r, \tag{4.6}$$

where $r \in \mathbb{N} \cup \{0\}$ denotes the size of a smaller SE and parameter $n \in \mathbb{N}$ is defined as the difference in sizes between the two SEs. By convention, the SE of size $r = 1$ is a window containing only one (center) pixel, while the SE of the size $r = 0$ is an empty set. In general, the SE of any size can be expressed as a layer SE with the r parameter set to zero ($r = 0$):

$$S_n = D_{0,n}. \tag{4.7}$$

Note that the equation (4.6) can be applied to creating both 2-D and 3-D structuring elements.

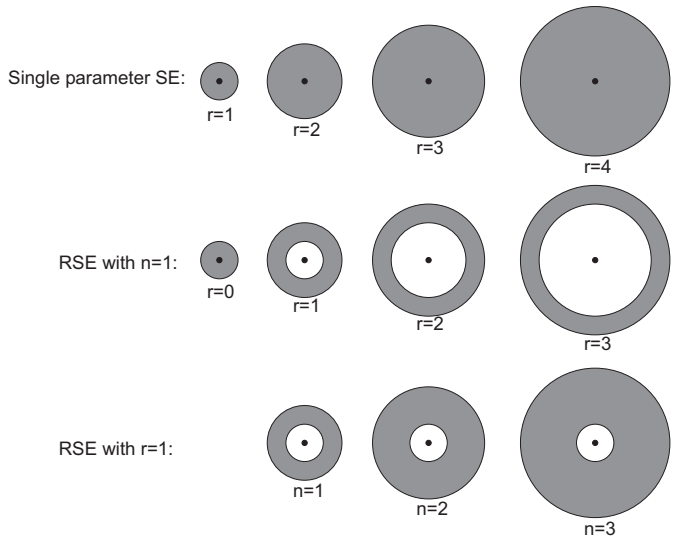

Figure 4.6: An illustration of the proposed ring-shaped structuring element (RSE) compared to standard SE. Top row: SE with different size r, middle row: RSE with varying r parameter and constant n parameter, bottom row: RSE with varying n parameter and constant r parameter.

The ring-shaped SE creation principle is illustrated in Fig. 4.6. Since we design the algorithm to perform segmentation of blood vessels, we will use only ring-shaped SE as defined in (4.6) and spherical layer SE shown in Fig. 4.7 for the results presented in this chapter. This means that we will perform our experiments with a 2-D SE in a slice-by-slice manner and a with a 3-D SE in the 3-D image.

In the first example of previous subsection we calculated the brightness of the neighborhood by averaging the pixel intensities in the neighborhood (4.2) (our example was with spherical mean, which is an average of pixel intensities in an RSE with $n = 1$). In the second example we calculated the brightness using the median of the pixel intensities in the neighborhood. If future, we will use various operators to estimate the brightness of the pixel neighborhood.

We will now extend the classical operator notation convention to arbitrary statistical operators. Let $g(\mathbf{p})$ be the gray value at position $\mathbf{p}$, and let:

$$f^{(i)}(r, n, \mathbf{p}) \stackrel{\triangle}{=} \underset{\mathbf{p}' \in R_{r,n}}{\mathrm{opr}^{(i)}} \; g(\mathbf{p} + \mathbf{p}') \tag{4.8}$$

have the following meaning: $\mathrm{opr}^{(i)}$ is the name of the operator. The

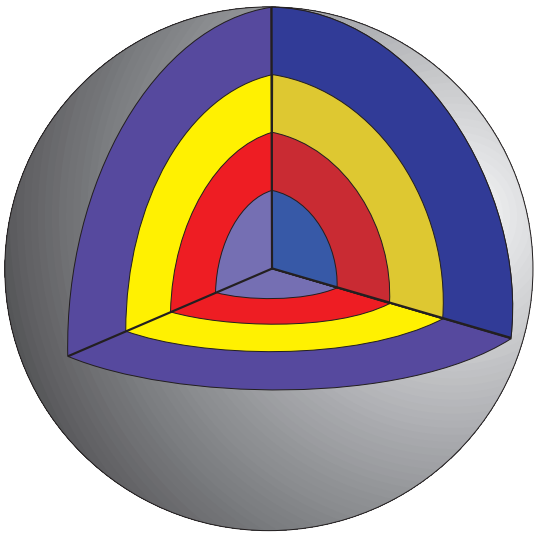

Figure 4.7: Illustration of the spherical layer SE as a 3-D structuring element. Each color represents a different layer (different r parameter value).

superscript (i) refers to which operator we are talking about, e.g. for $i = 1$ we may have: $\text{opr}^{(1)} = \min$. Hence, the operator is applied to the multi set (a set in which elements can appear more than once) of gray values of pixel positions defined by the SE centered at the position $\mathbf{p}$.

As discussed earlier, our idea is to determine the typical brightness of a neighborhood at multiple size and thickness of the neighborhood. The layer structuring element is defined by 2 parameters: r, which controls its size and n, which controls its thickness. For segmentation purposes, two cases of interest arise. The first case is when various equidistant neighborhoods are examined (in that case n parameter is fixed to a constant value, while the r parameter value is changed). This is of interest when the influence of the equidistant neighborhoods is examined (e.g. as in our case of AVM segmentation). The second case is when different neighborhoods at a constant distance from the central pixel are examined (in that case r parameter is fixed to a constant value, while the n parameter value is changed). This is of interest when segmenting images of vessels with higher radii values (r parameter value can be set to surpass the radii of small and irrelevant vessels).

Let $\mathbf{p} \in \mathbb{Z}^3$ denote the pixel position in a 3-D discrete image g with pixel gray value range [0,255]. The first approach we discussed is to vary the layer SE size (r parameter), while the thickness is predefined

(n parameter). The transformed (profile measure) image is obtained in the following fashion.

Definition 2 *Let $f^{(i)}(r', n, \mathbf{p})$ be the calculated value for a given operator and layer SE parameters r' and n at pixel position $\mathbf{p}$. Let r be the longest consecutive $r' \in \mathbb{N}$ for which $g(\mathbf{p}) \geq f^{(i)}(r', n, \mathbf{p})$ for a constant n value. We then define the* R-profile measure *as $\rho^{(i)}(n, \mathbf{p}) = r$.*

The second approach we discussed is to vary the layer SE thickness (n parameter), while the size is predefined (r parameter).The transformed (profile measure) image is obtained in the following fashion.

Definition 3 *Let $f^{(i)}(r, n', \mathbf{p})$ be the calculated value for a given operator and layer SE parameters r and n' at pixel position $\mathbf{p}$. Let n be the longest consecutive $n' \in \mathbb{N}$ for which $g(\mathbf{p}) \geq f^{(i)}(r, n', \mathbf{p})$ for a constant r value. We then define the* N-profile measure *as $\nu^{(i)}(r, \mathbf{p}) = n$.*

It should be noted that both definitions are adjusted for segmentation of CTA images. In case of black blood MRI images $\geq$ should be replaced with $\leq$.

The segmented image is obtained by thresholding the profile measure image. However, it is computationally beneficial to set the upper limit for the profile measure. In other words, as the algorithm iteratively compares the pixel gray value $g(\mathbf{p})$ and calculated operator value $f^{(i)}(r, n, \mathbf{p})$ for layer SEs of different r parameter, it should stop if it reaches value r_{max}. The output value will be r_{max}. With this approach we introduce the size of interest (r_{max}), which eliminates unneeded computations. The size of interest is easily defined by the size of blood vessels that need to be segmented. Our experience shows that optimal r_{max} value is twice as large as the maximum radius of the vessels for segmentation. Another important advantage is that we do not need to set the threshold value manually. Instead, we will set it to the size of interest value r_{max}, and only those pixels whose profile measure reaches this size will be included in the segmented image.

Definition 4 *Let r_{max} be the maximum R-profile measure. The segmented image contains only those pixels whose R-profile measure is maximum: $\rho^{(i)}(n, \mathbf{p}) = r_{max}$.*

The same reasoning is applied to N-profile measure, where the thickness of interest is n_{max}.

The segmentation of an artificial image is shown in Fig. 4.8. Gaussian blur is applied to the artificial image in Fig. 4.8a to simulate

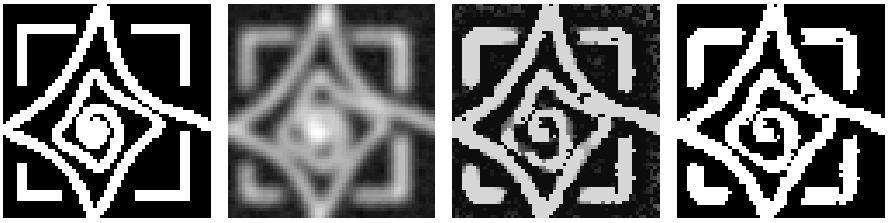

Figure 4.8: (a) An artificial image of size 60×62. (b) The artificial image after applied Gaussian blurring and added sample noise from the CTA image. (c) R-profile measure image for mid-range operator. (d) Segmentation obtained by including only pixels with profile measures reaching to r_{max}

.

the properties of CTA images of small objects, and the sample of noise from the original CTA image is added to it, as shown in Fig. 4.8b. For this image we calculate the R-profile measure for mid-range operator (filter coefficients $a_i : \{0.5, 0, \ldots, 0, 0.5\}$) and $r_{max} = 16$. The resulting image is shown in Fig. 4.8c. Only the pixels with profile measures equal to r_{max} are included in the segmentation in Fig. 4.8d.

4.2.3 Specification of profile operators

One of our conclusions from Subsection 4.2.1 was that we could benefit from introducing other operators to calculate the "brightness" of the neighborhood. For this reason we use the approach of order statistic filters (equation (4.3)) to define various operators. It is well known that image characteristics (e.g. local statistics) change from one image region to the other. Therefore, the pixel intensity distribution in an SE will vary. Hence, we will define here a number of operators to handle various intensity distributions (i.e. to achieve different levels of sensitivity to outliers). The benefit of our approach is that any (generalized) operator can be used. We introduce in Table 4.1 a set B of base operators (selected as the most widely used operators in image processing applications). The listed base operators have been chosen based on their sensitivity to distribution outliers, with the intent to describe both the outliers and the centrality of the distribution. Therefore, minimum and maximum operators represent outliers. The centrality is measured with: mid-range operator (average of minimum and maximum), which is

Table 4.1: A set of base operators B.

Operator	Values of a_i coefficients
mean	$\mu : \{1/\mathrm{D}, 1/\mathrm{D}, \ldots, 1/\mathrm{D}\}$
minimum	$\min : \{1, 0, \ldots, 0\}$
maximum	$\max : \{0, 0, \ldots, 1\}$
median low	$\mathrm{med}_L : \{0, \ldots, a_{\mathrm{D}/2} = 1, \ldots, 0\}$
median high	$\mathrm{med}_H : \{0, \ldots, a_{\mathrm{D}/2+1} = 1, \ldots, 0\}$
mid-range	$\mathrm{mdr} : \{0.5, 0, \ldots, 0, 0.5\}$
median	$\mathrm{med} : \{0, \ldots, a_{\mathrm{D}/2} = 0.5, a_{\mathrm{D}/2+1} = 0.5, \ldots, 0\}$

highly dependent on outliers; mean operator with moderate sensitivity to outliers, but being more robust than the mid-range; median operators with high robustness to outliers.

Our goal is to combine the listed filters from in Table 4.1 to get a good estimate of the centrality that represents the neighborhood's brightness. By combining base operators we can get a wide variety of results from which a "higher level" algorithm can select the best one. We propose to create a more complex profile operator as a combination of the base operators. Let us introduce weights c_i, which we assume to sum to 1. Some of these weights are 0, which means the corresponding base operator is not taken into account. The aggregation step computes:

$$f(r, n, \mathbf{p}) = \sum_{i=1}^{|B|} c_i \operatorname*{opr}_{\mathbf{p}' \in D_{r,n}}^{(i)} g(\mathbf{p} + \mathbf{p}'), \tag{4.9}$$

where $|B|$ is the number of base operators and $D_{r,n}$ is a layer SE. Typically we compute an average of a selected set of statistics (selected profile operators), so all c_i either equal a constant c or 0. The advantage of this approach is that by combining different second order base operators into complex ones, we obtain a qualitatively wider range of segmentation results.This is similar to the concept of separable and hybrid median filters in rank order statistics [Pitas 92] where the median filter is applied in multiple directions or is combined with other filters. Note that by computing an average of a selected set of statistics in (4.9)

we generate $2^{|B|} - 2 = 126$ new operator values (a combination of minimum and maximum operators exists as a mid-range base operator). Each of these would yield a different segmented image (we would have 126 segmentations) by thresholding as given in Definition 4. The algorithm for segmenting MRI images of the abdominal aorta evaluates all of the segmentation candidates and select the best candidate from the segmented vessel images (described in Chapter 7).

In case of CTA AVM images, we are not able to take the same approach (for selecting the best segmentation result) as for the vessels of the abdominal aorta, since there is no clear way to evaluate the segmented regions in case of an AVM. Therefore, we need a way to estimate the performance of each operator to be able to select the best one. In other words, AVM has such an unpredictable structure that we do not have sufficient criteria to evaluate the vessel segmentation result (there is no clear vessel radius, curvature, connectedness or structure to relate to). Instead, we will examine profile values in the image for each of the operators in order to estimate the overall number of pixels that will be segmented for each of the operators. In this fashion, we will grade and order the profile operators based on the number of pixels they segment. Based on the obtained order, the optimal profile operator can be (if needed) also manually selected in an easy to use "threshold value selection" manner.

Let us examine the R-profile of a single pixel from the original CTA AVM slice (bright object segmentation) depicted in Fig. 4.9. The R-profile is depicted for two base operators (mean and median). Based on the Definition 2 the R-profile measure will be the highest possible ($\rho_{\text{MEAN}} = r_{max}$) for mean operator. This is because none of the profile values are higher than the pixel gray value. Since the pixels with profile measure r_{max} are segmented, the currently processed pixel will be a part of the segmented vessel region for the mean operator. This is not the case for the median operator, since its profile measure is lower than r_{max} (at the place where the median gray value in the layer SE becomes higher than the gray value of the processed pixel $g(\mathbf{p})$. From this we conclude that the maximum profile value will determine if the pixel will be segmented or not (if maximum value is below $g(\mathbf{p})$ the pixel is segmented, otherwise it is not segmented). If we calculate the average of profile values for each r,n parameter and operator in the whole image, the maximum average profile value can be used to estimate the total number of segmented pixels in the image (higher maximum value yields less number of segmented pixels. Therefore, if we have maximum average

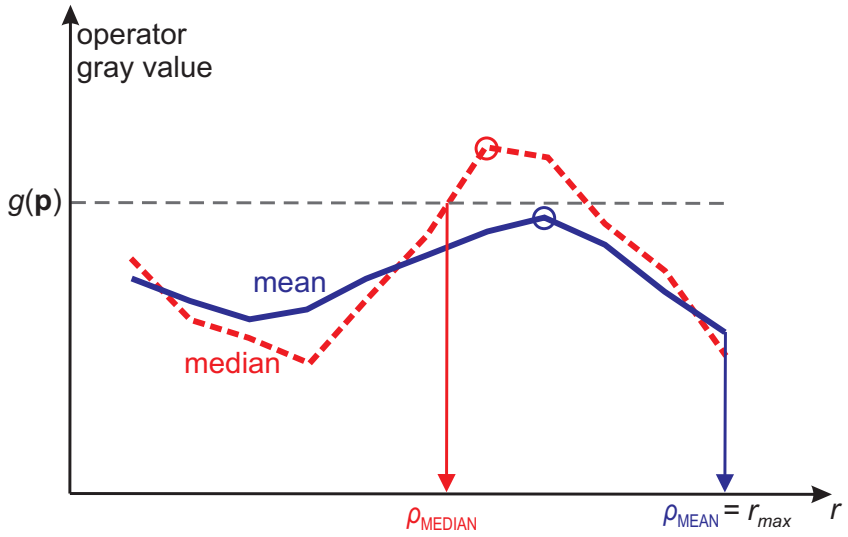

Figure 4.9: Illustration of R-profiles of a single pixel from the original CTA AVM image for mean and median operators. Maximum values of each profile are marked with a circle. The profile measure for mean operator is r_{max} because none of the profile values are higher than $g(\mathbf{p})$. The profile measure for median operator is lower than r_{max} because of the profile value that is higher than $g(\mathbf{p})$. The pixel is segmented only if its profile measure is r_{max}. Hence, we can know if the pixel will be segmented for a given operator if its maximum value in the profile is lower than $g(\mathbf{p})$.

profile values for each profile operator, we can sort them in the ascending order. Operators with lower values will result in a larger segmented area.

The average operator value $\overline{f}(r,n)$ in image g for layer SE parameters r and n is:

$$\overline{f}(r,n) = \frac{1}{m}\sum_{\mathbf{p}} f(r,n,\mathbf{p}), \tag{4.10}$$

where m represents the number of pixels in the image. An implementational advantage is that only average values of base operators (see Table 4.1) for each r and n parameter need to be calculated, from which the values of combined operators (4.9) are derived. This reduces memory requirements and computation time.

We define the maximum average R-profile value of as:

$$\overline{f}_{max}(n) = \max_{r}(\overline{f}(r,n)), \tag{4.11}$$

The maximum average N-profile value is defined similarly by maximizing over n parameter.

Finally, the maximum average R-profile values $\overline{f}_{max}(n)$ are sorted in an ascending order. Based on the ordered $\overline{f}_{max}(n)$ values, the profile operator is manually selected in the following fashion. The initial segmentation is obtained for an arbitrarily chosen operator. The user evaluates the segmentation. If a larger area needs to be segmented, the user selects another operator with lower $\overline{f}_{max}(n)$ value (to obtain a smaller area, higher $\overline{f}_{max}(n)$ value operator needs to be selected). The optimal segmentation is usually obtained in three to four steps. Since the segmentation step given in Definition 4 is easy to compute, the segmentation is fast.

4.2.4 Algorithm overview

The block diagram of the generalized profiling algorithm for AVM segmentation is shown in Fig. 4.10.

The proposed algorithm starts by calculating the values of R-profile operators for each pixel in the 3-D image using a specified structuring element (we use ring-shaped SE for the 2-D analysis and spherical layer SE for the 3-D analysis), the thickness $n = 1$ and the size of interest $r_{max} = 16$ for RSE and $r_{max} = 8$ for layer SE. The maximum average profile values $\overline{f}_{max}(n)$ (4.11) are calculated and sorted in an ascending order.

In the second step the user selects the profile operator and the segmented image is computed by comparing the profile measure with r_{max} value. Together with the blood vessels, some artifacts and noise pixels are segmented. The blood vessels are extracted as the largest connected region using binary connectivity filtering. The algorithm depends on the expertise of the user to select the optimal segmentation result. If the segmentation result is not satisfactory, the user can select another profile operator and repeat the comparison. An advantage of our approach is that the profile operators do not need to be recalculated. Since all the operators are ordered based on their resulting segmented area, the user can choose the best operator by trial-and-error. By examining the previous segmentation result the user can determine if the AVM is over- or under-segmented. Since the operators are ordered, the selection of a desired operator is done in a easy “threshold value selection” manner.

It should be emphasized that the only parameter that a user

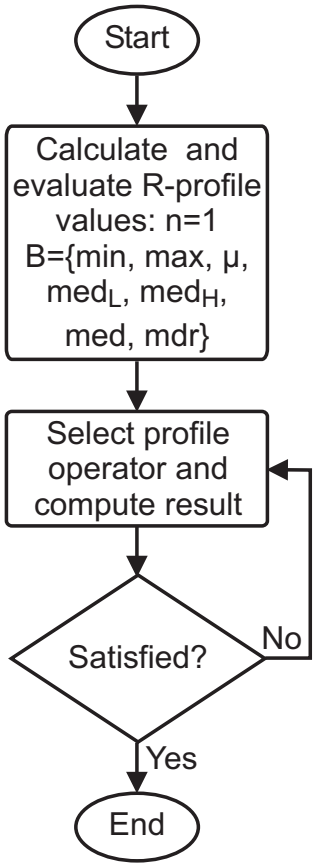

Figure 4.10: The block diagram of the algorithm for the AVM segmentation.

has to select is the profile operator. The base profile operator set is predefined (see Table 4.1), while r_{max} is easily determined as the maximum blood vessel diameter length, which is a clinically known parameter. The manual thresholding can be performed as an optional preprocessing step to obtain a mask for the presented algorithm (however, this is not necessary). This is useful when large data sets are processed because the multiscale analysis is a computationally demanding process. Since all the profile values have been calculated beforehand, obtaining different segmentation results when trying different profile operators is performed in a matter of seconds (the time interval needed for the comparison in Definition 4 to be executed).

Diagram in Fig. 4.11 shows the difference in obtained Dice co-

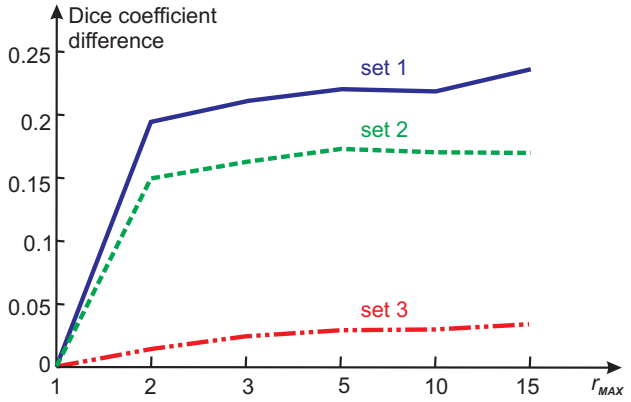

Figure 4.11: Difference in obtained Dice coefficients for different r_{max} values. Function becomes stable for values $r_{max} \geq 3$, which shows the insensitivity to change in the parameter value.

efficients as a function of r parameter limit r_{max} for the phantom data sets. It should be observed that the function takes constantly high values for r_{max} values higher or equal to 3, which shows the relative insensitivity of the segmentation to this parameter and it means that selecting any value $r_{max} \geq 3$ will yield sufficiently good segmentation results.

4.3 Results and discussion

In our experiments we use phantom data and real CTA data sets, where we compare our method with 8 different segmentation approaches. We use both 2-D approach with ring-shaped SE and 3-D approach with spherical layer SE. The segmentation is performed by the algorithm with the block diagram in Fig. 4.10.

4.3.1 Results on phantom data sets

For segmentation evaluation, we design 3-D phantom model data sets representing the random structure of the AVM. Our phantom models are tubular structures with random curvatures and tube radii (intertwined in a random way to simulate the unpredictable structure of the AVM nidus), as shown in Fig. 4.12. The user specified number of randomly placed points is generated with a random scalar which will indicate the radius of the vessel at this point. B-spline is fitted to the generated points (it is a closed curve). The curve is fitted to the discrete grid (3-D

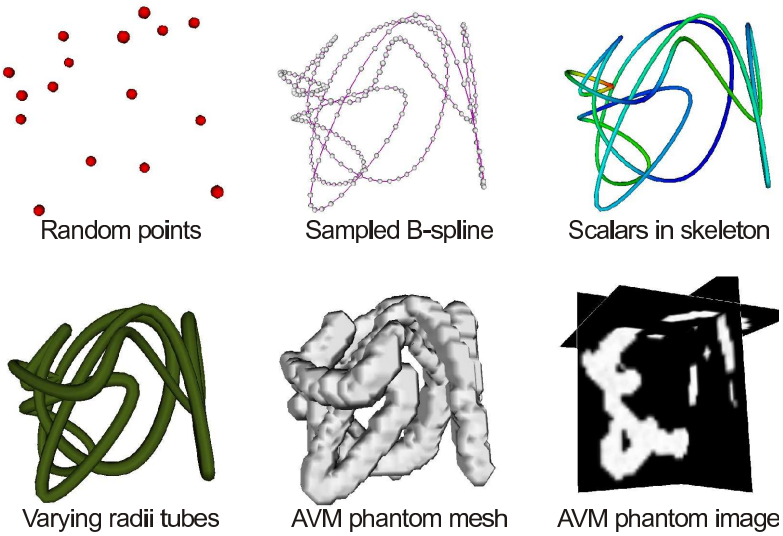

Figure 4.12: AVM phantom creation principle. B-spline is fitted to randomly generated points in space. Scalar values are assigned to the spline (skeleton) to form varying radii tube. Mesh and binary phantom image are generated from the tube.

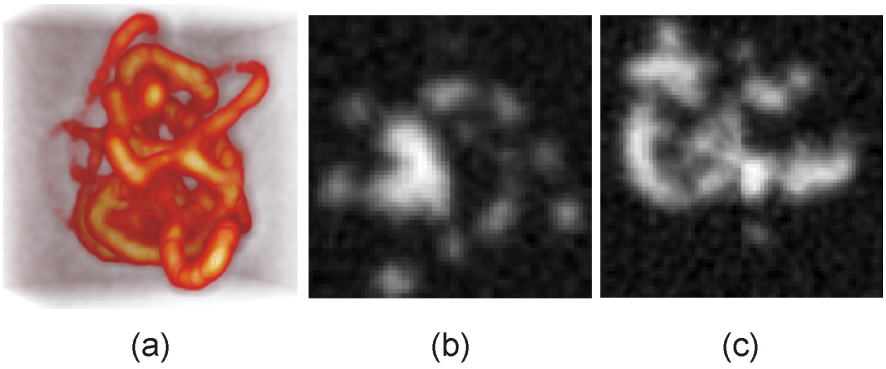

Figure 4.13: An example of phantom data set used for segmentation validation: (a) volume rendering of the phantom data set, (b) and (c) examples of two slices from the rendered data set.

image) and from these the vessels are formed by dilation with spherical structuring element with radius taken from the randomly generated scalars (prior to dilation the scalars for adjacent pixels are averaged to obtain a smooth variation of vessel radius). The main goal was to de-

sign a phantom that will contain vessels with the lowest possible radii in terms of voxels (this situation is also encountered in real CTA images). Hence, the minimum thickness vessels are one voxel wide tubes in the phantom. In order to obtain realistic CT images with noise, streaking artifacts and blurring we used the following procedure. First the images were transformed to sinogram space (using a sufficiently large number of projection angles) and the inverse logarithmic transform is applied to obtain the raw detector signal. The overlap of neighboring detector element responses is simulated through a Gaussian blurring operation of the data along the detector array. Poisson noise is added to the filtered data, in order to simulate the x-ray photon arrival process. Finally, the forward logarithmic transform is applied and the resulting sinograms are backprojected by the filtered backprojection algorithm using the ramp filter. An example of a CTA simulated phantom data set is shown in Fig. 4.13.

In total, 9 phantom data sets were used for validation (approximate dimensions 60×60×60), each with different parameter setting for simulating radiation quantity (which is signal amplitude, inverse to noise level) and blur. First, all segmentation methods that were selected for comparison were validated on 3 phantom data sets with parameters. After that, the best performing methods were further compared for 6 phantom data sets. CT reconstruction artifacts and noise have been added to each 3-D phantom data to simulate cases ranging from medium to high levels of blurring and from low to high levels of noise. Using blur and noise levels higher than our proposed range yields images with highly distorted vessel structures, which is beyond the level of noise and artifacts found in real CTA images. We evaluate the segmentation results using the Dice coefficient [Dice 45], which is a set similarity measure. It is defined as twice the ratio of the number of elements in the intersection of two sets and the number of elements contained in both of them:

$$s(I_S, I_G) = \frac{2|I_S \cap I_G|}{|I_S| + |I_G|}, \tag{4.12}$$

where one set indicates the set of segmented pixels and the other one the set of ground truth pixels.

Results obtained on the phantom data are shown in Fig. 4.14, where the ground truth phantom model is visualized in the first row, followed by the segmentation models obtained using the classical MPs [Pesaresi 01], enhanced MPs [Bellens 08], connected components [De Bock 10], region competition based active contour incorporating a Gaussian mixture model classifier (RCAC) [Shang 08, Shang 11],

geodesic active contours (GAC) [Caselles 95], curve evolution for vessel segmentation (CURVES) [Lorigo 01], vesselness measure (F. Vesselness) [Frangi 98], [Papademetris 06], vesselness measure (Q. Vesselness) [Qian 09], [Papademetris 06] and our proposed method, respectively. The GAC and CURVES segmentation was obtained using Vascular Modeling Toolkit (VMTK) [Antiga 06], using 3 manually set seed points in each data set.

The segmentation obtained using our proposed method shows the best delineation of the tubular structure of the phantom, while all other segmentation methods either remove significant parts of the phantom, or merge different tubular parts into a single region. Classical MPs [Pesaresi 01] result in poor quantity of segmented structure, with leaks present in some of the slices. Enhanced MPs [Bellens 08] show more structure segmented than in the case of classical MPs, but with the tubular structures "merged" into a single region (there is no clear separation between them). Connected components [De Bock 10] produce either an over-segmented or under-segmented results (depending on threshold values set). RCAC [Shang 11] method results in incomplete or "merged" segmentation. Results of GAC [Caselles 95] and CURVES [Lorigo 01] methods show more segmented structure than the previous methods, but still without segmenting the whole structure (results are very dependent on the seed points). The vesselness measure (F. Vesselness) [Frangi 98], [Papademetris 06] delineates well tubular structures, but tends to remove their interconnections. The vesselness measure (Q. Vesselness) [Qian 09], [Papademetris 06] performs well with clearly differentiated structures, but is not able to delineate the complex "entangled" vessels. The results of our method show a completely segmented phantom region with clear delineation between tubular structures (in case RSE is used). This statement is supported by the calculated Dice coefficients shown in Table 4.2, which have the highest values in case our proposed method (using ring-shaped SE) is used for any of the three phantom data sets. The result of the same method using spherical layer SE yields lower Dice coefficients. This demonstrates the advantage of 2-D over 3-D SEs, which comes from the fact that the 2-D SE contains smaller number of elements than the 3-D SE (this is important because it enables differentiation of small structures). Another important fact is that the 2-D SE contains pixels from a single transversal slice, while the 3-D SE contains voxels from multiple slices (this is elaborated in detail in Section 4.3.3). It should be emphasized that the input parameters for each method were tuned to produce the

Table 4.2: Calculated Dice coefficients for comparison of various segmentation methods applied to the phantom data

Dice	Data Set 1	Data Set 2	Data Set 3
Classical MP	0.7	0.74	0.74
Enhanced MPs	0.71	0.75	0.79
Connected components	0.8	0.79	0.83
RCAC	0.77	0.77	0.79
GAC	0.8	0.8	0.8
CURVES	0.8	0.81	0.83
F. Vesselness	0.81	0.78	0.8
Q. Vesselness	0.77	0.77	0.8
GP (spherical-layer SE)	0.76	0.76	0.77
GP (RSE)	0.84	0.85	0.85

segmentation with the highest resulting Dice coefficient.

The results in Table 4.3 present the absolute deviation of the segmented volumes from the volume of the ground truth. Our proposed method is the most accurate if the segmented volume is considered (only two cases of the CURVES and Q. Vesselness segmentation results had a slightly smaller deviation, but with a lower Dice coefficient). Moreover, other methods make big errors in calculating the volume when the best segmentation is determined by the highest Dice coefficient, which is not the case for our method that has good results both for Dice coefficients and calculated volumes. Besides obtaining higher Dice coefficient values and smaller volume deviation results, only our method is able to segment all the tubular structures, while separating them. Note that our method gives better results than the classical and enhanced MPs, which clearly proves the advantage of using RSE over single size parameter SE, as well as including new operators into segmentation process instead of only min and max. For a more detailed explanation of using RSE over single size parameter SE refer to the discussion in Section 4.3.3. Our GP method was designed for blurred (low resolution) images. Hence, the method is not suited for segmentation of sharp and noisy images (which is usually the case with large blood vessel tree images), but only for segmentation of small blurred structures. We performed additional experiments on 6 more phantom data sets with different noise and blur level settings, where we compared the best scoring (both in Dice coefficient values and

Table 4.3: Calculated volume absolute deviation for comparison of various segmentation methods applied to the phantom data

Volume deviation (%)	Data Set 1	Data Set 2	Data Set 3
Classical MP	62.7	49.7	54
Enhanced MPs	73.3	59.2	45.7
Connected components	20.7	13.5	18.1
RCAC	18.1	17.5	23.1
GAC	11.5	6.1	31.1
CURVES	4.5	8.2	20
F. Vesselness	4.6	18.6	11.3
Q. Vesselness	2.2	4.4	3.4
GP (RSE)	4.9	5.2	2.2

Table 4.4: Calculated Dice coefficients on additional test sets for best scoring algorithms of each segmentation approach

Dice	CURVES	Q. Vesselness	GP (RSE)
$a = 2^{11}$, $\sigma = 1.7$	0.85	0.74	0.88
$a = 2^{11}$, $\sigma = 1.9$	0.8	0.78	0.84
$a = 2^{10}$, $\sigma = 1.7$	0.85	0.79	0.86
$a = 2^{10}$, $\sigma = 2.1$	0.79	0.76	0.8
$a = 2^{9}$, $\sigma = 1.9$	0.83	0.77	0.82
$a = 2^{9}$, $\sigma = 2.1$	0.82	0.76	0.83

volume deviation) methods of profiling, vesselness measurements and deformable models. The resulting Dice coefficient values are shown in Table 4.4, supporting our previous conclusions.

4.3.2 Results on original AVM images

We apply the presented method of generalized pixel profiling and comparative segmentation for segmentation of 3-D CTA images of brain blood vessels with spacing between slices of 0.62mm and pixel spacing of 0.62mm×0.62mm. From the original data set, the data set containing only AVM is taken out, which consists of 68 slices with resolution 60×56 pixels. The goal is to segment the AVM with an insight into its inner structure.

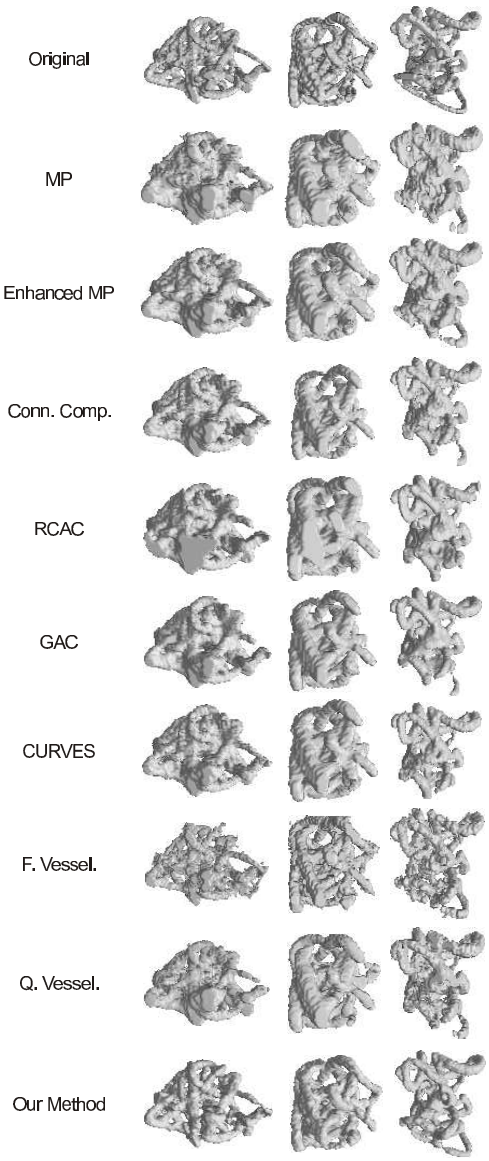

Figure 4.14: Comparison between different segmentation methods on three phantom data sets. Each row represents segmentation results on different phantom data sets.

Fig. 4.15 depicts segmentation results of various methods on the original CTA images. The segmentation result of the classical MP

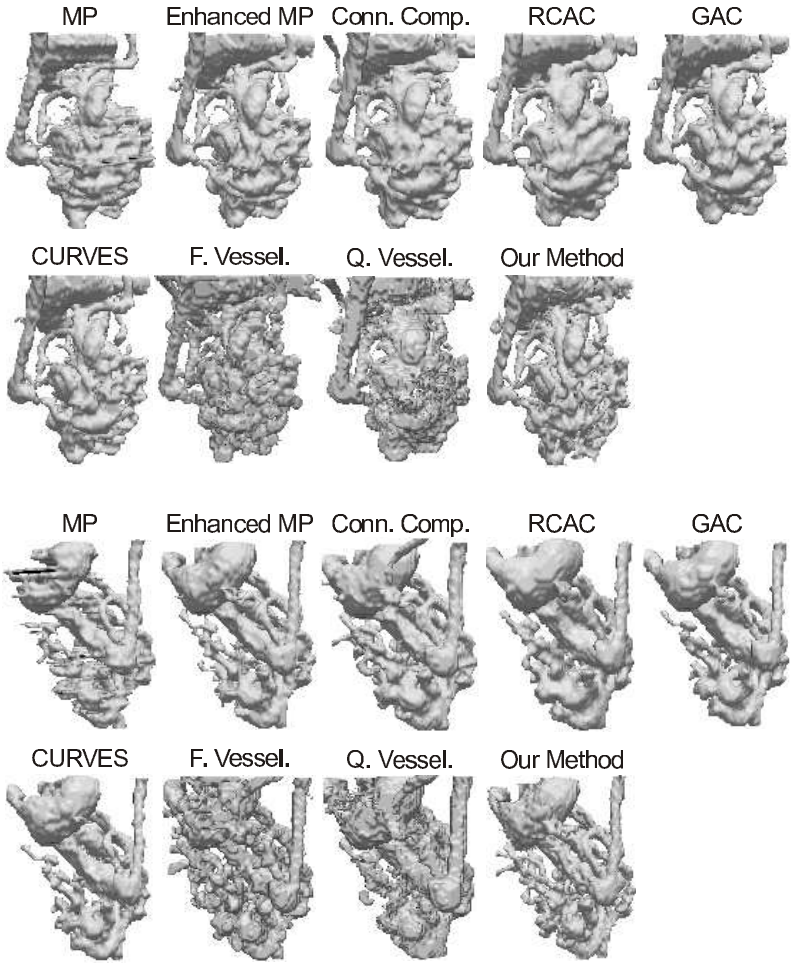

Figure 4.15: Results obtained using different methods for the segmentation of the AVM. Our proposed method segments more AVM structure than the other methods, while obtaining the clearest delineation of vessels comprising the AVM.

method shows that the AVM structure is poorly segmented with leaks present in some of the slices. The enhanced MP method results show further segmentation of the blood vessel structure than in the case of classical MPs, but still with some of the regions missing and without clear delineation between existing segmented vessels. The results of the connected components and RCAC method show that the structure of the blood vessels has been completely segmented, but the blood vessels

are poorly delineated and most of the vessel regions are merged together into a single region. GAC and CURVES methods outperform the previously listed ones (CURVES perform slightly better than GAC), but are still not able to segment and delineate structure to such an extent as our proposed method. The vesselness measures (F. Vesselness and Q. Vesselness) [Qian 09], [Frangi 98], [Papademetris 06] perform very well in delineating arteries prior to entering the AVM, but are not as good in delineating the AVM structure. Results of our proposed method show the most accurate blood vessel structure segmentation with a clear separation between the most important parts of the AVM, which are the feeding arteries, draining vein and the nidus.

4.3.3 Advantage of a layer structuring element

The main difference between the layer SE and single size parameter SE is that the shape of the layer SE is controlled by two parameters, while the SE is controlled by only one (size) parameter. Hence, layer SE is a generalization of SE. Any SE of arbitrary size can be represented as a special case of the layer SE, but the opposite is not true.

Generally the layer SE contains lower number of pixels than the size-based SE (this is clear when we consider that the single size-based SE can be decomposed into a number of layer SEs). This makes the layer SE suitable for segmenting high detail vessel structures. Hence, for the purpose of AVM segmentation we calculate the R-profile measure with the smallest possible n parameter ($n = 1$).

A comparison between segmentation results using the ring-shaped SE and the circular SE is illustrated in Fig. 4.16. The Dice coefficients [Dice 45] calculated for different threshold values of the profile measures with mid-range operator for the central part of the image are shown in Fig. 4.8. At each threshold value the segmented object area is also indicated. Results obtained using the ring-shaped SE yield higher Dice coefficients, while the segmented object areas do not differ much from the ground truth object area. The higher values of Dice coefficients for segmentations obtained using ring-shaped SE over circular SE show that the strength of the proposed method does not come solely from the multiscale approach, but also from the fact that layer SEs perform better in our segmentation method than the size-based SEs.

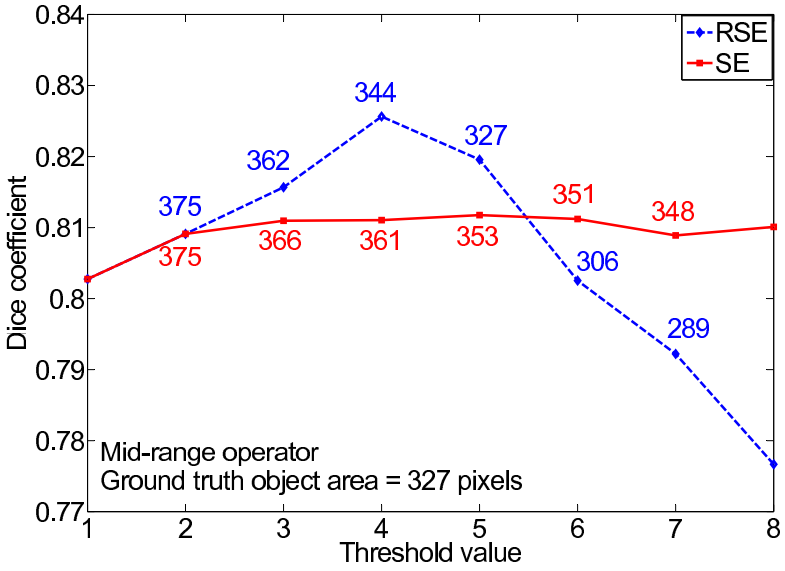

Figure 4.16: Dice coefficients calculated for different threshold values of the R-profile measures with mid-range operator using ring-shaped SE and circular SE. At each of the threshold values the segmented area is indicated at function points. Dice coefficient in case of ring-shaped SE reaches higher values than in the case when circular SE is used, while the segmented areas do not differ significantly. This proves the advantage of using ring-shaped SE over circular SE for the segmentation principle proposed in this chapter.

4.3.4 Segmentation using N-profiles

The ring-shaped SE of the N-profile is a ring with constant inner radius, and increasing outer radius (varying the n parameter value). Hence, the ring-shaped SE of the N-profile contains higher number of pixels than the R-profile with $n = 1$ (except for $n = 1$ parameter of N-profile, when both SEs have equal number of pixels). As discussed earlier, the ring-shaped SE containing a smaller number of pixels will be better for segmentation of fine details, but with low robustness to noise. Therefore, the N-profile segmentation method will be more robust to noise, but the resulting segmentation will be poorer in detail than the one using the R-profile. A special case of N-profile when $r = 0$ turns layer SE into single size parameter SE and represents the classical morphological profiles approach if only the minimum and the maximum operator are used.

Table 4.5: Calculated Dice coefficients for ground truth (G) and R-profile (R) and N-profile (N) segmentations

Dice	N&R	N&G	R&G
Phantom 1	0.84	0.81	0.84
Phantom 2	0.84	0.82	0.85
Phantom 3	0.85	0.82	0.85
AVM CTA	0.84	n/a	n/a

Table 4.6: Calculated Dice coefficients for ground truth (G) and R-profile segmentations in transversal (T), coronal (C) and sagittal (S) direction

Dice	T&S	T&C	C&S	T&G	C&G	S&G
Phantom 1	0.69	0.69	0.88	0.84	0.74	0.75
Phantom 2	0.71	0.7	0.86	0.85	0.79	0.79
Phantom 3	0.72	0.69	0.87	0.85	0.72	0.75
AVM CTA	0.8	0.8	0.83	n/a	n/a	n/a

The comparison of results for the segmentation using N-profiles ($r = 4$, $n_{max} = 6$), and R-profiles ($n = 1$, $r_{max} = 16$) is shown in Table 4.5. The resulting segmentation using N-profiles has high Dice coefficient values, but lacks in detail when compared to the R-profiles segmentation.

4.3.5 Direction of slice-by-slice processing

The resolution of typical 3-D CTA images is not isotropic. A 3-D CTA image is composed of 2-D transversal slices, which often differ from one another in terms of present artifacts, noise and signal level. Hence, we segment the slices in the transversal direction. A single profile operator is used for every slice. The method gives satisfactory results on sagittal and coronal slices too, but not as good as in the transversal direction, due to the fact that different artifacts and noise are less stationary (i.e. much more spatially varying) in sagittal and coronal slices. This statement is supported by calculated Dice coefficients in Table 4.6. High Dice coefficient values were obtained when comparing segmentation results in sagittal and coronal directions, while Dice values of transversal-sagittal segmentations and transversal-coronal segmentations are always smaller and almost equal for each data set.

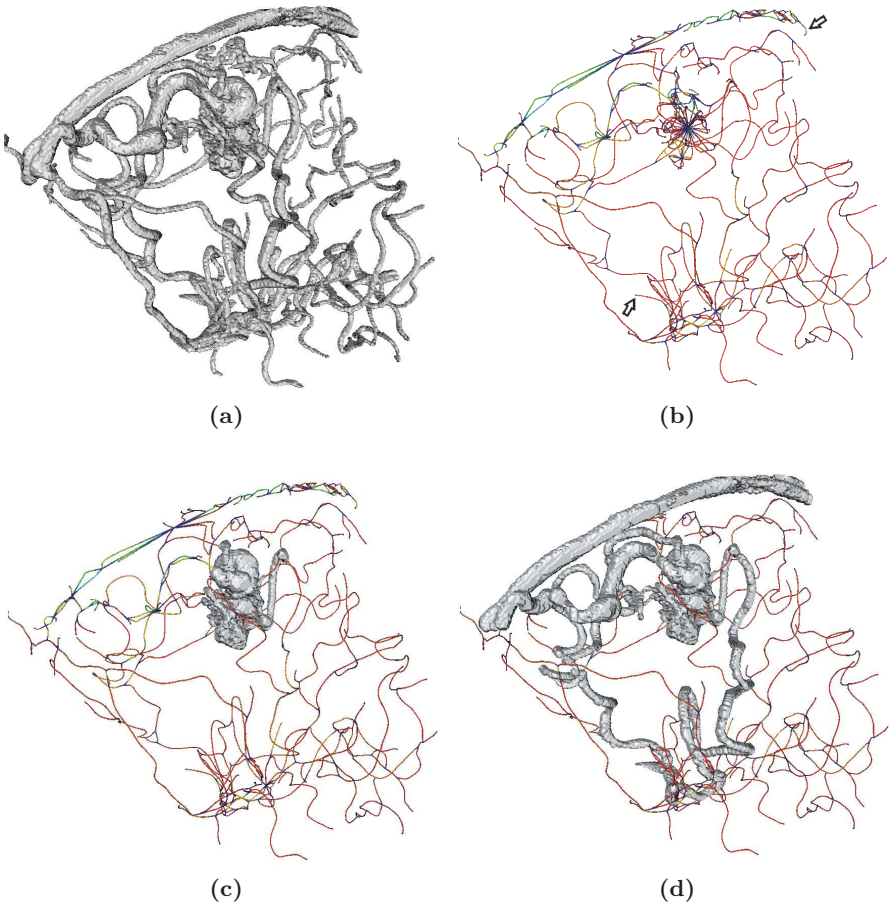

Figure 4.17: Extraction of major blood vessels. (a) segmented blood vessel tree, (b) blood vessel tree skeleton with calculated vessel radii (red indicates smaller radii values, green higher radii values). Arrow at the bottom of the image indicates the start of the arterial blood vessel tree, arrow at the top indicates the end of the draining vein. (c) skeleton with AVM model. (d) extracted feeding arteries, draining vein and AVM.

4.4 Application to AVM delineation

We designed an application for segmentation of cerebral blood vessels with an aim to aid a surgeon during endovascular embolization procedures or during surgical planning. During such procedures the delineation between feeding arteries, draining vein and nidus is essential.

The processed data sets are 3-D CTA images of brain blood vessels with approximately 230 slices of resolution 256×256, with spacing between slices of 0.62mm and pixel spacing of 0.62mm×0.62mm. The initial segmentation of the whole brain blood vessel tree is obtained using the connected components method [De Bock 10], due to its fast execution and satisfactory results, as shown in Fig. 4.17a. The segmented image is skeletonized using our binary skeletonization method presented in Chapter 6, and the skeleton image is converted to vector skeleton structure shown in Fig. 4.17b. The nodes in the vector skeleton are created from node voxels in the skeleton image (voxels that have more than 2 neighbors in their 26-neighborhood) by taking the average position of all the adjacent node voxels. Because of the entangled structure of the AVM, the skeleton image of the AVM will consist of a high number of adjacent node voxels, which will be merged into a single node in vector skeleton, as seen in the central part of Fig. 4.17b (it is the node with the highest number of links). Hence, the AVM structure at the given image resolution can be automatically extracted by selecting the region in the segmented image corresponding to the node with the most links in the vector skeleton, together with its links. This region is depicted in Fig. 4.17c together with the vector skeleton. We apply our proposed method only to the region of the automatically extracted AVM, for which the result is shown in the last column of Fig. 4.15. The skeleton links connected with the region of AVM will be vessels of feeding arteries and draining vein. If the user manually selects the starting point of the feeding arteries (arrow at the bottom in Fig. 4.17b) and the ending point of the draining vein (arrow at the top in Fig. 4.17b), these vessels can be extracted using the shortest path algorithm to the AVM with vessel radii as link cost (explained in detail in Chapter 6). The result of the vessel tree extraction is shown in Fig. 4.17d.

Since we are able to classify vessels going in and out of the AVM as feeding arteries and the draining vein, vessels in the extracted structure of the AVM are delineated by calculating vessel radii at each voxel. The radii calculation performed at each voxel of the segmented AVM is in fact a 3-D radius calculation done by fitting the largest sphere centered at the current voxel into the segmented structure and assigning the sphere radius as a new voxel value. Since the entry positions of arteries and their radii are known, the arteries inside the AVM are delineated by connecting the voxels close to each other with similar radii values, where the threshold radius and expansion are user controlled parameters. The same principle is applied to extracting the vein. The

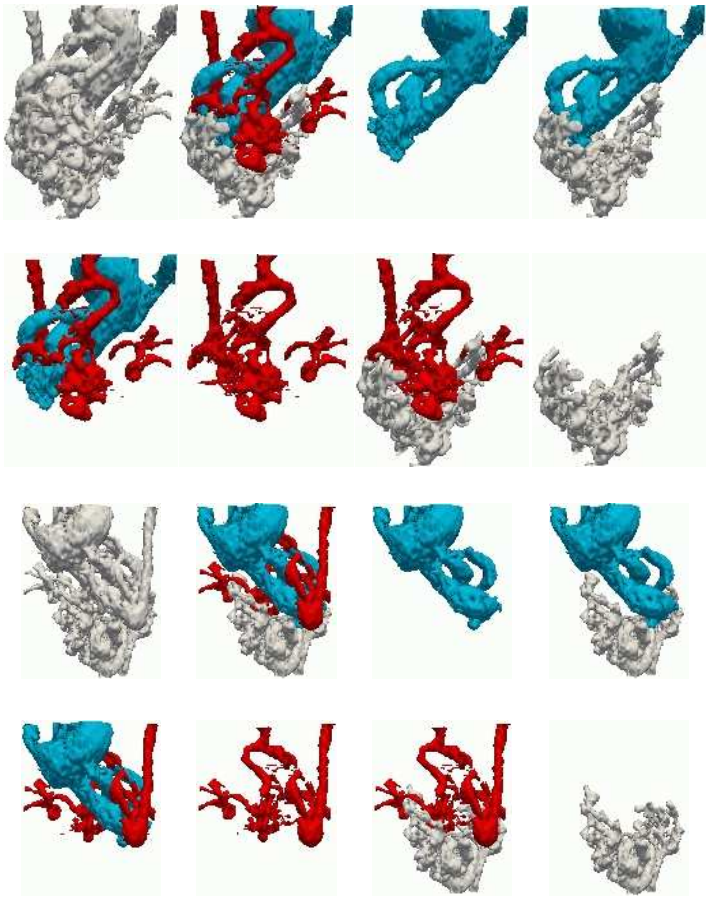

Figure 4.18: The AVM is "broken up" into its most important parts, where the draining vein is colored in blue, the feeding arteries in red and the nidus in white. The delineation is done by radius calculation in the segmented AVM data and thresholding at different radius size. The model shows clearly segmented vein as the largest blood vessel in the AVM, feeding arteries that go into the AVM from different directions and a nidus as a place where arteries and the vein meet.

remaining region after delineation of the vein and arteries is the nidus of the AVM. It should be emphasized that the threshold value can be automatically determined by examining the radii values of vessels (each vessel separately) in the blood vessel tree prior to the AVM region. With this principle we are able to "break up" the complicated structure of the AVM into its most important parts as depicted in Fig. 4.18. The drain-

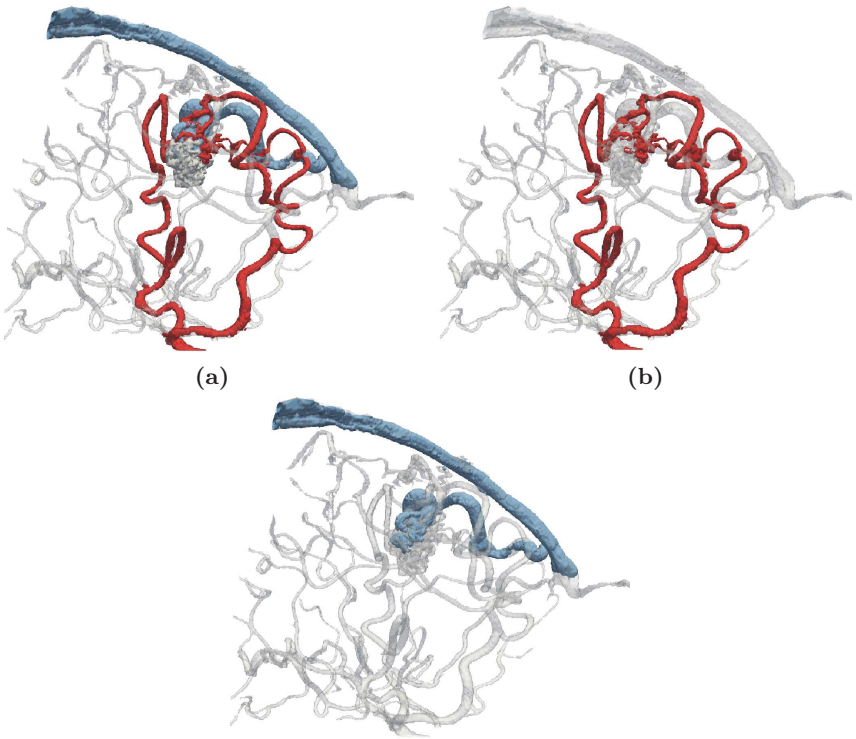

Figure 4.19: Various visualizations of major blood vessels inside the blood vessel tree. (a) draining vein (blue), feeding arteries (red) and nidus (white), (b) feeding arteries, (c) draining vein.

ing vein is colored in blue, the feeding arteries are red, while the nidus is white. In the final stage, we merge the extracted vessels of AVM and the blood vessel tree to obtain full delineation of cerebral blood vessels, as shown in Fig. 4.19.

The algorithm with block diagram shown in Fig. 4.10 takes approximately 8 minutes to segment the presented AVM data set on a 2.2 GHz processor for the AVM 3-D region of interest (in our case it is approximately of dimensions $70\times70\times70$). However, there is still a lot of space for algorithm optimization and for implementation of parallel execution, since the algorithm works on each slice separately. The strong points of our method in comparison to other methods include good vessel delineation results with highly accurate volume calculation. Since no

prior model is used, the method is able to detect even the smallest vessels accurately (unlike most of the state of the art methods that use either a tubular or a blob-like prior model, neither of which is good enough for AVM segmentation). In the final application, very little user intervention is needed (the segmentation is performed by setting a single main parameter). For enhanced visualization of presented data sets we used ParaView [Squillacote 06], while Visualization Toolkit (VTK) [Schroeder 03] was used to implement user interaction and visualization in our final application.

4.5 Conclusion

We have introduced in this chapter a novel method of generalized pixel profiling and comparative segmentation with an application to segmentation of 3-D CTA images of arteriovenous malformation. Our method generalizes morphological profiles, that were previously shown effective in remote sensing applications. Firstly, we introduced layer structuring element as a window with 2 parameters to control its size and thickness. The experiments in this chapter were conducted using ring-shaped structuring elements, which proved promising for delineation of fine vessel structures in low resolution images. Secondly, instead of using only the minimum and the maximum operator (as in mathematical morphology), we introduced a number of other base operators and their combinations called profile operators to obtain higher quality segmentation. Finally we designed an algorithm for aiding in selection of the optimal profile operator. For validation purposes we created a digital 3-D phantom model of randomly intertwined tubular structure with varying radii to which noise and CT artifacts were added. The results on the phantom and real CTA data demonstrate the effectiveness of the proposed method, especially on low resolution images with high intensity variations. Using the presented profiling method we have designed an application for segmenting the inner structure of the AVM. The obtained segmentation results give a nice insight into the structure of the AVM, clearly delineating between feeding arteries, the draining vein and the nidus. As the future work, subjective measures (human observer measures) could be used to evaluate the phantom images against the resulting segmentation. Ultimately, the information about segmentation uncertainty (variance in results introduced by different parameters) can be reported to the user, giving an idea on accuracy of the obtained results. This work is published in [Babin 09b, Babin 12a, Babin 12b].

5

Line-shaped Profiles

In Chapter 4 we introduced the method of *generalized profiling* (GP), where the main proposed novelties were the introduction of *layered structuring element* and *profile operators* as operators applied to the structuring element. The layered structuring element has proven valuable for purposes of fine structure segmentation and vessel delineation of an arteriovenous malformation (AVM). However, the method based on the multiscale structuring elements can be computationally inefficient when it is applied to the segmentation of large data sets due to the wide pixel neighborhoods that are taken into account. Hence, for the purposes of segmenting the whole cerebral blood vessel tree (including the AVM), in this chapter we examine the use of line segments as oriented SEs. The line segments will differ only in orientation, while having the maximum size (defined by the image). The main novelties of our method presented in this chapter are: (1) a new mathematical framework for orientation-dependent GP, (2) the demonstration of the advantage of using line segments as strictly oriented SEs (in terms of quality of results and the execution speed-up), (3) the introduction of a new type of profile operators (*second order profile operators*) and the method for their evaluation, and (4) the application to segmentation of the whole cerebral blood vessel tree. Our segmentation method requires selection of only one parameter to perform segmentation (implemented in an intuitive way), yielding very little user interaction. The work presented in this chapter has been published on international conferences [Babin 10, Babin 11c] and submitted to an international journal [Babin 13b].

5.1 Introduction

Examining the structure and configuration of cerebral blood vessels is especially important in embolization procedure. These are procedures to insert coils or glue for creating an occlusion in aneurysms or arteriovenous malformations (AVM). This type of procedure requires precise guiding of a catheter through the blood vessel tree to the aneurysm or the AVM nidus (the entangled vessels that need to be occluded). It is important to accurately steer the catheter in order not to damage the blood vessels and to insert the glue exactly at designated positions (a mistake in this procedure can rupture the blood vessels causing a stroke). For this reason we will focus on both the fine segmentation of the cerebral blood vessel tree and a structure delineation between the feeding arteries, the draining vein and the nidus of the AVM. Beside the exact computation of AVM geometry and volume, computational efficiency is also an important requirement. In this chapter we seek a solution to the problem of the accurate and detailed segmentation of a cerebral blood vessel tree with an AVM.

We have given an overview of major algorithms applicable for AVM segmentation in Chapter 4, which are also applicable to whole cerebral blood vessel segmentation. For this reason, we will now address only methods applicable specifically for blood vessel tree segmentation. Adaptive thresholding method [Carrillo 05] is a simple and fast segmentation approach. However, its main disadvantage is the difficulty in "separating" proximate blood vessels. Many segmentation method use prior information about vessel shape and blood flow [Pechaud 09]. Vesselness measure [Frangi 98, Jackowski 05], which is usually obtained on the basis of eigenvalues of the Hessian matrix is often used to characterize tubular or blob-like vessel structures. Atlas-based methods [Passat 05b] or methods incorporating anatomical prior knowledge [Passat 06] show good results for segmenting non-malformed vessels of the cerebral blood vessel tree, but lack prior knowledge concerning the AVM anatomy. Vessel segmentation methods based on centerline and path extraction [Dokladal 99, Wesarg 04] extract centerlines either from an existing segmentation or from ridges in the original image. Ridge-based methods have difficulties with gray value inhomogeneities in the AVM. Methods based on deformable models [Caselles 95, Lorigo 01] are able to segment even smaller blood vessels, but the parameters are highly dependent on the pixel gray value distribution, which can result in the incorrect thickness of the segmented vessels.

In this chapter we further extend our idea of generalized profiles by defining novel oriented structuring elements. The use of line-shaped SE, as one of our main novelties, transforms the idea of multiscale analysis into a multiorientation approach, which enhances the computational efficiency and shortens execution times. We will enhance the segmentation quality by introducing a combination of operators, namely second order operators. The method requires only manual setting of a single parameter (second order operator). We design a method for evaluation of profile operators based on their average values, which allows a user to easily perform segmentation. The segmentation results are nicely smoothed vessels. Finally, our method uses no prior information, which leaves space for its further development.

The chapter is organized as follows. In Section 5.2 we introduce lines as alternative structuring elements used with second order profile operators, as operators applied to the set of base operator values. Section 5.3 presents the results of the proposed algorithm applied to phantom data sets and CTA images of brain blood vessels. We discuss the applicability and results of the proposed method. Section 5.4 concludes this chapter.

5.2 The proposed method

5.2.1 Line-shaped profiling

The main novelty of this chapter is the introduction of a *line-shaped SE* as a set of positions defined by the line segment passing through a pixel position $\mathbf{p}$ and stretching through the whole image, as illustrated in Fig. 5.1. In this case the line-shaped SEs differ only in their orientation (while their size depends solely on the image dimensions). Hence, such SE shapes we call *oriented* SEs.

In the 3-D case, the SE is a set of pixel positions on a line segment defined by the direction unit vector $\mathbf{k}_n$:

$$L_n = \left\{ t\mathbf{k}_n \in \mathbb{Z}^3 \mid t \in \mathbb{R} \right\}. \tag{5.1}$$

The direction vector $\mathbf{k}_n$ is the unit vector that determines the line segment direction from a set of predefined direction unit vectors ($n \in [1, n_{max}]$).

This yields n_{max} number of line-shaped SEs. We generate the set of direction vectors in such way that the vectors are distributed uniformly in the 3-D space.

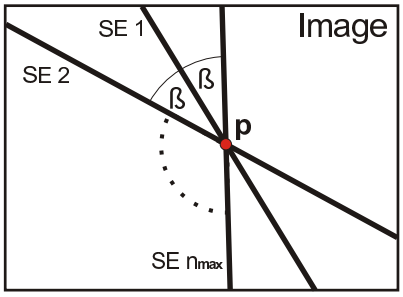

Figure 5.1: Multiorientation approach with line-shaped SEs as introduced in this chapter illustrated for the 2-D case. Each of the n_{max} SEs is represented by a line segment, limited by the image size. We tend to distribute SEs uniformly in the plain (space), hence the constant angle β between them.

In Chapter 4 we introduced a *profile operator* as an arbitrary operator on the gray values windowed by the SE. In this chapter we take a similar approach. Let $g(\mathbf{p})$ be the gray value at position $\mathbf{p}$. We will extend the classical operator convention to arbitrary statistical operators. Let:

$$f^{(i)}(n, \mathbf{p}) \stackrel{\triangle}{=} \underset{\mathbf{p}' \in L_n}{\text{opr}^{(i)}} g(\mathbf{p} + \mathbf{p}') \tag{5.2}$$

have the following meaning: $\text{opr}^{(i)}$ is the name of the operator. The superscript (i) refers to which operator we are talking about, e.g. for $i = 1$ we may have: $\text{opr}^{(1)} = \min$. Hence, the operator is applied to the multi set (a set in which elements can appear more than once) of gray values of pixel positions defined by the line-shaped SE centered at the position $\mathbf{p}$.

In order to analyze the multi set of windowed gray values, we introduce the following *base profile operators*: μ (mean), min (minimum) and max (maximum). The main advantage of line segments as strictly oriented SEs is that the minimum, maximum and mean base operators are easily calculated for all pixels belonging to a single line segment. This yields shorter computation times compared to the GP approach, where the operator values had to be recalculated for each pixel and SE size.

It should be noted that other operators defined on the multi set of gray values are possible (e.g. the median can also be used as a base profile operator, but we avoid its use due to required array sorting that prolongs execution times). Later in the chapter we will introduce a simple method for selecting the optimal profile operator for segmentation

purposes (as a combination of available base profile operators from the set of base profile operators B).

5.2.2 Second order profile operators

The base operators calculated on line-shaped SEs are directional, because the SEs differ only in their orientation. For the purposes of blood vessel segmentation we need to take into account all the directions. Hence, we propose in this subsection a way to efficiently combine the base operator values (calculated for each SE) into a single operator value for all SE directions.

Similarly to the concept of separable and hybrid median filters in rank order statistics [Pitas 92] (where the median filter is applied in multiple directions or is combined with other filters), we apply the base profile operators (minimum, mean and maximum) to the set of calculated base profile operators for each direction n. In this fashion we take into account the operator values obtained on multiple windowed gray value sets of SEs, instead on a single windowed gray value set. We call these operators the *second order base profile operators* (see Fig. 5.2).

Using the notation introduced in (5.2), the second order base profile operators can be written as:

$$h^{(j,i)}(\mathbf{p}) \stackrel{\triangle}{=} \operatorname*{opr}_{n}^{(j)} \operatorname*{opr}_{\mathbf{p}' \in L_n}^{(i)} g(\mathbf{p}+\mathbf{p}'). \tag{5.3}$$

Superscripts i and j define which of the base operators are used, e.g. for $j = 1$ and $i = 2$ and base operators min, max and μ, the equation is equivalent to:

$$h^{(1,2)}(\mathbf{p}) = \min_{n} \max_{\mathbf{p}' \in L_n} g(\mathbf{p}+\mathbf{p}').$$

Let us denote the set of base profile operators with B (in our example $B = \{\min, \max, \mu\}$). In that case, for $|B|$ base profile operators, $|B|^2$ different second order base profile operator values are generated using (5.3). Similarly to the profile operator combination principle in Chapter 4, a more complex second order profile operator value is created as a combination of the second order base profile operator values. Let us introduce weights $c_{i,j}$, which we assume to sum to 1. Some of these weights are 0, which means the corresponding second order base operator is not taken into account. The aggregation step computes:

$$q(\mathbf{p}) = \sum_{j=1}^{n_{max}} \sum_{i=1}^{|B|} c_{i,j} \operatorname*{opr}_{n}^{(j)} \operatorname*{opr}_{\mathbf{p}' \in L_n}^{(i)} g(\mathbf{p}+\mathbf{p}'). \tag{5.4}$$

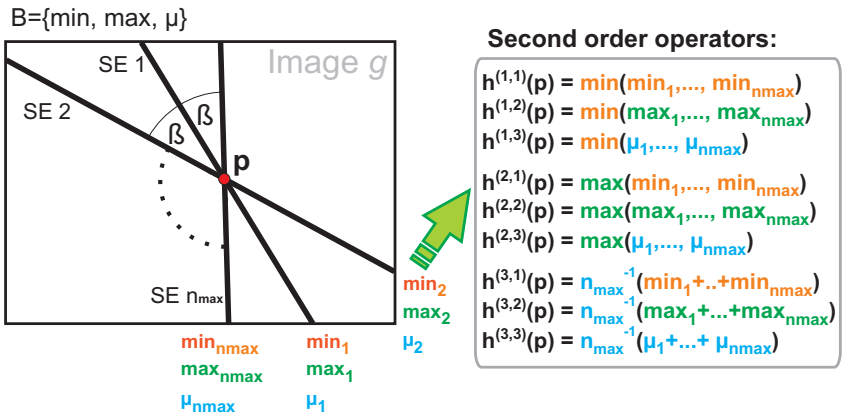

Figure 5.2: The principle behind the second order base profile operators. For each SE the base operator ($B = \{\min, \max, \mu\}$) values are calculated. These values are combined to form second order base profile operator values.

Typically we compute an average of a selected set of statistics (selected second order profile operators), so all $c_{i,j}$ either equal a constant c or 0.

The advantage of this approach is that by combining different second order base operators into complex ones, we obtain a qualitatively wider range of segmentation results, and we design an efficient way for the user to easily select the optimal one, which we describe in Section 5.2.4.

Similarly to the profile measure in Chapter 4, we obtain the final segmentation by comparing the calculated complex second order operator value from (5.4) with the original pixel gray value:

$$\lambda(\mathbf{p}) = \begin{cases} 1, & q(\mathbf{p}) < g(\mathbf{p}) \\ 0, & \text{otherwise} \end{cases} . \tag{5.5}$$

Fig. 5.3 shows an original CTA slice with its corresponding transformed and segmented image for an arbitrary second order profile operator.

5.2.3 Optimal number of line directions

In this subsection we explain the influence of the number of directions (SEs) on the final segmentation result and give an explanation on how the optimal number of directions was determined. Our proposed algorithm performs segmentation by comparing the current pixel gray value to its second order profile operator value (see (5.4) and (5.5)). Fig. 5.4

(a) (b) (c)

Figure 5.3: Illustration of segmentation using the line-shaped SE. (a) The original slice of the 3-D CTA brain blood vessel image with the illustration of 6 directions of line-shaped SEs ($n_{max} = 6$) for an arbitrary pixel. (b) Transformed image for an arbitrarily chosen profile operator (image is normalized) and (c) the corresponding segmentation for $n_{max} = 16$ line directions.

shows how increasing the number of directions affects segmentation result in the 2-D case (for a single second order profile operator). Fig. 5.4b shows the segmentation result when only one SE direction (horizontal) is used. It should be noted that pixels segmented as background appear mostly in horizontal lines where most of the high gray value pixels from the original image are situated. Fig. 5.4c shows the segmentation result when two SE directions (horizontal and vertical) are used. Notice that more pixels exist that are segmented as background. Clearly, by increasing the number of directions we increase the number of segmented background pixels and improve the detail of the segmentation. For this reason, the uniform distribution of SE directions is important, because it allows us to "separate" pixels containing noise and those containing vessel structures. This is illustrated in Fig. 5.5. Assuming that the current (central) pixel belongs to a vessel structure (i.e. it has a high gray value), increasing the number of directions will increase the number of segmented background pixels in the circular area surrounding the current pixel (we call it the *separation area*). Hence, with the increase in number of SE directions, we will improve the segmentation.

We determine the optimal number of directions based on the desired separation area, which we estimate by taking into account the maximum blood vessel size. Experience shows that the separation area should be at least the size of the maximum vessel radius (this is always a known parameter). Hence, in our experiments we use 45 SE directions in the 3-D space that are uniformly distributed.

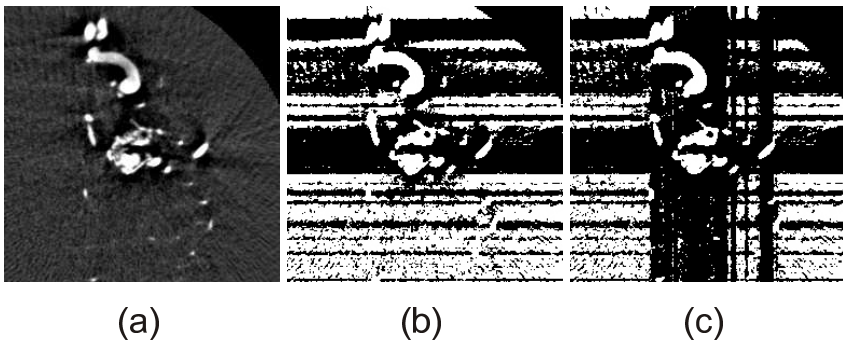

Figure 5.4: Increasing the number of directions increases the number of segmented background pixels and improves the detail of the segmentation. (a) Original CTA slice. Segmentation results using: (b) one and (c) two directions.

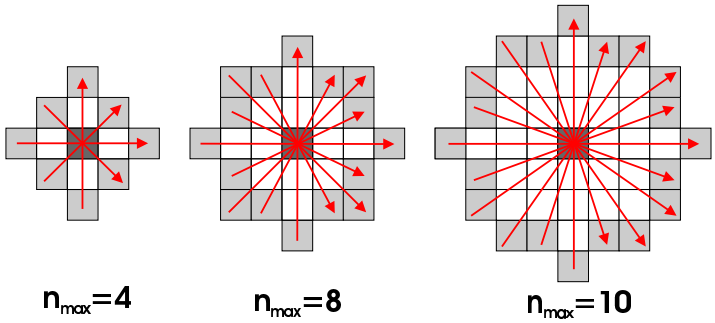

Figure 5.5: Increasing the number of directions increases the number of equidistant pixels covered by the resulting line-shaped SEs and enlarges separation area between the object and noise background pixels (in the 2-D case, 4, 8 and 10 directions create the circle shaped separation area with radii of 2, 3 and 4 pixels, respectively).

Due to the large enough separation area, the blood vessels are easily extracted as the largest connected 3-D region using 3-D binary connectivity filter (see Fig. 5.6c and Fig. 5.6f). Another way to remove the noisy background is to use a mask image in a preprocessing step, which can also further speed-up the computation. It should be emphasized that using the mask image is not necessary to obtain the final segmentation.

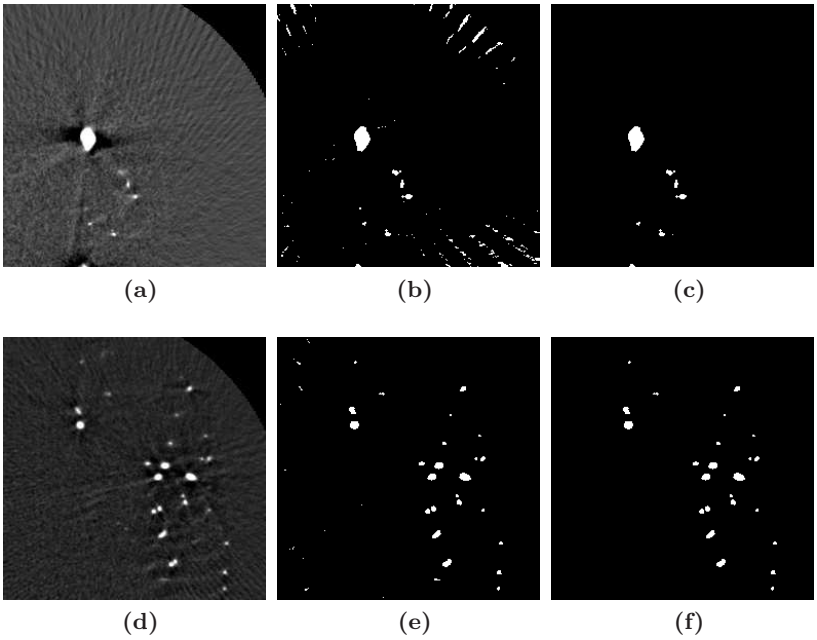

Figure 5.6: Example of the segmentation influenced by the area and gray values in the blood vessels ($n_{max} = 32$). (a), (d) The original 3-D CTA slices. (b), (e) The segmentation results before the binary connectivity filtering. (c), (f) The final segmentation of vessels (after applying the 3-D binary connectivity filtering).

5.2.4 Evaluation of profile operators

Second order profile operators take into account the pixel gray value distribution in a wider pixel neighborhood. For a given base operator set B, we can obtain $2^{|B|^2} - 1$ different second order profile operators (see equation (5.4)), and hence, different segmentation results. The segmentation is performed by comparing the pixel gray value to its second order profile operator value (5.5). The only parameter the user can select is the second order profile operator. As usual, the user performs the segmentation on trial and error basis. In other words, the user selects a second order operator and generates the result. If the result is not satisfactory, the user can select another operator. The problem is how to efficiently (in a fast and easy way) come to the satisfactory operator combination and the segmentation result. This problem is evident from the aggregation step (5.4), where adding or removing an operator

from an existing operator combination can produce completely different segmentation results.

Hence, it would be beneficial to grade (sort) the operators according to the area of segmented pixels. The segmented area for a given operator is inversely proportional to its average value for all pixels:

$$\overline{h}^{(i,j)} = \frac{1}{m} \sum_{\mathbf{p}} h^{(i,j)}(\mathbf{p}), \tag{5.6}$$

where m is the number of pixels in the image. This means that higher $\overline{h}^{(i,j)}$ values yield lower segmented area. Since the complex second order profile operator is generated in an aggregation step (5.4), the average value for all pixels is obtained in the same fashion:

$$\overline{q} = \sum_{j=1}^{n_{max}} \sum_{i=1}^{|B|} c_{i,j} \overline{h}^{(i,j)}. \tag{5.7}$$

Based on the ordered $\overline{q}$ values, the second profile operator is manually selected in the following fashion. The initial segmentation is obtained for an arbitrarily chosen operator. The user evaluates the segmentation. If a larger area needs to be segmented, the user selects another operator with lower $\overline{q}$ value (to obtain a smaller area, higher $\overline{q}$ value operator needs to be selected). The optimal segmentation is usually obtained in three to four steps. Since the comparison in (5.5) is easy to compute, the segmentation is fast.

5.2.5 Implementation

An important advantage of using oriented SEs over multiscale SEs (e.g. ring-shaped SEs) is a higher computational efficiency. When compared to multiscale SEs, the amount of calculations for the line-shaped SEs is significantly reduced. This is illustrated in Fig. 5.7, where the same SE (considered as a set of positions) is used when any of the pixels covered by that SE is the currently processed pixel (illustrated for two pixels). This is not the case for a ring-shaped SE, because of which the base operators (minimum, maximum and average) have different values for each of the SEs. Since the line-shaped SE can be a large window, it is of interest to use operators for which the result can be calculated by a single pass over the windowed gray values. Therefore, we use mean, minimum and maximum operator in our experiments, and we will show in Section 5.3 that they yield good quality results. For the calculation of

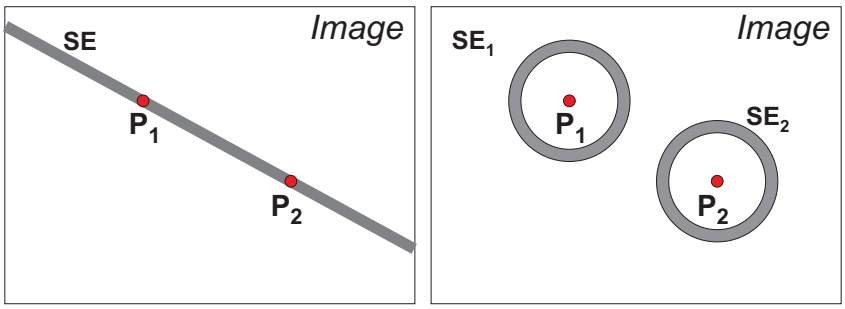

Figure 5.7: Computational efficiency of line-shaped profiles illustrated for two pixels. Left: a single line-shaped SE covers both pixels when either one of them is the currently processed pixel. Hence, the same values for minimum, maximum and average operator are used. Right: for ring-shaped SE the considered pixels have different neighborhoods. Hence, the values for operators in SE_1 will not be the same in SE_2, and have to be recalculated.

the mean pixel gray value in the line-shaped SE, the sum of all the pixel gray values in the SE and the number of elements of the SE need to be accumulated. As in case of the minimum and the maximum base profile operators, the resulting values are also determined by one pass over the windowed gray value multi set. Although other base operators can be used, for computational reasons it is of interest to avoid operators that require ordering (e.g. median operator).

5.2.6 Algorithm overview and application

Fig. 5.8 shows the block diagram of the line-shaped SE profiling using second order profile operators (the main novelty of our work besides introduction of line-shaped SEs), as proposed in Sections 5.2.2 and 5.2.4. The proposed algorithm starts by calculating the values of second order profile operators for each pixel in the 3-D image using a specified number of line-shaped SEs (in our experiments 45 directions in 3-D space were used). The average profile values $\overline{q}$ (5.7) are calculated and sorted in an ascending order. In the second step the user selects the second order profile operator and the segmented image is computed by comparing original pixel gray values with their calculated operator values (5.5). If the segmentation result is not satisfactory, the user can select another second order profile operator and repeat the comparison. An advantage of our approach is that the second order base profile operators do not need to be recalculated. By examining the obtained segmentation result,

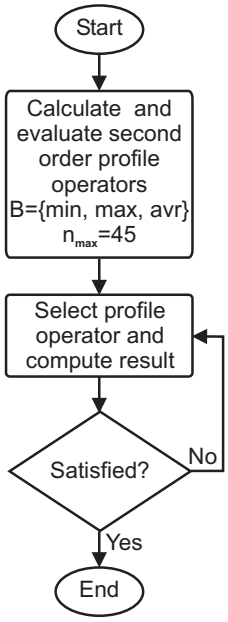

Figure 5.8: Block diagram of the algorithm using second order profile operators.

the user can easily determine if a larger or smaller area needs to be segmented and choose the adequate second order profile operator.

It should be emphasized that the only parameter that a user has to select is the second order profile operator. The base profile operator set is predefined ($B = \min, \max, \mu$), as well as the number of line directions, for which the only requirement is that it has to be sufficiently high. We set this value to default 45 directions (equally distributed in the 3-D space), which ensures the spherical separation area radius of 4 pixels, which is enough for segmenting CTA images of cerebral blood vessels. Since all the profile values have been calculated beforehand, obtaining different segmentation results when trying different profile operators is performed in a matter of seconds (the time interval needed for the comparison (5.5) to be executed).

5.3 Results and discussion

In order to compare various segmentation methods, we use phantom data and real CTA data sets of cerebral blood vessels in our experiments.

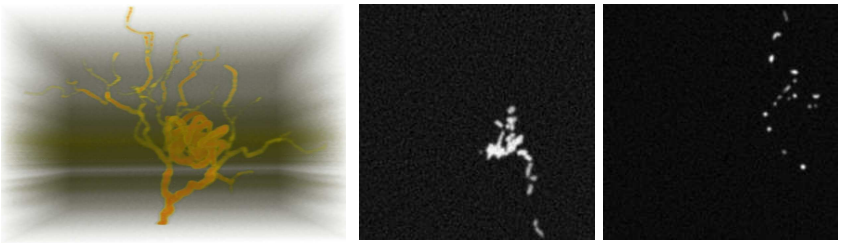

Figure 5.9: Vessel tree phantom data set after adding noise and CT artifacts (176 slices with resolution of 256×256 pixels). Left: volume rendering of the whole data set, center and right: slices from the data set.

Table 5.1: Calculated Dice coefficients for comparison of various segmentation methods applied to the binary tree phantom data

Dice	$a = 2^9, \sigma = 0.9$	$a = 2^{10}, \sigma = 0.8$	$a = 2^{11}, \sigma = 0.6$
MP	0.687	0.681	0.7
GAC	0.762	0.801	0.868
CURVES	0.799	0.844	0.892
Q.V.	0.701	0.715	0.787
GP	0.732	0.78	0.802
LP	0.874	0.897	0.902

5.3.1 Segmentation of phantom data

For evaluating the combined profile operators we have generated three 3-D phantom cerebral blood vessel tree data sets (each 3-D set consists of around 200 slices, see Fig. 5.9) and three 3-D phantom AVM data sets. The 3-D phantom model data sets of cerebral blood vessel tree represent a binary tree with a random branch distribution, and with a random shape and thickness corresponding to the random structure of the AVM. The phantom tree models are tubular structures with random curvatures and tube radii, while the AVM part of the phantom is intertwined in a random way to simulate the unpredictable structure of the AVM nidus, as shown in the first column of Fig. 5.10. The creation of 3-D AVM phantom data sets was addressed in detail in Section 4.3.1. A vessel tree phantom data set is depicted in Fig. 5.9.

Results obtained on the cerebral blood vessel tree phantom data are shown in Fig. 5.10, where ground truth phantom models are visualized in the first column, followed by the segmentation models obtained using the classical MP [Pesaresi 01], the vessel-

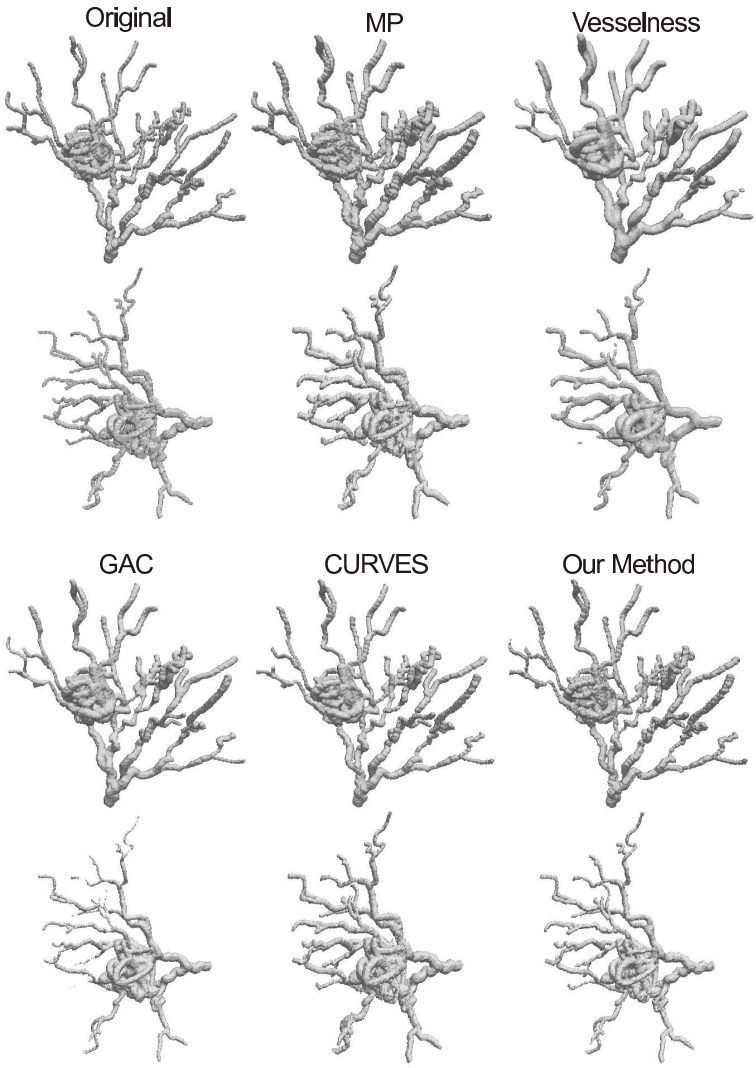

Figure 5.10: Comparison between different segmentation techniques on 3-D phantom data representing binary tree with AVM. The results are organized in two rows with two phantoms in consecutive columns: original phantom models, morphological profiles (MP) [Pesaresi 01], vesselness measure [Jackowski 05, Papademetris 06], geodesic active contours (GAC) [Caselles 95], curve evolution for vessel segmentation (CURVES) [Lorigo 01] and our line-shaped profiling method (LP) (block diagram in Fig. 5.8).

ness measure [Jackowski 05, Papademetris 06], geodesic active contours

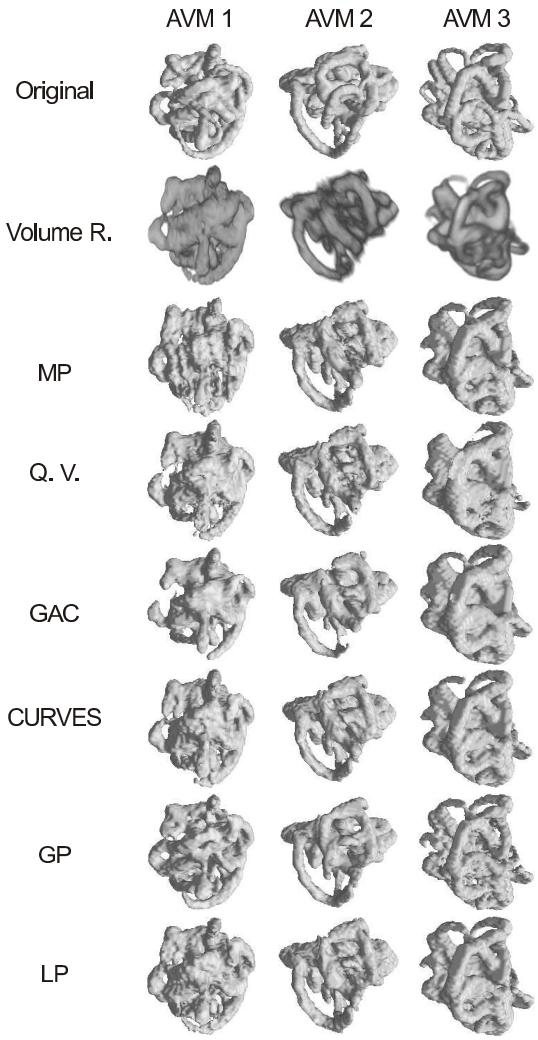

Figure 5.11: Comparison between different segmentation techniques on three 3-D AVM phantoms. The results are sorted in rows from left to right: original AVM phantom model, volume rendering of the model with CT artifacts, morphological profiles (MP) [Pesaresi 01], vesselness measure [Qian 09,Papademetris 06], geodesic active contours (GAC) [Caselles 95], curve evolution for vessel segmentation (CURVES) [Lorigo 01], generalized profiles [Babin 12a] (Chapter 4) and our line-shaped profiling method (LP) (see block diagram in Fig. 5.8).

(GAC) [Caselles 95], curve evolution for vessel segmentation (CURVES)

[Lorigo 01] and our LP method using the second order profile operators (block diagram in Fig. 5.8). The GAC and CURVES segmentation was obtained using Vascular Modeling Toolkit (VMTK) [Antiga 06] in 3D Slicer [Pieper 06], with manually set seed points. After the examination of the results by an expert, the following conclusions were drawn. The results of our LP method (depicted in the last column of Fig. 5.10) show the best delineation of the tubular structure of the phantom and the complex AVM phantom structure. While most of the other segmentation methods segment individual vessels well, they either remove significant parts of the AVM phantom, or merge them into a single region. This is confirmed by the calculated Dice coefficients [Dice 45] shown in Table 5.1, which have the highest values for our LP method with second order profile operators (block diagram in Fig. 5.8) for each phantom data set. We emphasize that the Table 5.1 shows results of binary tree segmentation (with an AVM), for which the GP method is not optimal, and is outperformed by few other methods (for this reason the LP method was designed).

To evaluate our proposed algorithm for the segmentation of AVM vessels, we design three 3-D phantom data sets of highly intertwined tubular structure of varying radii. The CT radiation quantity a and blur σ were set to different values for each data set. Fig. 5.11 shows the segmentation results for various segmentation methods. The original AVM phantom models and their corresponding CT data volume renderings are shown in the first two columns. The results of the following methods are shown: morphological profiles (MP) [Pesaresi 01], vesselness measure (Q. V.) [Qian 09, Papademetris 06], geodesic active contours (GAC) [Caselles 95], curve evolution for vessel segmentation (CURVES) [Lorigo 01], generalized profiles (GP) [Babin 12a] (see Chapter 4) and our proposed method (LP) as in the block diagram in Fig. 5.8. The tubular AVM structure is delineated the best using the generalized profiles (GP) approach. However, our LP method yields smoother segmentation results, which is supported by the Dice coefficients in Table 5.2, where the LP algorithm has the highest scores of all other methods. Table 5.3 shows relative volume errors for segmented models in comparison to the volume of the ground truth. The proposed algorithm gives the best scores for the least blurred images, but also estimates well the volume of other AVM phantoms. Finally, we use the Hausdorff distance as a measure of distance between two sets:

$$d_H(A,B) = \max\{\sup_{a\in A}\inf_{b\in B}(d(a,b)), \sup_{b\in B}\inf_{a\in A}(d(a,b))\} \tag{5.8}$$

Table 5.2: Calculated Dice coefficients for comparison of various segmentation methods applied to the AVM phantom data

Dice	$a = 2^9, \sigma = 1.9$	$a = 2^{10}, \sigma = 2.1$	$a = 2^{11}, \sigma = 1.7$
MP	0.753	0.796	0.854
GAC	0.819	0.795	0.794
CURVES	0.831	0.799	0.87
Q. V.	0.777	0.768	0.743
GP	0.826	0.819	0.882
LP	0.853	0.832	0.883

Table 5.3: Calculated relative volume errors for comparison of various segmentation methods applied to the AVM phantom data

Vol. % error	$a = 2^9, \sigma = 1.9$	$a = 2^{10}, \sigma = 2.1$	$a = 2^{11}, \sigma = 1.7$
MP	17.5	16.05	18.58
GAC	3.96	3	47.4
CURVES	27.18	39.86	17.36
Q. V.	20.17	26.08	29.6
GP	15.19	14.67	7.73
LP	8.3	16.3	8.1

Table 5.4: Calculated Hausdorff distances for comparison of various segmentation methods applied to the AVM phantom data

Hausdorff	$a = 2^9, \sigma = 1.9$	$a = 2^{10}, \sigma = 2.1$	$a = 2^{11}, \sigma = 1.7$
MP	4.12	4.35	2.44
GAC	14.86	6.48	2.82
CURVES	7.21	3.6	4.24
Q. V.	8.06	4.35	6.4
GP	4	5	4.12
LP	6.4	4.12	3.6

where one set indicates the set of segmented pixels and the other one the set of ground truth pixels. Table 5.4 presents the Hausdorff distance values for the obtained segmentation models, where our proposed algorithm gives the best results (overall) when compared to other methods.

To compare our proposed line-shaped profiling with the generalized profiles described in Chapter 4, we design 15 additional phantom AVM data sets with varying CT radiation a and blurring σ parameters. Table 5.5 shows the Dice coefficient values for our proposed LP method using second order line-shaped profiles (LP) and generalized profiling

Table 5.5: Calculated Dice coefficients for comparison of segmentation using second order line-shaped profiles (LP) and generalized R-profiling (GP).

Dice	LP	GP
$a = 2^9, \sigma = 1.7$	0.872	0.818
$a = 2^9, \sigma = 1.8$	0.86	0.803
$a = 2^9, \sigma = 1.9$	0.854	0.781
$a = 2^9, \sigma = 2.0$	0.839	0.763
$a = 2^9, \sigma = 2.1$	0.84	0.764
$a = 2^{10}, \sigma = 1.7$	0.877	0.871
$a = 2^{10}, \sigma = 1.8$	0.857	0.801
$a = 2^{10}, \sigma = 1.9$	0.855	0.831
$a = 2^{10}, \sigma = 2.0$	0.84	0.813
$a = 2^{10}, \sigma = 2.1$	0.84	0.807
$a = 2^{10}, \sigma = 1.7$	0.874	0.868
$a = 2^{10}, \sigma = 1.8$	0.877	0.859
$a = 2^{10}, \sigma = 1.9$	0.85	0.843
$a = 2^{10}, \sigma = 2.0$	0.848	0.841
$a = 2^{10}, \sigma = 2.1$	0.84	0.829

(GP) as described in [Babin 12a]. The obtained results show higher Dice coefficient values when the line-shaped profiling is used.

Fig. 5.12 illustrates the results of the skeletonization [Babin 08] for the original AVM phantoms and the corresponding LP segmentation results, where the skeleton is colored according to the calculated vessel radii. Skeletons obtained from the proposed segmentation algorithm are simplified in the inner AVM regions compared to the skeletons of the original models, while maintaining the correct information on the AVM structure. This allows us to efficiently determine the best paths in the AVM, used to navigate the catheter in the embolization procedure on the AVM.

5.3.2 CTA data segmentation

We apply the presented method of profiling using line-shaped SEs for segmentation of 3-D CTA images of brain blood vessels with spacing between slices of 0.62mm and pixel spacing of 0.62mm×0.62mm (the resolution of the images is 256×256 with around 230 slices in each data set). The results obtained by volume rendering, morphological profiles (MP) [Pesaresi 01], the vesselness measure [Jackowski 05, Papademetris 06],

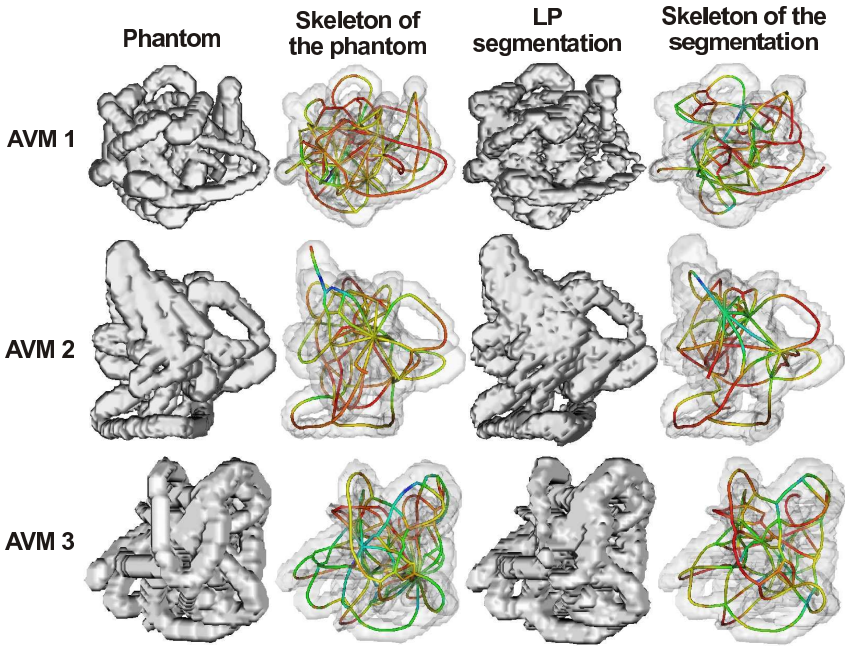

Figure 5.12: Comparison of skeletons obtained from the ground truth models and from segmented models of phantom AVMs. Columns from left to right: the binary AVM phantom model, the skeleton of the binary phantom model, the segmentation using our LP algorithm and the skeleton of the LP segmentation. The skeleton color mapping indicates the calculated vessel radii (red for smaller vessels and blue for larger). The original skeletons and the skeletons obtained from the segmentation show good correspondence in the outer vessel regions. The inner regions are simplified in the skeletons obtained from the segmentation, which makes it possible to extract larger vessels from the inside of the AVM.

geodesic active contours (GAC) [Caselles 95], curve evolution for vessel segmentation (CURVES) [Lorigo 01] and our LP method (block diagram in Fig. 5.8) are given in Fig. 5.13, respectively. The MP methods show poor segmentation of the blood vessel tree because the segmented regions are not connected in 3-D. The vesselness measure produces smooth results, with a bit more structure segmented than with the MP method. The GAC result shows even more segmented structure, but with a high impact of noise to the segmentation. Although CURVES method gives a visually nice segmentation result with high amount of segmented blood vessel structure, our LP method gives the most detailed segmentation of the blood vessel tree. This is obvious when the result of our method is

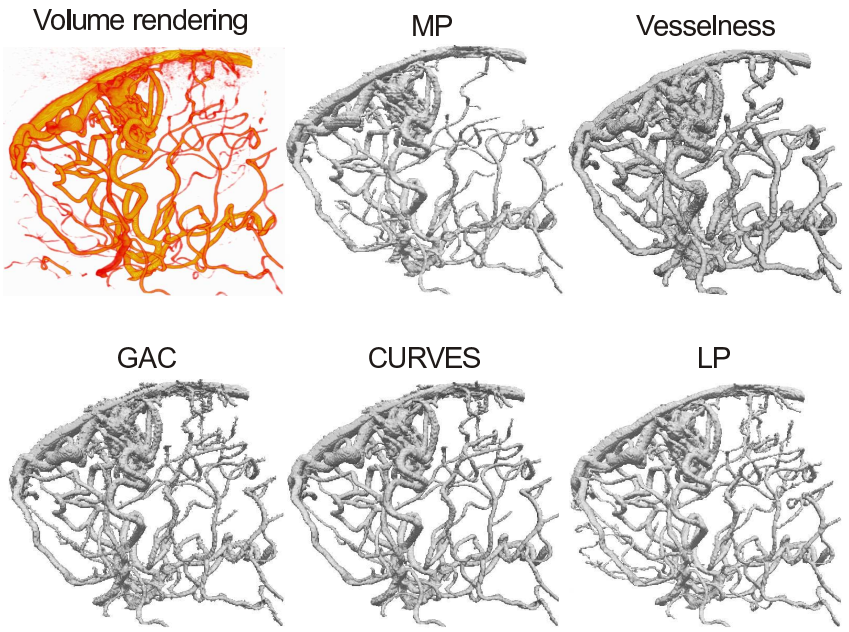

Figure 5.13: Different segmentation techniques applied to 3-D CTA images of brain blood vessels. The depicted results are obtained using volume rendering, morphological profiles (MP) [Pesaresi 01], vesselness measure [Jackowski 05,Papademetris 06], geodesic active contours (GAC) [Caselles 95], curve evolution for vessel segmentation (CURVES) [Lorigo 01] and our LP method (see block diagram in Fig. 5.8), respectively.

compared to volume rendering, where we observe that even the smallest blood vessels that are only partially visible in volume rendering are segmented using our LP method. The results of our LP method are nicely smoothed tubular-shaped vessels, which happens due to the radial positioning of line-shaped SEs for a single pixel. More results of segmenting the 3-D CTA images of brain blood vessels using our LP method for different data sets are shown in Fig. 5.14.

Fig. 5.15 shows comparison of skeletons obtained from segmentation using generalized profiles (GP) and the proposed line-shaped profiles (LP). Due to robustness to noise, the LP method yields more accurate skeletons, in which the draining vein and the largest arteries are easy to delineate because of high radii values. This is illustrated in the third row, where the best path through the largest vessels of the AVM are depicted. It should be noticed that the skeleton paths using the LP method represent the vessels accurately, while the best paths obtained

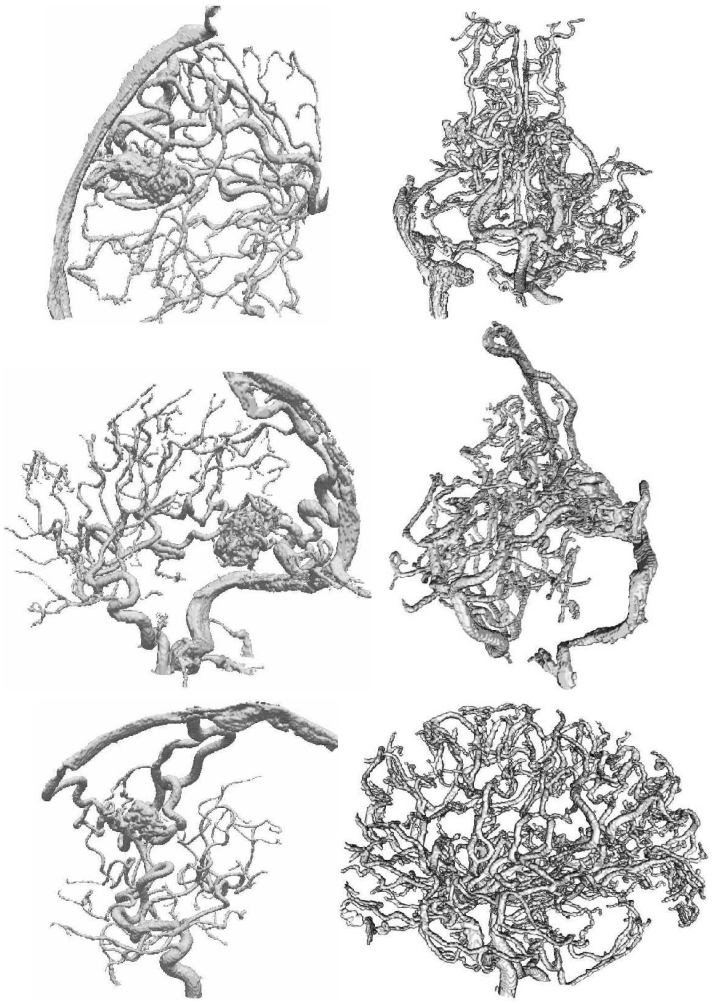

Figure 5.14: The segmentation of the blood vessel tree for different CTA data sets using our LP method. Each segmentation result shows a nicely segmented blood vessel tree with a clearly visible AVM area (where existing) with its feeding arteries and the draining vein.

using GP method tend to take shorter paths through the vessels that are not well delineated.

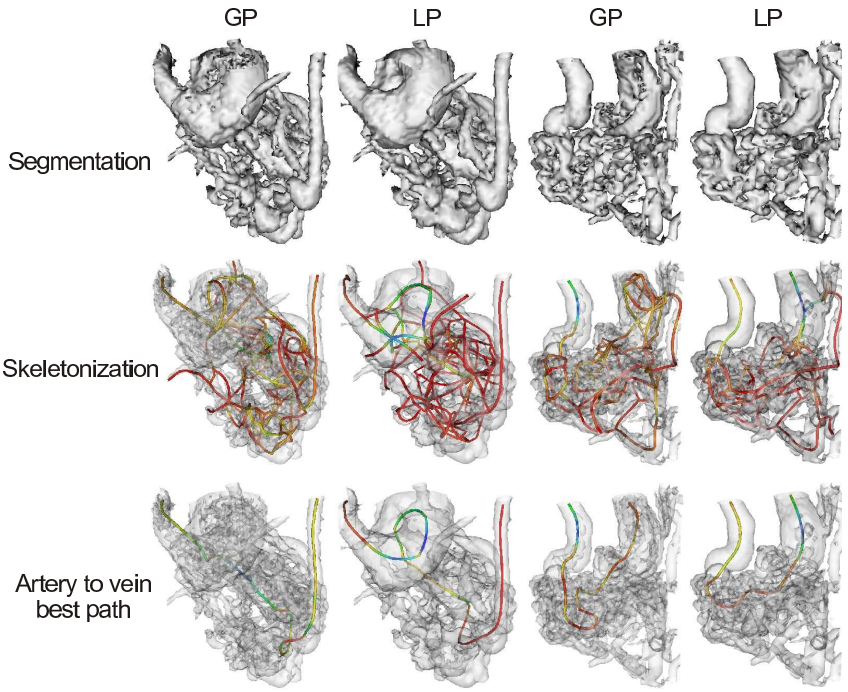

Figure 5.15: Comparison of skeletons and best paths calculated using the generalized profiles (GP) and line-shaped profiles (LP) method. The first row shows segmentation models of two AVM structures for each method. The corresponding skeletons are in the second row. The third row depicts the best paths from the vein to the arteries through the AVM. The skeleton of the LP method follows the vessels more accurately than the GP method.

5.3.3 Validation

The validation of our algorithm is performed on four data sets consisting of CTA images of blood vessels containing AVMs, the CTA images of blood vessels after the embolization procedure (where the AVM is no longer visible) and the CTA images of the onyx cast (glue used to occlude the AVM). To achieve a quantitative validation we segment the onyx cast images by thresholding with the highest skull pixel gray value in the image (the cast and the skull are clearly visible in the CTA images). The segmented onyx is further filled-in (closed) to obtain an onyx mask. We use the obtained onyx mask to extract the AVM region from the segmented blood vessel image. Finally, in order to validate our results we compare the extracted AVM and the onyx cast segmentations in Table 5.6.

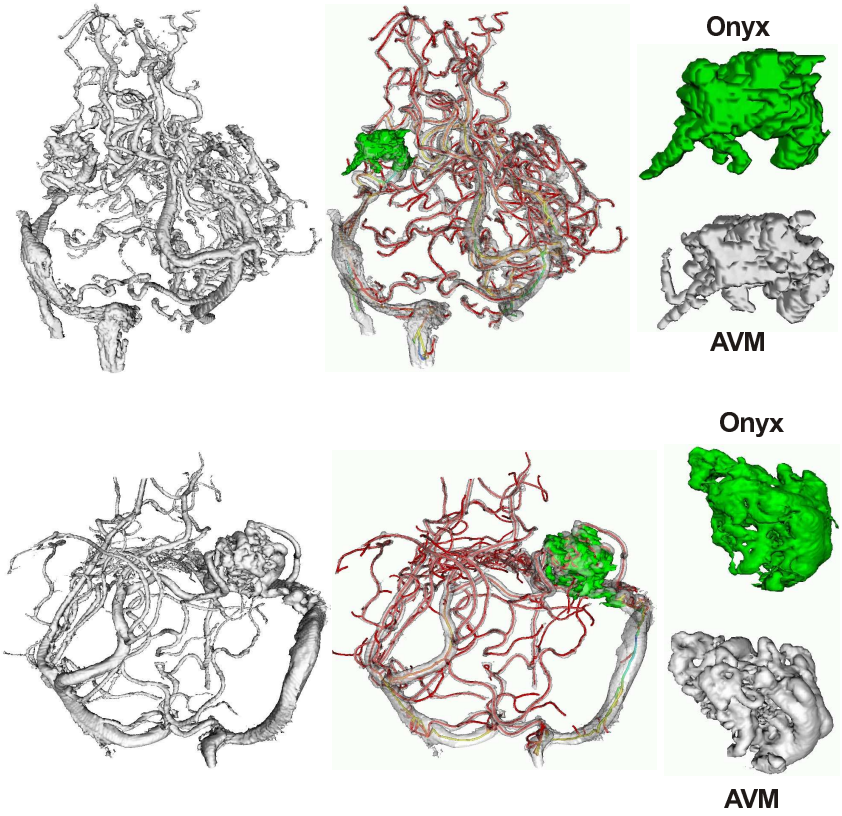

Figure 5.16: The segmentation of the blood vessel tree for two different CTA data sets using our proposed method. Each segmentation result shows a well segmented blood vessel tree with clearly visible AVM area with the skeleton structure clearly depicting feeding arteries and draining vein. The third column shows the extracted AVM region and the corresponding onyx cast segmentation.

It is important to take into account the fact that embolization procedure can deform some AVM vessels (especially in the nidus). However, this deformation is usually not extensive and allows us to perform validation. The obtained Dice coefficient and the relative volume error values in Table 5.6 show expected values for onyx and AVM segmentation comparisons (the Hausdorff distance was not calculated due to its high susceptibility to deformations). Fig. 5.16 shows two different validation data sets with visualized segmented blood vessels, skeleton, onyx casts and extracted AVM regions. Cerebral blood vessel CTA

Table 5.6: Comparison of the segmented onyx cast with the extracted AVM segmentation.

Validation	set 1	set 2	set 3	set 4
Dice	0.75	0.77	0.82	0.61
Vol. % error	6.58	12.54	10.9	10.5

data sets are segmented using our proposed algorithm. The segmented blood vessel images are skeletonized using our binary skeletonization method presented in Chapter 6, and the skeleton image is converted to a vector skeleton structure. The nodes in the vector skeleton are created from the node voxels (voxels that have more than 2 neighbors in their 26-neighborhood) in the skeleton image by computing the geometric median (position with the minimum cumulative distance to all other positions in an object) of the positions of all the adjacent node voxels. It can be observed that the segmented blood vessels correctly coincide with the feeding arteries and the draining vein of the AVM. The extracted AVM segmentation corresponds well to the onyx cast segmentation as depicted in the third column of Fig. 5.16.

The total computation time for a data set of 230 slices with resolution of images 256×256 on 2GHz CPU is 2 minutes. The visualization was done using Visualization Toolkit (VTK) [Schroeder 98] and ParaView [Squillacote 07].

In some cases the difference between the highest and the lowest pixel gray values in the vessel region is too large (sometimes, the lowest gray values fall under 5% of the highest gray values), and the vessels containing the lowest gray values do not get segmented. However, this happens only at the vessels with the low concentration of contrast fluid, and these vessel structures are most often no longer at the region of interest for the brain blood vessel structure analysis. On the other hand, if the low contrasted vessels need to be segmented, it can be done by setting the region of interest to contain only these vessels and applying our proposed algorithm.

5.4 Conclusion

In this chapter we have introduced line-shaped profiling with an application to segmentation of 3-D CTA images of brain blood vessels. The main novelty is the use of line-shaped SEs, which transforms the idea

of a multiscale approach from our earlier work into a multiorientation approach and significantly shortens execution times. Another major novelty is the introduction of second order profile operators, as a combination of various base operators. The strength of our LP method comes from the use of both local proximate (close) and a wider neighborhood of the processed pixel. The method requires only the selection of one parameter, which is easy to select (performed similarly to "threshold value selection" manner). The results on phantom data sets for various noise and artifact levels show high robustness of the proposed method. The validation was performed by comparison of the segmented AVM regions with the segmented images of the onyx cast after an embolization procedure. The obtained results on real CTA data are nicely smoothed tubular-shaped vessels, which is a consequence of the radial positioning of line-shaped SEs for a single pixel. Our method accurately segments the highest amount of blood vessel structure compared to other segmentation methods discussed in the chapter. The presented method uses no prior information, which could be implemented in the future. Due to its slice-by-slice processing, there is also a possibility of parallel execution. This work is published in [Babin 10, Babin 11c] and has also been submitted to an international journal [Babin 13b].

6

Skeletonization

In Chapter 4 and Chapter 5 we introduced our proposed segmentation methods and with an application to cerebral blood vessel and AVM segmentation. However, for the AVM embolization procedure, the segmentation alone is not enough. The segmented blood vessels need to be classified into feeding arteries, draining veins and the AVM nidus in order to successfully navigate the catheter and perform embolization. For this reason we address here the AVM decomposition using the segmentation and the vessel centerlines obtained from the original and segmented vessel images. We propose in this chapter a novel AVM vessel classification and extraction approach using ordered thinning-based skeletonization. The main contributions are: (1) a new method for calculation of distances in ordered skeletonization yielding highly accurate centerlines; (2) the method for inferring skeleton structure from the obtained skeletonization images; (3) an automatic method for AVM detection and extraction; (4) AVM decomposition into veins, arteries and the nidus (with an emphasis on the draining vein). The proposed approach is validated on blood vessel phantoms representing the vein and the AVM structure, as well as on brain CTA images before and after embolization. The vein extraction results show high correspondence to ground truth vein structures. The AVM detection was validated on real 3-D CTA images of cerebral blood vessels. The results indicate potentials for use in surgical planning. The work presented in this chapter has been published in international conferences [Babin 08,Babin 14] and submitted to an international journal.

6.1 Introduction

Inferring the structure and position of blood vessels from medical images is crucial for surgical and diagnostic purposes. In the abundant literature on the topic special attention is given to locating cerebral aneurysms and arteriovenous malformations (AVM). It is of utmost importance for surgery to precisely determine the exact locations of vessels going in and out of the malformation, as well as their radii, bending angles and entering (exiting) directions. The most important vessels are the feeding arteries that supply the AVM with blood, the draining vein that drains the blood from the AVM and the nidus, which is an entangled vessel structure that poses a hemorrhage risk and needs to be embolized. The embolization is a procedure of inserting coils (glue) into the blood vessels in order to occlude them to avoid their rupture.

An overview of software for analysis of a 3-D vasculature is given in [Bullitt 02]. Recent approaches for segmentation of cerebral blood vessels include direction-dependent level sets and vesselness measures [Forkert 11]. A method of [Bullitt 01] employs ridge detection using seed points for the analysis and visualization of the vascular anatomy. The approach of [Jackowski 05] traces blood vessels based on their vesselness measures [Frangi 98, Qian 09]. The *Vascular Modeling Toolkit* (VMTK) [Antiga 06,Piccinelli 09] is used for efficient delineation of cerebral aneurysms. A number of techniques combine various imaging approaches (and modalities) for visualization of cerebral aneurysms and AVMs, such as 3-D digital rotation angiography (3DRA) and 2-D digital subtraction angiography (DSA) [Hristov 11] or 3-D and 4-D MRA images [Forkert 12]. Albeit several accurate methods have been proposed to automatically analyze AVMs, none of these methods address the internal AVM structure decomposition.

Centerline extraction is essential for examining tubular structures allowing distance and radii calculations, best path determination and bifurcation detection. Commonly they are divided into two groups: tracking [Kirbas 03, Carrillo 05, Yu 04, Mohan 09, Kanitsar 01] and a skeletonization [Klette 02, Bühler 02, Krissian 04, Žitkevičius 07] approach.

Vessel tracking methods perform region growing from seed points and track the propagation of the grown surface. They extract blood vessel centerlines as a byproduct. The most common techniques are based on wave front propagation for ordered region growing [Kirbas 03], connected components evolution [Carrillo 05], generalized

cylinder model [Yu 04], variational energy optimization [Mohan 09] and the application of the Dijkstra's shortest path algorithm [Dijkstra 59] with the link costs derived from absolute difference of voxel gray values [Kanitsar 01].

Skeletonization algorithms produce centerlines from binary or gray-scale images by extracting medial axis or ridges. Common criteria for a skeleton are: that it is smooth, thin, continuous, preserves the topology of the original shape and allows full object recovery [Bühler 02]. Based on the type of input image, skeletonization algorithms are grouped into binary and gray-scale methods.

Binary skeletonization methods operate on binary images (i.e. segmented vessels). Many of these methods apply repeatedly the morphological thinning procedure on an object until one-pixel wide centerlines remain, using different definitions of pixel connectivity and junctions [Gerig 93, Lee 94, Saeed 10, Palágyi 08, Klette 06]. The medial axis transform extracts centerlines by finding pixels equidistant to at least two object boundaries [Blum 67]. In [Cornea 05], hierarchical curve-skeletons are extracted using repulsive force fields [Ahuja 97] and concepts from vector field topology to extract skeletons. This principle allows different hierarchies of skeletons to be computed using a multiscale approach, resulting in skeletons with different levels of detail, depending on the scale. Other common techniques are based on radial basis functions and the gradient vector field [Ma 03], gradient vector flow [Hassouna 07] and visible repulsive force [Wu 03]. Skeleton structures can also be extracted from point clouds, e.g. using rotational symmetry axis [Tagliasacchi 09].

Ordered skeletonization methods (also known as hybrid skeletonization) combine thinning and distance-based approaches, where a label (index) map is used to define the order of the thinning procedure. *Distance Ordered Homotopic Thinning* (DOHT) uses a distance map to define the order of the thinning procedure. This means that voxels are removed in increasing distance map order, leading to thinned, centered skeletons. The approach of [Schirmacher 98] uses a distance gradient map to control the thinning order. We will show in this chapter that the ordered skeletonization principle can be applied to original gray-scale values, resulting in a gray-scale skeletonization method.

Gray-scale skeletonization algorithms extract centerlines directly from gray-scale images. These methods usually extract and connect ridges of "maps" (images) obtained using various segmentation approaches. The most common approaches are based on anisotropic vector

diffusion [Yu 04], conditional morphological erosion [Mersa 99], thresholding prior to morphological erosion [Dokladal 99], pseudo-distance maps [Jang 02], the watershed algorithm [Wang 06] and planar images at angular rotations with unfiltered back-projection [Hanger 01]. [Abeysinghe 09] create an interactive method using a graph based representation for gray-scale image skeletonization.

Assuming that we have the segmentation of the cerebral blood vessel tree, two problems arise when AVM analysis is performed. The first is the automatic *locating and extracting the AVM* region from the segmented image. The main difficulties in this case are to determine the location of the AVM in an automatic way and to accurately extract the whole AVM region with its composing vessels.The second problem regarding AVM analysis is to perform the *AVM vessel classification*, which is a procedure of decomposing the AVM into its main vessels: arteries, veins and the nidus. This is done using the prior knowledge about the vessel characteristics. However, the AVM is the region where these vessels merge, and hence, their characteristics mix, which poses the main difficulty in their classification.

In order to solve the listed problems, we will perform skeletonization of the segmented image and use measured vessel radii from the segmented image, pixel gray values from the original CTA image (gray values correspond to contrast agent density in the vessels) and the prior knowledge about vessels (veins, arteries and the nidus). To obtain more accurate centerlines, we propose a novel method for calculating order labels for the ordered skeletonization. To efficiently analyze vessel structures, we introduce two approaches for creating graph-like skeletons and we show how these methods are used to perform AVM extraction and vessel classification. Moreover, we propose a novel method to exploit the characteristics of our thinning approach for locating and extracting the AVM, as well as for the AVM decomposition into its main vessels: the draining vein, the nidus and feeding arteries.

The skeletonization is performed on the segmented image and results in a skeletonized image. The skeletonized image is converted into a graph by turning every pixel into a vertex and adding edges between 26-connected pixels. The advantage of the graph representation over skeletonized image is that it allows for the better analysis of the vessels and the best path calculation. However, in order to map the vessel structures (branches and nodes) to the graph, we group together the graph structures to obtain a *graph-type skeleton*. This skeleton consists of skeleton nodes (parts of the graph that represent vessel bifurcations)

and skeleton links (parts of the graph that represent vessel branches). In other words, the graph-type skeleton allows us to analyze the blood vessel tree in terms of branches and bifurcations. The constituting elements of a skeleton are a skeleton node and a skeleton link, or just node and link. Although these terms are synonyms for a vertex and an edge, to avoid confusion, in this work we will use node and link strictly for the skeleton structure and vertex and edge strictly for the graph structure.

The chapter is organized as follows. In Section 6.2, we explain the proposed method in several subsections. First, we describe the general algorithm, followed by an explanation of profile volumes for ordered skeletonization principle. The main novelties are presented in separate subsections: pixel profile volume, graph-type skeleton creation methods, and AVM decomposition. In Section 6.3, we present and discuss the results of our proposed algorithm and we conclude this work in Section 6.4.

6.2 Materials and methods

In this chapter we propose a novel method for locating and extracting the AVM from the segmented image of cerebral blood vessels and the AVM decomposition into the nidus, the draining vein and feeding arteries. Our method is inspired by DOHT skeletonization, where distance transform (on the segmented image) is used to generate order labels for iterative thinning.

Fig. 6.1 gives an overview of our method. The first step is the segmentation of blood vessels (the resulting image has one label for the vessels and one for the background). The segmentation itself is not the focus of this chapter and we shall assume that the segmented image is available. In our experiments we use the segmentation method from Chapter 5, but other segmentation methods can be used instead (as long as they yield reasonably good results). The second step is the skeletonization using our novel profile volume measures (Section 6.2.2). In this step we create graph-type skeletons (Section 6.2.3) based on profile volumes and original pixel gray values. In the third step we automatically locate and extracts the AVM using the skeletons from the previous step (described in Section 6.2.4). The fourth step extracts the draining vein using the previously extracted AVM and a user specified vein vessel start position. Fine delineation between the draining vein and the AVM nidus is performed (Section 6.2.5). Finally, the last step extracts feeding arteries based on a user specified arterial position (Section 6.2.6).

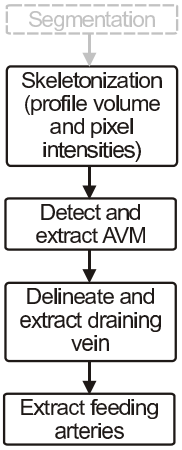

Figure 6.1: A block diagram of the proposed method for the decomposition of cerebral AVMs. The segmentation step is not the focus of this chapter.

6.2.1 Initial considerations

The proposed method is based on the following observations of blood vessels in CTA images (see Fig. 6.2):

- The vein usually (but not necessarily) constitutes the largest blood vessel in the scanned region of interest. Due to lower density of contrast agent in the vein, pixel gray values are spatially varying.

- The feeding arteries are most often smaller in diameter than the draining vein. Due to a high density of contrast fluid in the arteries, pixel gray values are the highest in the center of the arterial vessels and lower at vessel edges. In other words, pixel gray values in arterial vessels can be used as labels in the ordered skeletonization.

- The AVM is an entangled blood vessel structure from which the vein drains blood. Due to its high density of small intertwined vessels, the AVM is a region of highly inhomogeneous pixel gray values.

The goal of our work is to design a method to automatically locate and extract the AVM from the segmented image of cerebral blood vessels and decompose the AVM into its main vessels: the nidus, the draining vein and feeding arteries. To achieve this we will use the struc-

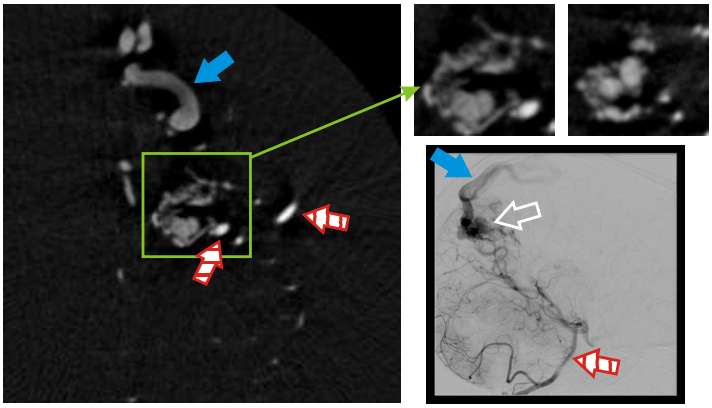

Figure 6.2: Left: a slice from a 3-D CTA image of cerebral blood vessels with close-up on the AVM (in the upper right). The AVM vessels show no clear structure compared to normal vessels. Arteries are brighter (striped arrows) due to higher density of contrast fluid. The vein (filled arrow) is the largest vessel with inhomogeneity in pixel gray values. Lower right: digital subtraction angiography (DSA) image of the brain blood vessel tree with marked AVM region (outlined arrow). Note that the AVM is a highly dense structure of entangled vessels.

tural (anatomical) vessel differences and the differences in distribution of their gray values (from the original images).

6.2.2 Profile volume for ordered skeletonization

Before explaining the proposed skeletonization method we will introduce definitions of pixel neighborhood, adjacency and connectivity.

In this chapter we consider a 3-D neighborhood $\mathcal{N}(\mathbf{p})$ of a pixel position $\mathbf{p}$ consisting of the 26 nearest neighbors. A pixel $\mathbf{q}$ belongs to a 26-neighborhood of a pixel $\mathbf{p}$ if and only if the difference in any of their coordinates equals 1:

$$\mathbf{q} \in \mathcal{N}(\mathbf{p}) \quad \text{iff} \quad \max(|x_\mathbf{p} - x_\mathbf{q}|, |y_\mathbf{p} - y_\mathbf{q}|, |z_\mathbf{p} - z_\mathbf{q}|) = 1, \tag{6.1}$$

If a pixel is in the neighborhood of another pixel we also say that these pixels are *adjacent*. A set of foreground (non-zero gray value) pixels is a *connected component* C if for every $D, E \subset C$, with $D \cap E = \emptyset$ and $D \cup E = C$, there exist at least one pixel in D that is adjacent to a pixel in E. Any two pixels that belong to the same connected component are *connected* pixels.

We will now explain the ordered skeletonization principle. The ordered skeletonization is an iterative thinning process of a binary image, where the pixels are removed in a predefined order. It consists of two steps:

- Compute profile volume for each pixel in the segmented image.
- Iteratively remove pixels from the segmented image in the ascending profile volume order using the pixel redundancy rule.

Obviously, the method is composed of two important principles: the pixel ordering and the pixel redundancy rule.

The *pixel redundancy rule* is a decision rule determining if a pixel from the segmented image should be removed in the thinning process. The goal is to iteratively remove pixels to obtain one pixel wide centerlines. The redundancy rule determines if a pixel can be removed from the segmented image while preserving pixel connectivity. In this chapter we use a condition from [Babin 08], where the 26-neighborhood of a pixel in a 3-D image is considered. The pixel redundancy rule is applied to any pixel with more than one foreground neighbor in the 26-neighborhood (if only one neighboring pixel exists, the processed pixel represents the end of a vessel and should not be removed). Considering the 26-neighborhood of a processed pixel, our goal is to preserve the connectivity of all neighboring pixels if the processed pixel is removed.

Definition 5 *Let $\mathcal{N}(\mathbf{p})$ be the 26-neighborhood of the pixel $\mathbf{p}$. The processed pixel $\mathbf{p}$ is considered **redundant** if all foreground (non-zero gray value) pixels in $\mathcal{N}(\mathbf{p})$ belong to a single connected component (considering only the pixels in $\mathcal{N}(\mathbf{p})$). If the number of foreground pixels in $\mathcal{N}(\mathbf{p})$ is 1, the pixel is not redundant.*

This means that we examine if the surrounding foreground pixels are connected to each other if the current pixel $\mathbf{p}$ is removed. In other words, if the processed pixel is not needed to sustain the connectivity between surrounding foreground pixels, it will be removed. The above reasoning applies only if the neighborhood contain more than one foreground pixel.

The redundancy function changes the pixel label to background (zero gray value) if the pixel is redundant:

$$\mathrm{s}(\mathbf{p}) = \begin{cases} 0, & \mathbf{p} \text{ is redundant} \\ 1, & \text{otherwise} \end{cases} . \tag{6.2}$$

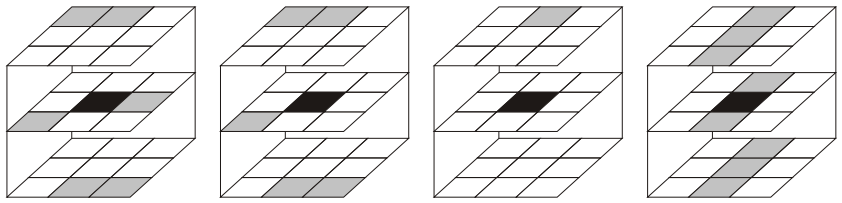

Figure 6.3: Illustration of a pixel redundancy rule. The processed pixel is colored black, while the object pixels are gray. The processed pixel $\mathbf{p}$ is redundant if all its adjacent pixels belong to the same connected component in $\mathcal{N}(\mathbf{p})$ (where the number of neighbors is more than 1).

By preserving the connectivity in the 26-neighborhood of the processed pixel, we ensure that the connectivity will be preserved in the whole binary image. The illustration in Fig. 6.3 shows various 26-neighborhood pixel configurations and the result of redundancy rule for each of them.

The order in which pixels are removed plays a crucial role in the thinning process. Various skeletonization results can be obtained using a different order of pixel removal. The order in which the pixels are removed is usually determined by the Euclidean distance transform, i.e. the minimum distance of a pixel from the edge of a vessel in the segmented image. Let B be the set of background (zero gray value) pixels from the segmented image. The Euclidean distance transform is defined as:

$$\delta(\mathbf{p}) = \min_{\mathbf{q} \in B} d(\mathbf{p}, \mathbf{q}) \tag{6.3}$$

where $d(\mathbf{p}, \mathbf{q})$ represents the Euclidean distance between the given pixels. Most usually squared values of the Euclidean distances are used to define the thinning order (which is always performed in the ascending manner), as depicted in Fig. 6.4.

The advantage of this metric is that the thinning will propagate from the vessel borders to the central parts of the vessels (where the highest values are situated). This yields a skeletonization result which represents well the medial axis of the skeletonized object.

One problem with the distance transform of a binary object is that it often results in a small range of distance values (Fig. 6.4). This means that a lot of pixels will be processed in the same thinning iteration. Pixels with the same label value (i.e. pixels that are processed in the same iteration) are removed in a "raster-scan" order. However,

the thinning in raster-scan order is not robust to shape irregularities (i.e. the places where the segmentation is not smooth) [Hilditch 69,Babin 08]. This is illustrated in Fig. 6.5, where the skeletonized image for the largest segmented vessel contains a lot of branches instead of only a centerline.

For the purpose of a more accurate skeletonization, we propose here a novel method for assigning pixel labels for the skeletonization thinning order. The main idea is to use the number of foreground pixels in a neighborhood of the processed pixel (i.e. a volume of the neighborhood), where the size of the neighborhood is determined as in case of the Euclidean distance transform. We call this measure the *profile volume*. The advantage of this is that the range of values we assign to pixels will be wider. Hence, there will be more thinning iterations (this will disrupt the raster-scan order in which many pixels were processed), which will yields higher robustness to segmentation noise.

Let W be the set of foreground pixels from the segmented image and $S_\delta(\mathbf{p})$ be the spherical neighborhood of radius δ calculated from the distance transform (6.3) at pixel $\mathbf{p}$. The profile volume is defined as the number of foreground pixels "covered" by the sphere neighborhood:

$$\varphi(\mathbf{p}) = |W \cap S_\delta(\mathbf{p})|. \tag{6.4}$$

With the profile volume we assign pixel labels from a wider range of values (when compared to the squared Euclidean distance) and obtain a higher accuracy for the thinning process. The calculated profile volumes for a binary object are depicted in Fig. 6.4. Comparison of skeletonization results using squared Euclidean distance and profile volume as the thinning order labels is illustrated in Fig. 6.5. Our proposed method results in fewer irrelevant details, while the centerline is accurately computed.

6.2.3 Graph-type skeletons

Before explaining methods for the graph-type skeleton creation, we will now introduce the needed graph notation and definitions. An undirected graph G is a pair (V, E), where V is a finite set of vertices and the edge set E consists of unordered pairs of vertices $\{u, v\}$, $u, v \in V$. The vertex v is *adjacent* to the vertex u if $\{u, v\}$ is an edge in E. In other words, vertices are adjacent if they share a common edge. Similarly, edges are *adjacent* if they share a common vertex. An edge $e = \{u, v\}$ is *incident* to vertices v and u. Given a set $V' \subset V$, the subgraph of $G = (V, E)$ *induced* by V' is the graph $G' = G[V'] = (V', E')$, where

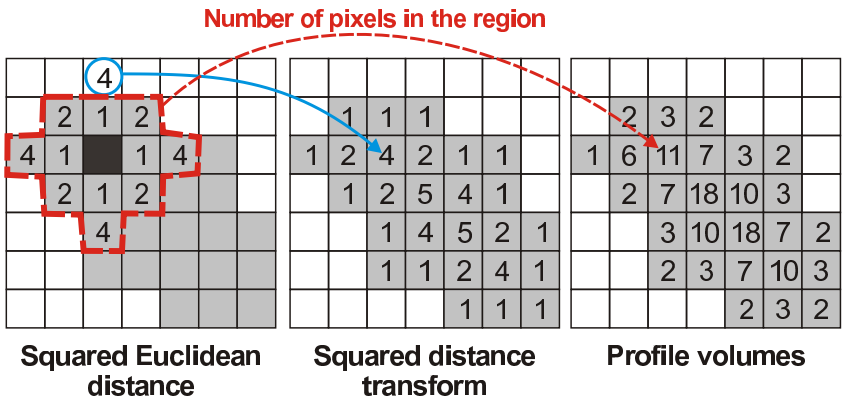

Figure 6.4: Pixel labels for ordered skeletonization of a binary structure (gray pixels). Left: the squared Euclidean distance (6.3) for a single pixel. Middle: distance transform using the squared Euclidean distance. Range of values is small (4 distinct values), and many pixels are processed in the same thinning iteration, which results in less accurate skeletonization images. Right: labels obtained using our proposed profile volume measure. The range of values (8 distinct values) is higher than in case of the distance transform, yielding a higher accuracy in the ordered skeletonization.

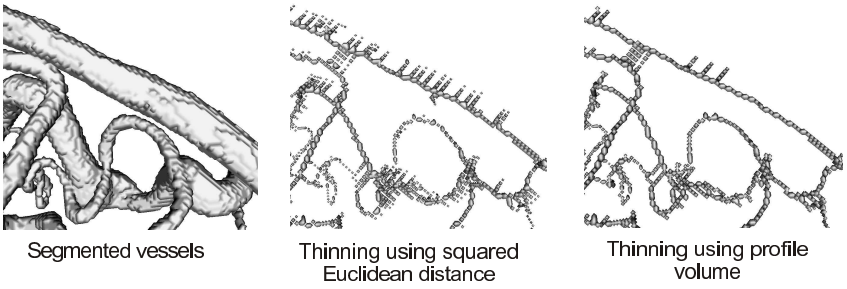

Figure 6.5: An ordered skeletonization of cerebral blood vessels. Left: close-up view of segmented vessels. Middle: the ordered skeletonization using squared Euclidean distance has a lot of irrelevant details. Right: the ordered skeletonization using our proposed profile volumes yields a much more accurate skeleton with fewer irrelevant details.

$E' = \{\{u, v\} \in E | u, v \in V'\}$. The set of adjacent vertices of a vertex v of G, other than v itself, is denoted by $A(v)$. If V' is a subset of the vertex set of G, then $A(V')$ is the set of those vertices that are not in V', but are adjacent to a vertex in V'. As we explained earlier, to avoid confusion, in this work we will use the expressions "node" and "link" strictly for the skeleton structure and "vertex" and "edge" strictly for

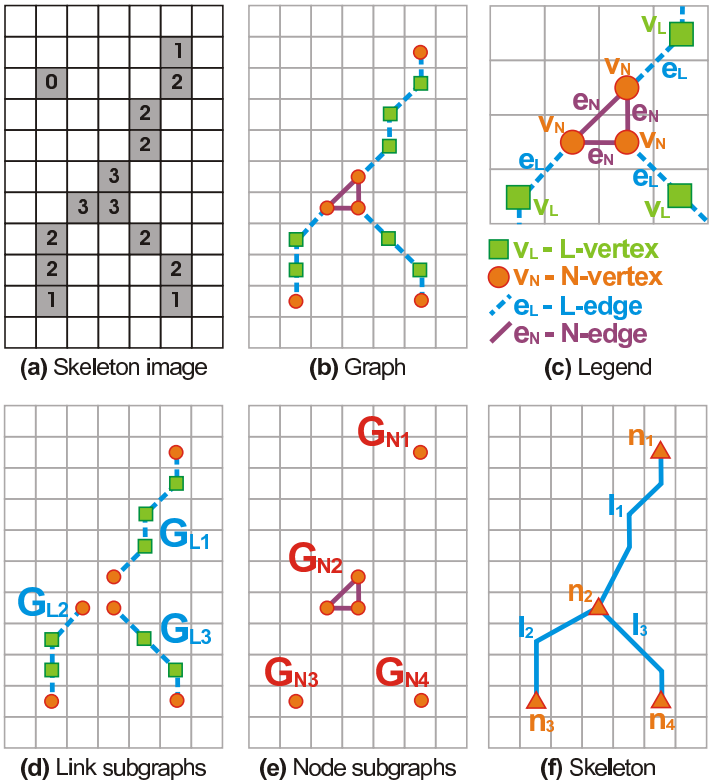

Figure 6.6: Skeleton creation principles. (a)The skeletonized image. Each pixel is labeled with its number of foreground neighbors. (b) The graph created from the skeletonized image. (c) The notation legend. (d) The link subgraphs G_L. (e) The node subgraphs G_N. (f) The skeleton obtained by creating skeleton nodes using node subgraph contraction and creating skeleton links from link subgraphs. The bifurcation is defined by a single skeleton node and each branch with a single skeleton link.

the graph structure.

As we mentioned earlier, in order to analyze the vessel structure, we need to convert the skeletonized image into a graph-type skeleton structure composed of nodes (to represent bifurcations and vessel ends) and links (to represent vessel branches). In the first step we convert the skeletonized image into a (simple) graph (the graph will not have any multiple edges between two vertices or loop edges). In the second step, the graph is partitioned into subgraphs comprising skeleton nodes and links (vessel bifurcations and branches). Ideally, each skele-

ton link should represent a vessel branch and each skeleton node should represent a bifurcation.

Let us consider a skeletonized image in Fig. 6.6a. The image represents three blood vessel branches with a single bifurcation. Each foreground pixel is represented together with a number of its foreground neighboring pixels. Pixels without any 26-neighbors are excluded from the creation of a graph. Pixels with two foreground neighbors are parts of paths connecting ends and bifurcations of blood vessels. Pixels with one foreground neighbor are the ends of blood vessels, and will be represented as nodes in the graph-type skeleton. In case a pixel has more than two foreground neighbors, it is obviously a part of a vessel bifurcation. It should be noted that in such situation, the bifurcation is characterized by several pixels (e.g. three pixels with three foreground neighbors in Fig. 6.6a).

We convert the skeletonized image into an undirected simple graph $G = (V, E)$ by considering every foreground pixel as a graph vertex (we emphasize that only the foreground pixels with non-zero number of foreground neighbors are considered). We create graph edges between vertices representing 26-neighboring pixels in the skeletonized image, as illustrated in Fig. 6.6b with a legend in Fig. 6.6c. It should be noted that the resulting graph is a *simple graph* (i.e. a graph that has no loops and not more than one edge between any two different vertices).

In order to analyze the graph we classify vertices by their *vertex degree* $\deg(v)$ representing the number of incident edges of the vertex (normally, loop edges are counted twice, but our graph is simple and does not contain loops). From the illustrations in Fig. 6.6a and Fig. 6.6b, it is clear that the vertices with degree 2 are parts of vessel paths and will constitute skeleton links, while the vertices with any other degree value represent vessel ends or bifurcations and will constitute skeleton nodes. Hence, we classify graph vertices into *L-vertices* v_L with degree 2 ($\deg(v_L) = 2$) and *N-vertices* v_N with any other degree value ($\deg(v_N) \neq 2$) In the same fashion, we classify edges into *L-edges* e_L, which are incident to at least one L-vertex v_L (these edges will constitute skeleton links) and *N-edges* e_N, which are incident only to N-vertices v_N. The edge and vertex classification principle is illustrated in Fig. 6.6b and Fig. 6.6c.

We will now introduce a graph decomposition into subgraphs that will represent vessel branches and bifurcations. As we concluded earlier, all pixels with two neighbors are parts of paths (i.e. vessel branches) and will be represented by links in the skeleton. In Fig. 6.6d,

these paths are the *link subgraphs* G_L between N-vertices v_N comprised of L-edges and L-vertices. Let V_L denote a set of connected v_L vertices. We define the link subgraph G_L as a graph induced by the vertex set V_L and their adjacent vertices $A(V_L)$:

$$G_L = G[V_L \cup A(V_L)]. \tag{6.5}$$

Fig. 6.6d shows link paths as subgraphs G_L of the graph G in Fig. 6.6b.

We concluded earlier that any pixel with one or more than two foreground neighbors in the skeletonized image represents either the end of a blood vessel or its bifurcation. In Fig. 6.6e, these are the *node subgraphs* G_N comprised of N-vertices v_N and node links e_N connecting them. Let V_N denote a set of connected N-vertices v_N. The node subgraph is a graph induced by the vertex set V_N:

$$G_N = G[V_N]. \tag{6.6}$$

Fig. 6.6e shows node subgraphs G_N of the graph G in Fig. 6.6b.

With equations (6.5) and (6.6) we have defined a graph *decomposition* $\mathcal{F}$ into subgraphs of type G_L and G_N. This is an edge decomposition since it creates a family of edge-disjoint subgraphs. Let $\mathcal{F}_N$ denote a subset of $\mathcal{F}$ consisting only of subgraphs G_N and $\mathcal{F}_L$ a subset of $\mathcal{F}$ consisting only of subgraphs G_L. Obviously, skeleton nodes n will be created from node subgraphs G_N, while skeleton links l will be created from link subgraphs G_L.

However, in order to define a skeleton node as a single position, we need to contract the subgraph G_N into a single vertex position. We do this using the geometric median. The *geometric median* of a set of positions D is the position from the set with the minimum sum of distances to all other positions in the set:

$$\text{medg}(D) = \arg\min_{\mathbf{p}\in D}\Big(\sum_{\mathbf{q}\in D} d(\mathbf{p},\mathbf{q})\Big), \tag{6.7}$$

where $d(\mathbf{p},\mathbf{q})$ denotes the Euclidean distance between the two positions. In our case the skeleton node will be represented as the geometric median of vertices in node subgraph $V(G_N)$. We define the skeleton node as:

$$n = \text{med}_g(V(G_N)). \tag{6.8}$$

In order to maintain a mapping from the skeleton node to its subgraph, we define the *node mapping* function m:

$$m(n) = G_N. \tag{6.9}$$

The function m maps the resulting node to the contracted subgraph G_N in order to maintain the information from all the skeletonization pixels to allow reconstruction of the segmented vessels from the skeleton.

A *skeleton link* connects two skeleton nodes:

$$l = \{n_i, n_j\}. \tag{6.10}$$

In order to maintain a mapping from the skeleton link to its subgraph, we define the *link mapping* function k:

$$k(l) = G_L. \tag{6.11}$$

As with the node mapping function, with the link mapping function m we maintain the information from all the skeletonization pixels to allow reconstruction of the segmented vessels from the skeleton.

Finally, we define the skeleton that consists of the set of skeleton nodes N, the set of skeleton links L and the two mapping functions: $m : N \to \mathcal{F}_N$ mapping a node to the node subgraph (6.9), and $k : L \to \mathcal{F}_L$ mapping a link to the link subgraph (6.11):

$$S = (N, L, m, k). \tag{6.12}$$

The graph-type skeleton of the skeletonized image in Fig. 6.6g is illustrated in Fig. 6.6f. The bifurcation from the skeletonized image is represented by a single node in the skeleton. This is an advantage because the blood vessels can be analyzed in terms of bifurcations and branches (e.g. locating bifurcations, filtering vessels based on their lengths, detecting segmentation errors, reconstruction of the segmentation for certain vessels, etc.). Important graph operations (e.g. best path calculation, graph cuts, pruning) are applicable to the skeleton as well. It should be noted that the skeleton can contain multiple links between two nodes, as well as link loops. The mapping between the skeleton links (or nodes) and their corresponding subgraphs is important for reconstruction purposes. While the skeleton allows us to easily divide the vessel structures, it is important to maintain their corresponding subgraphs that will allow us to extract individual (segmented) vessels.

However, the most important advantage is that malformations of blood vessels can be detected. This is illustrated in Fig. 6.7, where the skeleton representation in Fig. 6.7d shows that multiple links merge in a single node at the center of the malformation phantom. Visualization of the graph in Fig. 6.7c is done by rendering a line for each edge. The visualization of the skeleton in Fig. 6.7d is done by rendering lines skeleton link with ends modified to correspond to the incident skeleton nodes.

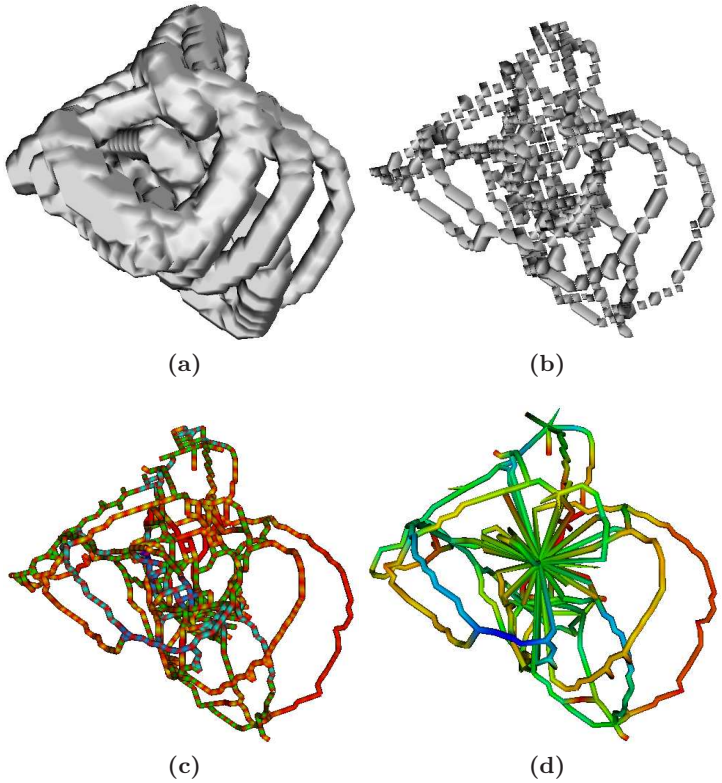

Figure 6.7: Skeleton creation method. (a) Segmentation of an intertwined structure. (b) Skeletonization of the segmented structure. (c) The graph of the segmentation. The intertwined structure is well represented, but bifurcations are not represented by single nodes. (d) The graph-type skeleton. Bifurcation is represented by a single node. Note that in case of intertwined (malformed) vessels the skeleton contains a node with high amount of links, which allows for malformation detection.

6.2.4 Locating and extracting the AVM

In this subsection we propose a novel method for locating and extracting the AVM automatically (the third step in the block diagram shown in Fig. 6.1). Fig. 6.8 shows an original CTA data set with its slice, the segmented vessels, corresponding skeletonizations and skeletons.

The skeletonization in Fig. 6.8c is a result of ordered thinning using our profile volumes on the segmented image. It should be observed that arterial and smaller blood vessels are represented well with one pixel thick paths, while the vein and the AVM are represented by a

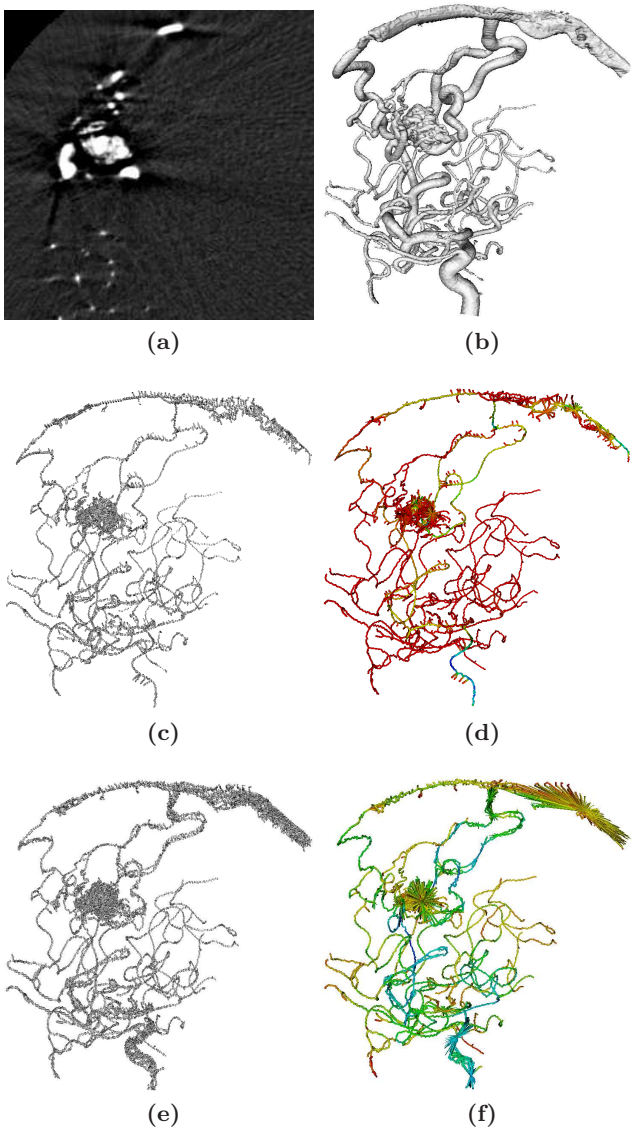

Figure 6.8: Skeletonization and skeleton creation. (a), (b) The original slice of the 3-D CTA cerebral blood vessels and the corresponding segmentation. (c), (d) Radii-based ordered skeletonization and the corresponding skeleton structure. (e), (f) Gray value-based ordered skeletonization and the corresponding skeleton structure. Color coding of skeleton links ranges from red (low values) to blue (high values).

"bundle" of pixels. The reason for this is that the segmented blood vessels contain cavities in the vein and the AVM structure. The cavities are caused by vessel anatomy and the flawed segmentation as a result of high inhomogeneity of pixel gray values. The skeleton of the profile volume ordered skeletonization is shown in Fig. 6.8d. Color coding of links represents vessel radii values (in fact, these are profile volumes that approximate radii values) inherited from skeletonization pixels and range from red (for low values) to blue (for high values).

Let us assign costs to each link as the highest vessel radius corresponding to the links. Two important observations follow. Firstly, high radii values are found in the vein and the main feeding arteries. Hence, the vein and the main arteries can be extracted by tracing the paths with the largest link costs for known starting seed points. Secondly, pixel "bundles" found in the skeletonization image are converted into skeleton nodes with large number of links. Such nodes are highly present in the vein, but their density is the highest in the AVM. Hence, nodes with the highest number of links can determine the location of the AVM.

The skeletonization in Fig. 6.8e is a result of ordered skeletonization using the original pixel gray values in the 3-D CTA image. It should be observed that pixel "bundles" in larger vessels and the AVM are even more common than in case of the profile volume ordered skeletonization. The corresponding skeleton is shown in Fig. 6.8f. The color coding of links represents the original pixel gray values inherited from the skeletonization pixels and range from red (low values) to blue (high values). Pixel gray values in the original image are proportional to the density of the contrast agent in the vessels.

Two important remarks about this skeleton follow. The highest link costs are found in the feeding arteries and partly in the vein. This means that main feeding arteries can be extracted by tracing paths with the highest link costs for known starting seed points. The second and our most important observation is that the node with the highest number of links is positioned in the AVM. The whole AVM region can be represented with only a few nodes in which numerous links merge. This means that we are able to automatically locate and extract the AVM.

We propose to locate the AVM by finding a node with the largest number of links in the skeleton of original pixel gray values:

$$n_{AVM} = \arg\max_{n \in N}(\deg(n)), \tag{6.13}$$

where $\deg(n)$ is a *node degree* representing the number of incident links

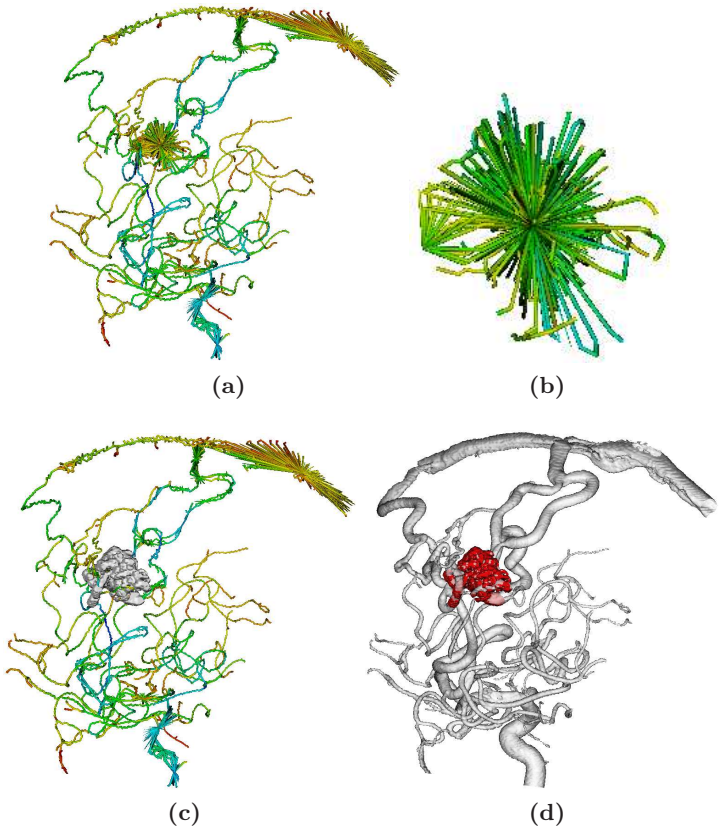

Figure 6.9: Automatic AVM detection and extraction. (a) Gray value based skeleton. (b) Detected (AVM) node with the most links. (c) Extracted AVM with the skeleton. (d) Extracted AVM in the whole blood vessel tree.

of the node, where the loop links are counted twice.

We will now define the rule for the AVM region extraction. We base this rule on the observations concerning vessel branchings. In case of a vessel bifurcation, its corresponding node will have three links. A common case in segmenting the cerebral blood vessels is that two vessels touch, in which case the corresponding node has four links. Hence, the AVM region will consist of all adjacent nodes of the n_{AVM} node, with number of links higher than four:

$$N_{AVM} = \{n \mid n \in A(n_{AVM}),\ \deg(n) > 4\} \cup \{n_{AVM}\}, \qquad (6.14)$$

where $A(n_{AVM})$ is a set of adjacent nodes of the node n_{AVM}. The subskeleton of the AVM is induced by the AVM node set $S_{AVM} =$

$S[N_{AVM}]$. The proposed AVM extraction principle is illustrated in Fig. 6.9. Fig. 6.9a shows the gray value based skeleton of the blood vessel tree. The extracted AVM subskeleton is shown in Fig. 6.9b. Our proposed skeleton creation method (Subsection 6.2.3), allows us to accurately map the AVM subskeleton (by region growing) to the corresponding region in the segmented image. The pixels are included into the region if they belong to the largest inscribed spheres from the skeletonization pixels of the corresponding skeleton links and nodes. The resulting segmented AVM region is shown together with the skeleton structure in Fig. 6.9c and as a part of the whole blood vessel tree in Fig. 6.9d. The AVM region is slightly overestimated (it contains a part of the vein), which is a desired property for the draining vein extraction. In the next step we will decompose the resulting AVM region, which means that we will classify its composing vessels as parts of the draining vein, the feeding arteries or the nidus.

6.2.5 Draining vein extraction

In this subsection we propose a novel method for extracting the draining vein of an AVM, as the fourth step of the block diagram in Fig. 6.1. Consider the segmented blood vessels shown in Fig. 6.10a. As we concluded in Section 6.2.4, the vein has higher radii than the other blood vessels. If we assign the calculated radii values as costs to skeleton links, the venous links have higher costs than the rest of the structure.

Hence, we are able to extract the vein by best path calculation, where the user has to specify the start position of the vein, while the end position is the AVM node $\mathbf{n}_{AVM}$, which is determined automatically. We use the Dijkstra's shortest path algorithm [Dijkstra 59], where the link costs are assigned from the vessel radii (larger radius value implies a higher link cost). The calculated best path skeleton and its corresponding segmentation are depicted in Fig. 6.10b and Fig. 6.10c, respectively. The obtained results are inaccurate, both in the centerline and the segmentation. This happens due to segmentation errors. The problem is that the shortest path approach tends to shorten the highly bended parts of the vein (because they appear as loop links in the skeleton) or pass into the vessels "leaning" onto the vein (which the segmentation is not able to separate).

Since the vein usually has the highest radii of all its surrounding vessels, we need to extract links with the highest costs (corresponding to the highest radii vessels). Also, as a part of the vein is often deeply

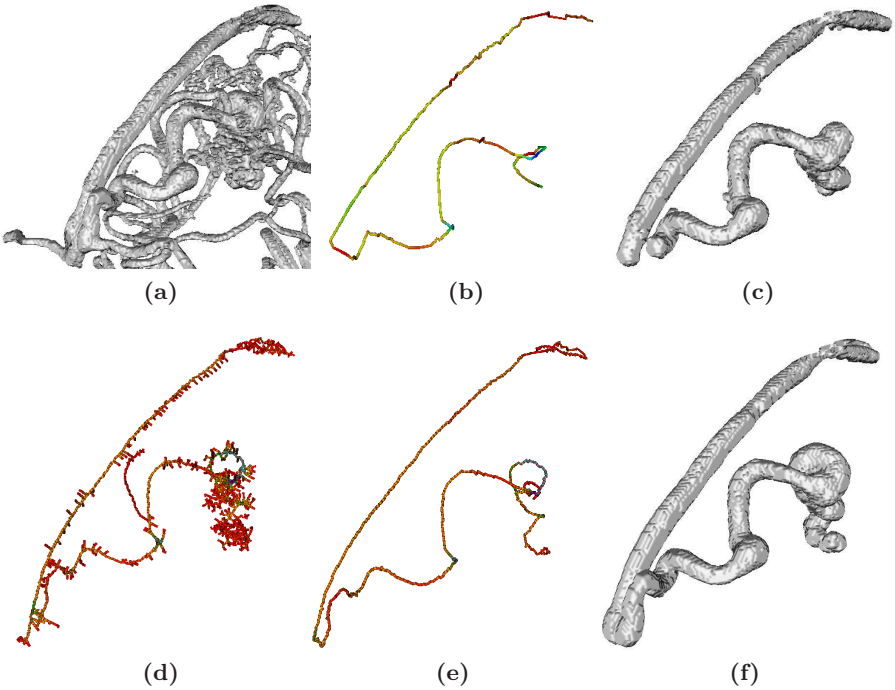

Figure 6.10: Vein extraction example. (a) Blood vessel tree segmentation. (b), (c) Best path from user selected vein start position and the corresponding extracted segmentation do not represent the vein well. (d) The HCVM graph for the vein. (e), (f) The resulting vein skeleton after stub link removal and the extracted segmented region.

embedded in the AVM region, we need to work on the graph structure instead of the skeleton. This is because the skeleton represents the whole AVM region as a single node with its neighbors (it does not contain the detailed structure of the AVM). On the other hand, the graph was created from the skeletonization image and contains all of its details.

We propose a novel method for vein extraction that is similar to ordered region merging. Our idea is to assign costs to graph vertices based on the highest cost of their incident edges. Then we perform the merging of the vertices with highest costs (this is also called *edge contraction*). Every contracted edge is copied to the new (output) graph that will contain the desired paths. The merged vertices form a new one with the cost that equals the average of the merged vertices. The loop edges created during merging will be deleted. Note that at each step

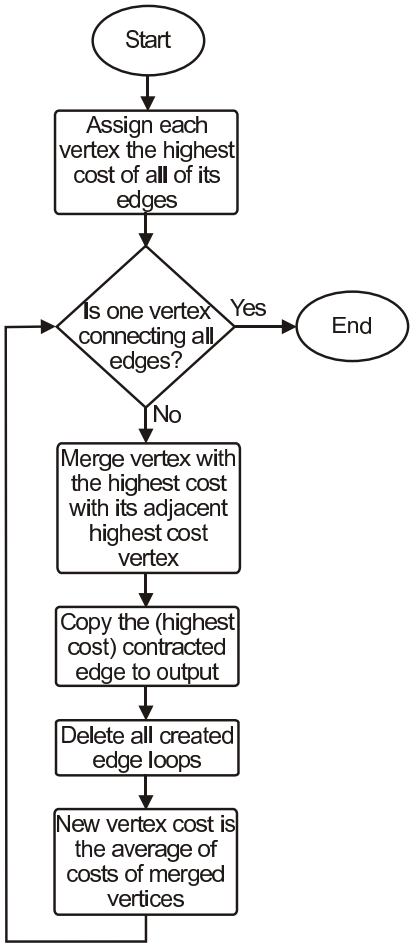

Figure 6.11: Block diagram of the proposed highest cost vertex merging (HCVM) method.

we merge only the vertex with the highest cost with its highest cost adjacent vertex. This way the processed graph will shrink, while the output graph will grow until a single vertex remains in the processed graph. The resulting graph will contain the paths with the highest costs, while all irrelevant low cost edges (which mostly correspond to segmentation error) will be removed. The vein can finally be extracted by shortest path calculation applied to the newly generated graph. We call this approach *the highest cost vertex merging* (HCVM) procedure.

The block diagram of the proposed algorithm is shown in

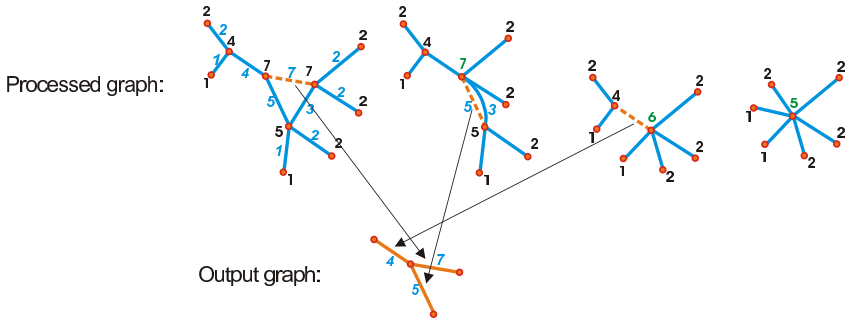

Figure 6.12: Highest cost vertex merging (HCVM) example. In the first step each vertex is assigned the highest cost of its incident edges. In each iteration the vertices with the highest costs are merged (through the highest cost edge, in case more edges between the vertices exist). Loop edges are discarded. The algorithm stops when all edges are incident to a single vertex.

Fig. 6.11. The algorithm starts by assigning each edge a cost equal to the maximum radius of the corresponding vessel (this information is acquired by radii measurements in the segmented image). The initial vertex cost is assigned as the maximum cost of all of its incident edges. Vertex costs are used to define the order in which the vertex merging will be performed, where the priority is given to higher costs. In the second step of the algorithm we check if all graph edges are connected to a single vertex and we repeat the rest of the algorithm while this condition is not fulfilled. The algorithm searches for a vertex with the highest cost (if multiple vertices exist, we select the one that has a neighboring vertex with the highest cost). The selected vertex and its neighboring vertex with the highest cost will be merged into a single new vertex and the edge connecting them is copied into the resulting graph. We denote the output graph of the vertex merging operation as $G' = (V', E')$:

$$\begin{aligned} V' &= (V \backslash \{v_i, v_j\}) \cup \{v'\} \\ E' &= E \backslash \{e_{i,j}\}, \end{aligned} \tag{6.15}$$

where V' and E' represent the new vertex and edge sets. Edge $e_{i,j}$ is the edge with the highest cost incident to vertices v_i and v_j. Vertex v' is the vertex obtained by merging of vertices v_i and v_j. If multiple edges connecting the two vertices exist, only the edge with the highest cost is added to the output graph. Loop edges generated in the process of merging are discarded (removed from the graph that is processed). In this fashion we ensure that there will be a single path leading to or from

any part of the graph. The cost of the new vertex is the average of costs of the two merged vertices. In this fashion, if a vertex with a high cost merges with vertices with lower costs, the cost of the resulting vertex decreases (compared to the highest cost of the merged vertices). Thus, the merging process may be continued at another part of the graph (on the vertex with the currently highest cost). At the point where all the edges are incident to a single vertex, the output graph will represent the resulting tree.

An example of the proposed algorithm is shown in Fig. 6.12. The first iteration in the example shows the graph with edge costs, from which vertex costs are assigned. The edge selected for merging is represented with a dashed line. Note that the process of merging creates a double edge between two vertices in the next iteration. Since these two vertices are selected for merging, the edge that is copied to the output is the one with the higher cost. It should also be noted that the other edge will become a loop by the process of vertex merging, and is therefore, removed. The merging process in the third iteration results in the graph with edges that are all connected to the same vertex, which indicates the end of the algorithm. The last graph in Fig. 6.12 represents the resulting graph, which is the "backbone" tree of the graph structure. It is composed of the edges with the highest costs. Each edge from the original graph is either included in the resulting graph or adjacent to an edge in it. Although we explained HCVM method on graphs, the same principle can be applied on graph-type skeletons. The presented method is similar to Karger's min-cut algorithm [Karger 96] in the sense of the vertex merging principle.

We apply the presented HCVM algorithm on the skeleton of the segmentation in Fig. 6.10a for connecting the manually set vein seed position and the automatically determined AVM center position. Since the start and end vein positions (vertices) are known, we run the HCVM algorithm until both vertices are not merged into a single one (instead of waiting for all the vertices in the graph to merge into a single vertex). The resulting graph is depicted in Fig. 6.10d. On the obtained graph we could calculate the shortest path between the given positions to obtain the vein centerline. However, that would yield a single path, while the vein often contains branches at the AVM region. Hence, we need a method to determine the best path together with its longest branches (the number of these branches would be specified by the user). In order to do this we will iteratively remove smaller branches until we are left with the desired number of branches. This principle is called *pruning*.

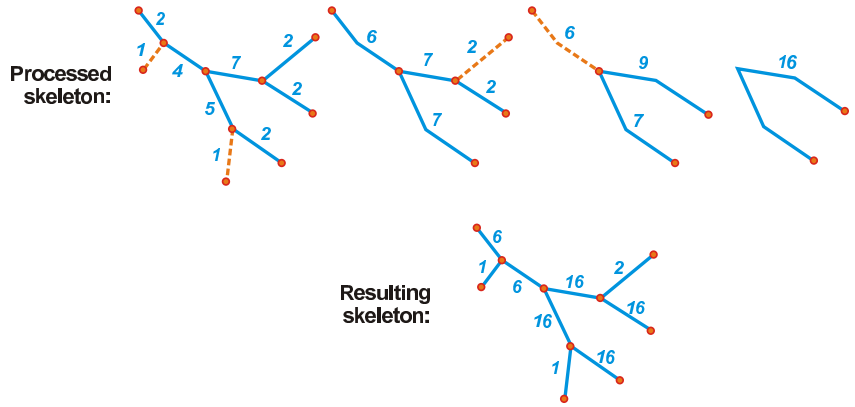

Figure 6.13: Stub link (node) iterative removal principle. The removal starts from links with the lowest costs. A node is merged into its links only if it is left with 2 links, where the new link cost equals the sum of costs of the two merged links.

The vertex containing only one edge is called a *stub vertex*, and the edge whose one vertex is a stub vertex is called a *stub edge*. The same reasoning is applied to skeletons, where similarly the *stub skeleton node* and the *stub skeleton link* are defined. It should be noticed that stub links are path dead ends. An example of pruning principle is shown in Fig. 6.13, where the skeleton is simplified by sequential removal of stub nodes (links), starting from the ones with the lowest costs. After removing each stub node, the nodes that are left with only two incident links are merged into a single link with the cost equal to the sum of the two merging links. In this fashion, we simplify the obtained skeleton by removing stub links until only major paths are left. The resulting order in which links are removed makes a *hierarchical skeleton*. The major paths can be defined in the term of length or the user specified number of links that need to remain. In our case we aim at delineating a single branching of the vein, which is an input parameter to stub link removal. However, we also leave a possibility of user adjusted number of links in the resulting skeleton. The results of pruning the graph in Fig. 6.10d is shown in Fig. 6.10e, which represents the vein centerline well. This is confirmed with the well extracted segmentation of the vein shown in Fig. 6.10f.

We obtain the segmented structure of the AVM nidus by removing the extracted draining vein from the complete AVM segmented region.

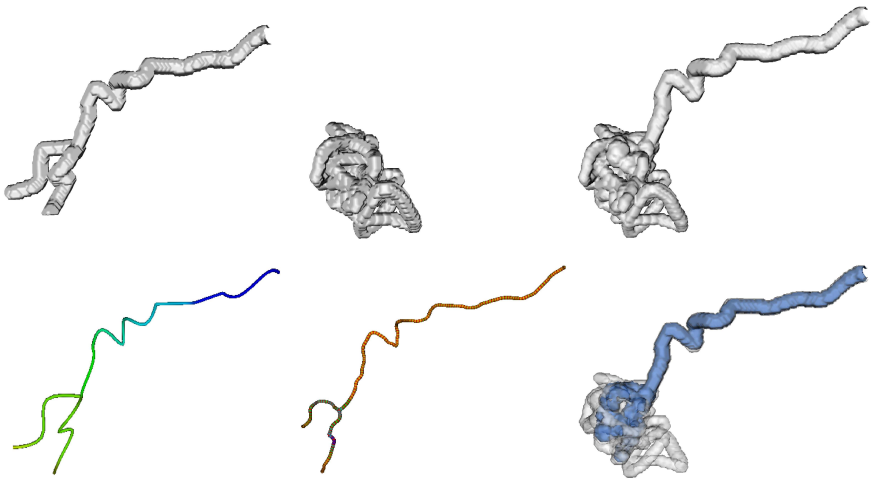

Figure 6.14: Decomposition of blood vessel phantom. First row: the vein and the AVM phantom are combined into a single region. Second row: the vein phantom skeleton, the skeleton after decomposition procedure and the delineated vein region in the original phantom.

6.2.6 Extracting the feeding arteries

In this subsection we explain the principle of extracting the feeding arteries as the last step of the block diagram in Fig. 6.1. After the extraction of the AVM and the draining vein from the segmented image, the remaining vessel structure represents the feeding arteries. In our images the arteries are the vessels with the high density of contrast fluid, which yields high pixel gray values. Hence, we use the Dijkstra's best path algorithm on the gray value based skeleton to extract the arteries. The user has to specify the start position of the arteries and the best paths are calculated to the AVM vessels, which are the closest to the nidus. Afterward, the algorithm automatically extracts the best paths to the links of the extracted AVM skeleton. To ensure that the arteries can also be extracted (if needed) based on their radii, we allow the use of the HCVM algorithm for the extraction of arteries.

6.3 Results and discussion

We validate our proposed algorithm for locating and extracting the AVM on three cases of cerebral vessels containing AVMs, where the onyx cast images were acquired after the embolization procedure. We apply a hole

Table 6.1: Comparisons of the filled segmented onyx cast with the filled extracted AVM segmentation

Validation	Set 1	Set 2	Set 3
Dice	0.83	0.77	0.81
Vol. % error	10	18	13
AVM location distance (pixels)	2.99	0.98	1.73

filling on the extracted AVM region and the corresponding onyx region to suppress the influence of segmentation algorithm on obtained models (in this fashion segmentation of the inner AVM structure does not influence the comparison). For evaluating the obtained results we use the Dice coefficient [Dice 45], which is a set similarity measure defined as twice the ratio of the number of pixels in the intersection of two sets (set of segmented pixels and set of ground truth pixels) and the number of elements contained in both of them:

$$s(X, Y) = \frac{2|X \cap Y|}{|X| + |Y|}. \tag{6.16}$$

Besides the Dice coefficient, we calculate the volume percent error and the distance between the calculated AVM center positions. The comparison of the obtained results is given in Table 6.1. In each case, our method was able to accurately determine the position of the AVM with slightly over-estimating the AVM volume, which is needed for the vein extraction procedure.

For validating our vein extraction algorithm we have generated three 3-D phantom data sets. The 3-D phantom model data consists of an AVM phantom and a vein phantom (see Fig. 6.14). The AVM phantom is generated as a tube intertwined in a random way (with randomly varying radii) to simulate the structure of the AVM nidus. The vein phantom is constructed as a part of a binary tree with the random branch distribution, shape and thickness. Each vein phantom was generated to contain different number of bifurcations (one containing a single vessel without bifurcations, one with a single bifurcation and one with two bifurcations). The vein model is merged with the AVM model to obtain a single vessel tree phantom (see first row of Fig. 6.14), which we use in our experiments.

The obtained phantom poses a hard decomposition problem due to a high number of intertwined vessels with similar radii values. The last row of Fig. 6.14 shows the well extracted vein region and skeleton

Table 6.2: Comparison of delineated and ground truth vein models (Dice coefficient) and skeletons (ratio of their lengths)

Vein phantoms	Dice	length ratio
Phantom 1	0,87	0.92
Phantom 2	0,84	0.86
Phantom 3	0,84	0.94

together with the vessel tree phantom. The results for the three phantom vein models with an AVM are given in Table 6.2. High Dice coefficient values indicate high accuracy of our decomposition method. The second column of the Table 6.2 represents the ratio of lengths of delineated vein skeleton and ground truth vein skeleton. The obtained ratios indicate a high accuracy in vessel length calculation.

An advantage of our proposed method is that it is applicable in combination with any (sufficiently good) segmentation algorithm. To demonstrate the robustness of our AVM and vein extraction approach, we perform the AVM decomposition on real CTA data set segmented using three different segmentation algorithms: thresholding, Curve Evolution for Vessel Segmentation (CURVES) [Lorigo 01] and projection based segmentation [Babin 11c]. The results of this comparison are given in Table 6.3. Firstly, we compare the Dice coefficients for the segmentation of the whole blood vessel tree and extracted AVM and vein using the listed segmentation algorithms. In each case high Dice coefficients were obtained, where the lowest values correspond to cases when the whole blood vessel tree segmentations are compared, which is expected. Secondly, the volume relative error comparison shows fairly good results, with the highest values in case the whole blood vessel tree segmentations are compared, which is in accordance with the Dice coefficient comparisons. Finally, the distance between the AVM centers is very low, showing the high accuracy of AVM locating method.

We compared our method for vein delineation with a centerline extraction method in Vascular Modeling Toolkit (VMTK) [Antiga 06, Piccinelli 09] and a vessel tracking tool [Jackowski 05] using vesselness measure [Qian 09] in BioImage Suite [Papademetris 06]. The extracted AVM region using our proposed algorithm is shown in Fig. 6.15a, where an expert indicated the most probable path of the draining vein. The vessel tracking tool needed multiple seed points for the vein extraction shown in Fig. 6.15b. Centerlines were computed by selecting seed points in the vein and multiple feeding arteries. Ideally, the result should show

Table 6.3: Analysis of extracted vein and AVM regions for CURVES (C), projections (P) and threshold (T) based segmentation

Robustness	T&C	C&P	P&T
Dice whole	0.874	0.829	0.848
Dice vein	0.933	0.899	0.909
Dice AVM	0.942	0.911	0.918
Vol % err. whole	6.99	18.06	31.22
Vol % err. vein	2.34	5.44	3.33
Vol % err. AVM	2.97	14.37	13.41
AVM center dist.	0.308	0.737	0.338

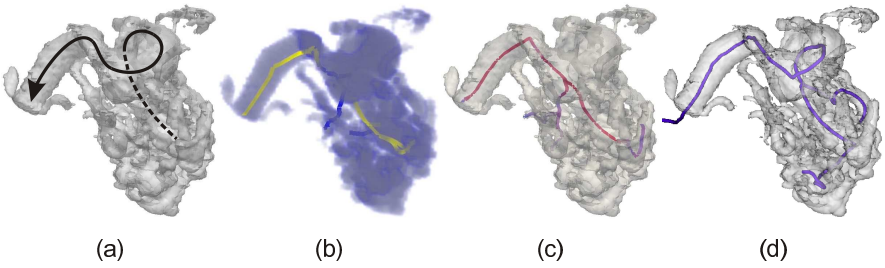

Figure 6.15: Comparisons of the draining vein centerline calculation algorithms. (a) Extracted AVM region with vein path indicated by an arrow, drawn by an expert. (b) Centerlines of vessel tracking algorithm [Jackowski 05] using a vesselness measure [Qian 09]. The vein is shorter than expected. (c) VMTK centerlines [Antiga 06, Piccinelli 09] are also shorter than they should be. (b) Our proposed method delineates the vein very well, with detailed representation including vein bifurcations.

correct venous centerlines with the connection to the arteries (a similar principle is usually used when aneurysm delineation is performed). However, the obtained centerlines using vessel tracking tool do not follow the correct vein path, which is clear when compared to expert drawn centerline in Fig. 6.15a. VMTK centerline extraction yields similar results (see Fig. 6.15c), although with a higher accuracy than the vessel tracking approach. The result of our vein delineation method (Fig. 6.15d) is more accurate than the others and is the only one that reveals the vein bifurcation.

The strength of our approach for locating the AVM and its decomposition comes from the ordered skeletonization and the graph-

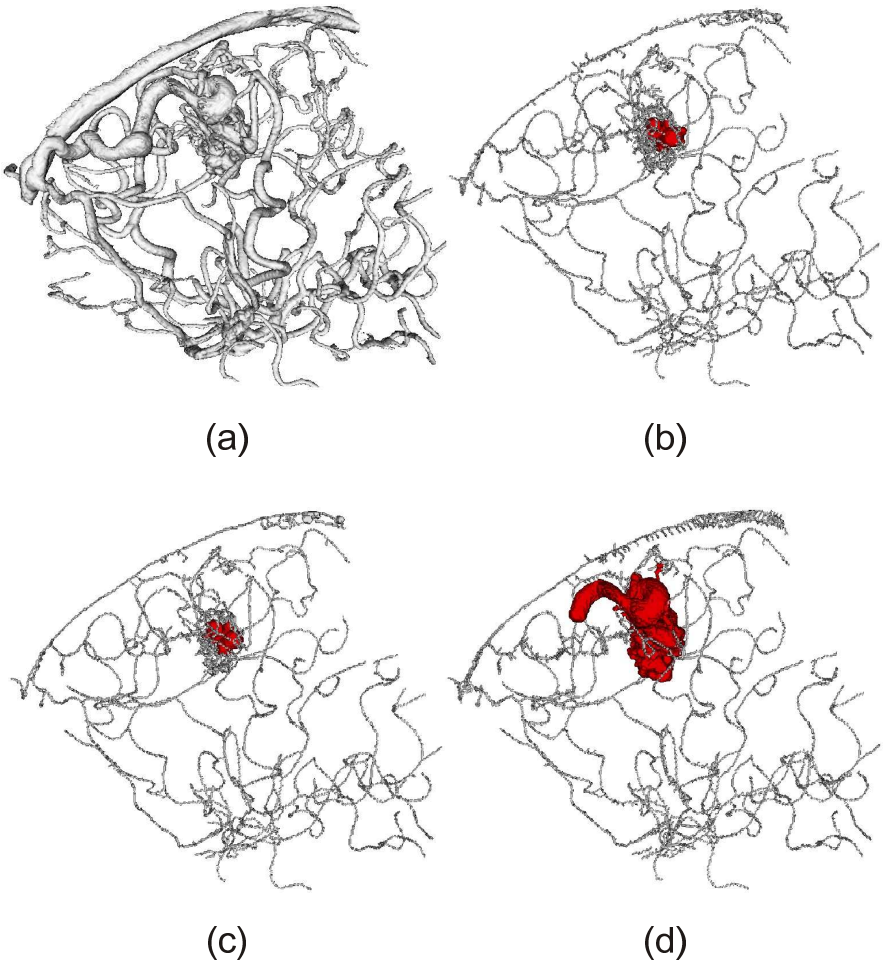

Figure 6.16: Comparison of different skeletonization techniques in combination with our AVM locating and extraction step. (a) Segmented blood vessels. (b) Result of the [Gerig 93] skeletonization method (from Slicer3D image processing application [Pieper 04, Pieper 06]) with extracted AVM. (c) Result of the [Lee 94] skeletonization method (from Fiji image processing application [Schindelin 12]) with extracted AVM. (d) The result of our proposed skeletonization. We observe that our skeleton creation method was able to locate the AVM for any presented skeletonization method. However, the entire AVM region was extracted only for our proposed algorithm.

based skeleton creation principle. The pixel redundancy rule in our skeletonization is highly sensitive to inhomogeneities in pixel gray values, where each of smaller variations is considered as a cavity in ordered

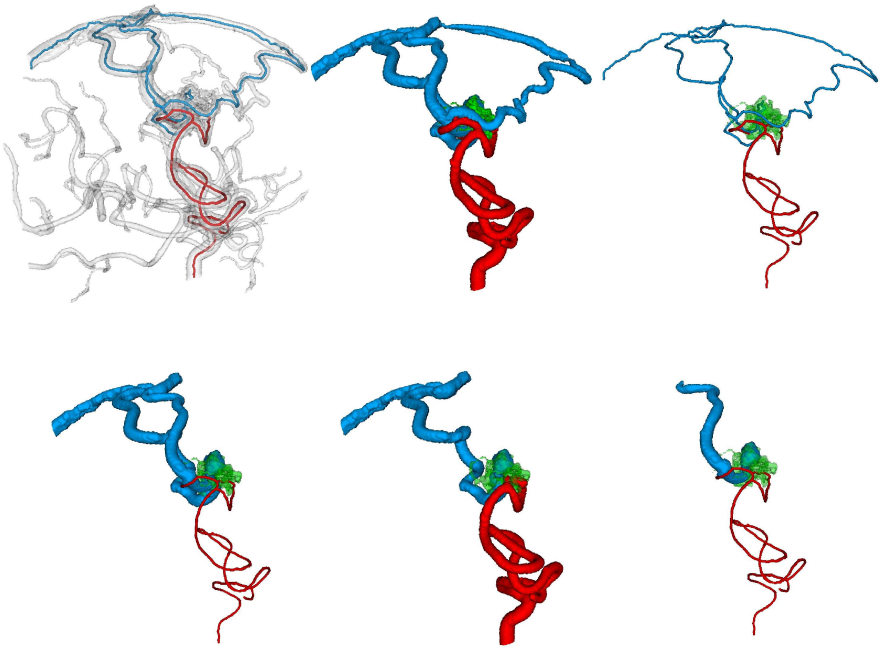

Figure 6.17: Delineation result of a real cerebral 3-D CTA data set. The vein skeleton and segmented region are colored blue, the feeding arteries are red and the nidus is green. The AVM structure is clearly delineated into details. The obtained delineation allows the surgeon to separately visualize appropriate vessels to obtain a better view of the AVM structure.

skeletonization process. Hence, the resulting skeletonization image contains a lot of cavities itself, which are turned into a single node using our skeleton creation principle. This allows us to easily identify the region with the highest amount of cavities. To illustrate the strength of our skeletonization method, we use different skeletonization methods in combination with our AVM extraction step (see Fig. 6.16). The result of [Gerig 93] in Fig. 6.16b, shows that the location of the AVM was accurately determined, but the AVM extraction is not correct (only a small part of the nidus is extracted). Similarly, the method of [Lee 94] under-determines the AVM region (Fig. 6.16c). On the other hand, our proposed skeletonization accurately locates and extracts the AVM (Fig. 6.16d).

The result of AVM vessel classification is shown in Fig. 6.17 with close-up on AVM in Fig. 6.18. The obtained skeleton results show good correspondence to the real vessel anatomy, while clearly delineating

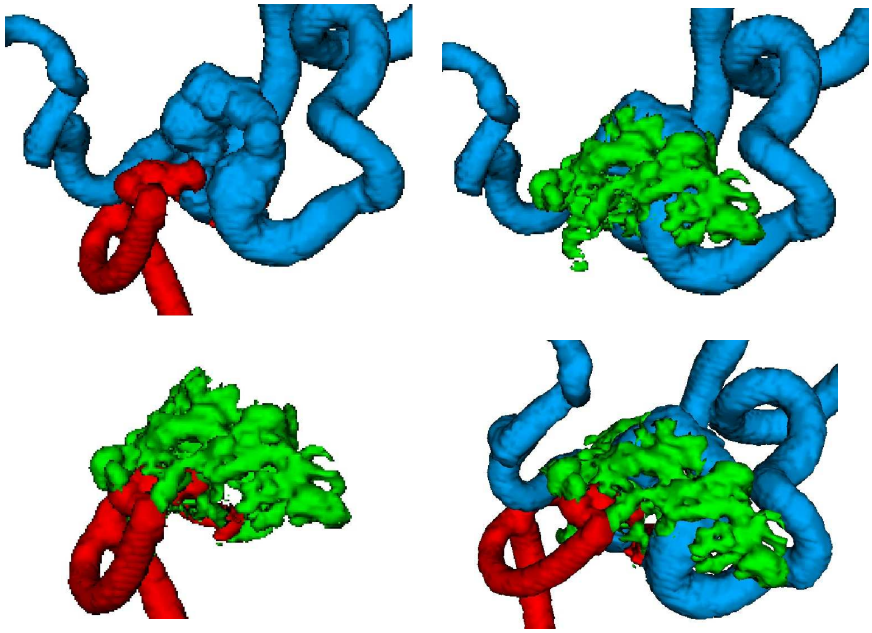

Figure 6.18: Close-up of AVM decomposition result. The veins are colored blue, the arteries are red and the nidus is green. The AVM structure is decomposed into details.

the main vessels of the AVM. The presented method is automatic, with little user interaction required. The algorithm needs about 6 minutes to execute on a 2.2 GHz processor.

6.4 Conclusion

We designed an effective inner AVM decomposition method based on the ordered skeletonization principle. We introduced an advanced method of profile volume calculation to obtain a higher accuracy of ordered skeletonization in terms of structure representation. Moreover, we described an approach for creating a graph-type skeleton structure from skeletonized images and use it to extract main AVM vessels. Using the proposed skeleton structures, we introduced a new method for automatic AVM detection and extraction. In order to extract the draining vein, we designed methods for determining the highest cost path in the skeleton graph and a stub link removal principle. Based on the delineated nidus and the draining vein, feeding arteries were extracted from the remaining

part of the data set by the best path calculation. The AVM detection and extraction method was validated on real 3-D CTA data sets of cerebral vessels with the scan of onyx cast after embolization procedure. In each case the AVM position was accurately determined, with the well extracted region of the AVM. We evaluated the vein extraction algorithm on the three 3-D phantom data sets representing the vein and the AVM region merged together into a single region. The obtained high Dice coefficient values indicate high accuracy of our proposed algorithm. We demonstrated the robustness of our algorithm on segmentation methods, by applying it to various segmentation results. The designed application requires little manual intervention to perform delineation. This work is published in [Babin 08] and has also been submitted to an international journal [Babin 13c] and conference [Babin 14].

7

Pulse Wave Velocity Calculation

In previous chapters we have introduced segmentation and skeletonization techniques for analysis of vascular images. In this chapter we combine and modify these methods with the goal to create an application for estimating aortic stiffness. The aortic stiffness has proven to be an important diagnostic and prognostic factor of many cardiovascular diseases, as well as an estimate of overall cardiovascular health. Pulse wave velocity (PWV) represents a good measure of the aortic stiffness, while the aortic distensibility is used as an aortic elasticity index. Obtaining the PWV and the aortic distensibility from magnetic resonance imaging (MRI) data requires diverse segmentation tasks, namely the extraction of the aortic centerline and the segmentation of aortic regions, combined with signal processing methods for the analysis of the pulse wave. In this chapter we present a novel robust segmentation technique for the PWV and aortic distensibility calculation as a complete image processing toolbox. We introduce a novel graph-based method for the centerline extraction of a thoraco-abdominal aorta for the length calculation from 3-D MRI data, robust to artifacts and noise. Moreover, we design a new projection-based segmentation method for transverse aortic region delineation in cardiac magnetic resonance (CMR) images that is robust to high presence of phase-encoded motion artifacts. Finally, we propose a novel method for analysis of velocity curves in order to obtain pulse wave propagation times. In our study non-contrasted MRI images of abdomen were used in healthy volunteers (22 data sets) for the sake of non-invasive analysis and contrasted magnetic resonance (MR) images were used for the aortic examination of Marfan syndrome patients (8 data sets). In order to validate the proposed method we compare

the obtained results with manually determined aortic centerlines and a region segmentation by an expert, while the results of the PWV measurement were compared to a validated software (LUMC, Leiden, the Netherlands). The obtained results show high correctness and effectiveness of our method for the aortic PWV and distensibility calculation.

7.1 Introduction

Aortic stiffness is an important factor in estimating the cardiovascular risk in several disease conditions. The pulse wave velocity (PWV) is a good indicator of the aortic stiffness in patients with hypertension [Brandts 09], Marfan syndrome [Groenink 98, Kröner 12], Metabolic syndrome [Roes 08], Diabetes [van Elderen 11], etc. The PWV is a cardiovascular parameter which is intensively studied [Hirata 06] both in humans and animals [Wang 00]. Aortic PWV is a strong predictor of cardiovascular events and all-cause mortality [Vlachopoulos 10]. The PWV is measured using various techniques [Ibrahim 10, Gatehouse 05]. The main idea behind the PWV calculation is to track the propagation of the pulse wave from the ascending level of the aorta to its abdominal level in order to obtain the transition speed. Another way to estimate the aortic stiffness is to calculate the aortic distensibility (the extent to which the aortic wall is stretched under a given pressure condition).

We classify approaches for the PWV measurement into three categories: the blood pressure, ultrasound Doppler and magnetic resonance (MR) techniques. The blood pressure PWV analysis is done using a cuff sphygmomanometer on a peripheral limb, where the measured values reflect the pressure throughout the arterial tree in large conduit arteries. The commercially available hardware (TensioClinic Arteriograph) [Horváth 10] uses the time interval between the pulse wave (the early systolic peak) and its reflection from the abdominal aortic bifurcation (the late systolic peak). However, the PWV values are obtained using an estimate of the aortic length between the jugulum and the symphysis, which introduces inaccuracies in measurements. The pulsed wave (PW) ultrasound Doppler hardware (e.g. Siemens, Philips) uses the Doppler effect to determine the transition time of the pulse wave in the aorta. However, the length of the aorta still needs to be estimated, resulting in a lower accuracy of the PWV measures. The same approach is taken if a heart sound sensor is used.

Various approaches exist to PWV calculation using MR images. The transit time (TT) approach requires modulus and phase-contrast

images at various aortic levels to calculate the velocity curves and a whole MR abdomen and thorax image to calculate aortic lengths between the given levels. The PWV is calculated as the speed of wave propagation. Often only two cross-sectional slices are required for calculating the velocity wave profiles, where the aortic length is measured from an oblique sagittal slice. The time interval between pulse wave is often determined by the "foot" of the wave curve [Boese 00]. Algorithms based on finding the maximum (or the minimum) velocity of the pulse wave depend on the assumption that the sampling rate at which the images were taken is sufficiently high to accurately capture the peak of the wave. Similar approach is to define the wave arrival moment as the time instant in which the wave reaches its mid-range value (the average of the minimum and the maximum value). The flow area (QA) approach [Vulliémoz 02] uses one data set at one site across the aorta (cross-sectional through-plane velocity encoding), where the aortic area is acquired from magnitude images and the flow from phase-contrast images. The PWV is estimated as the ratio of difference in the total (the maximum and the minimum) flow and difference in the total area at early systole. The extension to TT approach is a *multisite method* that uses a single para-sagittal slice of aorta, which allows for obtaining flow waveforms at multiple locations along the aorta. The multisite method [Giri 07] uses the maximum velocity change (at a single cross section) to define the arrival moment of the pulse (at the given cross section). The cross-correlation (XC) approach [Fielden 08] is a multisite method that uses cross-correlation to determine the time interval between flow waves at different locations along the aorta. A flow-sensitive 4D MRI approach for PWV measurements has also been proposed [Markl 10]. An axial velocity profile method for estimating the PWV of the descending aorta was developed in [Yu 06], which allows visualization of the pulse wave propagation. Apart from these, methods based on deformable surfaces are applied to the segmentation of modulus images for an aortic distensibility calculation [Herment 10]. The comparison of MR PWV calculation approaches was done in [Ibrahim 10] and concluded that TT and XC methods result in a closer and a more reproducible aortic PWV measurement than in the QA method.

The main idea of our approach is to design a complete PWV analysis software tool for subjects scanned without injection of contrast agent (for aorta check-up purposes), as well as for patients (studied with contrasted images). In our case, the non-contrast enhanced MR approach results in "black-blood" images (the aorta appears as a black

blood vessel). This poses a much harder segmentation problem due to the fact that the structures surrounding the aorta appear in the same range of (low) gray values (lungs, veins and heart), with low visibility of separating tissues.

The current reviews on vessel extraction techniques [Kirbas 04, Lesage 09] show a wide variety of segmentation methods developed for angiographic vessel images. The work of [Zhao 09] combines level-set and optimal surface segmentation algorithms. The aortic segmentation based on robust machine learning algorithms is proposed in [Vitanovski 12] to estimate the personalized aortic model parameters. The work of [Tek 05] describes the segmentation of the aortic wall by detecting the edges along 1-D rays in multiple scales using mean shift analysis and combining them using the properties of mean-shift clustering. "Black-blood" vessel extraction methods show good results on segmenting the vessel wall, usually with some user interaction needed. A semi-automatic method is described in [Ladak 01], where the discrete dynamic contour is approximately initialized, deformed to the inner vessel boundary, dilated, and finally deformed to the outer vessel boundary. The method of [Rueckert 97] uses deformable models in combination with the Markov Random Field framework. For segmenting low quality MRI images we developed a multiscale method [Babin 09b] robust enough to deal with slice discontinuities and blood flow artifacts. However, the mentioned method is not fast enough. Most common methods for the segmentation of the abdominal aorta are methods for segmenting aortic aneurysms, which work on angiographic images of much higher quality than in our case. The methods based on gradients and vessel unwrapping [Wang 04] need fine parameter tuning to surpass image discontinuities and avoid connecting unrelated tissues in MRI images, where different regions of the aorta might need to be segmented separately with different parameters. The existence of discontinuities of aortic regions in neighboring slices is also a problem these methods are not able to cope with.

In this chapter we propose novel and robust segmentation methods for the PWV measurement. First, we propose a novel method for extracting the centerline of the abdominal aorta in contrasted and black-blood MR images by combining graphs and our previous work on multiscale profiling in Chapter 4. The main novelty of this approach is the efficient method for creating the image subsampling grid (graph), which allows a fast and robust centerline extraction. Next, we introduce a method for the segmentation of the aortic region in modulus CMR im-

ages by selection of candidate regions obtained using projections (based on line-shaped profiles in Chapter 5). The main idea of this approach is to apply various operators on images to obtain a range of segmentation candidates. The best candidate is chosen as the final segmentation based on the circularity (roundness) and the size of the aortic region. Finally, we propose a novel method for the analysis of the pulse wave by taking into account its steepest slopes and deformation over time. In order to validate our algorithm, we compare our results to the results of already validated method for pulse wave analysis using the QFlow package for analysis of phase-contrast images and an in-house developed PWV tool [van der Geest 98, Grotenhuis 09, Westenberg 10] (LUMC, Leiden, the Netherlands). The results of our method show good correspondence to the PWV results obtained by the validated method, both for data sets of healthy volunteers and Marfan syndrome patients. However, unlike the LUMC and QFlow software combination, our method (and application) an integrated image and signal processing toolbox that allows processing of black-blood MR images and robust pulse wave curve analysis.

The chapter is organized as follows. In Section 7.2, we explain the proposed method. In subsections we describe the used data sets, the centerline extraction and the modulus image segmentation. We complete the section by proposing a novel algorithm for pulse wave analysis. In Section 7.3, we present and validate the results of our proposed algorithm. Section 7.4 concludes this work.

7.2 Materials and methods

7.2.1 Problem definition and data sets

The data sets for the PWV calculation consist of a 3-D MRI image (as a series of 2-D slices) of an abdomen and an arbitrary number of CMR series of modulus and phase-contrast images at different aortic levels. In our case, the CMR images were acquired at four different aortic positions: ascending, descending, diaphragmal and abdominal levels (see Fig. 7.1). Fast imaging with steady-state free precession (True-FISP) modulus images are acquired as a retrospective electrocardiogram (ECG) gated scan with reconstruction of 40 images per RR-interval, slice thickness 6mm, repetition time (TR) 26ms, echo time (TE) 1ms, flip angle (FA) 80^o, field of view (FOV) 240mm×320mm and matrix size 192×256 pixels adjusted to body habitus to avoid ghosting artifacts.

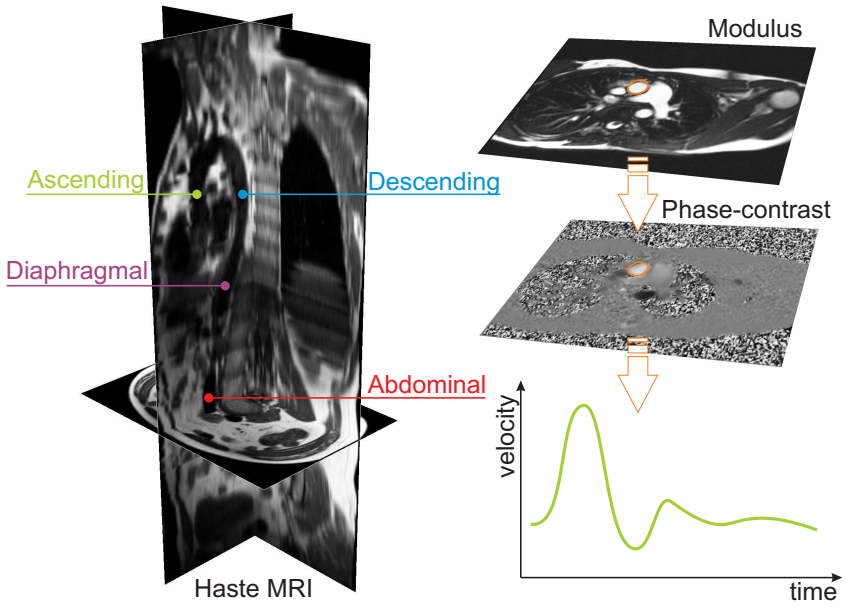

Figure 7.1: The 3-D HASTE MRI data set of a healthy volunteer ("black-blood" images) with marked cardiac axes at the ascending, descending, diaphragmal and abdominal level. At each level the modulus images need to be segmented and used as a mask for velocity calculation on phase-contrast images in order to obtain the pulse wave.

Fast Low Angle Shot (FLASH) 2-D phase-contrast images were acquired as a retrospective ECG gated scan with reconstruction of 40 images per RR interval, slice thickness 6mm, TR=61ms, TE=3ms, FA=30^o, velocity encoding (VENC) of 150cm/s, where the matrix size and slice position were adjusted to the TrueFISP image allowing their mapping. Phase-encoded motion artifacts appear as bright noise or repeating densities oriented in the phase direction. They occur as the results of motion (e.g. arterial pulsations, swallowing, breathing, peristalsis and physical movement of a patient) during image acquisition. In our case phase-encoded motion artifacts are visible in modulus images at the ascending level of the aorta influencing up to 20% of the sequence. For this reason we need a robust method for the modulus image segmentation.

The main idea of our research is to develop an image processing toolkit for the PWV calculation for contrast enhanced or non-contrast enhanced MRI images. Hence, the experiments are conducted on the images of healthy volunteers (22 data sets) and Marfan syndrome pa-

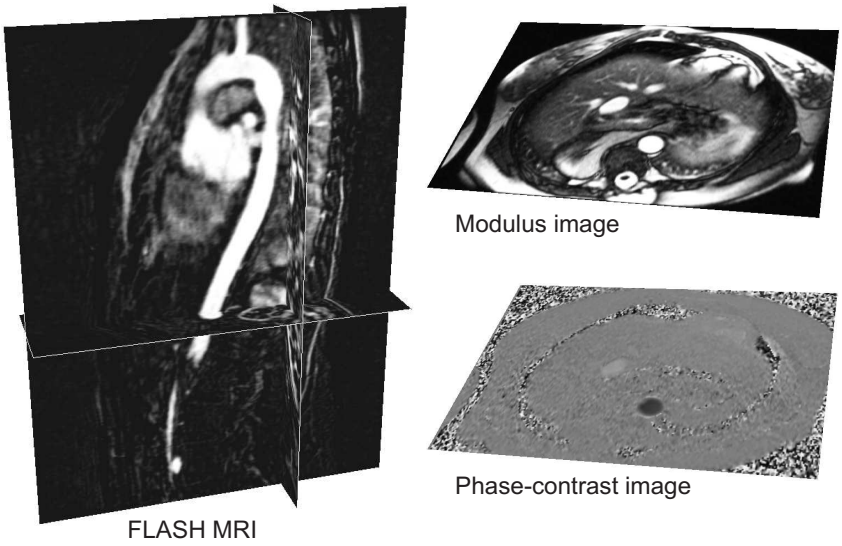

Figure 7.2: A Marfan Syndrome patient data set. Left: the 3-D FLASH MR data set of a patient obtained by subtracting the contrast-enhanced data set with the non-contrast enhanced image. Right: a modulus image and its corresponding phase-contrast CMR image at the diaphragmal aortic level.

tients (8 data sets) obtained from the Ghent University Hospital (UZ Gent). The 3-D MR images of healthy volunteers were acquired using the Half Fourier Acquisition Single Shot Turbo Spin Echo (HASTE, properties: slice thickness 6mm, TR=700ms, TE=26ms, FA=160^o, FOV=233mm×340mm and a matrix of 176×256 pixels adjusted to a body habitus) technique on a 1.5T scanner using a high inter-slice spacing of 6.6mm without injected contrast agent, yielding low quality "black-blood" images (see Fig. 7.1). The black-blood aorta images pose a hard segmentation problem due to unclear boundaries between the aorta and surrounding organs (veins, heart and lungs). However, the advantage of such scanning process is the increased acquisition speed with a non-invasive approach. The 3-D MR images of patients were obtained using Fast Low Angle Shot (FLASH, properties: slice thickness 0.9mm, TR=3.8ms, TE=1.3ms, FA=20^o and a matrix of 288×384 pixels adjusted to body habitus) technique on a 1.5T scanner by subtracting the contrast-enhanced data set with the non-contrasted scan in order to obtain clear images of an aorta as shown in Fig. 7.2. All the subject gave their consent to their inclusion in this study.

Fig. 7.3 shows the block diagram of our proposed algorithm

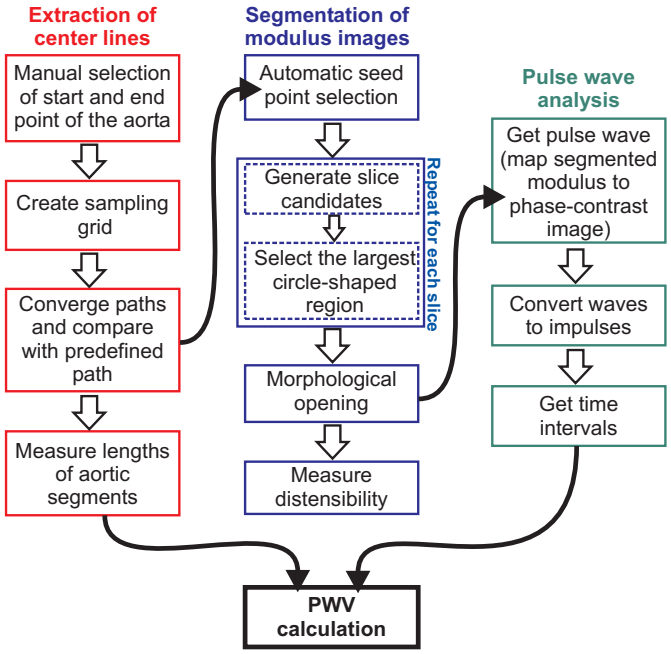

Figure 7.3: Block diagram of the proposed algorithm.

decomposed into three major parts representing the main contributions of this chapter. The left column represents the centerline extraction algorithm, the central column shows the algorithm for segmenting modulus CMR images, while the column on the right represents the pulse wave analysis method. The PWV is measured by "tracking" the propagation of the pulse wave from the ascending level to the abdominal level to determine the transition time. For this the aortic region in the modulus images is segmented and the obtained result is used as a mask for the mean velocity calculation in phase-contrast images as depicted in Fig. 7.1. The length of the aorta between each of the levels is obtained by extracting the centerline from 3-D MRI images and is used in combination with the obtained propagation time intervals to obtain the speed of the pulse wave, which is the PWV. Another important parameter is the distensibility of the aortic wall, which is represented through the maximum, minimum and average circumference of the aortic wall calculated for each aortic level.

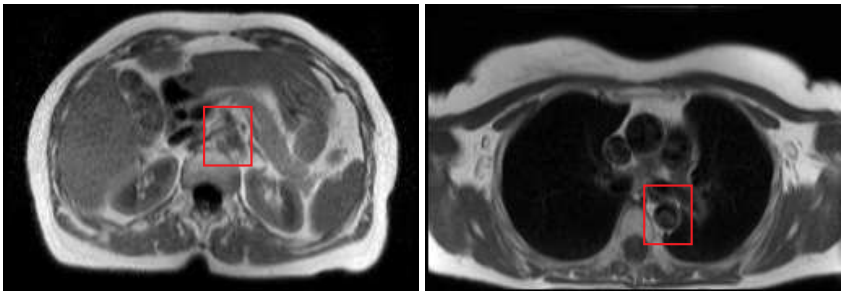

Figure 7.4: Artifacts found in "black-blood" MRI images are marked in red. Left: the aorta is not visible in the transversal slice at the diaphragmal position, right: noise in the descending aorta.

7.2.2 Aorta centerline extraction

In this subsection we describe our proposed algorithm for extracting the centerline of the aorta, as depicted in the left column of the block diagram in Fig. 7.3. The extraction of the aortic centerline is a necessary step in PWV calculation in order to obtain the length of the aortic vessel between the four levels of the abdominal aorta. Our goal is to create a general algorithm applicable for both contrast-enhanced and "black-blood" MRI images. The black blood aortic images pose a hard segmentation problem [Babin 09b] due to their low quality with high presence of artifacts and a high inter-slice spacing of 6.6mm (pixel spacing is 1.32mm×1.32mm), which often causes the effect of a single object not being connected in the neighboring slices. Fig. 7.4 illustrates artifacts found in the "black-blood" MRI data sets, where the aorta is often not clearly visible in a number of adjacent slices due to blood flow. For this reason, the centerline extraction method has to be robust, while requiring as little user interaction as possible.

The main idea of our approach is to build a structured grid graph, where node and link values are sampled from the image. The centerline of the aorta is extracted in a semi-automatic way, where the user has to specify the start and end point of the aorta. We design our algorithm to allow a quick examination of multiple alternative paths for the extraction of complicated vessel structures.

7.2.2.1 Creating the sampling grid

In order to eliminate the influence of artifacts that appear in certain slices of black-blood MRI images of abdomen we propose construction

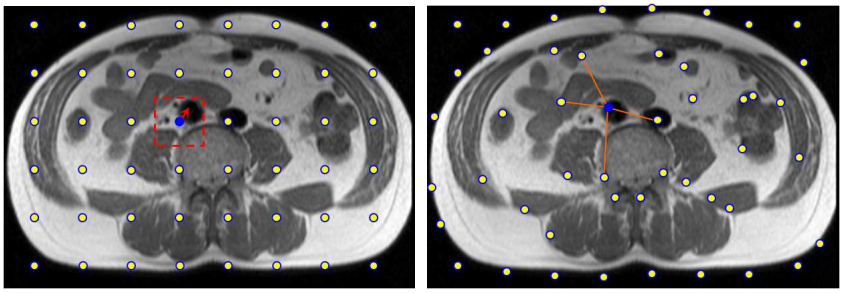

Figure 7.5: Illustration of a 2-D sampling grid. Left: regular grid with many nodes placed at "invalid" (bright) regions. Nodes are repositioned in the region defined as the half of the node spacing in each direction (dashed square). Right: repositioned nodes in the darkest regions. Links between adjacent nodes form a grid (illustrated for a single node).

of a sampling grid that takes into account only the "valid" (since the aorta appears dark, these are the darkest pixels in a predefined neighborhood) candidate pixels of the abdominal aorta. This means that nodes of the grid will be positioned only at those pixels that have the highest possibility of belonging to the region of the aorta in a given neighborhood (e.g. in case of MRI images the aorta is dark, and therefore, the grid nodes will be positioned at the darkest pixels of a predetermined neighborhood). We create an initial regular structured grid (graph) of arbitrary size, whose nodes are equally distributed with the constant spacing in each direction (x, y and z directions). The node spacing is determined by the user specified number of sampling nodes in each of directions. Our experiments show that sampling grid of dimensions $25\times25\times25$ results in the best balance of given results and required processing times. Advantage of the sampling approach is reduced processing times compared to techniques that process every voxel of the 3-D image.

Since the nodes in the initial grid are regularly distributed, some of them are situated in bright regions of the MRI image, which are not likely to be the region of the aorta. For this reason it is of interest to move the nodes to the pixels that can be a part of the aorta. However, in order to maintain a relatively regular distribution of the nodes in the image, we can reposition the nodes only in the region up to the half of the node spacing in each direction. This principle is illustrated in Fig. 7.5 for a 2-D case. This method ensures that the nodes will not overlap after repositioning, while we increase the possibility that they fall in a region of the aorta. This means that our algorithm searches for

the darkest region around each node (search areas do no overlap).

The multiscale approach to defining the darkest regions was explained in detail in Chapter 4, and we use it now to reposition the nodes to the darkest region of their neighborhood. We consider an equidistant neighborhood (that is a ring-shaped structuring element) of a pixel. We use the mean operator to estimate the "darkness" of the neighborhood. This is the principle of spherical means in equation (4.2). The darkness of the pixel $\mathbf{p}$ with respect to its neighborhood is the profile measure $\rho(\mathbf{p})$ defined in Definition 1 of Chapter 4.

Finally, we define the position of the darkest region as the position of the pixel with the gray value belonging to the lowest 10% of all searched values in the given node area, which has the highest transformed value $\rho(\mathbf{p})$, as defined in Definition 1. In this fashion we combine the pixel intensities with the range of influence of their neighborhoods, which constitutes valid candidate positions of the aorta. When the position of the darkest region for a given node is located, the node of the grid is moved to the found position. In this fashion, we reposition all the nodes to the darkest regions while making sure that the nodes do not overlap. We finalize the grid construction by entering costs for the links connecting each node to its six closest neighbors from the initial grid. The cost of a link $c(l)$ is calculated as the average of all the pixel gray values belonging to the line segment set L connecting the two nodes of the link:

$$c(l) = \frac{1}{|L|} \sum_{\mathbf{p} \in L} g(\mathbf{p}), \tag{7.1}$$

where $g(\mathbf{p})$ represents the gray value of the pixel $\mathbf{p}$. Fig. 7.6(a) shows the modified grid of size $25 \times 25 \times 25$, where the red color indicates higher link values and blue indicates lower link values.

7.2.2.2 Centerline extraction

The centerline extraction algorithm is illustrated in Fig. 7.6. In order for the centerline to be extracted, the user must specify the start and the end position of the desired centerline path. These positions are entered into the existing sampling grid as new nodes, which we connect with their closest six neighboring nodes and enter their link costs as described by (7.1). We use the link costs of the sampling grid to converge the graph using Dijkstra's shortest path algorithm [Dijkstra 59] with respect to the entered start and end nodes separately. This means that each of the nodes contains the shortest distance and path to both the user selected

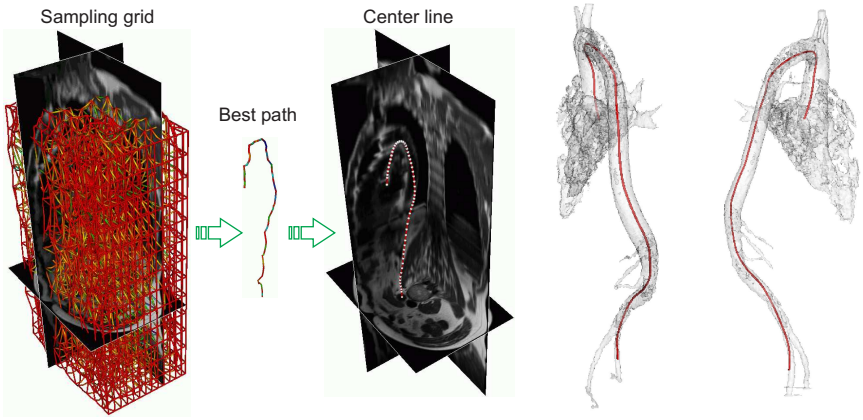

Figure 7.6: Illustration of the sampling skeleton grid construction and the centerline extraction. (a) Left: the final sampling grid, center: calculated (intermediate) best path, right: the aortic centerline (smoothed best path). (b) Extracted centerlines from the Marfan syndrome patient data set.

start and end node. In this fashion, the final metric for each of the nodes $m(n)$ is calculated as the sum of distances from both the start and end node:

$$m(n) = d(n, n_{start}) + d(n, n_{end}), \tag{7.2}$$

where $d(n_1, n_2)$ represents shortest path between the given nodes (obtained using the Dijkstra's shortest path algorithm). All distinct paths between the start and end nodes are calculated by going through all grid nodes and extracting paths to start and end node while keeping track which paths have already been considered. In order to obtain only distinct paths, nodes that are a part of already found paths are not taken into account. The found distinct paths are sorted based on the calculated path distances. Finally, the obtained paths are smoothed as shown in Fig. 7.6(a). Fig. 7.6(b) shows an extracted centerline for a Marfan syndrome patient where contrast enhanced MR images were used.

We designed our algorithm in such way that it can be used with a predefined aortic model (given as a calculated centerline). In this case each link in the sampling grid is compared to the corresponding link on the predefined aortic path (model). The corresponding link in the model is determined by projecting the point situated at the middle of the link (when considered as a line segment) to the links (line segments) of the

predefined model. The corresponding link is the one where the projection falls on the link line segment while having the shortest distance from the given (original) link line segment. This way the directions of the link l and its corresponding link on the predefined model l_S are compared and used as a weighting factor $w(l; l_S)$ for link costs:

$$w(l; l_S) = 1 - \cos(\alpha(l, l_S)), \tag{7.3}$$

where $\alpha(l, l_S)$ denotes the angle between the link l and its corresponding link in the model l_S. In this case, the link cost is:

$$c_w(l) = w(l; l_S)c(l). \tag{7.4}$$

It should be noted that in the case of contrast enhanced images, the priority will be given to brighter pixels and image regions, unlike in the case of "black-blood" images, where the priority is assigned to dark regions of the image.

The first column of the block diagram in Fig. 7.3 shows the implementation of our proposed robust aorta centerline extraction method by creating the sampling grid using image characteristic values. The default size of the sampling graph is set to 25×25×25 nodes, although the user can specify the sampling grid of any dimensions. The user is required to manually select the start and end positions of the aorta, after which the sampling graph is created and the best path is extracted. We implement our application in such a way that the user can select the best centerline out of all calculated found paths (however, in 80% of cases, the automatically selected path is the optimal one).

7.2.3 Segmenting modulus images

This subsection describes our proposed algorithm for the segmentation of modulus CMR images, as presented in the middle column of the block diagram in Fig. 7.3. The aorta does not significantly change its position or shape throughout the time sequence. Although this fact can be used for the delineation of the aortic region, the exact segmentation of the aortic wall is a hard segmentation problem due to phase-encoded motion artifacts (see Fig. 7.7). Hence, we propose a robust segmentation method using line-shaped profiles explained in Chapter 5. The idea is to process the images with different second order profile operators (equation (5.3)) and to obtain a segmentation for each of these operators (5.5), which yields a multitude of candidate segmentations. To select the

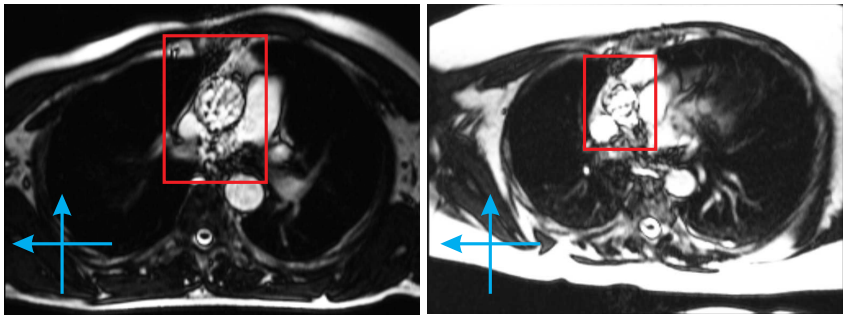

Figure 7.7: Modulus images of the ascending aorta affected by phase-encoded motion artifacts (rectangle). Only two directions of line-shaped structuring elements are used for the segmentation (arrows).

best segmentation candidate, we will introduce here the "higher level" algorithm that performs this selection.

As each profile operator produces a different segmentation candidate, the final result is obtained by selecting the most round and large enough candidate region. The region is a connected component in the segmented image, which is defined by a seed point generated from the intersection of the calculated aortic centerline and the image plane (positioned in 3-D space). The advantage of this approach is that the segmentation method is not constrained by an assigned predefined shape of the aorta. Instead, our algorithm is capable of segmenting various aortic shapes by generating candidate regions, from which the most appropriate aortic region is later selected. Since the TrueFISP images have clearly differing vessel regions in comparison to surrounding tissues, we use only two directions of line-shaped SEs, as illustrated in Fig. 7.7. The user specified seed point is required only in case all data sets are being processed in parallel. Otherwise, the calculated centerline is used for the seed point initialization. To insure the smoothness of the final segmentation, morphological opening of the whole segmented volume is performed after the candidate selection. Segmented TrueFISP images are depicted in Fig. 7.8, where the segmented modulus sequence is represented as a 3-D volume, enabling us to easily observe the evolution and movement of the aortic wall at the given level over time. From the segmented aorta the aortic distensibility can be calculated using measured difference in the maximum and minimum aortic area and by a remotely controlled sphygmomanometer used to measure blood pressure during each of the TrueFISP scans.

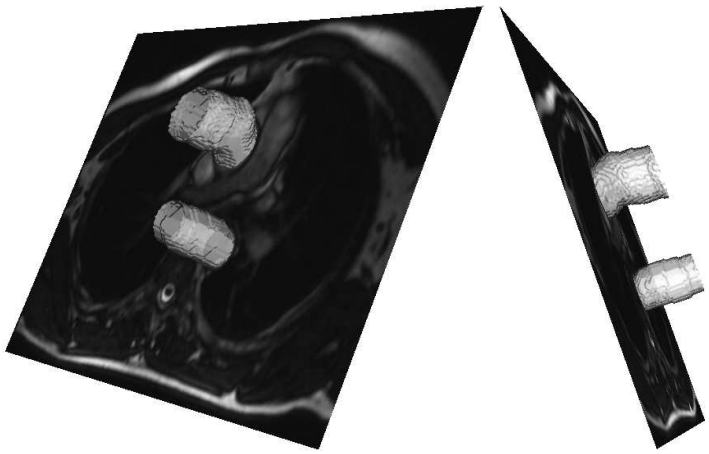

Figure 7.8: Segmented regions of the ascending and descending aorta on a single TrueFISP data set, where the models represent the variation of a 2-D region over time. The ascending aortic region varies in position and area, while the descending aorta has only a small variation in its area.

Optionally, the region of interest can be defined to limit the volume of the image processed by our algorithm. The default value of the ROI is set to 50mm, which is higher than the normal diameter of the aorta, insuring that the region of the aorta falls inside the ROI.

7.2.4 Pulse wave propagation

The method described in this subsection is represented as the right column of the block diagram in Fig. 7.3. After the successful segmentation of modulus images, we calculate the pulse wave for each of the aortic positions as an average value of pixels of phase-contrast images masked by the corresponding segmented modulus regions (see Fig. 7.1). In our case the pulse wave consist of 40 samples for each aortic position (forty 2-D slices of CMR images), as depicted in Fig. 7.9, where full lines represent pulse waves at the ascending, descending, diaphragmal and abdominal position. It should be noticed that different time intervals exist between the observed pulse waves, which will (in combination with calculated lengths of the aorta) define the speed of the pulse wave (the pulse wave velocity). During the transition the pulse wave is deformed [Westenberg 98] (e.g. compare the ascending and the abdominal wave in Fig. 7.9), which raises a question on how to determine the exact moment when the wave passes through a given aortic position.

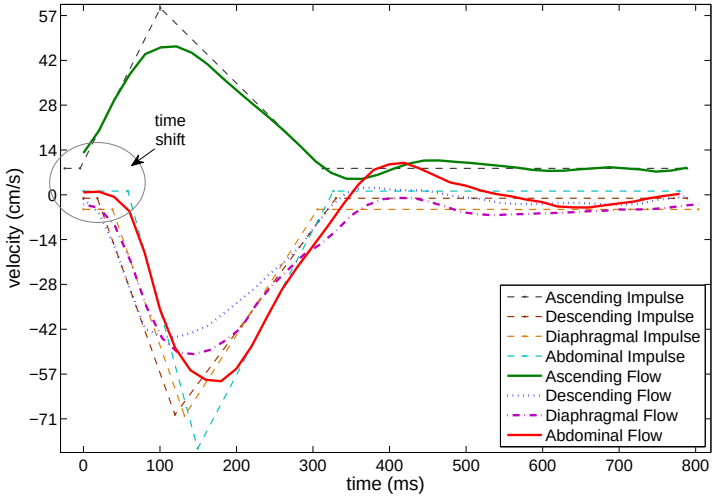

Figure 7.9: The pulse wave propagation. Full lines represent pulse waves and dashed lines their corresponding impulse representations. The time interval between the pulse waves is calculated as the time interval between the start of the first slopes of their corresponding impulses.

We will now examine existing algorithms for pulse wave analysis, which determine the time interval between the deformed pulse waves. Algorithms based on finding the maximum (or the minimum) velocity of the pulse wave depend on the assumption that the sampling rate at which the images were taken is sufficiently high to accurately capture the peak of the wave. However, this assumption is not always fulfilled, which can lead to inaccurate results. Similar approach is to define the wave arrival moment as the time instant in which the wave reaches its mid-range value (the average of the minimum and the maximum value). Besides requiring the sufficient sampling rate to accurately determine the extreme positions of the wave, this approach can be influenced by turbulence in the aorta, which produces strange wave shapes and corrupts real extremes of the pulse wave. The experience has shown that the steepest slopes (especially, the upslope) are the wave characteristics that are the least influenced by the wave deformation [Dogui 11], resulting in the impulse representation of the pulse wave. The impulse representation can be intuitively defined as an impulse that best illustrates the start and end of the pulse wave, consisting of steepest slopes and a constant "base" value, where the intersection of the steepest slope

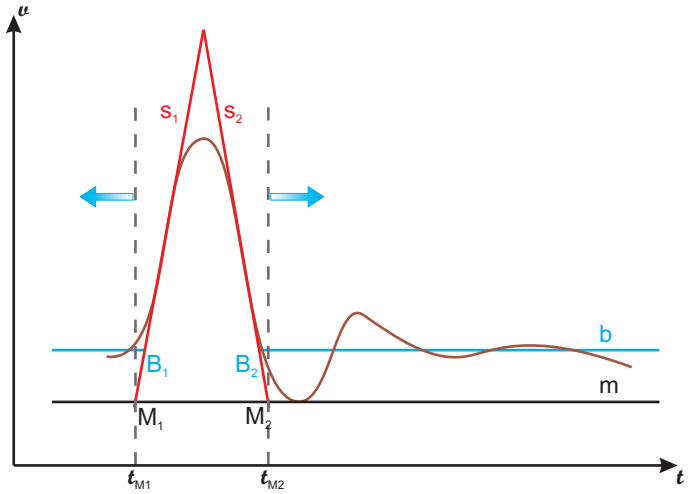

Figure 7.10: The impulse representation of the pulse wave. The wave minimum value m, the steepest slopes (s_1 and s_2) and their intersections M_1 and M_2 are determined. The base value b is the average of all samples outside the range of projected intersections (t_{M1} and t_{M2}). The impulse start instance B_1 is determined by an intersection of the first steepest slope s_1 and the base value b.

and the base value defines the starting point of the impulse (see Fig. 7.9). Obviously, the impulse start instant depends on the calculation of the base value, for which various approaches exist (e.g. some methods take the median value of the whole pulse wave or the average of a predefined number of its last samples). However, the listed approaches often highly depend on the number of total samples or the number of samples taken into account.

We propose a new approach to calculate the arrival time of the pulse wave. Our method uses the steepest slopes and introduces a novel approach for determining the base of the impulse representation. The steepest slopes are determined as the largest difference in consecutive wave values for the rising and the falling edge. We define the base of the impulse representation as the average value of all wave samples that do not belong to the range of the slopes, determined by intersections of the steepest slopes with the wave minimum (or the maximum) value (see Fig. 7.10). The algorithm starts by calculating the steepest slopes s_1, s_2 and the wave minimum value m. The average of all samples that are not in the interval of projected intersections of steepest slopes and

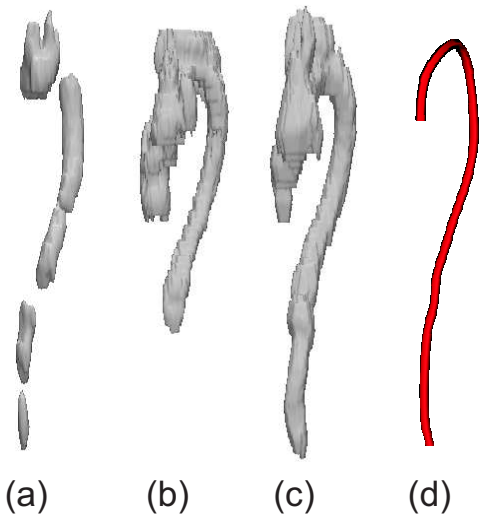

Figure 7.11: The segmentation and aortic centerline extraction of the HASTE MRI data. (a) MiaLite [Wang 11] (b) ITK-SNAP [Yushkevich 06], (c) robust statistics driven active contours from 3D Slicer [Gao 12], (d) our proposed centerline extraction method.

minimum value on the x axis (t_{M1} and t_{M2}) are used to obtain the base value b. The intersection of the first steepest slope s_1 and the base value b determines the impulse start instant B_1. Fig. 7.9 shows the obtained pulse waves at different aortic positions and their corresponding impulse representations. The time interval needed for the pulse wave to pass from one aortic position to another is determined as a time shift between the impulse representations of the corresponding pulse waves. A good property of our approach is its invariance to the number of wave samples, constituting a robust method for creating impulse representations. Another advantage of this method is that it uses both steepest slopes in the calculation, thus taking into account the deformation of the pulse wave during transition.

The last step of our proposed algorithm calculates the PWV values from obtained time intervals and lengths of aortic segments.

7.3 Results and discussion

In order to demonstrate the need for a robust centerline extraction method for HASTE MRI images, we compare the obtained centerline

with the results of various aorta segmentation methods, as shown in Fig. 7.11. The method of [Wang 11] (MiaLite application) is optimized for the segmentation of the abdominal aorta and uses a modified sparse field level set method, with a periodic monotonic speed function, resulting in coherent propagation of the contour boundary. Although the method is fast, the results are not satisfactory even with selecting six seed and blocking points. The resulting segmented aortic region is either not connected (see Fig. 7.11(a)) or "leaks" into neighboring regions. The ITK-SNAP application [Yushkevich 06] implements two well-known 3-D active contour segmentation methods: Geodesic Active Contours [Caselles 95] and Region Competition [Zhu 96]. The segmentation result obtained using ITK-SNAP in Fig. 7.11(b), shows an incomplete segmentation result of the aorta, although six seed points have been placed to cover each aortic region. Setting higher parameters for contour boundary movement created "leakages" (although smoothness parameter was increased to prevent leaking). The method of [Gao 12] (implemented in 3D Slicer) uses seed points to extract the local robust statistics to describe the object features. It evolves several active contours simultaneously with their interactions being motivated by the principles of action and reaction. With this principle the contours interact and converge to equilibrium at the desired positions of multiple objects. The segmentation result of this method depicted in Fig. 7.11(c), shows relatively small "leak" regions (however, the leak regions are large enough to influence accurate centerline calculation), where six seed points and fine contour parameter tuning were needed to obtain the segmentation. None of the described segmentation methods yield sufficiently good segmentation result for an accurate centerline extraction. Finally, Fig. 7.11(d) shows the aortic centerline extracted using our proposed method. The centerline is accurate due to positioning grid nodes to valid positions and interconnecting them.

We perform a sensitivity analysis by shifting the initial sampling grid by half of the grid size in x and y directions (see Fig. 7.12). The largest obtained difference in the aortic centerline length is 5.1mm (423.3mm compared to 428.4mm) in case the length of the whole aorta is measured, which is small enough, proving that the sufficiently dense sampling grid was used.

We compare the calculated lengths between the given aortic levels obtained using our method with the aortic lengths of manually determined centerlines by an expert (centerlines were drawn in the 3-D application of the Siemens MR workstation). The results presented

Figure 7.12: The obtained centerline in case of shifting the sampling grid by half of the grid size (red) compared with the originally obtained centerline (green). The lengths of the shown aortic centerlines are 423.3mm and 428.4mm, which yields the largest centerline length difference of 5.1mm.

in Table 7.1 show the average values and standard deviations for all 22 HASTE data sets. The results show good correspondence between measured and manually determined lengths, where the highest average difference of 7mm was obtained for the aortic segment between the descending and diaphragmal aorta, while the differences in lengths of other segments are significantly smaller.

We compare our modulus image segmentation results with the manually determined expert segmentation for images of the ascending aorta where phase-encoded motion artifacts were present. For this purpose we use the Dice coefficient [Dice 45], defined as :

$$s(A,B) = \frac{2|A \cap B|}{|A| + |B|}, \tag{7.5}$$

where one set represents the set of segmented pixels and the other one the set of ground truth pixels. The results of the comparison are given in Table 7.2 for 8 TrueFISP data sets containing severe phase-encoded motion artifacts in the region of the ascending aorta. High Dice coefficient values (all above 0.85, except one) indicate high accuracy of our segmentation method. The radius of the aorta was estimated through

Table 7.1: HASTE MRI centerline length comparison

Centerline lengths (mm)	mean	st. dev.
Asc-Desc manually det.	115.81	22.13
Asc-Desc our method	110.47	20.13
Desc-Diaph manually det.	107.13	17.08
Desc-Diaph our method	99.76	17.52
Diaph-Abd manually det.	173.22	19.23
Diaph-Abd our method	179.48	19.24

Table 7.2: The ascending level TrueFISP image segmentation under influence of phase-encoded motion artifacts. Comparison of the Dice coefficients, radii estimated from aortic areas of expert and our segmentation and the ratios of the given radii.

n	Dice	our r (mm)	expert r (mm)	r ratio
1.	0.91	16.43	17.79	0.92
2.	0.89	11.56	12.8	0.9
3.	0.93	15.8	16.9	0.93
4.	0.91	11.5	12.49	0.92
5.	0.64	15.17	16.62	0.91
6.	0.91	13.2	14.5	0.91
7.	0.86	11.86	13.54	0.87
8.	0.85	11.1	12.8	0.86

the calculated aortic area, where the circular aortic wall shape is assumed. The radii of the aorta calculated using our proposed method and the manual segmentation by an expert differ in approximately 1mm and the ratio of these values is almost constant in all examined cases. This makes it possible to estimate the radius measured by an expert by multiplying the radius value obtained using our algorithm with the average calculated ratio that equals 0.9 (this is possible even in the case of the lowest calculated Dice coefficient, since the ratio of radii in that case is 0.91). The aortic area and radii results obtained on the TrueFISP images of healthy volunteers are presented in Table 7.3 for all aortic levels. The results compare average values of aortic area a, circumference c and radii estimated from the aortic area r_a and circumference r_c. It should be noted that all values decrease from the ascending to the abdominal level, which is in accordance with the expected results, showing the correctness of the proposed segmentation method. The aortic region area and radii results obtained on modulus images of Marfan syndrome

Table 7.3: The segmentation of the aortic region for healthy volunteers. Comparison of measured areas, circumference and radii estimated from the area and the circumference.

Aortic level	a (mm^2)	c (mm)	r_a (mm)	r_c(mm)
Ascending	676.18	117.43	14.67	18.69
Descending	402.56	90.24	11.32	14.36
Diaphragmal	322.35	80.85	10.13	12.87
Abdominal	155.96	56.03	7.04	8.92

Table 7.4: The segmentation of the aortic region for Marfan syndrome patients. Comparison of measured areas, circumference and radii estimated from the area and the circumference.

Aortic level	a (mm^2)	c (mm)	r_a (mm)	r_c(mm)
Ascending	490.750	99.875	12.5	15.9
Descending	396.125	86.875	11.23	13.83
Diaphragmal	268.875	73.375	9.25	11.68
Abdominal	218.000	64.250	8.33	10.23

patients are presented in Table 7.4.

Finally, in order to validate the measured pulse wave velocities, we compare our PWV results to the validated software QFlow and an in-house developed and validated PWV calculation tool (LUMC, Leiden, Netherlands). The aortic centerlines of healthy volunteers (black-blood HASTE MRI images) were manually delineated by an expert in the 3-D application of the Siemens MR workstation. The expert used a few methods for the analysis of the pulse wave in the PWV tool application (see Section 7.2.4) in order to obtain the most realistic values of PWV. The comparison of obtained PWV values of 22 healthy volunteers for different aortic segments using the validated software and our application are presented in Table 7.5 with scatter plots in Fig. 7.13. The comparison of PWV results for 8 Marfan syndrome patients are presented in Table 7.6 with scatter plots in Fig. 7.14.

Our calculated PWV values correspond very well to the calculated PWV values of the validated software. Moreover, the calculated values fall inside the range of expected values of PWV for each of the aortic segments of healthy volunteers [Mattace-Raso 10], proving the correctness of the proposed method. The calculated PWV values for Marfan syndrome patients show higher values (in comparison to healthy volunteers) in the part of the aorta between descending and diaphrag-

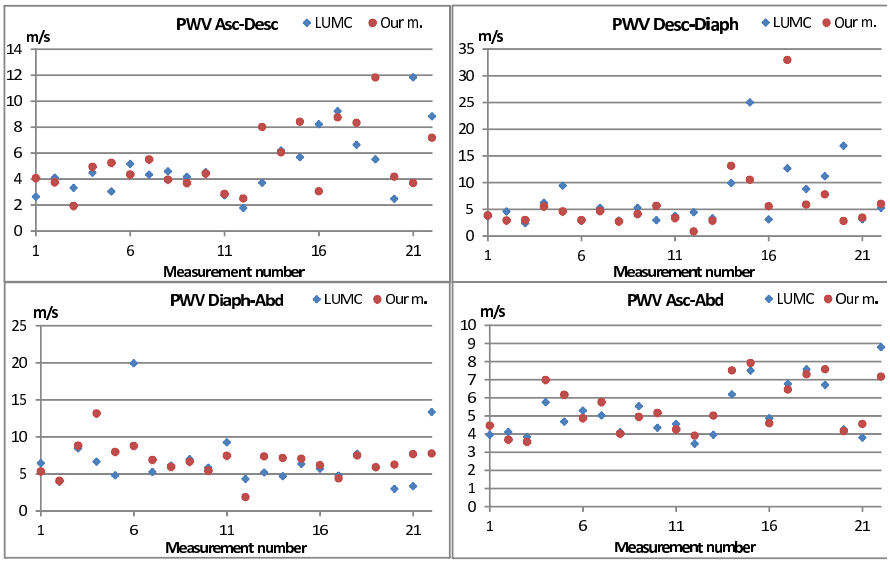

Figure 7.13: Results of PWV calculations on healthy volunteers for LUMC and our method for each of the aortic regions.

Table 7.5: Healthy volunteers PWV comparison

PWV (m/s)	mean	st. dev.
Asc-Desc LUMC	5.14	2.51
Asc-Desc our method	5.3	2.47
Desc-Diaph LUMC	6.92	5.55
Desc-Diaph our method	6.14	6.58
Diaph-Abd LUMC	6.71	3.69
Diaph-Abd our method	6.8	2.14
Asc-Abd LUMC	5.23	1.45
Asc-Abd our method	5.45	1.42

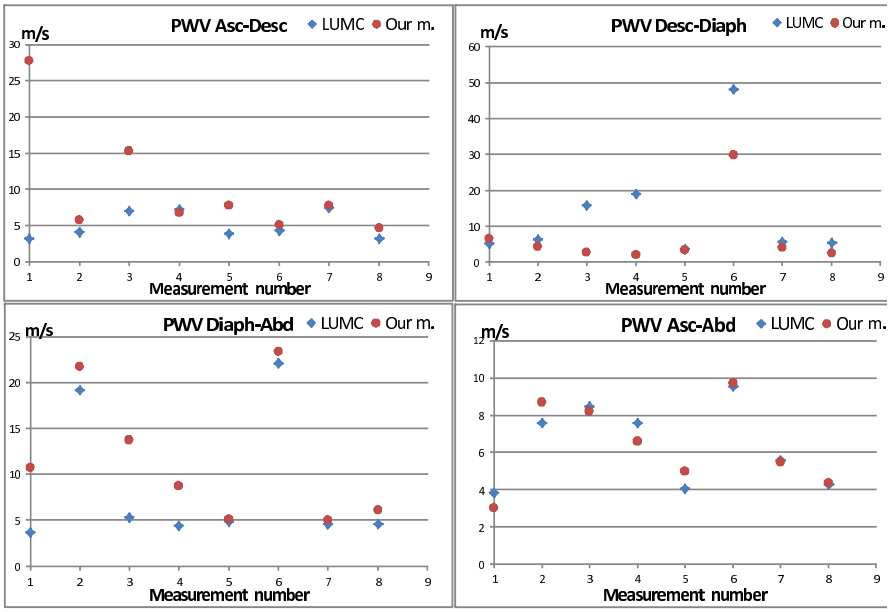

Figure 7.14: Results of Marfan Syndrome PWV calculations for LUMC and our method for each of the aortic regions.

mal level, as well as slightly higher values for the part of the aorta between diaphragmal and abdominal level. The expected PWV values for Marfan syndrome patients are higher than in the case of healthy volunteers [Hirata 91], which again verifies the correctness of the proposed method.

To determine the pulse wave propagation times, we use impulse representation method that takes into account both steepest slopes of the pulse wave (see Section 7.2.4). It is well known that the downslope (the second slope) of the pulse wave is often affected by wave reflections. However, this does not significantly affect the impulse modeling in our approach because the second slope of the impulse is only used to determine the range of values that are not included for calculation of the impulse representation base value. Independently of the quantity of wave reflections, the end of the second slope always defines the range of values where the wave goes into "relaxation", which is an important factor in the calculation of the impulse representation base value. The upslope (the first steepest slope) and the base value define the start of the modeled impulse, where the upslope is not significantly affected by reflected waves [Stevanov 01]. Hence, our proposed method of impulse

Table 7.6: Marfan syndrome PWV comparison

PWV (m/s)	mean	st. dev.
Asc-Desc LUMC	5.06	1.85
Asc-Desc our method	6.3	1.34
Desc-Diaph LUMC	13.66	14.96
Desc-Diaph our method	10.99	12.47
Diaph-Abd LUMC	8.58	7.47
Diaph-Abd our method	8.26	7.23
Asc-Abd LUMC	6.37	2.2
Asc-Abd our method	6.38	2.33

modeling is robust to wave reflections.

In our case the TrueFISP scans use a much shorter acquisition window than the acquisitions for phase-contrast images, which often implies that lumen area in modulus images is over-estimated. This can be observed by mapping the aortic regions of modulus images to the corresponding phase-contrast images. Hence, the aortic region in TrueFISP image needs to be slightly under-segmented (a smaller region needs to be taken into account) in order to map well to the aortic region in the phase-contrast image. This has been solved by our segmentation method using projections (line-shaped SEs) with selecting the most circular aortic region candidate as the final segmentation result (see Section 7.2.3). Due to the radial positioning of projections (line-shaped SEs) when observed from the currently processed pixel, our approach gives priority to circular objects while excluding its edges. This means that the obtained aortic region from the TrueFISP image is slightly under-segmented, which is a benefit when mapping to phase-contrast image for velocity calculation. This is supported by the measurements in Table 7.2, where the expert aortic region segmentation area is always slightly larger than in the case of our proposed method.

The performance of our algorithm was tested on a 2GHz CPU. The calculation of centerlines and the length measurement last approximately 1.5 minutes for the HASTE data set of dimensions $120\times180\times256$. The segmentation of modulus images depends on the size of the aortic region that is being segmented and the volume defined by the region of interest, lasting from 0.5 to 2 minutes (the average time is approximately 1.3 minutes) for series of forty slices (dimensions 192×256). Note that the segmentation can be performed in parallel for each aortic level, while the method would benefit from implementation on a graphics pro-

cessing unit (GPU). It should be emphasized that our algorithm and application are capable of processing aortic data sets consisting of an arbitrary number of CMR series with any plane position and orientation. For the future work, the method should be tested with intra-aortic catheterization procedure. Although the catheterization is considered the gold standard for validating the PWV, it can change cardiovascular conditions, since the subjects are sedated at that time. Another future possibility is to design an aortic phantom, where we would be able to control the important flow parameters.

7.4 Conclusion

We introduced in this chapter a novel tool for the aortic pulse wave velocity (PWV) measurements on magnetic resonance (MR) images. We have designed an effective segmentation and centerline extraction algorithm, with an optional use of a predefined aortic model. The segmentation of modulus aortic images is robust to intense phase-encoded motion artifacts. The extracted centerlines and segmented aortic regions were compared to the expert segmentation, proving the accuracy of our proposed methods. We introduced a novel method for analysis of the pulse wave by taking into account the steepest slopes and deformation of the pulse wave over time in order to obtain a robust automatic method. The pulse wave velocity measurement on 22 healthy volunteers shows good correspondence to the results obtained by validated PWV measurement software (QFlow and LUMC PWV tool). The calculated PWV values fall in the range of values that are expected in case of healthy volunteers. The PWV measurements on 8 Marfan syndrome patients also correspond to the measurements performed with the validated software, while showing other range of values compared to the healthy volunteers.

8

Conclusions

This thesis dealt with the analysis of cardiovascular images by developing segmentation and skeletonization methods for quantifying vascular structures and functions. The goal was to aid a physician in decision making for diagnostics and treatment of problems in connection to vascular structures: quantifying the aortic stiffness and accurate AVM decomposition for the embolization procedure. The main problem was finding an efficient way to accurately extract the clinically relevant information from vascular images.

In case of the aortic stiffness we needed to allow for pulse wave velocity and distensibility calculation (to estimate the aortic stiffness). We developed methods required to extract the aortic centerline and measure its length, to segment the aortic wall and analyze propagation of pulse waves. In case of the AVM decomposition we required methods for complete cerebral blood vessel tree analysis to aid in the AVM embolization procedure. The methods had to allow for segmentation of the cerebral blood vessels tree, extraction of vessel centerlines, calculating best paths through the vessel tree for different criteria and extracting the AVM region with its decomposition to arteries, veins and the nidus.

In Chapter 4 we introduced a novel method of generalized pixel profiling and comparative segmentation with an application to segmentation of 3-D CTA images of arteriovenous malformation. The experiments were conducted using circular RSEs, which proved promising for delineation of fine vessel structures in low resolution images. For validation purposes we created a digital 3-D phantom model of randomly intertwined tubular structure with varying radii to which noise and CT artifacts were added. The results on the phantom and real CTA data demonstrate the effectiveness of the proposed method, especially on low resolution images with high intensity variations. Using the presented

profiling method we have designed an application for segmenting the inner structure of the AVM. The obtained segmentation results gave a nice insight into the structure of the AVM, clearly delineating between feeding arteries, the draining vein and the nidus.

Besides the introduction of multiple operators, our novelty was the use of structuring elements (SE) controlled by two parameters. The main advantage of this approach was the possibility to create broader range of shapes. The (2-D) ring-shaped SE proved the best for fine delineation of AVM vessels when compared to other 2-D and 3-D SEs. That means that for the purpose of AVM segmentation, the 3-D analysis is not necessarily better than the 2-D approach. We concluded that this was because the 2-D ring-shaped SE contains less pixels than the other SEs. This means that constructing the SEs with even fewer pixels might be interesting in the future. The experiments using the 2-D SE showed that the direction of slice processing (transversal, sagittal or coronal) influences the result of the segmentation. The best results were obtained for slice-by-slice approach in transversal direction. This is the case because the resolution of typical 3-D CTA images is not isotropic. A 3-D CTA image is composed of 2-D transversal slices, which often differ from one another in terms of present artifacts, noise and signal level.

The number of pixels contained in the ring-shaped SE plays an important role also when the thickness (parameter n) is increased. This increases the outer radius of the SE. The results concur with our previous conclusions: the ring-shaped SE containing a smaller number of pixels is better for segmentation of fine details, but with lower robustness to noise. Therefore, the segmentation method using thicker SEs will be more robust to noise, but the resulting segmentation will be less detailed. In general, our conclusion is that larger SEs should be used for the segmentation of larger vessels (or those vessels where less detail is needed), while smaller SEs should be used for delineating between fine details in the segmentation.

In Chapter 5 we introduced line-shaped profiling with an application to segmentation of 3-D CTA images of brain blood vessels. The goal was to segment the cerebral blood vessel tree together with an AVM, while achieving high computational efficiency (which is reduced when multiscale SEs are used). The main novelty was the introduction of line-shaped SEs, which yields a multiorientation approach and significantly shortens execution times when compared to classical SE shapes. Another major novelty was the combination of base operators

to form more complex second order profile operators. Their strength comes from combining the use of both local proximate (close) and a wider neighborhood of the processed pixel. The results on phantom data sets for various noise and artifact levels showed high robustness of the proposed method. The validation was performed by comparison of the segmented AVM regions with the segmented images of the onyx cast after an embolization procedure. The obtained results on real CTA data are nicely smoothed vessels.

In some cases the difference between the highest and the lowest pixel gray values in the vessel region is too large (sometimes, the lowest gray values fall under 5% of the value of the highest gray values), and the vessels containing the lowest gray values do not get segmented. Although this happens only at the vessels with the low concentration of contrast agent (vessel structures that are most often no longer at the region of interest), the future work should be directed towards segmentation of all vessel structures.

In Chapter 6 we designed an effective inner AVM structure delineation method based on the ordered skeletonization principle. The goal was to classify vessels of an AVM into draining veins, feeding arteries and the nidus. We introduced an advanced method for distance calculation to obtain a higher accuracy of ordered skeletonization in terms of structure representation. Moreover, we proposed two approaches for creating a graph-type skeleton structure from skeletonized images and use advantages of these approaches to extract main AVM vessels. Using the proposed skeleton structures, we introduced a new method for automatic AVM detection and extraction. In order to extract the draining vein, we designed methods for determining the highest metric path in the skeleton graph and a stub link removal principle. Based on the delineated nidus and the draining vein, feeding arteries were extracted from the remaining part of the data set by the best path calculation. The AVM detection and delineation method was validated on three cases of cerebral vessels containing AVMs, where the onyx cast images were acquired after the embolization procedure. In each case, our method was able to accurately determine the position of the AVM with slightly over-estimating the AVM volume, which is needed for the vein extraction procedure.

For validating our vein extraction algorithm we generated three 3-D phantom data sets. Each phantom data set is comprised of the AVM phantom (generated as a tube intertwined in a random way, with randomly varying radii) and the vein phantom (constructed as a part of a

binary tree with the random branch distribution, shape and thickness). The vein model was merged with the AVM model to obtain a single vessel tree phantom. The results indicate high accuracy of our delineation method in terms of lengths and volumes of delineated vein. To demonstrate the robustness of our AVM and vein extraction approach, we performed the AVM delineation on real CTA data set segmented using three different segmentation algorithms. The results of this comparison showed high robustness of our method in terms of the Dice coefficient, calculated volume and the distance between the located AVM centers. The future work on the topic will be adjusting the algorithm for use on cerebral aneurysms.

In Chapter 7 we introduced a tool for the aortic pulse wave velocity (PWV) measurements on magnetic resonance (MR) images. The goal was to estimate aortic stiffness by analysis of CMR images. The main problem was that various image segmentation (and signal processing) methods had to be used to analyze the images. We have designed an effective segmentation and centerline extraction algorithm, with an optional use of a predefined aortic model. Our novel method for the segmentation of modulus aortic images is robust to intense phase-encoded motion artifacts. The extracted centerlines and segmented aortic regions were compared to the expert segmentation, proving the accuracy of our proposed methods. We introduced a novel method for analysis of the pulse wave by taking into account the steepest slopes and deformation of the pulse wave over time in order to obtain a robust automatic method. The results of pulse wave velocity measurement on 22 healthy volunteers show good correspondence to the results obtained by validated PWV measurement software (QFlow and LUMC PWV tool). The calculated PWV values fall in the range of values that are expected in case of healthy volunteers. Our results of PWV measurements on 8 Marfan syndrome patients also correspond to the measurements performed with the validated software, while showing other range of values compared to the healthy volunteers.

To summarize, this research has resulted in following main vessel analysis contributions:

1. The method of generalized profiling used for the detailed segmentation of arteriovenous malformations [Babin 12a].

2. The method of line-shaped profiles used for the segmentation of cerebral blood vessel system containing arteriovenous malformations [Babin 13b].

3. The vessel skeletonization method to automatically locate an AVM in the blood vessel tree and decompose it into constituting vessels (arteries, veins and the nidus) [Babin 13c, Babin 14].

4. The method for the aortic pulse wave flow analysis comprising of the method for segmentation of cardiac magnetic resonance images and the pulse wave analysis method [Babin 13a].

5. AVM and blood vessel tree phantoms used for validation of the segmentation and skeletonization results.

6. The aortic centerline extraction and segmentation method [Babin 12b, Babin 09b].

In terms of clinical use, the listed methods have been implemented for two cases:

1. The application for complete cerebral blood vessel tree analysis with an emphasis on aiding in the AVM embolization procedure. It performs extraction of the AVM region and decomposes it to its main vessels.

2. The application for aortic pulse wave velocity (PWV) and aortic distensibility calculation to estimate stiffness of the aorta.

In terms of publications, so far this work resulted in two A1-publications [Babin 12a, Babin 13b], with three other A1-papers that are currently in review: [Babin 13c, Babin 13a, Devos 13]. Next to that, six publications were published in the proceedings of international peer-reviewed conferences: [Babin 08, Babin 09b, Babin 10, Babin 11c, Babin 12b, De Vylder 12] and three publications and abstracts in national conferences [Babin 09a, Babin 11a, Babin 11b].

Bibliography

[Abdul-Karim 03] M. Abdul-Karim, K. Al-Kofahi, E. B. Brown, R. K Jain & B. Roysam. *Automated tracing and change analysis of angiogenic vasculature from in vivo multiphoton confocal image time series*. Microvascular Research, vol. 66, no. 2, pages 113–125, 2003.

[Abeysinghe 09] S. Abeysinghe & T. Ju. *Interactive skeletonization of intensity volumes*. The Visual Computer, vol. 25, pages 627–635, 2009.

[Ahuja 97] N. Ahuja & Jen-Hui Chuang. *Shape representation using a generalized potential field model*. Pattern Analysis and Machine Intelligence, IEEE Transactions on, vol. 19, no. 2, pages 169–176, feb 1997.

[Al-Diri 09] B. Al-Diri, A. Hunter & D. Steel. *An Active Contour Model for Segmenting and Measuring Retinal Vessels*. Medical Imaging, IEEE Transactions on, vol. 28, no. 9, pages 1488–1497, sept. 2009.

[Al-Kofahi 02] K.A. Al-Kofahi, S. Lasek, D.H. Szarowski, C.J. Pace, G. Nagy, J.N. Turner & B. Roysam. *Rapid automated three-dimensional tracing of neurons from confocal image stacks*. Information Technology in Biomedicine, IEEE Transactions on, vol. 6, no. 2, pages 171–187, june 2002.

[Al-Rawi 07] M. Al-Rawi, M. Qutaishat & M. Arrar. *An improved matched filter for blood vessel detection of digital retinal images*. Computers in Biology and Medicine, vol. 37, no. 2, pages 262–267, 2007.

[Antiga 06] L. Antiga & D.A. Steinman. *VMTK - Vascular modeling toolkit*. URL http://www. vmtk. org, vol. na, pages nn–nn, 2006.

[Antunez 08] E. Antunez & L. Guibas. *Robust extraction of 1D skeletons from grayscale 3D images.* In Pattern Recognition, 2008. ICPR 2008. 19th International Conference on, pages 1–4, dec 2008.

[Aylward 96] S. Aylward, E. Bullitt, S. Pizer & D. Eberly. *Intensity ridge and widths for tubular object segmentation and description.* In Mathematical Methods in Biomedical Image Analysis, 1996., Proceedings of the Workshop on, pages 131–138, jun 1996.

[Babin 08] D. Babin, J. De Bock, A. Pižurica & W. Philips. *The shortest path calculation between points of interest in 3-D MRI images of blood vessels.* In Annual Workshop on Semiconductor Advances for Future Electronics and sensors, 11th, Proceedings, pages 295–298. STW Technology Foundation, 2008.

[Babin 09a] D. Babin, A. Pižurica & W. Philips. *Length measurement of abdominal blood vessels through segmentation and skeletonization.* In Proceedings of the PhD symposium 2009, Ghent, Belgium, 2009.

[Babin 09b] D. Babin, E. Vansteenkiste, A. Pižurica & W. Philips. *Segmentation and length measurement of the abdominal blood vessels in 3-D MRI images.* In Proc. Annual Int. Conf. of the IEEE Engineering in Medicine and Biology Society EMBC 2009, pages 4399–4402, 2009.

[Babin 10] D. Babin, E. Vansteenkiste, A. Pižurica & W. Philips. *Segmentation of airways in lungs using projections in 3-D CT angiography images.* In IEEE Engineering in Medicine and Biology Society Conference Proceedings, pages 3162–3165. IEEE, 2010.

[Babin 11a] D. Babin, A. Pižurica & W. Philips. *Robust segmentation methods for aortic pulse wave velocity measurement.* In IEEE EMBS Benelux Chapter, Annual symposium, Abstracts (2011), 2011.

[Babin 11b] D. Babin, A. Pižurica & W. Philips. *Segmentation of abdominal aorta for pulse wave velocity calculation.* In

Proceedings of the PhD symposium 2011, Ghent, Belgium, 2011.

[Babin 11c] D. Babin, E. Vansteenkiste, A. Pižurica & W. Philips. *Segmentation of brain blood vessels using projections in 3-D CT angiography images.* In 2011 33rd Annual International Conference of the IEEE Engineering in Medicine and Biology Society, pages 8475–8478. IEEE, 2011.

[Babin 12a] D. Babin, A. Pižurica, R. Bellens, J. De Bock, Y. Shang, B. Goossens, E. Vansteenkiste & W. Philips. *Generalized Pixel Profiling and Comparative Segmentation With Application to Arteriovenous Malformation Segmentation.* Medical Image Analysis, Elsevier, vol. 16, no. 5, pages 991–1002, 2012.

[Babin 12b] D. Babin, E. Vansteenkiste, A. Pižurica & W. Philips. *Centerline calculation for extracting abdominal aorta in 3-D MRI images.* In 2012 34th Annual International Conference of the IEEE Engineering in Medicine and Biology Society, pages 3982–3985. IEEE, 2012.

[Babin 13a] D. Babin, D. Devos, A. Pižurica, J. Westenberg, E. Vansteenkiste & W. Philips. *Robust segmentation methods with an application to aortic pulse wave velocity calculation.* Submitted to: Computerized Medical Imaging and Graphics, 2013.

[Babin 13b] D. Babin, A. Pižurica, J. De Vylder, E. Vansteenkiste & W. Philips. *Brain blood vessel segmentation using line-shaped profiles.* Accepted for publication in: Physics in Medicine and Biology, 2013.

[Babin 13c] D. Babin, A. Pižurica, J. De Vylder, E. Vansteenkiste & W. Philips. *Skeletonization method for vessel delineation of arteriovenous malformation.* Submitted to: Medical Image Analysis, 2013.

[Babin 14] D. Babin, M. Spyrantis, A. Pižurica & W. Philips. *Skeleton calculation for automatic extraction of arteriovenous malformation in 3-D CTA images.* In Sub-

mitted to: 2014 IEEE International Symposium on Biomedical Imaging, page nn, 2014.

[Bellens 08] R. Bellens, S. Gautama, L. Martinez-Fonte, W. Philips, J. C.-W. Chan & F. Canters. *Improved Classification of VHR Images of Urban Areas Using Directional Morphological Profiles*. IEEE Transactions on Geoscience and Remote Sensing, vol. 46, no. 10, pages 2803–2813, 2008.

[Benediktsson 03] J. A. Benediktsson, M. Pesaresi & K. Amason. *Classification and feature extraction for remote sensing images from urban areas based on morphological transformations*. IEEE Transactions on Geoscience and Remote Sensing, vol. 41, no. 9, pages 1940–1949, 2003.

[Benediktsson 05] J. A. Benediktsson, J. A. Palmason & J. R. Sveinsson. *Classification of hyperspectral data from urban areas based on extended morphological profiles*. IEEE Transactions on Geoscience and Remote Sensing, vol. 43, no. 3, pages 480–491, 2005.

[Berger 08] M. Berger, R. Anxionnat, E. Kerrien, L. Picard & M. Söderman. *A methodology for validating a 3D imaging modality for brain AVM delineation: application to 3DRA*. Computerized Medical Imaging and Graphics, vol. 32, no. 7, pages 544–553, 2008.

[Blum 67] H. Blum*et al.* *A transformation for extracting new descriptors of shape*. Models for the perception of speech and visual form, vol. 19, no. 5, pages 362–380, 1967.

[Boese 00] J.M. Boese, M. Bock, S.O. Schoenberg & L.R. Schad. *Estimation of aortic compliance using magnetic resonance pulse wave velocity measurement*. Physics in medicine and biology, vol. 45, no. 6, pages 1703–1713, 2000.

[Bombardier 97] V. Bombardier, M.-C. Jaulent, A. Bubel & J. Bremont. *Cooperation of two fuzzy segmentation operators for digital substract angiograms analysts*. In Fuzzy Systems, 1997., Proceedings of the Sixth IEEE International Conference on, volume 2, pages 1057–1062, jul 1997.

[Bouchet 07] A. Bouchet, J. Pastore & V. Ballarin. *Segmentation of medical images using Fuzzy Mathematical Morphology.* Journal of Computer Science & Technology, vol. 7, no. 3, pages 256–262, 2007.

[Brandts 09] A. Brandts, S. van Elderen, J.J.M. Westenberg, J. van der Grond, M.A. van Buchem, M.V. Huisman, L. Kroft, J. Tamsma & A. de Roos. *Association of Aortic Arch Pulse Wave Velocity with Left Ventricular Mass and Lacunar Brain Infarcts in Hypertensive Patients: Assessment with MR Imaging.* Radiology, vol. 253, no. 3, pages 681–688, 2009.

[Brink 96] A. D. Brink & N. E. Pendock. *Minimum cross-entropy threshold selection.* Pattern Recognition, Elsevier, vol. 29, pages 179–188, 1996.

[Bühler 02] K. Bühler, P. Felkel & A. La Cruz. *Geometric Methods for Vessel Visualization and Quantification–A Survey.* In In Geometric Modelling for Scientific Visualization. Citeseer, 2002.

[Bullitt 01] E. Bullitt, S. Aylward, E. Bernard & G. Gerig. *Computer-Assisted Visualization of Arteriovenous Malformations on the Home PC.* Neurosurgery, vol. 48, pages 576–583, 2001.

[Bullitt 02] E. Bullitt & S. Aylward. *Patient-specific vascular models for endovascular and open operative procedures.* International Congress Series, vol. 1247, no. 0, pages 129–138, 2002.

[Bushberg 11] J.T. Bushberg. The essential physics of medical imaging. Lippincott Williams & Wilkins, 2011.

[Carrillo 05] J. Carrillo, M. Orkisz & M. Hoyos. *Extraction of 3D Vascular Tree Skeletons Based on the Analysis of Connected Components Evolution.* In Andra Gagalowicz & Wilfried Philips, editeurs, Computer Analysis of Images and Patterns, volume 3691 of *Lecture Notes in Computer Science*, pages 604–611. Springer Berlin, Heidelberg, 2005.

[Caselles 95] V. Caselles, R. Kimmel & G. Sapiro. *Geodesic active contours*. In Proc. Conf. Fifth Int Computer Vision, pages 694–699, 1995.

[Castro 07] M. A. Castro & J. R. Cebral. *Computational Fluid Dynamics Modeling of Intracranial Aneurysms: Effect of Parent Artery Segmentation on Intra-Aneurysmal Hemodynamics*. American Journal of Neuroradiology, vol. 27, pages 1703–1709, 2007.

[Cebral 05] J. R. Cebral, M. A. Castro, S. Appanaboyina, C. M. Putman, D. Millan & A. F. Frangi. *Efficient Pipeline for Image-Based Patient-Specific Analysis of Cerebral Aneurysm Hemodynamics: Technique and Sensitivity*. IEEE Transactions on Medical Imaging, vol. 24, no. 4, pages 457–467, 2005.

[Chan 00] R.C. Chan, W.C. Karl & R.S. Lees. *A new model-based technique for enhanced small-vessel measurements in X-ray cine-angiograms*. Medical Imaging, IEEE Transactions on, vol. 19, no. 3, pages 243–255, march 2000.

[Chang 07] S. Chang. *Extracting Skeletons from Distance Maps*. International Journal of Computer Science and Network Security, vol. 7, no. 7, pages 213–219, 2007.

[Cheng 00] F. Cheng & A.N. Venetsanopoulos. *Adaptive Morphological Operators, Fast Algorithms and Their Applications*. Pattern Recognition, Elsevier, vol. 33, pages 917–933, 2000.

[Chillet 03] D. Chillet, J. Jomier, D. Cool & S. Aylward. *Vascular Atlas Formation Using a Vessel-to-Image Affine Registration Method*. In Medical Image Computing and Computer-Assisted Intervention - MICCAI 2003, volume 2878 of *Lecture Notes in Computer Science*, pages 335–342. Springer Berlin / Heidelberg, 2003.

[Choi 97] H.I. Choi, S.W. Choi & H.P. Moon. *Mathematical theory of medial axis transform*. Pacific J. Math, vol. 181, no. 1, pages 57–88, 1997.

[Chuang 00] J.-H. Chuang, C.-H. Tsai & M.-C. Ko. *Skeletonisation of three-dimensional object using generalized potential*

field. Pattern Analysis and Machine Intelligence, IEEE Transactions on, vol. 22, no. 11, pages 1241–1251, nov 2000.

[Chung 99] A. C. S. Chung & J. A. Noble. *Statistical 3D vessel segmentation using a Rician distribution*. Medical image computing and computer-assisted intervention: MICCAI '99. Lecture Notes in Computer Science, Berlin, Germany: Springer-Verlag, vol. 1679, pages 82–89, 1999.

[Chwialkowski 96] M. P. Chwialkowski, Y. M. Ibrahim, H. F. Li & R. M. Peshock. *A method for fully automated quantitative analysis of arterial flow using flow-sensitized MR images*. Computerized Medical Imaging and Graphics, vol. 20, no. 5, pages 365–378, 1996.

[Coenen 05] V.A. Coenen, S. Dammert, M.H.T. Reinges, M. Mull, J.M. Gilsbach & V. Rohde. *Image-guided Microneurosurgical Management of Small Cerebral Arteriovenous Malformations: The Value of Navigated Computed Tomographic Angiography*. International Neuroradiology, Springer Berlin, vol. 47, pages 66–72, 2005.

[Cool 03] D. Cool, D. Chillet, J. Kim, J.-P. Guyon, M. Foskey & S. Aylward. *Tissue-Based Affine Registration of Brain Images to form a Vascular Density Atlas*. In Medical Image Computing and Computer-Assisted Intervention - MICCAI 2003, volume 2879, pages 9–15. Springer Berlin / Heidelberg, 2003.

[Cornea 05] N.D. Cornea, D. Silver, X. Yuan & R. Balasubramanian. *Computing hierarchical curve-skeletons of 3D objects*. The Visual Computer, vol. 21, pages 945–955, 2005.

[Coste 01] E. Coste, D. Gibon, X. Leclercq, B. Verdonck, C. Vausseur & J. Rousseau. *3D reconstruction of the encapsulating contour of arteriovenous malformations for radiosurgery using digital subtraction angiography*. International Journal of Radiation Oncology, Biol. Phys., Elsevier, vol. 50, no. 1, pages 247–255., 2001.

[Cremers 07] D. Cremers, M. Rousson & R. Deriche. *A Review of Statistical Approaches to Level Set Segmentation: Integrating Color, Texture, Motion and Shape*. International Journal of Computer Vision, vol. 72, pages 195–215, 2007.

[De Bock 05] J. De Bock, P. De Smet & W. Philips. *Image segmentation using watersheds and normalized cuts*. In Proc. SPIE 5675, volume 164, 2005.

[De Bock 10] J. De Bock & W. Philips. *Fast and memory efficient 2D connected components using linked lists of line segments*. IEEE Transactions on Image Processing, vol. 19, pages 3222–3231, 2010.

[De Vylder 12] J. De Vylder, J. Aelterman, D. Babin, M. Vandewoestyne, T. Lepez, D. Deforce & W. Philips. *A novel dictionary based detection method for cell nuclei*. In 34th Annual International Conference of the Engineering in Medicine and Biology Society, Abstracts (2012), 2012.

[Deschamps 04] T. Deschamps, P. Schwartz, D. Trebotich, P. Colella, D. Saloner & R. Malladi. *Vessel segmentation and blood flow simulation using Level-Sets and Embedded Boundary methods*. International Congress Series, vol. 1268, no. 0, pages 75–80, 2004.

[Devos 13] D. Devos, E. Rietzschel, C. Heyse, P. Vandemaele, S. Huybrecht, S. Vermeersch, D. Babin, P. Segers, J. Westenberg & E. Achten. *MR Pulse Wave Velocity increases with age faster in the thoracic aorta than in the abdominal aorta*. Submitted to: Journal of Cardiovascular Magnetic Resonance, 2013.

[Dice 45] L. R. Dice. *Measures of the Amount of Ecologic Association Between Species*. Ecology, vol. 26, no. 3, pages 297–302, 1945.

[Dijkstra 59] E. W. Dijkstra. *A note on two problems in connection with graphs*. Numerische Mathematik, vol. 1, pages 269–271, 1959.

[Dogui 11] A. Dogui, A. Redheuil, M. Lefort, A. DeCesare, N. Kachenoura, A. Herment & E. Mousseaux. *Measurement of aortic arch pulse wave velocity in cardiovascular MR: Comparison of transit time estimators and description of a new approach*. Journal of Magnetic Resonance Imaging, vol. 33, no. 6, pages 1321–1329, 2011.

[Dokladal 99] P. Dokladal, C. Lohou, L. Perroton & G. Bertrand. *A New Thinning Algorithm and Its Application to Extraction of Blood Vessels*, 1999.

[Eberly 94] D. Eberly, R. Gardner, B. Morse, S. Pizer & C. Scharlach. *Ridges for image analysis*. Journal of Mathematical Imaging and Vision, vol. 4, pages 353–373, 1994.

[Fetics 99] B. Fetics, E. Nevo, C.-H. Chen & D.A. Kass. *Parametric model derivation of transfer function for noninvasive estimation of aortic pressure by radial tonometry*. Biomedical Engineering, IEEE Transactions on, vol. 46, no. 6, pages 698–706, 1999.

[Fielden 08] S.W. Fielden, B.K. Fornwalt, M. Jerosch-Herold, R.L. Eisner, A.E. Stillman & J.N. Oshinski. *A new method for the determination of aortic pulse wave velocity using cross-correlation on 2D PCMR velocity data*. Journal of Magnetic Resonance Imaging, vol. 27, no. 6, pages 1382–1387, 2008.

[Florez-Valencia 06] L. Florez-Valencia, J. Azencot, F. Vincent, M. Orkisz & I.E. Magnin. *Segmentation and Quantification of Blood Vessels in 3D Images using a Right Generalized Cylinder State Model*. In Image Processing, 2006 IEEE International Conference on, pages 2441–2444, oct. 2006.

[Florin 06] C. Florin, N. Paragios & J. Williams. *Globally Optimal Active Contours, Sequential Monte Carlo and On-Line Learning for Vessel Segmentation*. In Computer Vision, ECCV 2006, volume 3953 of *Lecture Notes in Computer Science*, pages 476–489. Springer Berlin / Heidelberg, 2006.

[Forkert 09] N.D. Forkert, D. S´aring, K. Wenzel, T. Illies, J. Fiehler & H. Handels. *Fuzzy-Based Extraction of Vascular Structures from Time-of-Flight MR Images*. Medical Informatics in a United and Healthy Europe, IOS Press, vol. 150, pages 816–820, 2009.

[Forkert 11] N. D. Forkert, D. Säring, T. Illes, J. Fiehler, J. Ehrardt, H. Handels & A. Schmidt-Richberg. *Direction-dependent Level Set Segmentation of cerebrovascular Structures*. In Progress in biomedical optics and imaging, volume 12, 2011.

[Forkert 12] N.D. Forkert, J. Fiehler, T. Illies, D.P.F. Mäller, H. Handels & D. Säring. *4D blood flow visualization fusing 3D and 4D MRA image sequences*. Journal of Magnetic Resonance Imaging, vol. 36, pages 443–453, 2012.

[Fouard 04] C. Fouard, E. Cassot, G. Malandain, C. Mazel, S. Prohaska, D. Asselot, M. Westerhoff & J.P. Marc-Vergnes. *Skeletonization by blocks for large 3D datasets: application to brain microcirculation*. In Biomedical Imaging: Nano to Macro, 2004. IEEE International Symposium on, volume 1, pages 89–92, april 2004.

[Frangi 98] A.F. Frangi, W. Niessen, K. L. Vincken & M. Viergever. *Multiscale vessel enhancement filtering*. In Medical Image Computing and Computer-Assisted Interventation-MICCAI'98, pages 130–137. Springer-Verlag, 1998.

[Friedlander 07] R.M. Friedlander. *Arteriovenous malformations of the brain*. New England Journal of Medicine, vol. 356, no. 26, pages 2704–2712, 2007.

[Gagvani 99] N. Gagvani & D. Silver. *Parameter-Controlled Volume Thinning*. Graphical Models and Image Processing, vol. 61, no. 3, pages 149–164, 1999.

[Gao 12] Y. Gao, R. Kikinis, S. Bouix, M. Shenton & A. Tannenbaum. *A 3D Interactive Multi-object Segmentation Tool using Local Robust Statistics Driven Active Contours*. Medical Image Analysis, vol. 16, pages 1216–1227, 2012.

[Gatehouse 05] P.D. Gatehouse, J. Keegan, L. A. Crowe, S. Masood, R.H. Mohiaddin, K.-F. Kreitner & D.N. Firmin. *Applications of phase-contrast flow and velocity imaging in cardiovascular MRI.* European radiology, vol. 15, no. 10, pages 2172–2184, 2005.

[Gerig 93] G. Gerig, T. Koller, G. Székely, C. Brechbühler & O. Kübler. *Symbolic description of 3-D structures applied to cerebral vessel tree obtained from MR angiography volume data.* In Harrison Barrett & A. Gmitro, editeurs, Information Processing in Medical Imaging, volume 687 of *Lecture Notes in Computer Science*, pages 94–111. Springer Berlin / Heidelberg, 1993.

[Giri 07] S.S. Giri, Y. Ding, Y. Nishijima, A. Pedraza-Toscano, P.M. Burns, R.L. Hamlin & O.P. Simonetti. *Automated and accurate measurement of aortic pulse wave velocity using magnetic resonance imaging.* In Computers in Cardiology, 2007, pages 661–664, oct 2007.

[Groenink 98] M. Groenink, A. de Roos, B. J. M. Mulder, J. A. E. Spaan & E.E. van der Wall. *Changes in aortic distensibility and pulse wave velocity assessed with magnetic resonance imaging following beta-blocker therapy in the marfan syndrome.* The American Journal of Cardiology, vol. 82, no. 2, pages 203–208, 1998.

[Grotenhuis 09] H.B. Grotenhuis, J.J.M. Westenberg, P. Steendijk, R.J. van der Geest, J. Ottenkamp, J.J. Bax, J. W. Jukema & A. de Roos. *Validation and reproducibility of aortic pulse wave velocity as assessed with velocity-encoded MRI.* Journal of Magnetic Resonance Imaging, vol. 30, no. 3, pages 521–526, 2009.

[Gupta 08] R. Gupta, A.C. Cheung, S.H. Bartling, J. Lisauskas, M. Grasruck, C. Leidecker, B. Schmidt, T. Flohr & T.J. Brady. *Flat-Panel Volume CT: Fundamental Principles, Technology, and Applications.* Radiographics, vol. 28, no. 7, pages 2009–2022, 2008.

[Hanger 01] C.C. Hanger, S.T. Haworth, R.C. Molthen & C.A. Dawson. *Semiautomated skeletonization of the pulmonary*

arterial tree in micro-CT images. In Society of Photo-Optical Instrumentation Engineers (SPIE) Conference Series, volume 4321 of *Society of Photo-Optical Instrumentation Engineers (SPIE) Conference Series*, pages 510–516, may 2001.

[Haris 98] K. Haris, S. N. Efstratiadis, N. Maglaveras & A. K. Katsaggelos. *Hybrid Image Segmentation Using Watersheds and Fast Region Merging.* IEEE Transactions on Image Processing, vol. 7, no. 12, pages 1684–1699, 1998.

[Haris 01] K. Haris, S. Efstratiadis, N. Maglaveras, J. Gourassas & G. Louridas. *Artery skeleton extraction using topographic and connected component labeling.* In Image Processing, 2001. Proceedings. 2001 International Conference on, volume 2, pages 339–342, oct 2001.

[Hassouna 07] M.S. Hassouna & A.A. Farag. *On the Extraction of Curve Skeletons using Gradient Vector Flow.* In Computer Vision, 2007. ICCV 2007. IEEE 11th International Conference on, pages 1–8, oct. 2007.

[Herment 10] A. Herment, N. Kachenoura, M. Lefort, M. Bensalah, A. Dogui, F. Frouin, E. Mousseaux & A. De Cesare. *Automated segmentation of the aorta from phase contrast MR images: Validation against expert tracing in healthy volunteers and in patients with a dilated aorta.* Journal of Magnetic Resonance Imaging, vol. 31, no. 4, pages 881–888, 2010.

[Hernandez 07] M. Hernandez & A. F. Frangi. *Non-parametric geodesic active regions: Method and evaluation for cerebral aneurysms segmentation in 3DRA and CTA.* Medical Image Analysis, vol. 11, no. 3, pages 224–241, 2007.

[Hernelahti 05] M. Hernelahti, H.O. Tikkanen, J. Karjalainen & U.M. Kujala. *Muscle Fiber-Type Distribution as a Predictor of Blood Pressure A 19-Year Follow-Up Study.* Hypertension, vol. 45, no. 5, pages 1019–1023, 2005.

[Hilditch 69] C. J. Hilditch. *Linear skeletons from square cupboards.* Machine inteligence, Edinburgh University Press, vol. 4, pages 403–420, 1969.

[Hirata 91] K. Hirata, F. Triposkiadis, E. Sparks, J. Bowen, C. F Wooley & H. Boudoulas. *The Marfan syndrome: abnormal aortic elastic properties.* Journal of the American College of Cardiology, vol. 18, no. 1, pages 57–63, 1991.

[Hirata 06] K. Hirata, M. Kawakami & M.F. O'Rourke. *Pulse wave analysis and pulse wave velocity: a review of blood pressure interpretation 100 years after Korotkov.* Circulation journal : official journal of the Japanese Circulation Society, vol. 70, pages 1231–1239, 2006.

[Hoi 04] Y. Hoi, H. Meng, S. H. Woodward, B. R. Bendok, R. A. Hanei, L. R. Guterman & L. N. Hopkins. *Effects of arterial geometry on aneurysm growth: three dimensional computational fluid dynamics study.* J Neurosurg., vol. 101, pages 676–681, 2004.

[Hoover 00] A. D. Hoover, V. Kouznetsova & M. Goldbaum. *Locating blood vessels in retinal images by piecewise threshold probing of a matched filter response.* IEEE Transactions on Medical Imaging, vol. 19, no. 3, pages 203–210, 2000.

[Horváth 10] I. Horváth, Á. Németh, Zs. Lenkey, N. Alessandri, F. Tufano, P. Kis, B. Gaszner & A. Cziráki. *Invasive validation of a new oscillometric device (Arteriograph) for measuring augmentation index, central blood pressure and aortic pulse wave velocity.* Journal of Hypertension, vol. 28, no. 10, pages 2068–2075, 2010.

[Hristov 11] D. Hristov, L. Liu, J. R. Adler, I. C. Gibbs, T. Moore, M. Sarmiento, S.D. Chang, R. Dodd, M. Marks & H. M. Do. *Technique for Targeting Arteriovenous Malformations Using Frameless Image-Guided Robotic Radiosurgery.* International Journal of Radiation Oncology, Biol. Phys., Elsevier, vol. 79, no. 4, pages 1232–1240, 2011.

[Huang 06] S. Huang & E. Zhang. *A Method for Segmentation of Retinal Image Vessels.* In The Sixth World Congress on Intelligent Control and Automation, WCICA 2006., volume 2, pages 9673–9676, 2006.

[Ibrahim 10] E.-S. Ibrahim, K. Johnson, A. Miller, J. Shaffer & R. White. *Measuring aortic pulse wave velocity using high-field cardiovascular magnetic resonance: comparison of techniques*. Journal of Cardiovascular Magnetic Resonance, vol. 12, no. 1, pages 26–26, 2010.

[Iyer 05] N. Iyer, S. Jayanti, K. Lou, Y. Kalyanaraman & K. Ramani. *Three-dimensional shape searching: state-of-the-art review and future trends*. Computer-Aided Design, vol. 37, no. 5, pages 509–530, 2005.

[Jackowski 05] M. Jackowski, X. Papademetris, L. Dobrucki, A. Sinusas & L. Staib. *Characterizing Vascular Connectivity from microCT Images*. In James Duncan & Guido Gerig, editeurs, Medical Image Computing and Computer-Assisted Intervention MICCAI 2005, volume 3750 of *Lecture Notes in Computer Science*, pages 701–708. Springer Berlin / Heidelberg, 2005.

[Jang 01] J.-H. Jang & K.-S. Hong. *A pseudo-distance map for the segmentation-free skeletonization of gray-scale images*. In Computer Vision, 2001. ICCV 2001. Proceedings. Eighth IEEE International Conference on, volume 2, pages 18–23, 2001.

[Jang 02] J.-H. Jang & K.-S. Hong. *Detection of curvilinear structures and reconstruction of their regions in gray-scale images*. Pattern Recognition, vol. 35, no. 4, pages 807–824, 2002.

[Jiang 03] X. Jiang & D. Mojon. *Adaptive local thresholding by verification-based multithreshold probing with application to vessel detection in retinal images*. IEEE Transactions on Pattern Analysis and Machine Intelligence, vol. 25, no. 1, pages 131–137, 2003.

[Jiang 10] J. Jiang, P. Trundle & J. Ren. *Medical image analysis with artificial neural networks*. Computerized Medical Imaging and Graphics, vol. 34, no. 8, pages 617–631, 2010.

[Kalitzin 02] S. N. Kalitzin, J. Staal, B. M. ter Haar Romeny & M.A. Viergever. *A Computational Method for Segmenting*

Topological Point-Sets and Application to Image Analysis. IEEE Transactions on Pattern Analysis and Machine Intelligence, vol. 23, no. 5, pages 447–459, 2002.

[Kanitsar 01] A. Kanitsar, D. Fleischmann, R. Wegenkittl, D. Sandner, P. Felkel & E. Groller. *Computed tomography angiography: a case study of peripheral vessel investigation*. In Visualization, 2001. VIS '01. Proceedings, pages 477–593, oct. 2001.

[Karger 96] D.R. Karger & C. Stein. *A new approach to the minimum cut problem*. J. ACM, vol. 43, no. 4, pages 601–640, jul 1996.

[Kass 88] M. Kass, A. Witkin & D. Terzopoulos. *Snakes: Active contour models*. International Journal of Computer Vision, vol. 1, pages 321–331, 1988.

[Kaus 04] M. R. Kaus, J. von Berg, J. Weese, W. Niessen & V. Pekar. *Automated segmentation of the left ventricle in cardiac MRI*. Medical Image Analysis, vol. 8, no. 3, pages 245–254, 2004.

[Kelly 01] R.P. Kelly, S.C. Millasseau, J.M. Ritter & P.J. Chowienczyk. *Vasoactive drugs influence aortic augmentation index independently of pulse-wave velocity in healthy men*. Hypertension, vol. 37, no. 6, pages 1429–1433, 2001.

[Kerrien 00] E. Kerrien. *Outils d'imagerie multimodalite pour la neuroradiologie interventionnelle*. PhD thesis, Loria, 2000.

[Kindlmann 06] G. Kindlmann, X. Tricoche & C.-F. Westin. *Anisotropy Creases Delineate White Matter Structure in Diffusion Tensor MRI*. In Rasmus Larsen, Mads Nielsen & Jon Sporring, editeurs, Medical Image Computing and Computer-Assisted Intervention, MICCAI 2006, volume 4190 of *Lecture Notes in Computer Science*, pages 126–133. Springer Berlin, Heidelberg, 2006.

[Kindlmann 07] G. Kindlmann, X. Tricoche & C.-F. Westin. *Delineating white matter structure in diffusion tensor MRI with anisotropy creases*. Medical Image Analysis, vol. 11, no. 5, pages 492–502, 2007.

[Kirbas 03] C. Kirbas & F.K.H. Quek. *Vessel extraction in medical images by 3D wave propagation and traceback.* In Bioinformatics and Bioengineering, 2003. Proceedings. Third IEEE Symposium on, pages 174–181, march 2003.

[Kirbas 04] C. Kirbas & F. K. H. Quek. *A review of vessel extraction techniques and algorithms.* ACM Computing Surveys, vol. 36, pages 81–121, 2004.

[Kittler 86] J. Kittler & J. Illingworth. *Minimum error thresholding.* Pattern Recognition, vol. 19, issue 1, pages 41–47, 1986.

[Klepac 06] S.R. Klepac & E.J. Samett. *Cardiac MRI–technical aspects primer.* emedicine from WebMD,(Jul. 2005), vol. n/a, page n/a, 2006.

[Klette 02] G. Klette. *Skeletons in Digital Image Processing.* Rapport technique, ResearchSpace@Auckland (New Zealand), 2002.

[Klette 06] G. Klette. *Branch Voxels and Junctions in 3D Skeletons.* In Ralf Reulke, Ulrich Eckardt, Boris Flach, Uwe Knauer & Konrad Polthier, editeurs, Combinatorial Image Analysis, volume 4040 of *Lecture Notes in Computer Science*, pages 34–44. Springer Berlin / Heidelberg, 2006.

[Kobashi 01] S. Kobashi, N. Kamiura, Y. Hata & F. Miyawaki. *Volume-quantization-based neural network approach to 3D MR angiography image segmentation.* Image and Vision Computing, vol. 19, no. 4, pages 185–193, 2001.

[Krissian 04] K. Krissian, R. Kikinis & C.F. Westin. *Algorithms for extracting vessel centerlines.* Rapport technique 3, Department of Radiology, Brigham and Women's Hospital, Harvard Medical School, Laboratory of Mathematics in Imaging, 2004.

[Kröner 12] E. Kröner, R. van der Geest, A. Scholte, P. van den Boogaard, D. Hendriksen, L. Kroft, M. Groenink, T. Radonic, J. Bax, A. de Roos, J. Reiber & J. Westenberg. *Evaluation of sampling density on the accuracy of aortic pulse wave velocity from velocity-encoded MRI in*

patients with Marfan syndrome. Journal of Cardiovascular Magnetic Resonance, vol. 36, no. 6, pages 1470–1476, 2012.

[Kwong 06] R.Y. Kwong. Cardiovascular magnetic resonance imaging. Springer, 2006.

[Ladak 01] H. M. Ladak, J. B. Thomas, J. R. Mitchell, B. K. Rutt & D. A. Steinman. *A semi-automatic technique for measurement of arterial wall from black blood MRI.* Medical Physics, vol. 28, pages 1098–1107, jun 2001.

[Lasch 06] P. Lasch, M. Diem, W. Hansch & D. Naumann. *Artificial neural networks as supervised techniques for FT-IR microspectroscopic imaging.* Journal of Chemometrics, vol. 20, no. 5, pages 209–220, 2006.

[Laurent 01] S. Laurent, P. Boutouyrie, R. Asmar, I. Gautier, B. Laloux, L. Guize, P. Ducimetiere & A. Benetos. *Aortic stiffness is an independent predictor of all-cause and cardiovascular mortality in hypertensive patients.* Hypertension, vol. 37, no. 5, pages 1236–1241, 2001.

[Lee 94] T. C. Lee, R.L. Kashyap & C.N. Chu. *Building Skeleton Models via 3-D Medial Surface Axis Thinning Algorithms.* CVGIP: Graphical Models and Image Processing, vol. 56, no. 6, pages 462–478, 1994.

[Lemaitre 11] C. Lemaitre, M. Perdoch, A. Rahmoune, J. Matas & J. Miteran. *Detection and matching of curvilinear structures.* Pattern Recognition, vol. 44, no. 7, pages 1514–1527, 2011.

[Lesage 09] D. Lesage, E.D. Angelini, I. Bloch & G. Funka-Lea. *A review of 3D vessel lumen segmentation techniques: models, features and extraction schemes.* Medical Image Analysis, vol. 13, no. 6, pages 819–845, 2009.

[Li 07] C. Li, C.-Y. Kao, J.C. Gore & Z. Ding. *Implicit Active Contours Driven by Local Binary Fitting Energy.* In Computer Vision and Pattern Recognition, 2007. CVPR '07. IEEE Conference on, pages 1–7, june 2007.

[Lorigo 00] L. M. Lorigo, O. Faugeras, W. E. L. Grimson, R. Keriven, R. Kikinis, A. Nabavi & C.-F. Westin. *Codimension-two geodesic active contours for the segmentation of tubular structures*. In Proc. IEEE Conf. Computer Vision and Pattern Recognition, volume 1, pages 444–451, 2000.

[Lorigo 01] L.M. Lorigo, O.D. Faugeras, W.E.L. Grimson, R. Keriven, R. Kikinis, A. Nabavi & C.-F. Westin. *CURVES: Curve evolution for vessel segmentation*. Medical Image Analysis, vol. 5, no. 3, pages 195–206, 2001.

[Lowell 04] J. Lowell, A. Hunter, D. Steel, A. Basu, R. Ryder, E. Fletcher & L. Kennedy. *Optic nerve head segmentation*. IEEE Transactions on Medical Imaging, vol. 23, no. 2, pages 256–264, feb. 2004.

[Luboz 05] V. Luboz, X. Wu, K. Krissian, C.-F. Westin, R. Kikinis, S. Cotin & S. Dawson. *A Segmentation and Reconstruction Technique for 3D Vascular Structures*. In James Duncan & Guido Gerig, editeurs, Medical Image Computing and Computer-Assisted Intervention, MICCAI 2005, volume 3749 of *Lecture Notes in Computer Science*, pages 43–50. Springer Berlin, Heidelberg, 2005.

[Ma 03] W.-C. Ma, F.-C. Wu & M. Ouhyoung. *Skeleton extraction of 3D objects with radial basis functions*. In Shape Modeling International, 2003, pages 207–215, may 2003.

[Makowski 02] P. Makowski, T. S. S. S. V. Therkildsen, A. Materka, H. Stodkilde-Jorgensen & E. M. Pedersen. *Two-phase active contour method for semiautomatic segmentation of the heart and blood vessels from MRI images for 3D visualization*. Computerized Medical Imaging and Graphics, vol. 26, no. 1, pages 9–17, 2002.

[Malladi 95] R. Malladi, J.A. Sethian & B.C. Vemuri. *Shape modeling with front propagation: a level set approach*. Pattern Analysis and Machine Intelligence, IEEE Transactions on, vol. 17, no. 2, pages 158–175, feb 1995.

[Manniesing 06] R. Manniesing, B.K. Velthuis, M.S. van Leeuwen, I.C. van der Schaaf, P.J. van Laar & W.J. Niessen. *Level set based cerebral vasculature segmentation and diameter quantification in CT angiography.* Medical Image Analysis, vol. 10, no. 2, pages 200–214, 2006.

[Markl 10] M. Markl, W. Wallis, S. Brendecke, J. Simon, A. Frydrychowicz & A. Harloff. *Estimation of global aortic pulse wave velocity by flow-sensitive 4D MRI.* Magnetic Resonance in Medicine, vol. 63, no. 6, pages 1575–1582, 2010.

[Mattace-Raso 10] F. Mattace-Raso, A. Hofman, G.C. Verwoert, J. Witteman, I. Wilkinson, J. Cockcroft, C. McEniery, L. Yasmin, P. Boutouyrie, E. Bozec*et al.* *Determinants of pulse wave velocity in healthy people and in the presence of cardiovascular risk factors:'establishing normal and reference values.* European Heart Journal, vol. 31, no. 19, pages 2338–2350, 2010.

[Mersa 99] S. S. Mersa & A. M. Darwish. *A new parallel thinning algorithm for gray scale images.* In IEEE Nonlinear Signal and Image Proc. Conf, pages 409–413, 1999.

[Mohan 09] V. Mohan, G. Sundaramoorthi, A. Stillman & A. Tannenbaum. *Vessel Segmentation with Automatic Centerline Extraction Using Tubular Tree Segmentation.* In CI2BM09 - MICCAI Workshop on Cardiovascular Interventional Imaging and Biophysical Modelling, pages 666–673, 2009.

[Monga 94] O. Monga, R. Lengagne & R. Deriche. *Crest lines extraction in volume 3D medical images: a multi-scale approach.* In Pattern Recognition, 1994. Vol. 1 - Conference A: Computer Vision Image Processing., Proceedings of the 12th IAPR International Conference on, volume 1, pages 553–555, oct 1994.

[Montanari 68] U. Montanari. *A Method for Obtaining Skeletons Using a Quasi-Euclidean Distance.* J. ACM, vol. 15, no. 4, pages 600–624, oct 1968.

[Moret 98] J. Moret, R. Kemkers, J. Op De Beek, R. Kloppe, E. Klotz & M. Grass. *3D rotational angiography: Clinical value in endovascular treatment.* Medicamundi, vol. 42, pages 8–14, 1998.

[Musse 03] O. Musse, F. Heitz & J. P. Armspach. *Fast deformable matching of 3D images over multiscale nested subspaces. Application to atlas-based MRI segmentation.* Pattern Recognition, vol. 36, no. 8, pages 1881–1899, 2003.

[Naf 96] M. Naf, O. Kubler, R. Kikinis, M.E. Shenton & G. Szekely. *Characterization and recognition of 3D organ shape in medical image analysis using skeletonization.* In Mathematical Methods in Biomedical Image Analysis, 1996., Proceedings of the Workshop on, pages 139–150, jun 1996.

[Näf 97] M. Näf, G. Székelykely, R. Kikinis, M.E. Shenton & O. Kübler. *3D Voronoi Skeletons and Their Usage for the Characterization and Recognition of 3D Organ Shape.* Computer Vision and Image Understanding, vol. 66, no. 2, pages 147–161, 1997.

[Nain 04] D. Nain, A. Yezzi & G. Turk. *Vessel Segmentation Using A Shape Driven Flow.* In Proceedings of MICCAI, St. Malo, France, 2004.

[Nowinski 09] W. Nowinski, A. Thirunavuukarasuu, I. Volkau, Y. Marchenko, B. Aminah, F. Puspitasari & V. Runge. *A Three-Dimensional Interactive Atlas of Cerebral Arterial Variants.* Neuroinformatics, vol. 7, pages 255–264, 2009.

[Nowinski 11] W.L. Nowinski, B.C. Chua, Y. Marchenko, F. Puspitsari, I. Volkau & M.V. Knopp. *Three-dimensional reference and stereotactic atlas of human cerebrovasculature from 7 Tesla.* NeuroImage, vol. 55, no. 3, pages 986–998, 2011.

[Okada 07] T. Okada, Y. Miki, K. Kikuta, N. Mikuni, S. Urayama, Y. Fushimi, A. Yamamoto, N. Mori, H. Fukuyama, N. Hashimoto & K. Togashi. *Diffusion Tensor Fiber*

Tractography for Arteriovenous Malformation: Quantitative Analyses to Evaluate the Corticospinal Tract and Optic Radiation. American Journal of Neuroradiology, vol. 28, pages 1107–1113, 2007.

[Osher 88] S. Osher & J.A. Sethian. *Fronts propagating with curvature-dependent speed: Algorithms based on Hamilton-Jacobi formulations.* Journal of Computational Physics, vol. 79, no. 1, pages 12–49, 1988.

[Otsu 79] N. Otsu. *A Threshold Selection Method from Gray-Level Histograms.* IEEE Transactions on Systems, Man and Cybernetics, vol. 9, no. 1, pages 62–66, 1979.

[Palágyi 02] K. Palágyi. *A 3-subiteration 3D thinning algorithm for extracting medial surfaces.* Pattern Recognition Letters, vol. 23, no. 6, pages 663–675, 2002.

[Palágyi 08] K. Palágyi. *A 3D fully parallel surface-thinning algorithm.* Theoretical Computer Science, vol. 406, pages 119–135, 2008.

[Papademetris 06] X. Papademetris, M. Jackowski, N. Rajeevan, M. DiStasio, H. Okuda, R. T. Constable & L.H. Staib. *BioImage Suite: An integrated medical image analysis suite: An update.* Computer software. Available from http://www. bioimagesuite. org, vol. n/a, pages n/a–n/a, 2006.

[Passat 05a] N. Passat, C. Ronse, J. Baruthio, J.-P. Armspach & C. Maillot. *Cerebral vascular atlas generation for anatomical knowledge modeling and segmentation purpose.* In Computer Vision and Pattern Recognition, 2005. CVPR 2005. IEEE Computer Society Conference on, volume 2, pages 331–337, june 2005.

[Passat 05b] N. Passat, C. Ronse, J. Baruthio, J.-P. Armspach, C. Maillot & C. Jahn. *Region-growing segmentation of brain vessels: An atlas-based automatic approach.* Journal of Magnetic Resonance Imaging, vol. 21, no. 6, pages 715–725, 2005.

[Passat 06] N. Passat, C. Ronse, J. Baruthio, J. P. Armspach & C. Maillot. *Magnetic resonance angiography: From*

anatomical knowledge modeling to vessel segmentation. Medical Image Analysis, vol. 10, no. 2, pages 259–274, 2006.

[Passat 07] N. Passat, C. Ronse, J. Baruthio, J. P. Armspach & J. Foucher. *Watershed and multimodal data for brain vessel segmentation: Application to the superior sagittal sinus.* Image and Vision Computing, Elsevier, vol. 25, pages 512–521, 2007.

[Pechaud 09] M. Pechaud, R. Keriven & G. Peyre. *Extraction of tubular structures over an orientation domain.* In Computer Vision and Pattern Recognition, 2009. CVPR 2009. IEEE Conference on, pages 336–342, june 2009.

[Pellot 94] C. Pellot, A. Herment, M. Sigelle, P. Horain, H. Maitre & P. Peronneau. *A 3D reconstruction of vascular structures from two X-ray angiograms using an adapted simulated annealing algorithm.* Medical Imaging, IEEE Transactions on, vol. 13, no. 1, pages 48–60, mar 1994.

[Perfetti 07] R. Perfetti, E. Ricci, D. Casali & G. Costantini. *Cellular Neural Networks With Virtual Template Expansion for Retinal Vessel Segmentation.* Circuits and Systems II: Express Briefs, IEEE Transactions on, vol. 54, no. 2, pages 141–145, feb. 2007.

[Pesaresi 01] M. Pesaresi & J. A. Benediktsson. *A new approach for the morphological segmentation of high-resolution satellite imagery.* IEEE Transactions on Geoscience and Remote Sensing, vol. 39, no. 2, pages 309–320, 2001.

[Piccinelli 09] M. Piccinelli, A. Veneziani, D. A. Steinman, A. Remuzzi & L. Antiga. *A Framework for Geometric Analysis of Vascular Structures: Application to Cerebral Aneurysms.* IEEE Transactions on Medical Imaging, vol. 28, no. 8, pages 1141–1155, 2009.

[Pieper 04] S. Pieper, M. Halle & R. Kikinis. *3D Slicer.* In Proceedings of the 1st IEEE International Symposium on Biomedical Imaging: From Nano to Macro 2004, pages 632–635. IEEE International Symposium on Biomedical Imaging ISBI 2004, 04 2004.

[Pieper 06] S. Pieper, B. Lorensen, W. Schroeder & R. Kikinis. *The NA-MIC Kit: ITK, VTK, pipelines, grids and 3D slicer as an open platform for the medical image computing community.* In Biomedical Imaging: Nano to Macro, 2006. 3rd IEEE International Symposium on, pages 698–701, april 2006.

[Pitas 92] I. Pitas & A.N. Venetsanopoulos. *Order statistics in digital image processing.* Proceedings of the IEEE, vol. 80, no. 12, pages 1893–1921, dec 1992.

[Pizer 98] S.M. Pizer, D. Eberly, D. S. Fritsch & B. S. Morse. *Zoom-Invariant Vision of Figural Shape: The Mathematics of Cores.* Computer Vision and Image Understanding, vol. 69, no. 1, pages 55–71, 1998.

[Plaza 04] A. Plaza, P. Martinez, R. Perez & J. Plaza. *A New Approach to Mixed Pixel Classification of Hyperspectral Imagery Based on Extended Morphological Profiles.* Pattern Recognition, Elsevier, vol. 37, pages 1091–1116, 2004.

[Prinet 95] V. Prinet, O. Mona & J. M. Rocchisani. *Multidimensional vessels extraction using crest lines.* In Engineering in Medicine and Biology Society, 1995., IEEE 17th Annual Conference, volume 1, pages 393–394, sep 1995.

[Qian 09] X. Qian, M.P. Brennan, D.P. Dione, W.L. Dobrucki, M.P. Jackowski, C.K. Breuer, A.J. Sinusas & X. Papademetris. *A non-parametric vessel detection method for complex vascular structures.* Medical Image Analysis, vol. 13, no. 1, pages 49–61, 2009.

[Quek 01] F.K.H. Quek & C. Kirbas. *Vessel extraction in medical images by wave-propagation and traceback.* Medical Imaging, IEEE Transactions on, vol. 20, no. 2, pages 117–131, feb 2001.

[Roes 08] S.D. Roes, R. Alizadeh Dehnavi, J.J.M. Westenberg, H.J. Lamb, B.J.A. Mertens, J.T. Tamsma & A. de Roos. *Assessment of Aortic Pulse Wave Velocity and Cardiac Diastolic Function in Subjects With and Without the*

Metabolic Syndrome. Diabetes Care, vol. 31, no. 7, pages 1442–1444, 2008.

[Rönnback 07] M. Rönnback, M. Hernelahti, E. Hämäläinen, P.H. Groop & H. Tikkanen. *Effect of physical activity and muscle morphology on endothelial function and arterial stiffness*. Scandinavian Journal of Medicine & Science in Sports, vol. 17, no. 5, pages 573–579, 2007.

[Rost 98] U. Rost, H. Münkel & C.-E. Liedtke. *A Knowledge Based System for the Configuration of Image Processing Algorithms*, 1998.

[Rueckert 97] D. Rueckert, P. Burger, S.M. Forbat, R.D. Mohiaddin & G.-Z. Yang. *Automatic tracking of the aorta in cardiovascular MR images using deformable models*. Medical Imaging, IEEE Transactions on, vol. 16, no. 5, pages 581–590, 1997.

[Saeed 10] K. Saeed, M. Tabedzki, M. Rybnik & M. Adamski. *K3M: A universal algorithm for image skeletonization and a review of thinning techniques*. International Journal of Applied Mathematics and Computer Science, vol. 20, no. 2, pages 317–335, 2010.

[Santamarıa-Pang 06] A. Santamarıa-Pang, T.S. Bıldea, C.M. Colbert, P. Saggau & I.A. Kakadiaris. *Towards segmentation of irregular tubular structures in 3D confocal microscope images*. In Proc. MICCAI International Workshop in Microscopic Image Analysis and Applications in Biology, Copenhangen, Denmark, pages 78–85, 2006.

[Säring 07] D. Säring, J. Fiehler, N. Forkert, M. Piening & H. Handels. *Visualization and Analysis of Cerebral Arteriovenous Malformation combining 3D and 4D MR Image Sequences*. International Journal of Computer Assisted Radiology and Surgery, vol. 2, pages 75–79, 2007.

[Sarwal 94] A. Sarwal & A. P. Dhawan. *3-D reconstruction of coronary arteries*. In Proceedings of the 16th Annual International Conference of the IEEE Engineering in Medicine and Biology Society,, volume 1, pages 504–505, 1994.

[Sato 98] Y. Sato, S. Nakajima, N. Shiraga, H. Atsumi, S. Yoshida, T. Koller, G. Gerig & R. Kikinis. *Three-dimensional multi-scale line filter for segmentation and visualization of curvilinear structures in medical images.* Medical Image Analysis, vol. 2, no. 2, pages 143–168, 1998.

[Schindelin 12] J. Schindelin, I. Arganda-Carreras, E. Frise, V. Kaynig, M. Longair, T. Pietzsch, S. Preibisch, C. Rueden, S. Saalfeld, B. Schmid, J.-Y. Tinevez, D. J. White, V. Hartenstein, K. Eliceiri, P. Tomancak & A. Cardona. *Fiji: an open-source platform for biological-image analysis.* Nature Methods, vol. 9, no. 7, pages 676–682, 2012.

[Schirmacher 98] H. Schirmacher, M. Zöckler, D. Stalling & H.-C. Hege. *Boundary Surface Shrinking - a Continuous Approach to 3D Center Line Extraction.* In In Image and Multidimensional Digital Signal Processing, pages 25–28. IEEE, 1998.

[Schmitt 04] S. Schmitt, J. F. Evers, C. Duch, M. Scholz & K. Obermayer. *New methods for the computer-assisted 3-D reconstruction of neurons from confocal image stacks.* NeuroImage, vol. 23, no. 4, pages 1283–1298, 2004.

[Schroeder 98] W. Schroeder, K.M. Martin & W.E. Lorensen. The visualization toolkit (2nd ed.): an object-oriented approach to 3d graphics. Prentice-Hall, Inc., 1998.

[Schroeder 03] W. Schroeder, K. Martin & B. Lorensen. The visualization toolkit: an object-oriented approach to 3d graphics (3rd edition). Kitware, Inc, 2003.

[Serra 82] J. Serra. Image analysis and mathematical morphology, volume 1. Academic Press, 1982.

[Shang 08] Y. Shang, X. Yang, L. Zhu, R. Deklerck & E. Nyssen. *Region competition based active contour for medical object extraction.* Computerized Medical Imaging and Graphics, Elsevier, vol. 32, no. 2, pages 109–117, 2008.

[Shang 11] Y. Shang, R. Deklerck, E. Nyssen, A. Markova, J. de Mey, X. Yang & K. Sun. *Vascular Active Contour for Vessel Tree Segmentation.* IEEE Transactions on Biomedical Engineering, vol. 58, no. 4, pages 1023–1032, 2011.

[Siddiqi 02] K. Siddiqi, S. Bouix, A. Tannenbaum & S.W. Zucker. *Hamilton-Jacobi Skeletons.* International Journal of Computer Vision, vol. 48, pages 215–231, 2002.

[Söderman 00] M. Söderman, B. Karlsson, L. Launnay, B. Thuresson & K. Ericson. *Volume measurements of cerebral arteriovenous malformations from angiography.* Neuroradiology , Springer-Verlag, vol. 42, pages 697–702, 2000.

[Soille 86] P. Soille. *Introduction to Mathematical Morphology.* Comput. Vis., Graph., Image Process., vol. 35, pages 283–305, 1986.

[Squillacote 06] A.H. Squillacote & J. Ahrens. The paraview guide. Kitware, 2006.

[Squillacote 07] A. H. Squillacote. The paraview guide: A parallel visualization application. Kitware, 2007.

[Staal 04] J. Staal, M. D. Abrámoff, M. Niemeijer, M. A. Viergever & B. Van Ginneken. *Ridge-Based Vessel Segmentation in Color Images of the Retina.* IEEE Transactions on Medical Imaging, vol. 23, no. 4, pages 501–509, 2004.

[Stevanov 01] M. Stevanov, J. Baruthio, D. Gounot & D. Grucker. *In vitro validation of MR measurements of arterial pulse-wave velocity in the presence of reflected waves.* Journal of Magnetic Resonance Imaging, vol. 14, no. 2, pages 120–127, 2001.

[Suri 02] J. S. Suri, K. Liu, L. Reden & S. Laxminarayan. *A review on MR vascular image processing: skeleton versus nonskeleton approaches: part II.* IEEE Transactions on Information Technology in Biomedicine, vol. 6, no. 4, pages 338–350, 2002.

[Tagliasacchi 09] A. Tagliasacchi, H. Zhang & D. Cohen-Or. *Curve skeleton extraction from incomplete point cloud.* ACM Trans. Graph., vol. 28, no. 3, pages 711–719, 2009.

[Tek 05] H. Tek, A. Ayvacı & D. Comaniciu. *Multi-scale vessel boundary detection.* In Computer Vision for Biomedical Image Applications, pages 388–398. Springer, 2005.

[Thirion 92] J.-P. Thirion & A. Gourdon. *The 3D marching lines algorithm and its application to crest lines extraction.* Rapport de recherche 1672, INRIA, 1992.

[Toledo 00] R. Toledo, X. Orriols, P. Radeva, X. Binefa, J. Vitria, C. Canero & J.J. Villanuev. *Eigensnakes for vessel segmentation in angiography.* In Pattern Recognition, 2000. Proceedings. 15th International Conference on, volume 4, pages 340–343, 2000.

[Tsai 85] W. H. Tsai. *Moment-preserving thresolding: A new approach.* Computer Vision, Graphics, and Image Processing, Elsevier, vol. 29, pages 377–393, 1985.

[Tyrrell 07] J.A. Tyrrell, E. di Tomaso, D. Fuja, R. Tong, K. Kozak, R.K. Jain & B. Roysam. *Robust 3-D Modeling of Vasculature Imagery Using Superellipsoids.* Medical Imaging, IEEE Transactions on, vol. 26, no. 2, pages 223–237, feb. 2007.

[van Bemmel 03] C.M. van Bemmel, L.J. Spreeuwers, M.A. Viergever & W.J. Niessen. *Level-set-based artery-vein separation in blood pool agent CE-MR angiograms.* Medical Imaging, IEEE Transactions on, vol. 22, no. 10, pages 1224–1234, oct. 2003.

[van der Geest 98] R.J. van der Geest, R.A. Niezen, E.E. van der Wall, A. de Roos & J.H.C. Reiber. *Automated Measurement of Volume Flow in the Ascending Aorta Using MR Velocity Maps: Evaluation of Inter- and Intraobserver Variability in Healthy Volunteers.* Journal of Computer Assisted Tomography, vol. 22, no. 6, pages 904–911, 1998.

[van Elderen 11] S.G.C. van Elderen, A. Brandts, J. van der Grond, J.J.M. Westenberg, L.J.M. Kroft, M.A. van Buchem,

J.W.A. Smit & A. de Roos. *Cerebral Perfusion and Aortic Stiffness Are Independent Predictors of White Matter Brain Atrophy in Type 1 Diabetic Patients Assessed With Magnetic Resonance Imaging.* Diabetes Care, vol. 34, no. 2, pages 459–463, 2011.

[van Rooij 08] W.J. van Rooij, M.E. Sprengers, A.N. de Gast, J.P.P. Peluso & M. Sluzewski. *3D rotational angiography: the new gold standard in the detection of additional intracranial aneurysms.* American Journal of Neuroradiology, vol. 29, no. 5, pages 976–979, 2008.

[Vitanovski 12] D. Vitanovski, K. Ralovich, R. Ionasec, Y. Zheng, M. Suehling, W. Krawtschuk, J. Hornegger & D. Comaniciu. *Personalized learning-based segmentation of thoracic aorta and main branches for diagnosis and treatment planning.* In Biomedical Imaging (ISBI), 2012 9th IEEE International Symposium on, pages 836–839. IEEE, 2012.

[Vlachopoulos 10] C. Vlachopoulos, K. Aznaouridis & C. Stefanadis. *Prediction of Cardiovascular Events and All-Cause Mortality With Arterial StiffnessA Systematic Review and Meta-Analysis.* Journal of the American College of Cardiology, vol. 55, no. 13, pages 1318–1327, 2010.

[Vulliémoz 02] S. Vulliémoz, N. Stergiopulos & R. Meuli. *Estimation of local aortic elastic properties with MRI.* Magnetic resonance in medicine, vol. 47, no. 4, pages 649–654, 2002.

[Žitkevičius 07] E. Žitkevičius, D. Grigaitis & D. Navakauskas. *On Skeletonization of Blood Vessels in Angiographic MRI Images of Human Brain.* Information Technology and Control, vol. 36, no. 4, pages 372–376, 2007.

[Wang 00] Y.-X. Wang, M. Halks-Miller, R. Vergona, M. E. Sullivan, R. Fitch, C. Mallari, B. Martin-McNulty, V. da Cunha, A. Freay, G. M. Rubanyi & K. Kauser. *Increased aortic stiffness assessed by pulse wave velocity in apolipoprotein E-deficient mice.* AJP - Heart and Circulatory Physiology, vol. 278, pages 428–434, 2000.

[Wang 04] Q. Wang, M.D. Robson, J.M. Francis, S.E. Petersen, K.M. Channon, S. Neubauer & F. Wiesmann. *Accuracy of Quantitative MR Vessel Wall Imaging Applying a Semi-Automated Gradient Detection Algorithm- A Validation Study.* Journal of Cardiovascular Magnetic Resonance, vol. 6, no. 4, pages 895–907, 2004.

[Wang 06] L. Wang & G. Leedham. *Gray-Scale Skeletonization of Thermal Vein Patterns Using the Watershed Algorithm in Vein Pattern Biometrics.* In Computational Intelligence and Security, 2006 International Conference on, volume 2, pages 1597–1602, nov. 2006.

[Wang 11] C. Wang, H. Frimmel & Ö. Smedby. *Level-set based vessel segmentation accelerated with periodic monotonic speed function.* In SPIE Medical Imaging, pages 79621M–79621M, 2011.

[Webb 12] S. Webb. Webb's physics of medical imaging. Taylor & Francis, 2012.

[Wesarg 04] S. Wesarg & E. A. Firle. *Segmentation of vessels: the corkscrew algorithm.* In Proceedings of SPIE The International Society for Optical Engineering, volume 3, pages 1609–1620, 2004.

[Westenberg 98] J.J.M. Westenberg, M.N.J.M. Wasser, R.J. van der Geest, P.M.T. Pattynama, A. de Roos, J. Vanderschoot & J.H.C. Reiber. *Variations in blood flow waveforms in stenotic renal arteries by 2D phase-contrast cine MRI.* Journal of Magnetic Resonance Imaging, vol. 8, no. 3, pages 590–597, 1998.

[Westenberg 10] J.J.M. Westenberg, A. de Roos, H.B. Grotenhuis, P. Steendijk, D. Hendriksen, P.J. van den Boogaard, R.J. van der Geest, J.J. Bax, J.W. Jukema & J.H.C. Reiber. *Improved aortic pulse wave velocity assessment from multislice two-directional in-plane velocity-encoded magnetic resonance imaging.* Journal of Magnetic Resonance Imaging, vol. 32, no. 5, pages 1086–1094, 2010.

[Wilkinson 97] I.B. Wilkinson, J.R. Cockcroft & D.J. Webb. *Pulse wave analysis and arterial stiffness.* Journal of cardiovascular pharmacology, vol. 32, pages S33–7, 1997.

[Wilkinson 03] M. Wilkinson, T. Wijbenga, G. De Vries & M. Westenberg. *Blood vessel segmentation using moving-window robust automatic threshold selection.* In International Conference on Image Processing - ICIP 2003, Proceedings 10th International Conference, Vol. 2, IEEE Signal Processing Society, Barcelona, Spain, 1093-1096, 2003.

[Wink 00] O. Wink, W.J. Niessen & M.A. Viergever. *Fast delineation and visualization of vessels in 3-D angiographic images.* Medical Imaging, IEEE Transactions on, vol. 19, no. 4, pages 337–346, april 2000.

[Worz 07] S. Worz & K.. Rohr. *Segmentation and Quantification of Human Vessels Using a 3-D Cylindrical Intensity Model.* Image Processing, IEEE Transactions on, vol. 16, no. 8, pages 1994–2004, aug. 2007.

[Wu 03] F.-C. Wu, W.-C. Ma, P.-C. Liou, R.-H. Laing & M. Ouhyoung. *Skeleton Extraction of 3D Objects with Visible Repulsive Force*, 2003.

[Yan 06] P. Yan & A. A. Kassim. *Segmentation of volumetric MRA images by using capillary active contour.* Medical Image Analysis, vol. 10, no. 3, pages 317–329, 2006.

[Yaniv 06] Z. Yaniv & K. Cleary. *Image Guided Procedures: A Review.* Computer Aided Interventions and Medical Robotics, vol. 3, pages na–na, 2006.

[Yim 00] P.J. Yim, P.L. Choyke & R.M. Summers. *Gray-scale skeletonization of small vessels in magnetic resonance angiography.* Medical Imaging, IEEE Transactions on, vol. 19, no. 6, pages 568–576, june 2000.

[Yu 04] Z. Yu & C. Bajaj. *A segmentation-free approach for skeletonization of gray-scale images via anisotropic vector diffusion.* In Computer Vision and Pattern Recognition, 2004. CVPR 2004. Proceedings of the 2004 IEEE Computer Society Conference on, volume 1, pages 415–420, 2004.

[Yu 06] H.-Y. Yu, H.-H. Peng, J.-L. Wang, C.-Y. Wen & W.-Y. I. Tseng. *Quantification of the pulse wave velocity of the descending aorta using axial velocity profiles from phase-contrast magnetic resonance imaging*. Magnetic Resonance in Medicine, vol. 56, no. 4, pages 876–883, 2006.

[Yuan 09] X. Yuan, J. Trachtenberg, S. Potter & B. Roysam. *MDL Constrained 3-D Grayscale Skeletonization Algorithm for Automated Extraction of Dendrites and Spines from Fluorescence Confocal Images*. Neuroinformatics, vol. 7, pages 213–232, 2009.

[Yushkevich 06] P. A. Yushkevich, J. Piven, H.C. Hazlett, R.G. Smith, S. Ho, J. C. Gee & G. Gerig. *User-Guided 3D Active Contour Segmentation of Anatomical Structures: Significantly Improved Efficiency and Reliability*. Neuroimage, vol. 31, no. 3, pages 1116–1128, 2006.

[Zana 01] F. Zana & J. C. Klein. *Segmentation of vessel-like patterns using mathematical morphology and curvature evaluation*. IEEE Transactions on Image Processing, vol. 10, no. 7, pages 1010 –1019, 2001.

[Zhang 03] X. Zhang, H. Shirato, H. Aoyama, S. Ushikoshi, T. Nishioka, D. Zhang & K. Miyasaka. *Clinical significance of 3D reconstruction of arteriovenous malformation using digital subtraction angiography and its modification with CT information in stereotactic radiosurgery*. Int. J. Radiation Oncology Biol. Phys., Elsevier, vol. 57, no. 5, pages 1392–1399, 2003.

[Zhao 09] F. Zhao, H. Zhang, A. Wahle, M.T. Thomas, A.H. Stolpen, T.D. Scholz & M. Sonka. *Congenital aortic disease: 4D magnetic resonance segmentation and quantitative analysis*. Medical image analysis, vol. 13, no. 3, pages 483–483, 2009.

[Zhu 96] S.C. Zhu & A. Yuille. *Region competition: Unifying snakes, region growing, and Bayes/MDL for multiband image segmentation*. Pattern Analysis and Machine Intelligence, IEEE Transactions on, vol. 18, no. 9, pages 884–900, 1996.